ANCHORAGE CAPACITY OF HEADED REINFORCED BARS IN CONCRETE

A Thesis

Submitted in partial fulfilment of the requirement for the award of degree of

Doctor of Philosophy

in

Civil Engineering

Submitted By

Payal Sachdeva

Reg. No.: 951602007

Supervisor(s)

Dr. Naveen Kwatra,

Professor
Department of Civil Engineering
Thapar Institute of Engineering & Technology
Patiala

Dr. A.B. Danie Roy,

Assistant Professor
Department of Civil Engineering
Thapar Institute of Engineering & Technology
Patiala

PATIALA - 147004

MAY 2022

CERTIFICATE

I, Payal Sachdeva, hereby declare that the thesis entitled, "Anchorage Capacity of Headed Reinforced Bars in Concrete," submitted to Thapar Institute of Engineering and Technology, Patiala, in partial fulfilment of the requirement of the award of Degree of **Doctor of Philosophy** in **Civil Engineering** is a record of original and independent research work done by me during 2016-2021. This thesis has been conducted under the supervision and guidance of **Dr. Naveen Kwatra**, Professor, Department of Civil Engineering, Thapar Institute of Engineering and Technology, Patiala, and **Dr. A.B. Danie Roy**, Assistant Professor, Department of Civil Engineering, Thapar Institute of Engineering and Technology, Patiala. It has not formed the basis for the award of any Degree to any candidate of any university.

Payal Sachdeva

Payal Sachdeva **Date: 31-05-2022**

Reg. No.: 951602007

This is to certify that the above-mentioned statement made by the candidate is correct to the best of my knowledge.

Dr. Naveen Kwatra,

Professor
Department of Civil Engineering
Thapar Institute of Engineering & Technology
Patiala

Dr. A.B. Danie Roy,

Assistant Professor
Department of Civil Engineering
Thapar Institute of Engineering & Technology
Patiala

ACKNOWLEDGEMENT

Working on a Ph.D. thesis has been a fantastic and, at times, overwhelming experience. Many people contributed to the effective completion of this thesis, and I would want to use this opportunity to thank them for their efforts.

Primarily, I would like to express my gratitude to the Almighty, who has given me the strength to carry out this task with honesty and dedication.

I consider it an honor to express my heartfelt gratitude to my supervisors, Dr. Naveen Kwatra, Professor, and Dr. A.B. Danie Roy, Assistant Professor, Civil Engineering Department, for their guidance, sound advice, excellent supervision, insightful suggestions, and assistance throughout this thesis. They helped me complete the tasks by sharing their vast experience and providing essential advice.

I extend my thanks to Dr. Prem Pal Bansal, Head of the department, Civil Engineering, Thapar Institute of Engineering and Technology, for his support and advice in my journey of Ph.D. I owe a debt of gratitude to the members of the doctorate committee, Dr. Heaven Singh, Dr. Sandeep Sharma, and Dr. Shweta Goyal, for their continuous encouragement and insightful comments.

Further, I wish to thank all technicians & workers in the structural and concrete lab, particularly Mr. Ram Sumiran, Mr. Virender Sharma, Mr. Roop Kumar, and many others.

I'm also grateful to the Thapar Institute of Engineering and Technology, Patiala for providing the research facility. Words cannot express my gratitude to the Civil Engineering Department's other academic and staff members for their intellectual support during my time here.

This acknowledgment would be incomplete if I don’t mention the deepest appreciation, blessings, and encouragement that I have received from my beloved father, Mr. Pawan Sachdeva, my mother, Mrs. Kamlesh Rani, and my family, without whose constant support and prayers this Ph.D. would have been a distant dream. I am extremely grateful to my loving

husband, Dr. Akshay Chaudhary, and my beloved in-laws for their moral encouragement and continuous support throughout my research work. I would also like to express my gratitude to my good friends and well-wishers who assisted me with my thesis work.

Needless to say, errors and omissions are mine.

Payal Sachdeva

ABSTRACT

In reinforced cement concrete (RCC) structures, the bond between the concrete and the steel bar is critical. When the member geometry is insufficient for the full development of straight bars, headed bars can be used to anchor reinforcing steel due to the shorter development lengths and compact size, they can reduce congestion in the beam-column joints. Fiber-reinforced cementitious composites have been increasingly used in recent years on beam-column joints and the introduction of headed bars is a practical solution to eliminate the congestion problem caused by hooked bars in beam-column joints. The key in this study is the headed reinforced bar, which is used to anchor the steel in the concrete instead of straight or hooked bars. There has been very little research on the behavior of headed bars in RCC structures, especially when they are used with high-strength concrete. The ASTM A970 and ACI 318-19 codes are used to design and manufacture headed bars. The design provisions of ACI 318-19 limit the yield strength of headed bars to 413.68 MPa and concrete compressive strength to 41.6 MPa due to the limited research performed on headed bars to date. The main parameters in this study are concrete compressive strength, steel bar diameter, percentage of steel fibers, and head shape. The influence of head shapes (Square, Circular, and Rectangular), concrete compressive strength (M20, M40, and M60), the diameter of steel bar (16, 20, and 25 mm), and steel fibers (0, 0.5, 1, and 1.5%) on the anchorage capacity of headed bars have been evaluated. The behavior of headed bars in concrete is investigated through 324 pullout tests, embedded concentrically at depth of eight times the bar diameter in the cylindrical specimens having size 150 X 300 mm. Additionally, the International Federation for Structural Concrete (fib) provides the code MC2010 for advanced design methods for concrete structures and the application of improved structural materials, and EN 1992-1-1 gives a general basis for the design of structures in plain and reinforced concrete. Therefore, the comparison analysis of bond stress for all the specimens have been made using these three codes as mentioned above. Also, the bearing capacity of concrete has been calculated and compared with the pullout capacity of the headed bars. Two failure modes namely, steel and concrete-blowout have been observed and the prevailing mode of failure is steel failure. Based on load-deflection curves and derived descriptive equations, it is observed that the circular headed bars have displayed the highest peak load.

The present study also emphasizes the evaluation of the performance of steel fiber reinforced concrete (SFRC) external beam-column joints (BCJ) using headed bars as an anchorage mechanism and the comparison has been made with the conventional bars which have been detailed in accordance with ACI 318-19 and ACI 352R-02. The repository of previous BCJ work has been further expanded by researching the effect of structural parameters i.e. compressive strength (M20 and M40) and steel fibers (1 and 1.5%) on the hysteresis curve, ductility, stiffness, energy dissipation, and cracking on all specimens. The experimental results have revealed that the conventional bars can be significantly replaced by the headed bars for the areas vulnerable to earthquakes due to their higher load carrying capacity with better ductility and stiffness response and reducing congestion in BCJ. The anchorage strength of headed bars has been determined using the test results of beam-column joint specimens. A numerical model for improving the anchorage capacity of headed bars has also been proposed using non-linear regression analysis through dummy variables. Results have revealed that the anchorage capacity of headed bars increases with the increase in concrete compressive strength, the diameter of steel bar, and steel fibers, which have been validated by non-linear regression analysis using dummy variables. The developed equations using non-linear regression analysis have been compared to test results from previous studies to come up with new development length design criteria. Genetic programming has been used to create a model that predicts the maximum load-carrying capacity of headed bars when subjected to direct pull-out load in this research. The GP model is based on a large and reliable database containing 324 test specimens and four variables that control the load-carrying capacity of headed bars: concrete compressive strength, bar diameter, bar embedment depth, and percentage of steel fibers. In comparison to the peak load equation developed using regression analysis, the proposed model using GP provides the most accurate peak load prediction and is the most fitting to the experimental database. Also, the bond strength equation for the headed bars has been predicted using regression analysis and has been compared to the bond strength formula given by ACI 318-19, in which two main factors i.e., compressive strength of concrete and percentage of steel fibers are missing. After analyzing the bond strength, it has been determined that the bond strength has been improved by adding compressive strength and steel fiber factors. Thus, these two factors should be included in the ACI 318-19 code.

TABLE OF CONTENT

LIST OF FIGURES

LIST OF TABLES

ABBREVIATIONS & NOTATIONS

SYMBOL	REMARK
A_b	Area of bar
A_{nh}	Net head area
A_N	Projected area of concrete breakout failure
A_{No}	Projected area of a single anchored bar
A_{ts}	Area of tension reinforcement
ACI	American Concrete Institute
ASTM	American Society for Testing and Materials
BCJ	Beam-Column Joint
B.S	Bond strength
b_{js}	Effective width of the joint transverse to the direction of shear
CBF	Concrete blowout failure
CCD	Concrete capacity design
CED	Cumulative energy dissipation
CFRP	Concrete fiber reinforced polymer
CS	Control specimen
CSA	Canadian Standards Association
d_b	Diameter of reinforced bar
d_c	Depth of the column
E	Young's modulus
EN	European standards
f_{bd}	Design bond strength
$f_{bd,0}$	Basic bond strength

f_c’	Compressive strength of concrete
f_{cm}	Measured compressive strength
f_{ctd}	Design value of concrete tensile strength
f_{ctm}	Mean value of axial tensile strength of concrete
$F_{ctk, 0.05}$	Characteristic tensile strength
fib	International Federation for Structural Concrete
$f_{s, ACI}$	Peak load applied on a specimen divided by the area of headed bars (Calculated bar stress)
f_{su}	Peak load applied on a specimen divided by the area of headed bars (Experimental bar stress)
f_y	Yield stress of reinforcement
f_{yk}	Yield strength for reinforcing steel in tension
GP	Genetic Programming
HRC	Headed reinforcement corporation
HS	Headed bar specimen
h_{st}	Height of the column
l_d	Development length of hooked bars
l_{dh}	Development length of headed bars
l_{eh}	Embedment depth
LVDT	Linear variable differential transformer
MC	Model code
M_{pr}	Beam support moment
NC	Normal concrete
N_p	Pull-out strength of a single-headed bar as per ACI 318-19 code
N_{pr}	Pull-out strength of a single-headed bar as per CSA A23.3-19 code
P_{max}	Maximum load carried by the headed bar

P_n	Bearing capacity of the specimen
P_{tr}	Mean compression stress
P_u	Ultimate load
P_{UPC}	Pullout cone capacity
R^2	R-squared/Coefficient of determination
RC	Reinforced concrete
RCC	Reinforced cement concrete
RED	Relative energy dissipation
REG	Regression Analysis
SBF	Steel bar failure
SF	Steel fibers
SFRC	Steel fiber reinforced concrete
T	Average load of the bar in failure divided by number of headed bars (Test failure load)
T_c	Average load of the bar in failure divided by number of headed bars (Calculated failure load)
T_h	Anchorage capacity of headed bars
T_f	Tension force in the reinforcement
T_s	Peak load of closely spaced headed bars
UFC	Ultra high strength
UTM	Universal testing machine
V_c	Shear in the column calculated based on M_{pr} for beam
V_n	Nominal shear strength of the joint
V_u	Horizontal joint shear force
ϕ_c	Nominal diameter of the bar
γ	Shear strength factor reflecting confinement of joint by lateral member

α	Stress multiplier for longitudinal reinforcement at joint-member interface for Type-2
α_2	Influence of passive confinement from cover
α_3	Coefficient of transverse reinforcement
α_{ct}	Coefficient taking account of long-term effects on the tensile strength and of unfavorable effects
δ_u	Ultimate displacement
δ_y	Yield displacement
μ	Ductility factor
η_1	Coefficient for ribbed bars
η_2	Casting position of the bar
η_3	Bar diameter
η_4	Characteristic strength of steel reinforcement

CHAPTER 1

INTRODUCTION

1.1 Background

The anchorage capacity of reinforcing bars in reinforced concrete structures is the most important aspect of structural design, and the type of anchorage mechanism determines it. Using straight bars or hooked bars to anchor longitudinal flexural reinforcing bars terminating at the joint of beam-column leads to steel congestion, which causes fabrication issues, concrete compaction, honeycombing, joint strength, and other construction issues.

Hooked bars are used to reduce anchorage length, but the bend of the hook will often not fit within the dimensions of a member, or the hooks will cause congestion and make an element challenging to construct (Shao 2016). A standard hook provides additional anchorage when there is insufficient length to develop a deformed bar. The minimum embedment length required under the ACI 318-19 Building Code is called the development length. However, due to the limited column depth, such as in external beam-column joints, straight reinforcement cannot always meet the development length requirement because they require a much shorter development length than hooked bars, which can be provided by headed reinforcing bars (Bashandy 1996).

Mechanical anchorages (headed bars) have been used in the reinforced concrete structures to simplify the design and construction of complex details. However, research conducted over the last fifty years has revealed how they behave and how effective they are compared to traditional solutions (Marques and Jirsa 1975; Bashandy 1996). A mechanical anchorage system with heads attached to the ends of the reinforcing bar is known as a headed bar. There are varieties of head attachment techniques available, including friction welding, forged welding, and threading. Headed bars have been first used in Europe to construct offshore oil platforms and then in North America, where they have been used extensively on the Hibernia platform in Newfoundland, Canada. Headed bar as longitudinal and transverse reinforcement

for relatively large reinforced concrete structures subjected to high seismic loads is becoming more popular. Platforms for the offshore oil industry have been constructed with headed reinforcement. However, headed bars have not been widely used in other structures such as bridges, buildings, and other traditional concrete structures. There is currently little guidance in code provisions or published research for the design of headed bar anchorage (Thompson *et al.* 2002). The current requirements in ACI 318-19 place far more restrictions on the use of headed bars than on hooked bars. As a result, higher-strength steel or concrete provides far less benefit when using headed bars than hook anchorage.

Additionally, the exact spacing between bars anchored with heads must be at least four times the diameter of the bar ($4d_b$) (Bashandy 1996). Headed bars with head sizes, obstructions, or interruptions that do not meet the ASTM A970 requirements cannot be used in building structures (Bashandy 1996). As a result, creating a larger experimental database that would improve the understanding of headed bar behavior and allow for improved code provisions that would remove many of the current restrictions on headed bars would be extremely beneficial.

The research of the last few decades shows that using nonuniform steel fibers in concrete in smaller quantities to improve shear strength without using a higher stirrups ratio is a viable option. These randomly distributed discontinuous steel fibers increase the tensile strength and strain capacity by arresting the early crack formation and decreasing the crack formation rate by bridging the cracks after initiation (Ganesan *et al.* 2007; Holschemacher *et al.* 2010; Kaikea *et al.* 2014; Brantschen *et al.* 2016). Therefore, SFRC is an effective and alternative way to improve the structural member's shear strength and inelastic response without special confinement in the joint region. SFRC also improves the anchorage capacity of headed bars in beam-column joints despite its short anchorage length. The steel fibers reduce the formation of the cracks at an early stage in the headed reinforced concrete structures (Hameed *et al.* 2013). It is also effective in terms of one other important parameter, i.e., toughness, and used mainly for the application of fiber-reinforced concrete in earthquake-resistant structures (Yang *et al.* 2010). Also, steel fibers significantly reduce the risk of cracking and make the joints stronger by reducing the spalling of joint edges (Kamel *et al.* 2006). Additionally, the fibers provide the mechanical bond with the concrete to resist pull-out (Chiu *et al.* 2016). To enhance the post-

cracking behavior of the concrete, fibers can be imparted in concrete as they control the opening or dissemination of the crack by acting as a bridge (Bentur and Mindess 1990). In this context, several researchers explored the influence of steel fibers on the bonding of steel-concrete (Harajli and Shalloukh 1997; Harajli *et al.* 2002; Harajli and Gharzeddine 2007; Dancygier *et al.* 2010; Dancygier and Katz 2012). Some investigators observed that the fibers are only effective in concrete with a higher strength (65 MPa) and bars with a higher diameter (20 mm) and, in some instances, often decrease bonding strength by up to 30 % (Robins *et al.* 2002). The mechanical behavior of concrete mix often differs by varying the percentage and types of fibers in the concrete mix. However, in few cases it has been observed steel fibres exhibit brittle behaviour. In general, less percentage of steel fiber content (< 2% of the concrete volume) in the mix only improve the compression and tension behavior after cracking. In contrast, higher percentage of steel fiber content (> 2% of the concrete volume) improves both peak load and post cracking (Abbas and Iqbal Khan 2016). However, the same parameters related to the fiber, such as their size, modulus of elasticity, tensile strength, aspect ratio, and the bond between the concrete mix, affect the material's overall behavior (Kaikea *et al.* 2014).

1.2 Problem Statement

For better performance of beam-column joints, a proper reinforcement anchorage system is essential. To simplify and speed up the construction process, an effective and innovative technology should be introduced in the industry (Choi et al. 2002). However, conventional reinforcement in beam-column joints of reinforced concrete structures is reported to cause congestion and construction difficulties. The present need of construction should take care of the following issues: (i) Congestion due to hooks or bend up bars used in the beam-column joints (Figure 1.1) (ii) application of a high amount of reinforcement which increases the amount of construction material leading to cost overrun, (iii) availability of a massive number of skilled and semi-skilled workers at the site, and (iv) completion of construction projects within the scheduled time (Bashandy 1996).

Old building constructions made of reinforced concrete (RC) may have serious structural flaws and are considered substandard by current seismic design criteria (Setia *et al.* 2009). Failure of beam-column joints is the main cause of building collapse during earthquakes around the world. The main points of vulnerability are anchorage failure of main reinforcing bars in beams and columns, and column shear failures (Delhomme *et al.* 2015). Traditional failure modes have also been identified and shown in Figure 1.2. Figure 1.2 (a) is due to longitudinal concrete splitting, while Figure 1.2 (b) is primarily due to the shearing failure of concrete between lugs, these reduce the element's bonding capacity, and it may cause a phenomenon known as blowout, which involves a violent eruption of concrete around the bar (Marchetto 2015).

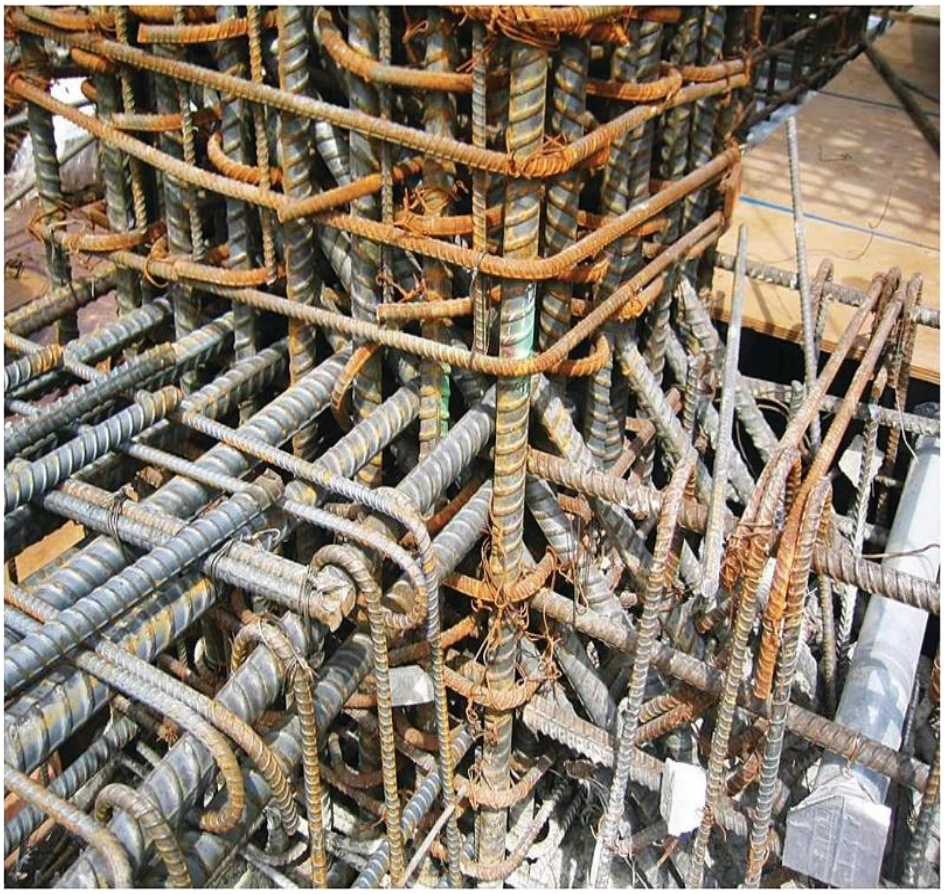

Figure 1. 1 Congestion in the beam-column joint due to the use of conventional bars (Bashandy 1996)

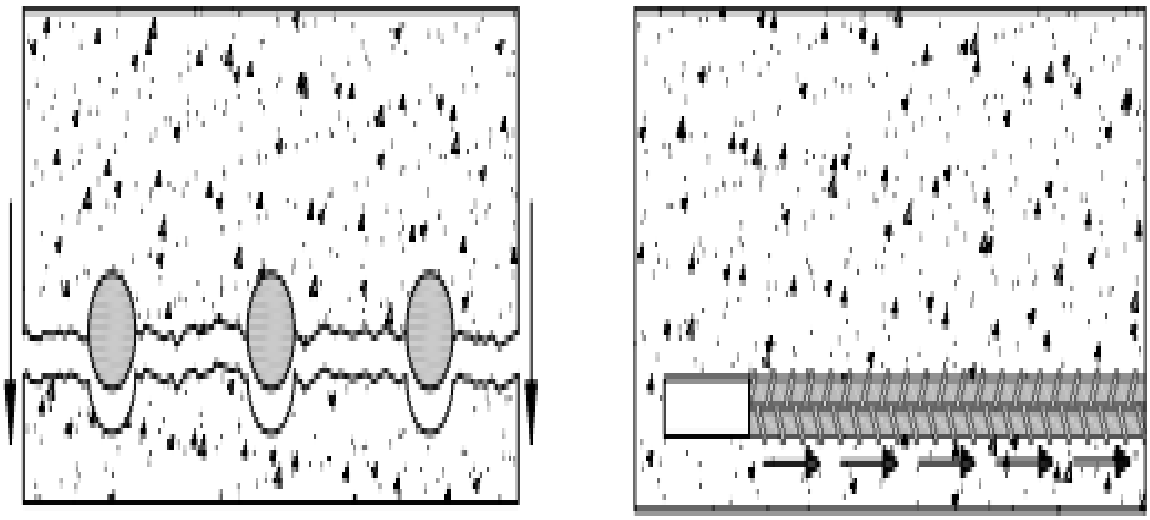

(a) **(b)**

Figure 1. 2 Failure modes: splitting and pull-out (Marchetto 2015)

The headed bars can replace the conventional bars to reduce congestion, as shown in Figure 1.3. The American Concrete Institute (ACI)-352 recommends further research on T-headed bar (mechanical anchorage) to design beam-column connections in concrete structures. Thus, headed bars have been developed to solve all the above problems, as these require a much shorter development length than straight reinforcing bars (Figure 1.4) (Stoker *et al.* 1974). This study brings to the attention of the designers the theoretical background of the design and detailing of beam-column joints using headed bars.

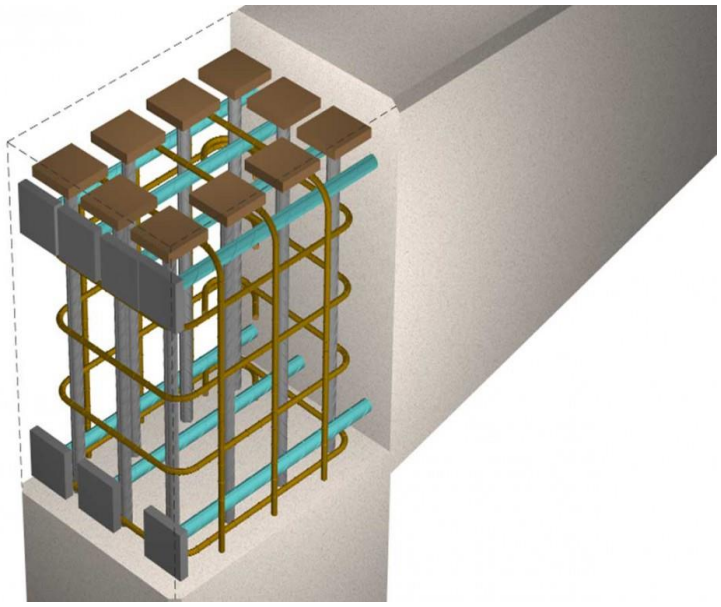

Figure 1. 3 Reduced congestion after using the headed bars in the beam-column joints (Choi *et al.* 2002)

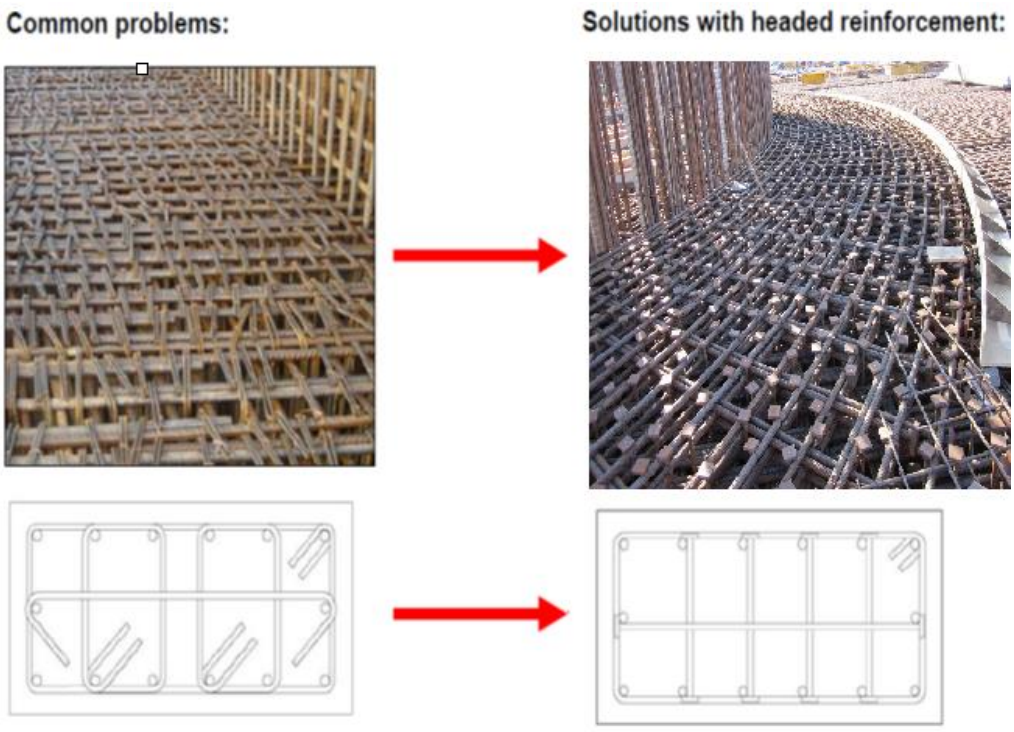

Figure 1. 4 Solutions with headed reinforcement (Park *et al.* 2003)

1.3 Research Significance

A headed bar combines a deformed bar, and the steel plate joined at one or both sides of the bar through various methods such as threaded joint, welding joint, or nuts or bolts. The tensile load applied on the bar is ultimately being taken to the head. Thus, the bond between the bar and the surrounding concrete gets affected (Naito *et al.* 2001; Delhomme *et al.* 2015, 2016; Alrasyid *et al.* 2017), as shown in Figure 1.5. The different shapes of heads have been used until now, such as square, rectangular and circular (Stoker *et al.* 1947; Naito *et al.* 2001; Choi *et al.* 2002; Choi 2006) plates have been fixed according to the American Concrete Institute (ACI), and American Society for Testing and Materials (ASTM).

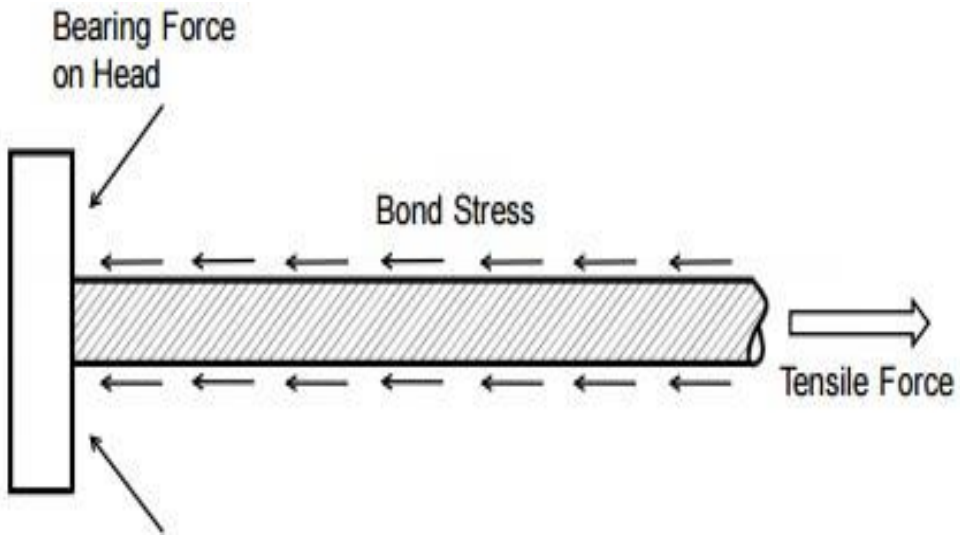

Figure 1. 5 Force transfer on a headed bar (ASTM A970)

Several types of research have been executed on headed bars' behavior until now, but there is limited research on the headed bars, including steel fibers. Thus, the objective of this research is to check the anchorage capacity of headed bars in the steel fiber-mixed concrete. Additionally, the International Federation for Structural Concrete (fib) provides the code MC2010 for advanced design methods for concrete structures and the application of improved structural materials. EN 1992-1-1 provides a broad base for the design of structures in plain

reinforced concrete. Therefore, the comparison analysis of bond stress for the specimens has been made using these three codes as mentioned above.

1.4 Research gaps

Previous research has looked into headed bars in RCC structures based on pull-out tests and beam-column joints' properties. Many researchers (Jeffrey and Wright (1997); Bindhu *et al.* 2008; Ramanjaneyulu *et al.* 2013a; Hasaballa (2018)) have conducted pull-out tests on headed bars experimentally and validated through the analytical models. The provisions of ACI 318-19 on headed bars place limitations on concrete compressive strength, bar yield strength, bar spacing, cover and the effect of steel fibers in RCC. As a result, more research is required to look into the impact of the percentage of steel fibers added in the concrete mix on the behavior of joints with headed reinforcement. Though many researchers have studied the effect of fibers on conventional bars in RCC structures, but only a few have looked at the impact of fibers on headed bars. It is recommended by ACI 318-19 that headed reinforcement be inserted into the joint core at a depth of at least $12d_b$. Shorter lengths may be possible; however, further testing is required to confirm this for bars anchored within a joint or isolated bar pull-out test. The effect of epoxy coating on the anchorage behavior of headed bars can be considered in further research. The impact of lightweight aggregate concrete on the anchorage behavior of headed bars should also be investigated in the future. It is a good idea to look into the conduct of non-contact spliced-headed bars and the use of large-diameter bars. A general nonlinear finite element model of lap splice joints with headed bars is also required. More research is needed to fully understand whether a rectangular loading plate differs from a square plate of the same area. Chun *et al.* (2009) limited his analysis on high-strength headed bars to a specific type of headed bar with a net area four times the bar area. In this field, research that is more experimental is required. Also, there is limited research on the shapes of headed bars used in RCC. As a result, future research should focus on incorporating steel fibers in RCC structures with headed reinforcement, and various shapes of headed bars should be investigated. In addition, there has been no model developed for headed bars using Genetic Programming (GP).

1.5 Scope and Objectives of the study

The present research aims to develop design criteria for headed bars covering a more comprehensive range of material and member properties. Additionally, the objective of this study is to see how different diameters of headed bars with varying types of head shapes cast with varying percentages of steel fibers affect the strength of the bond between the concrete and headed bar. The use of headed bars in conjunction with steel fibers added to the concrete matrix is a unique feature of this study. The addition of steel fibers reduces the risk of cracking and strengthens the joints by reducing the spalling of joint edges. The fibers also provide a mechanical bond with the concrete, preventing pull-out (Canzac 2019).

The development length provisions for headed reinforcing bars in the current ACI 318-19 Building Code include limits on concrete compressive strength, bar yield strength, and bar spacing. Due to an absence of experimental data when developed, the Code provisions imposed these limitations.

The scope of this research is to gain a better understanding of headed bar behavior and its application to a broader range of reinforced concrete members, such as headed bars with steel fibers, shallow embedment of headed bars in reinforced cement concrete (RCC) structures, and beam-column joints subjected to reversed cyclic loading, for developing suitable alternatives.

Based upon the gaps as reported earlier, the objectives of the proposed study are as follows:

1. To investigate the effectiveness of headed bars having particular emphasis on parameters: different head shapes, steel fibers percentage, compressive strength of concrete, the diameter of bars, and embedment length of bars.
2. To study the anchorage capacity of headed bars in beam-column joints (T-joint) having steel fibers.
3. To develop an analytical model to predict the anchorage behavior of headed bars.

1.6 Thesis organization

This thesis is divided into six chapters:

Chapter 1 of this thesis includes an introduction. It identifies the problems that motivated this research and briefly discusses the importance of headed bars and their anchorage capacity in reinforced concrete structures.

Chapter 2 provides an extensive literature review on the behavior of headed bars. Their anchorage capacity in steel fibers reinforced concrete structures, research gaps, scope, and current research objectives.

Chapter 3 discusses the experimental methodology, including properties of materials used in the experimental work, casting, and testing procedure in detail.

Chapter 4 reports the results and discussion of headed bars through the pull-out test.

Chapter 5 reports the results and discussion of headed bars in beam-column joints.

Chapter 6 presents the findings and conclusions of this study and the possibilities for further research.

CHAPTER 2

LITERATURE REVIEW

2.1 Introduction

Various researchers have performed the pull-out test to depict headed bars' anchorage capacity and bond strength in different concrete structures such as beams, cylinders, cubes, beam-column joints, slabs, etc. The anchorage capacity of headed bars is affected by a variety of factors including bar diameter, head area, head aspect ratio, embedment length, concrete strength, and confinement effects. Using various mathematical models generated from Genetic Programming (GP) and regression analysis, the researchers have also developed development length equations required for headed bars.

2.2 Effect of the anchorage capacity of headed reinforcing bars in concrete

Due to lack of experimental data needed to develop detailed design criteria, Stoker et al. 1947; Jeffrey and Wright 1997; Naito et al. 2001; Choi et al. 2002; Choi 2006 have used headed bars to construct structures globally by the late twentieth century, despite their increasing use in offshore platforms and bridges. As a result, scientists began testing to establish code provisions for headed bar anchorage.

The study of headed anchorage began when Viest (1956) evaluated the shear transfer mechanism between beam and plate in 12 specimens where the concrete plate had been joined with wide-flange steel bolts. He used headed steel bolts with a smooth shank. One of the earliest ways to describe the shear strength of headed studs was proposed by Viest (1956). McMackin *et al.* (1973) put 32 concrete block specimens with headed anchor studs through their paces by loading them in tension and shear. The research has contributed in the enhancement of headed steel stud anchorage design requirements. Using Grade 60 No. 11, No. 14, and No. 18 headed deformed bars with square steel plates attached to their ends, Stoker *et al.* (1974) discovered that the embedment length required to generate a headed bar is 62 percent of that necessary to develop a straight bar. Dilger and Ghali (1981) examined the use of headed studs as shear

reinforcement in slabs to address challenges in concrete placement caused by closely placed stirrups. Headed studs made reinforcement construction easier and allowed large shear stresses to be transferred, according to the results of 40 full-scale slab-column joint specimens. Dilger and Ghali (1981) proposed rules for the placement and spacing of headed studs for shear based on their research. These rules have been updated over time and are now included in ACI 318-14 Section 22.6. In their original form, they are no longer in use. Wright and McCabe (1997) used ASTM A944-95 to test 70 beam-end specimens with friction-welded headed bars, 180° hooked bars, and straight bars, as shown in Figure 2.1. The tests revealed that headed bars never failed at lower loads than hooked bars and that their load-slip and failure behavior has been similar. As the provision of transverse reinforcement and cover dimension changed, the performance of headed bars varied similarly to that of hooked bars. However, as more transverse reinforcement was added, the benefit of the increased cover was reduced.

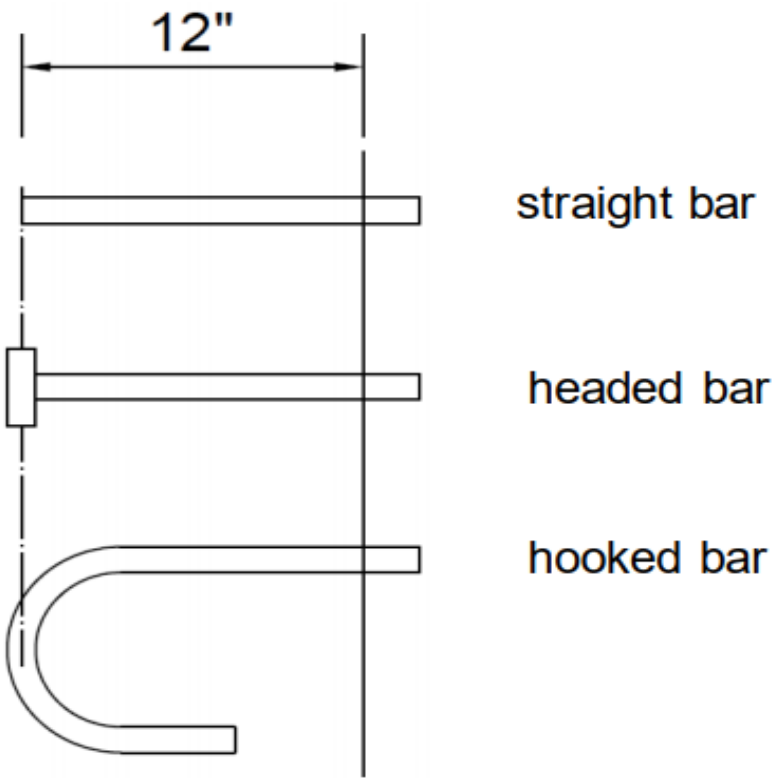

Figure 2. 1 Embedment length for different types of bars (Wright and McCabe 1997)

For the satisfactory performance of headed bars, ASTM A970 recommends a minimum yield strength of 420 MPa, close to the 413 MPa recommended by ACI 318-14. Cairns (2015) and Rabi (2020) conducted an experimental study to determine the effect of concrete strength on anchor load carrying capacity and discovered that anchorage capacity increases with concrete strength. Danie *et al.* (2016) and Vella *et al.* (2018) found similar results when flexural and tensile tests have been performed using headed bars. Bjorhovde (1983) and Lee and Chang (2017) suggested using high-strength concrete and high-strength reinforcement to achieve desired anchorage or bond behavior. Dong (2002) and Kang *et al.* (2003) also suggested that higher cross-sectional dimensions provide a larger surface area for failure, as well as a large angle of inclination for anchoring near the concrete surface. Thompson *et al.* (2005, 2006) investigated whether bond stress and slip are reduced by increasing the relative head area. Rao and Sundeep (2013) conducted another experiment on the anchorage strength of bonded anchors; on the other hand, the head diameter did not affect the anchors' load-carrying capacity. According to the study of Kang *et al.* (2003) and Kawale and Patil (2016), circular-headed bars are the most efficient among various head anchor shapes (circular, rectangular, square, and elliptical).

2.3 Effect of headed bars on bond strength of concrete

Breen (1964) investigated specimens with deeply embedded anchor bolts with bond lengths of 15 times the bolt diameter (Figure 2.2). Breen noticed three different failure mechanisms: longitudinal concrete cover splitting, side blowout of the concrete cover near the head, and bolt-steel failure. In some specimens, a combination of these failure mechanisms had been observed. Breen (1964) concluded from his analysis of the loaded end slip that the bond along the bolt provided an initial anchorage. As the loading increased, the bond deteriorated, causing the anchorage to be transferred to the head. The amount of cover provided and the concrete strength were the most critical factors determining the anchor bolts' ultimate capacity.

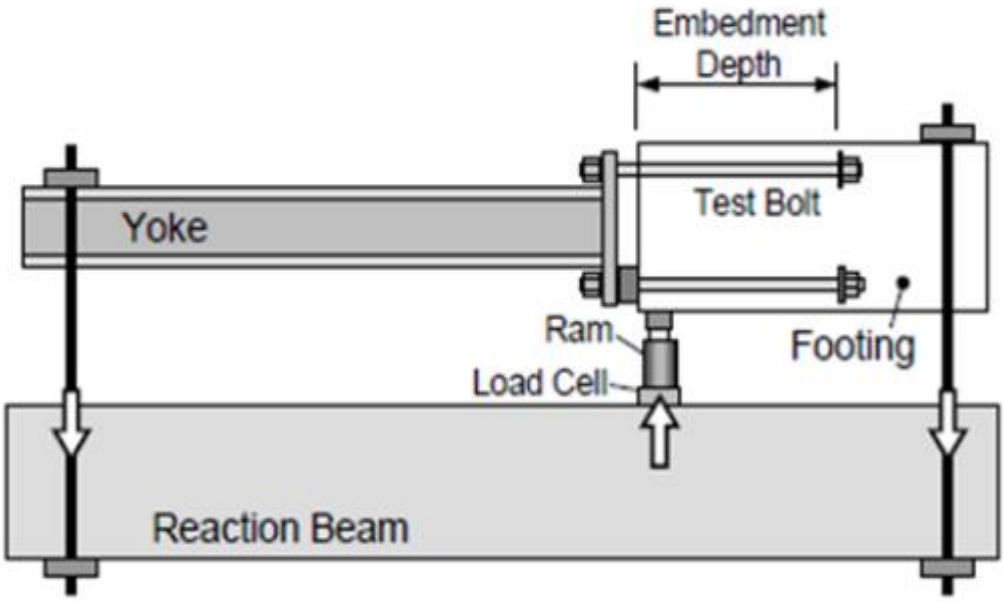

Figure 2. 2 Test setup and specimen (Breen 1964)

Similar tests have been carried out by Hasselwander *et al.* (1977); Kanchanadevi and Ramanjaneyulu (2019) to observe the behavior of anchor bolts with a variety of variables. The three failure mechanisms identified by Breen (1964) have been demonstrated once more in these tests. The authors noted how a wedge of crushed and compressed concrete, formed at the bearing face of the nut had been generated the lateral forces that split the concrete cover. The anchorage strength is thus influenced by the concrete cover and bearing area of the head and the concrete grade. Significant gains in strength and ductility have been observed when the specimens have included transverse reinforcement, especially those with a small cover. Furche and Eligehausen (1991) examined the parameters like embedment depth, cover, head area, and head angle while investigating single-headed anchors embedded in concrete specimens. Concrete breakout and side blowout were the failure modes that occurred (Figure 2.3). The load capacity was heavily influenced by the load-bearing area, with capacities dropping by up to 50% for head angles less than 90° due to increased lateral splitting forces (Figure 2.4). The diameter of the side blowout cone on specimens that failed in this mode was approximately 6 to 8 times the cover dimension.

The side blowout cone protruded only as the peak bolt capacity approached, according to measurements taken.

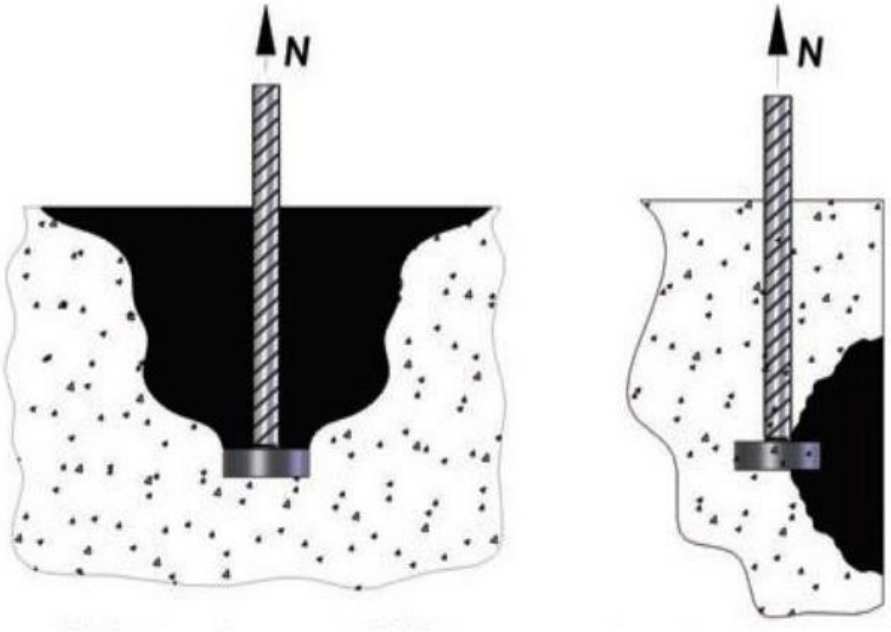

Figure 2. 3 (i) Concrete breakout and (ii) Side blowout (Thompson *et al.* 2002)

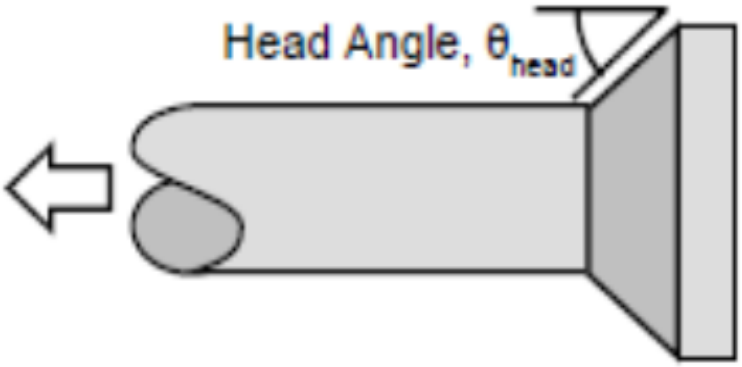

Figure 2. 4 Angle of the head (Thompson *et al.* 2002)

DeVries and Bashandy (1996) carried out shallow and deep embedment tests on headed bars at the University of Texas. They found that samples with transverse reinforcement had increased post-peak leftover anchorage strength as compared with unreinforced specimens in shallow embedment tests. When transverse reinforcement has been used, the bond development length provided some additional anchorage. As a result, the head slip was also reduced. Based on the CCD approach for side blowout, he proposed a model for pull-out cone capacity (PUPC (kN)), with an adjustment for the lower head bearing stresses arising in headed bars. DeVries and Bashandy (1996) also proposed that the failure cone start at the head perimeter rather than the centre of the bar. DeVries (1999) carried out deep embedment analysis on beam end specimens, in which variables included embedment depth, length of development, head geometry and orientation, transverse reinforcement, concrete strength, cover and corner, edges, and bars with close spacing. The majority of the specimens failed due to side blowout. According to his findings, increasing the bond length improved the headed bar's ultimate capacity and slipped resistance slightly (Figure 2.5). The head's shape, thickness, and aspect ratio did not affect the ultimate capacity. With increase in head size, side blowout failure increased linearly due to the less cover of concrete provided with in the specimen. The total head area that was tested ranged from two to thirteen times that of the bar. Increased capacity was achieved by increasing concrete strength and edge distance. Specimens with bars closer to a corner and bars that are closely spaced had reduced capacity.

Transverse reinforcement, such as U-bars that anchor the bar to the concrete specimen or bars that cross in front of the head, significantly improved residual post-peak capacity. By numerically modeling column base plate connections subjected to combined bending moment, axial, and shear loads, Bruckner *et al.* (2001) investigated the effect of compressive forces acting close to a tensioned anchor. The authors concluded that compressive forces improved the efficiency of adjacent tensile anchors and proposed a modification factor, moment, to be applied to the CCD method when calculating concrete cone resistance in these situations. Henriques *et al.* (2013) investigated the effect of adding additional confining reinforcement to headed anchors with embedment depths ranging from 150 to 260 mm. Surface grid reinforcement increases

capacity by up to 38 % in tests, with the benefit being more significant for shallower embedment depths.

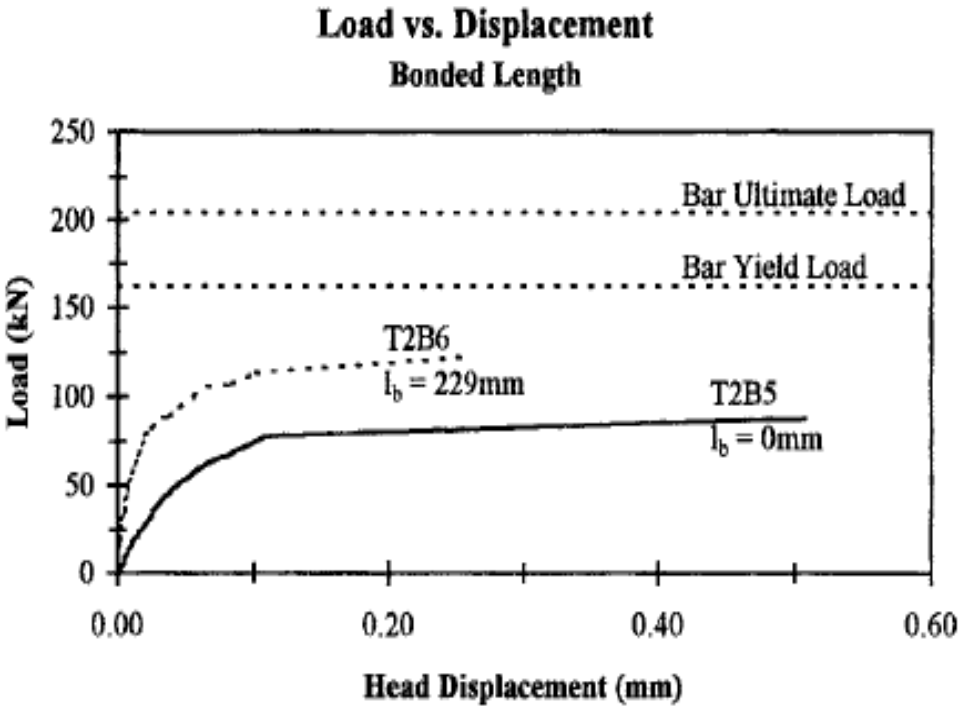

Figure 2. 5 Effect of bonded length on load-displacement behavior (DeVries *et al.*1999)

2.4 Effect of using headed bars in beam-column joints

Bashandy (1996) used regression analysis to develop a model for headed bar anchorage in 32 exterior beam-column joints and investigated the effects of embedment length, confining reinforcement, concrete cover to the bar, bar diameter, and head size on anchorage strength of headed bar. Side blowout, also known as concrete side cover spalling, caused the failure of eighteen specimens. In the other fourteen specimens, failure occurred along diagonal cracks in the joint region. The diagonal cracks formed along the strut head and the top face of a bearing plate have been used to simulate the compression zone of the beam. The anchorage strength of the headed bars increased with increasing embedment length, confining reinforcement, head size, and concrete cover, according to the test results.

Several researchers, Naito *et al.* (2001); Chun *et al.* (2007); Kang (2009a); Kang *et al.* (2009b); Lee and Yu (2009); Chun and Shin (2014); Kaliluthin and Kothandaraman (2017)) and Kumar and Chaudhary (2019) conducted experiments using headed reinforcement in beam-column joints, in addition to Bashandy (1996). Naito *et al.* (2001) tested four large-scale beam-column joints with headed longitudinal and transverse reinforcement. The experiments show that using headed transverse reinforcement gives similar results for using conventional reinforced joints. Chun *et al.* (2007) and Chun and Shin (2014) tested the exterior beam-column joints under cyclic loading using a 90-degree standard hook and mechanical anchorage. The experimental results revealed that specimens with mechanical anchorage behaved similarly to or better than joints constructed with hooked bars. The energy dissipation and ductility ratio were better in specimens with mechanical anchorage. The results of the tests revealed that transverse reinforcement is required to maintain joint strength after cracking. According to Chutarat and Aboutaha (2003), using straight-headed bars in the exterior beam-column joint for cyclic response effectively relocates potential plastic hinges in the beam for a seismic design using special detailing by headed bars. In structural moment resisting frames, plastic hinges usually form on the face of the column. Lee and Yu (2009b) used double mechanical anchorage to test six exterior beam-column joints with or without eccentricity. The results showed that the cyclic behavior of beam-column connections have been improved by using double mechanical anchorage at each beam bar. This device can reduce yield penetration and bond deterioration along the beam bar into the joint and prevent push-out on the back of the joint. Chun *et al.* (2009) and Hong *et al.* (2009) tested 24 exterior beam-column joints, and the model has been validated by comparing test results. According to analysis, a ratio of predicted-to-test values ranged from 0.87 to 1.24, with mean and coefficient of variation 1.00 and 10.6%, respectively. The performance of 30 full-scale simulated exterior beam-column joint specimens was investigated by Chun *et al.* (2009). There has been a total of twenty-four heads and six 90° hooked bars. In specimens with shallow embedment (50 percent of column depth), diagonal cracks extended above and below the anchored bar and failed due to concrete breakout similar to that seen in anchorage failure. According to Chun *et al.* (2009), anchorage strength increased as embedment length increased (Figure 2.6). According to Chun *et al.* (2009), failure modes such as side face blowout, concrete breakout, splitting, and joint shear used in models for the

anchorage strength of headed bars proposed by Bashandy (1996), DeVries (1996), and Thompson *et al.* (2006) do not accurately predict the concrete contribution to anchorage strength. As a result, Chun *et al.* (2009) proposed a model for the anchorage strength of headed bars based on bearing on the head and bond along the bar. The contributions of head bearing and bond to anchorage strength have been calculated using the strain distribution along the bar. Chun *et al.* (2009) calculated the anchorage strength as the sum of contributions from head bearing and bond along the bar. Kang *et al.* (2009a, 2009b, 2010, 2011) and Kang and Mitra (2012) experimented to see if headed bars with small heads could be used in exterior beam-column joints. Twelve pull-out tests have been conducted to examine the anchorage behavior of headed bars subjected to monotonic and repeated loading, with test variables including head size, shape, and head attaching technique. The seismic test results showed that the joint using small-headed bars performed better than the joint using hooked bars in damage index, lateral drift capacity, and energy dissipation. They can effectively anchor in exterior beam-column joints under inelastic deformation reversals. Chun *et al.* (2009) conducted additional tests to determine the side-face blowout capacity of 43 mm and 57 mm diameter bars anchored in beam-column joints. These large-diameter bars fall outside of the limits set by ACI 318-14. The authors concluded that as embedment length and side cover increase, side-face blowout strength increases. Hairpin reinforcement improved anchorage by limiting bond-splitting cracks and limiting head bearing confinement, whereas the ties used in these tests had little impact on anchorage strength. The yield strength of the headed bars tested has been achieved with a clear cover to the bar's shaft equal to one bar diameter by adding transverse reinforcement, increasing embedment length, or increasing concrete compressive strength. The authors used regression analysis and data from Bashandy (1996) to develop a model for headed bar anchorage in exterior beam-column joints, which included the effects of side cover and transverse reinforcement, with some limitations based on the variables in their test dataset. Shao (2016) investigated the anchorage behavior of headed bars under monotonic loading using 202 simulated exterior beam-column joint specimens. The test results revealed that headed bars with large obstructions ($2d_b$ diameter and $5.25d_b$ length) and bearing areas adjacent to the obstructions of at least $4.5A_b$ performed satisfactorily. In addition, damage to the structure must be avoided at all costs (Daniel *et al*. 2015). To withstand lateral force, beam-column joints must be properly designed and

detailed. This research raises designers' and field engineers' awareness of beam-column joint design and detailing.

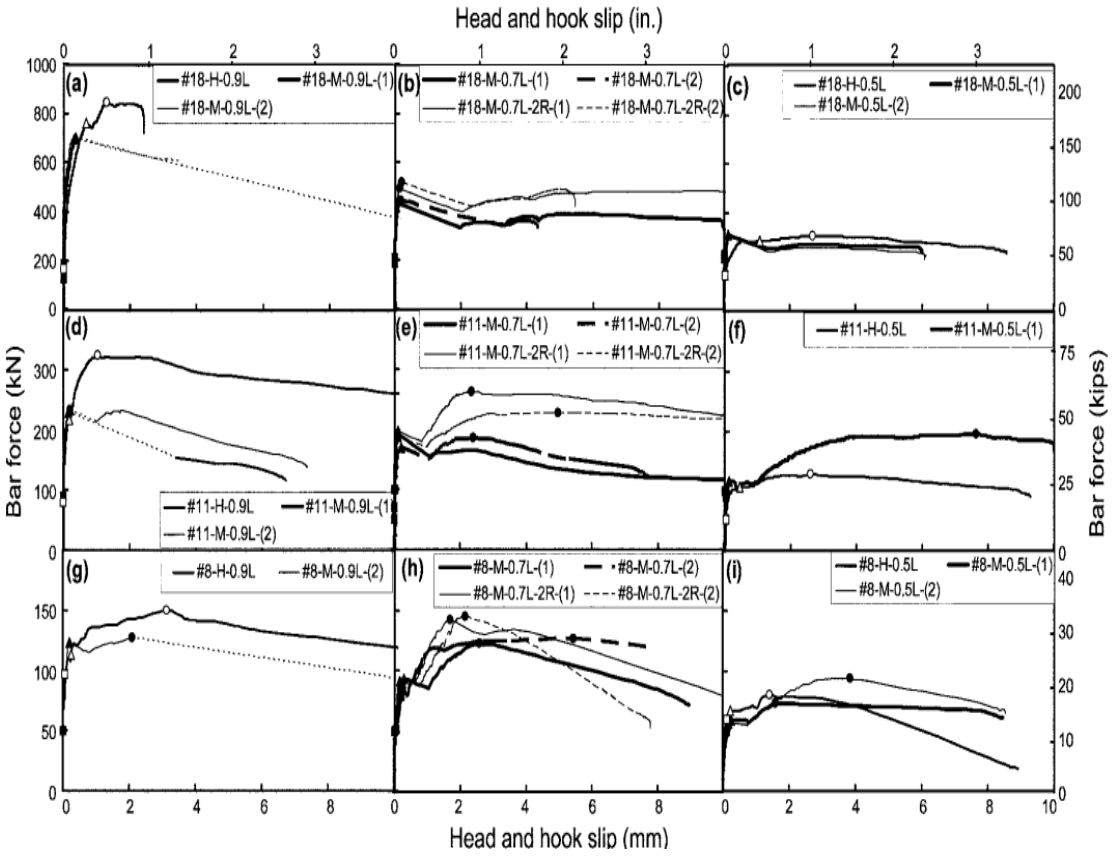

Figure 2.6 Bar force - head and hook slip (Chun *et al.* 2009)

2.5 Effect of steel fibers on conventional bars

SFRC joints should be considered in seismically prone areas, according to Paulay *et al.* (1986). Jiuru *et al.* (1992) investigated the effect of SFRC in the joint core on the cyclic behavior of beam-column joints and concluded that using SFRC in the joint core could improve ductility while avoiding steel congestion. The seismic performance of fiber-reinforced concrete joints has been investigated by Sallal *et al.* (2020). They discovered that concrete fibres' crack bridging mechanism improved shear resistance capacity, reducing the need for stiffer joint confinement. The volume and aspect ratio of the fibers determine the SFRC's performance. Andre *et al.* (1995)

compared the ductility of four full-scale beam-column joints with and without SFRC during earthquake excitation and found that SFRC improved joint ductility. The seismic behavior of steel-fiber reinforced beam-column joints has been studied by Lee and Yu (2009a). They came to the conclusion that SFRC's bridging and tensile behavior effectively controlled crack formation, effectively arresting diagonal cracks.

Hiremath and Yaragal (2018) and Farhan *et al.* (2020) found that SFRC can improve shear strength while reducing steel congestion in the joint region. The effect of ultra-high-strength steel fiber reinforced concrete (UFC) in beam-column joint strengthening has been investigated by Yung *et al.* (2007). They looked at the cyclic behavior of the UFC beam-column joint and found that it increased the rebar bond strength and joint shear strength. Ganesan *et al.* (2014) looked into the effect of fiber hybridization on the cyclic behavior of joints and found that it improved strength and ductility (Figure 2.7). They also suggested that hybrid fibers could be used in concrete to avoid steel congestion. David (2014) and Moreno *et al.* (2014) investigated how steel fiber reinforcement affected load distribution in statically indeterminate systems and concluded that the different traditional reinforcement content determined the load redistribution resulting from cracking. The majority of the additional load carrying capacity has been obtained by improving redistribution of steel fibers, which needs to be further investigated. Bilal *et al.* (2015) investigated the impact of SFRC and CFRP sheets on beam-column joint performance. Dhaval *et al.* (2015) investigated the use of hybrid fiber reinforced concrete for beam-column connection ductility enhancement and damage tolerance capacity. The hybrid fiber reinforced concrete could be used in seismically prone areas without critical shear reinforcement at the joint.

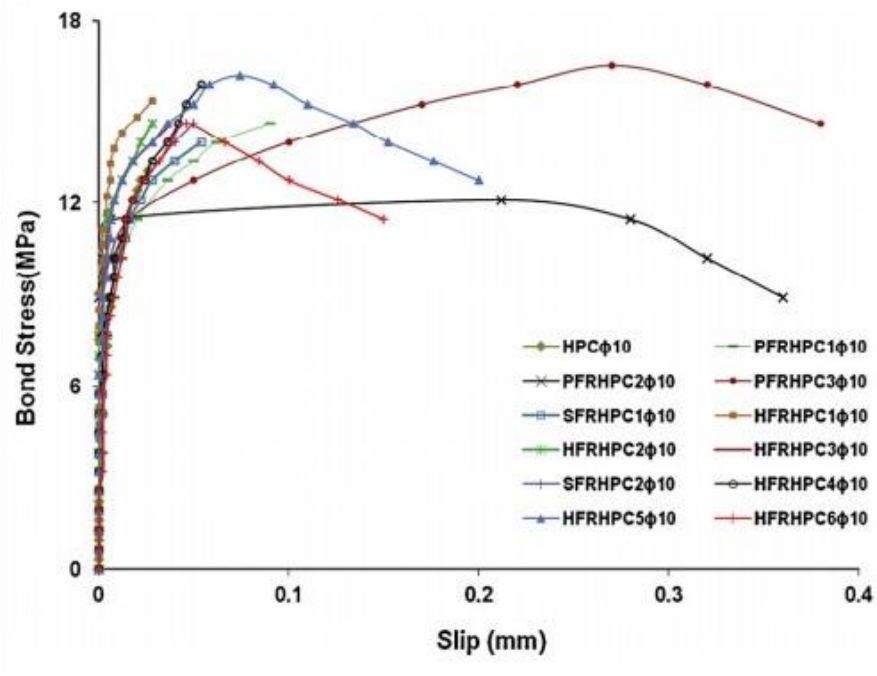

Figure 2. 7 Bond stress versus slip (Ganesan *et al.* 2014)

2.6 Effect of steel fibers on headed bars

The effect of steel fibers on the pull-out capacity of short-headed anchor bolts embedded in high-strength concrete has been investigated in the study of Al-Jaffal (2007). The results of the tests revealed that the embedment depth has a significant impact on the pull-out capacity. The addition of steel fibers and concrete compressive strength, an indirect measure of concrete's tensile strength, increases the pull-out capacity. The presence of steel fibers changed the brittle type of failure of the unreinforced specimens to a ductile type of failure (Banthia 1990). The failure angle with the horizontal plane varied between 20 and 30 degrees for all specimens. The tensile behavior and strength of cast-in-place short-headed anchor bolts embedded in both normal concrete (NC) and steel fiber reinforced concrete (SFRC) are discussed in the research of Al-Ta'An *et al.* (2013). A total of 108 specimens were subjected to monotonic tensile loading. 90 specimens failed due to a large concrete failure cone that exceeded the specimen's dimensions and, in the majority of cases, broke into pieces (concrete failure), while the remaining specimens failed due to bolt yielding or fracture (steel failure). The addition of steel fibers to the concrete

significantly increased the anchors' breakout capacity (P_u), and the size of the failure cone in (SFRC) specimens was smaller than the size of failure in (NC) specimens, according to the results of the tests.

Ishikawa *et al.* (2012) investigated the effect of steel fibers on beams having longitudinal headed bars and concluded that steel fibers effectively improve anchorage strength despite the poor bond between headed bar and the concrete. The volume ratio of steel fibers to concrete volume had a proportional reinforcing effect. Higher concrete strength resulted in higher anchorage strength (Figure 2.8). Rajagopal and Prabavathy (2015) assessed the performance of an exterior beam-column joint with proper reinforcement anchorage and joint core reinforcement bars. According to the results of the experimental tests, T-type mechanical anchorage systems as defined by ACI-352 provide better performance and crack control than specimens reinforced with conventional 90 bent hook anchorage as defined by ACI-318 and full anchorage defined by IS-456. In addition, the T-type mechanical anchorage joint detail has a higher moment carrying capacity, which improves seismic performance without sacrificing ductility and stiffness. Furthermore, compared to traditional 90 bent hook anchorage, this arrangement of reinforcement detail in the exterior beam-column joint core reduces reinforcement congestion, allows for easier concrete placement, and speeds up construction on site.

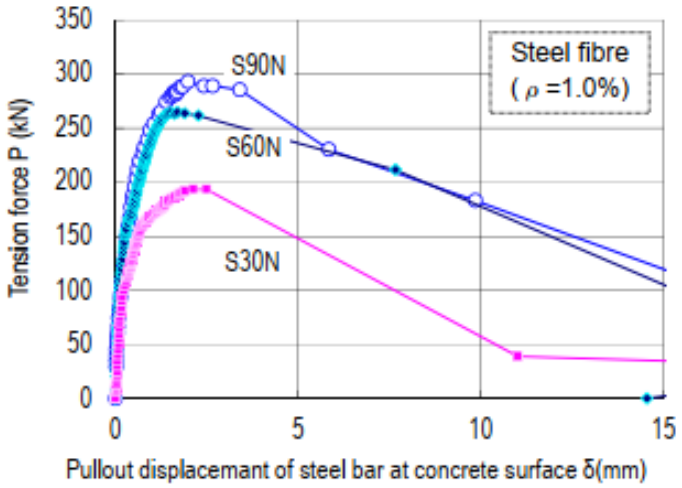

Figure 2. 8 Tension force vs. Pull-out displacement of steel bar (Ishikawa *et al.* 2012)

2.7 Code Provisions

2.7.1 ACI Building Code

The ACI 318-08 Building Code has been the first to include design requirements for developing headed bars, and the current ACI 318-19 provisions have not changed significantly. The development length l_{dt} required for anchoring headed bars in tension, according to Section 25.4.4.2 of ACI 318-19, is calculated as follows:

$$l_{dt} = \left(\frac{0.19 f_y \Psi_e}{\sqrt{f_c'}} \right) d_b \qquad (2.1)$$

In equation (2.1), the yield strength of the bar, f_y, is limited to 60,000 psi; factor Ψe is 1.2 for epoxy-coated reinforcement and 1.0 elsewhere; and the concrete compressive strength, f_c', is limited to 6,000 psi when calculating l_{dt}. Bar size (no. 11 or smaller), concrete (normal weight), bar cover, and bar spacing are also restricted (not less than $2d_b$ and $4d_b$, respectively).

To determine the development length of headed bars, the critical section is measured from the bearing face of the head. Figure 2.9 depicts a typical exterior beam-column joint with a headed bar that is long enough to meet the development length requirement. In this case, the critical section refers to the face of the column for beam-column joints in non-seismic areas, which is located at a point where the maximum stress is reached.

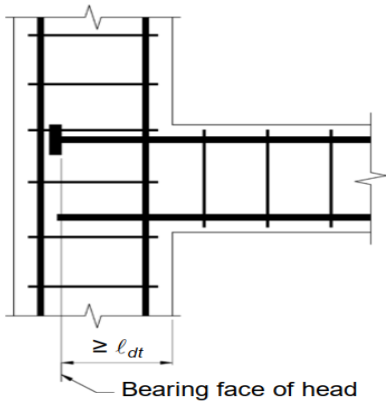

Figure 2. 9 Exterior beam-column joint with headed bars that meet the ACI 318-19 development length requirement (ACI 318-19)

2.7.2 ASTM A970 Code Provisions

The ASTM A970 standard covers welded headed bars with any welded connection between the head and the bar. The specification focuses on head-bar weld quality control standards, as well as head size requirements. The specification addresses the quality control of the weld connection and requires a number of performance tests, including static tension and bend tests for the head-bar connection. This specification must be followed for welded headed bars. According to the requirements of ASTM A970, the gross head area for each bar size should correspond to 10 times the bar area (or $A_{nh}/A_b = 10$). These head sizes ensure that concrete crushing failure does not occur beneath the head, based on a concrete compressive strength of 30 MPa (4.4 ksi) and a bar yield strength of 420 MPa. In addition, in the ASTM A970 code, the specified head sizes are required for bar anchorage solely by the head. Smaller heads are permitted as long as the headed bar manufacturer confirms the head's suitability for the intended application. The head size specifications in this ASTM Specification are uncertain. Some designers and manufacturers believe that the ASTM document should not specify head size and that the structural engineer should decide. According to Wright and McCabe (1997), who wrote the standard, the head size recommendations have been developed as a result of a collaborative effort that included SINTEF tests performed for Metalock "studies of these headed bars in various locations on both sides of the Atlantic." The size recommendations have been influenced by a 10 times bar area requirement for head size in the Canadian CSA Code.

The document's quality control measures are also very similar to those used by HRC. Friction-welded headed bars are preferred over other types of welded headed bars, according to the code. McCabe stated that he worked with HRC representatives during the development of the ASTM specifications. Given that HRC is the only manufacturer of friction welded headed bars and thus has the only documented methods for welded headed bar quality control, their production standards may have had an undue influence on the code's development. The ASTM specification is biased in favor of HRC's headed bars and against ERICO's Lenton Terminator because of the head size requirements and the language of the quality control standards. New proposals of the ASTM A970 specification are being developed as a result of the controversy surrounding the first proposal. Other head-bar connections, such as ERICO's tapered thread,

may be included in newer proposals as quality control standards, and minimum head size standards may be modified or dropped.

2.7.3 ACI 352R-02 Code Provisions

The Indian standard code contains no information on how to design beam-column connections in concrete structures using a T-headed bar (mechanical anchorage). More research on using T-headed bar (mechanical anchorage) to design beam-column connections in concrete structures is recommended by the American Concrete Institute (ACI)-352. For beam-column connections in cast-in-place concrete frames, ACI 352R-02 design recommendations are less restrictive than ACI 318-19. Based on the loading conditions and anticipated deformations of members connected to the joint under lateral load, ACI 352R-02 classifies beam-column joints as Type 1 or Type 2. Non-seismic loading that is not expected to cause significant inelastic deformation, is detailed in Type 1 joints.

Type 2 joints, on the other hand, are designed to withstand seismic loads while taking into account deformation into the inelastic range during load reversals. At the joint-member interface, the critical section for transferring member forces to the connection is defined differently for Type 1 and Type 2 joints. As shown in Figure 2.10, the critical section for Type 1 joints is taken at the face of the column, while for Type 2 joints, it is taken at the outside edge of the column core (outer edge of hoops).

Each head should be transversely restrained by a stirrup or hoop leg anchored in the joint for headed bars adjacent to a free face of the joint with a side cover normal to the longitudinal axis of the bar less than 3db. The strength of the hoop leg in Type 2 connections should be equal to 1/2 of the yield strength of the bar being developed if significant inelastic deformations are expected; otherwise, the strength of the hoop leg should be equal to 1/4 of the yield strength of the bar being developed. The use of headed reinforcement instead of standard hooks in disturbed areas of a concrete member with nonlinear strain distribution is a viable option with no significant design issues (Wallace 1997).

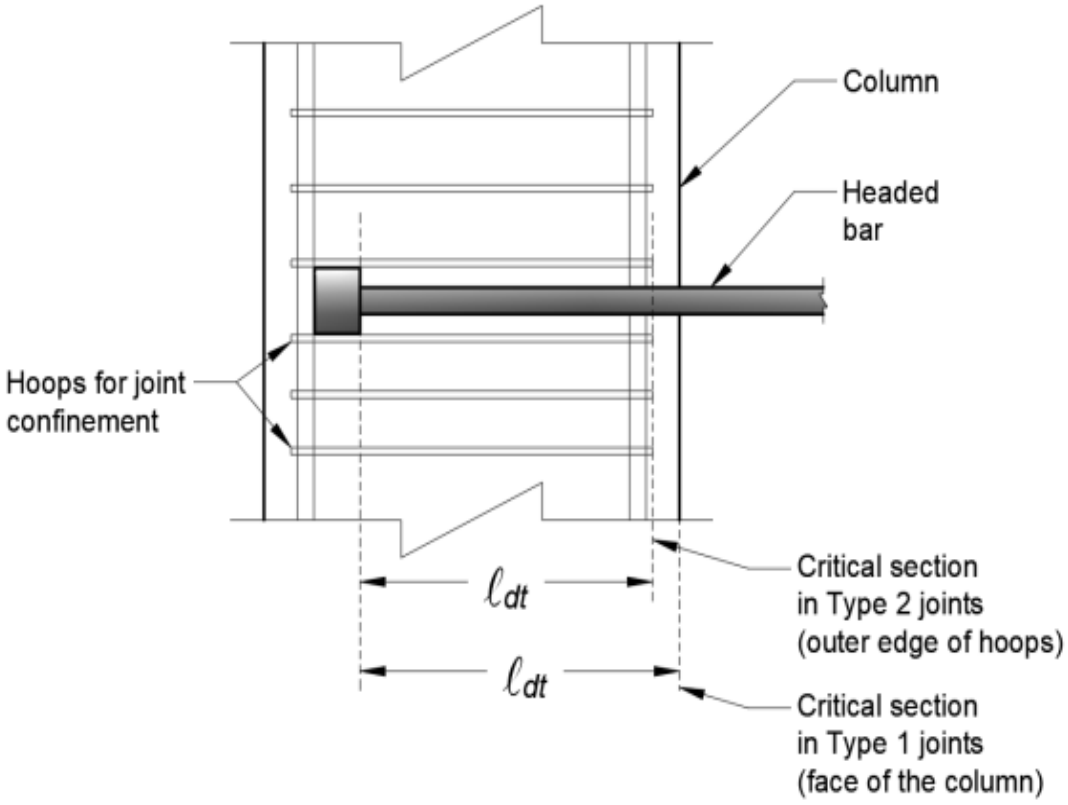

Figure 2. 10 Critical section for the headed bar in Type 1 and Type 2 joints (ACI 352R-02)

The recommendations for the development length l_{dt} of headed bars in ACI 352R-02 are based on those for hooked bars. According to ACI 352R-02, the tension l_{dh} enclosed within the confined core of a Type 2 connection is equal to the development length of a 90° standard hooked bar (standard hooks are defined in Section 25.3.1 of ACI 318-19).

$$l_{dh} = \left(\frac{\alpha f_y}{75\sqrt{f_c'}} \right) d_b \qquad (2.2)$$

where α is the anchored bar's critical section stress multiplier, which raises the stress under large deformation. ASTM A706 or equivalent reinforcing type 2 connections should have

a value of α equal to 1.25 or greater, while all other reinforcing should have a value of α greater than 1.25. An ideal length of development of the bar is 8 d_b and 6 inches, whichever is shorter. An adjustment factor of 0.7 may be used in accordance with ACI 318-19 Section 25.4.3.2 for standard hooked bars whose side cover is no less than 2.5 inches, and whose covers extend no further than 2 inches past the hook. If the bar is connected by a Type 2 connection, the confined core will be at least 2.5 inches wide, with a clear cover on the side normal to the plane of the hook; this cover will go atleast 2 inches beyond the hook. If the hooked bar's development length is to be modified by 0.7, use equation (2.2). A modification factor of 0.8 can be applied to the development length calculated with equation (2.2) if confining reinforcement in the joint region is provided at a spacing less than $3d_b$.

The development length of a headed bar in tension is 3/4 the development length of a hooked bar in a Type 2 joint, as calculated by equation (2.3), which equals

$$l_{dh} = 3/4 \left(\frac{\alpha f_y}{75\sqrt{f_c'}} \right) d_b \qquad (2.3)$$

Type 1 connections have a stress multiplier (α) of 1.0, while Type 2 connections have a stress multiplier of 1.25. The maximum concrete compressive strength f_c (psi) allowed for calculating development length in ACI 352R-02 is 15,000 psi, which is significantly higher than the upper limit of 6,000 psi in ACI 318-19 and not supported by experimental results at the time the recommendations in ACI 352-02 was developed. The length of the development must be greater than the lesser of $8d_b$ and 6 inches. Joint confinement reinforcement should be provided in accordance with Section 4.2 of the ACI 352R-02 joint confinement requirements. In corner beam-column joints where both beam and column terminate at the joint, ACI 352R-02 recommends headed bars adjacent to the free face with a side clear cover less than $3d_b$ confined by stirrups perpendicular to the longitudinal axis of the headed bars. The strength of the stirrup legs in a Type 2 corner joint should be one-half the force required to yield the headed bars adjacent to the joint's free face if significant inelastic deformations of the headed bars are expected. The strength of the stirrup legs should be one-quarter of the force required to yield the

headed bars adjacent to the free face of the joint in other cases. If the side cover is greater than $3d_b$, minimum confining reinforcement per Section 4.2 of ACI 352R-02 should be provided.

A Type 1 joint ($\alpha = 1.0$) can be used to compare the approaches used in ACI 318-19 and ACI 352R to compute the development length of headed bars. Equations (2.4) and (2.5) give the respective development lengths of an uncoated headed bar ($\Psi_e = 1.0$) in this case.

$$l_{dt} = \left(\frac{0.19 f_y \Psi_e}{\sqrt{f_c'}} \right) d_b \qquad \text{(ACI 318-19)} \qquad (2.4)$$

$$l_{dt} = \left(\frac{0.01 f_y}{\sqrt{f_c'}} \right) d_b \qquad \text{(ACI 352R-02)} \qquad (2.5)$$

Equations (2.4) and (2.5) calculate development lengths for headed bars as functions of $f_y\, d_b / (\sqrt{f_c'})$. However, the length of development required by ACI 353-02 using equation (2.5) is 37.5 % shorter than that required by ACI 318-19 using equation (2.4). The primary reason for this is that, in contrast to ACI 352R-02, which incorporates modification factors for hooked bars based on side concrete cover (0.7) and confining reinforcement (0.8), ACI 318-19 disregards these factors when determining the development length of headed bars. Additionally, ACI 318-19 imposes additional restrictions on the use of high-strength concrete (6,000 psi in ACI 318-19 versus 15,000 psi in ACI 352R-02).

2.7.4 Canadian Standards Association (CSA) Code, CSA A23.3-94

The Canadian Standards Association (CSA) Code, CSA A23.3-94 for the Design of Concrete Structures, permits the use of headed shear reinforcement in clause 13.4.8. Sub clauses 13.4.8.1-3 of this code impose the following requirements:

1. The bar's full yield strength must be developed by the headed anchorage.
2. There must be at least ten times the area of the bar's head unless experimental evidence justifies a smaller size.

3. Shear stress resistance must not exceed $0.8\lambda\phi_c\sqrt{f_c'}$ (in SI units), which is 1.33 times the maximum allowed for members reinforced with conventional shear.
4. Concrete's factored shear stress contribution (in SI units) must not exceed $0.3\lambda\phi_c\ (\sqrt{f_c'})$, which is 1.5 times higher than the maximum allowed for members with conventional reinforcement.

The second statement is undoubtedly based on Dilger and Ghali's (1981) headed stud research at the University of Calgary. The improved confinement effect that headed bars should presumably provide results in increased concrete shear capacity.

2.7.5 Fib Model Code 2010

According to MC2010's various approaches, if the head provides the full capacity, a minimum diameter of $3d_b$ and a minimum clear cover from the end of the plate of $2d_b$ are required. Other requirements include a minimum spacing of $6d_b$ between bar centers and $f_{cd} > f_{yd}/24$. The anchorage capacity of reinforcement anchored by a combination of bond along the bar and bearing on the plate can be evaluated in one of the following ways:

1. Using laboratory tests to determine it;
2. As the head's capacity alone, ignoring any contribution from bonding (a cautious approach);
3. As the bar with a hook or bend at the end, the head's net-projected area is the same as a standard bend.

According to these different approaches of MC2010, there has been no consensus model developed for the anchorage of headed bars yet. Thus, the bond strength has been calculated using the conservative approach based on the bars terminating in a hook or bend. As per fib MC2010, the design bond strength (f_{bd}) is calculated using equation 2.6.

$$f_{bd} = (\alpha_2+\alpha_3)f_{bd,0}-2P_{tr} < 2.0f_{bd,0}-0.4P_{tr} < (1.5/\gamma_{cb})\times\sqrt{f_{ck}} \quad (2.6)$$

where: α_2 and α_3 represent the influence of passive confinement from cover (α_2) and transverse reinforcement (α_3) and may conservatively be taken as 1.0. P_{tr} (P_{max}/area of the section) is the mean compression stress perpendicular to the potential splitting failure surface at the ultimate limit state. Basic bond strength ($f_{bd,0}$) is given by equation 2.7.

$$f_{bd,0} = \eta_1 \eta_2 \eta_3 \eta_4 (f_{ck} / 25)^{0.5/\gamma_{cb}} \quad (2.7)$$

where: η_1 is a coefficient for ribbed bars and taken as 1.75 (including galvanized and stainless reinforcement), η_2 represents the casting position of the bar is taken as 0.7 for all the cases, η_3 represents the bar diameter (ϕ) is 1.0 for $\phi \leq 25$ mm, and η_4 represents the characteristic strength of steel reinforcement being anchored or lapped is taken as 1.0 for yield strength for reinforcing steel in tension (f_{yk}) = 500 MPa, f_{ck} represents the compressive strength of concrete and γ_{cb} represents the partial safety coefficient for bond taken as 1.5.

2.7.6 Eurocode 2

As per Eurocode 2 (EN 1992-1-1), the ultimate bond strength (f_{bd}) is calculated in equation 2.8.

$$f_{bd} = 2.25 \eta_1 . \eta_2 . f_{ctd} \quad (2.8)$$

where: η_1 is a coefficient related to the quality of the bond condition and the bar's position during concreting and is taken as 1.0 for good condition. η_2 is related to bar diameter (ϕ). It is taken as 1 when $\phi \leq 32$ mm. f_{ctd} is the design value of concrete tensile strength and is calculated using equation 2.9.

$$f_{ctd} = \alpha_{ct} F_{ctk,0.05} / \gamma_c \quad (2.9)$$

where: α_{ct} is a coefficient taking account of long-term effects on the tensile strength and unfavorable effects. The recommended value for use is 1. γ_c is the partial safety factor for concrete and is taken as 1.5 for 'persistent & transient' design situations. $F_{ctk,\ 0.05}$ is the characteristic tensile strength and is computed using equation 2.10.

$$F_{ctk,\ 0.05} = 0.7 f_{ctm} \quad (2.10)$$

where: f_{ctm} is the mean value of axial tensile strength of concrete ($f_{ctm} = 0.3\ f_{ck}^{2/3}$) for concrete class ≤ C50/60. f_{ck} represents the compressive strength of concrete.

2.8 Descriptive Equations

Shao *et al.* (2016) developed descriptive equations to describe the anchorage strength of heading bars containing and not containing strengthening in simulated beam-column joints based on the experiment. They made the equations easier to understand by varying the variables' values. A similar expression for hooked bars has been developed by Sperry *et al.* (2017) and guided the changes. With the help of descriptive equations developed from beam-column joint specimens tested under monotonic loading, Ghimire *et al.* (2019) examined the anchorage strength of headed bars in beam-column joints subjected to reversal loading. There is a relationship between the headed bar's anchorage strength and factors such as embedment length, concrete compressive strength, and the distance between bars and bar diameter.

2.9 Genetic Programming

Kermani *et al.* (2009) has provided a method for estimating the equations for the ratio of maximum velocity to maximum acceleration (V_{max}/a_{max}) of strong ground motions using genetic programming. The prediction equations for three types of faulting mechanisms, strike-slip, normal, and reverse, have been developed utilizing a credible database released by the Pacific Earthquake Engineering Research center (PEER). In practical applications, the presented models have given reasonable accuracy in estimating the frequency content of site ground vibrations.

Using wind data, Nitsure *et al.* (2009) have employed Genetic Programming (GP) to estimate an essential oceanic metric, i.e., Significant Wave Height (SWH). The GP models have been developed using wave and wind measurements collected by fixed ocean signals. The GP-based estimations accurately estimate significant wave heights as evidenced by wave plots and strong correlation coefficient values.

Using Linear Genetic Programming (LGP), Gandomi *et al.* (2013) have proposed a formula for predicting the compressive strength of carbon fiber reinforced plastic (CFRP) confined cylinders. Two different sets of input data have been used to build the LGP-based models. The first inputs have been the concrete cylinder diameter, unconfined concrete strength, CFRP laminate tensile strength, and the total thickness of CFRP layers used. The second set includes the most commonly used parameters in existing models, i.e., CFRP confinement, unconfined concrete strength, and ultimate confinement pressure. The models have been created using experimental data gathered from the accessible literature. The results have shown that the LGP-based formulations have been capable of accurately predicting ultimate compressive strength. The LGP results have also been compared to many CFRP confinement models published in the literature, and they are more accurate in almost every case.

Saridemir (2010) has used a gene expression programming (GEP) approach to construct two models for forecasting compressive strength of concrete containing rice husk ash at 1, 3, 7, 14, 28, 56, and 90 days. Experimental results for 188 specimens produced with 41 different mixing proportions have been acquired from the literature to create the models. The models have been created using seven different input variables in the GEP technique based on the experimental data. The compressive strength values from the mechanical properties of concretes containing rice husk ash have been predicted using these input variables in GEP approach models. The experimental results have been compared to the training, testing, and validation sets of the models. GEP is a robust technique for predicting compressive strength values of concretes containing rice husk ash, according to all of the findings.

Genetic Programming has been implemented by Aggarwal (2013) to generate mathematical models to forecast wind-induced pressures on tall buildings. The database for the gable roof building is built using the data from the experimental investigation. For the formulation of equations for estimating wind-induced pressure on gable roof buildings, the angle of wind incidence, roof slope, and pressure coefficients for various zones have been employed as parameters. Gust factor and Base Moment on tall buildings have also been calculated using GP.

Muduli *et al.* (2013) has used an extensive database of post-liquefaction cone penetration test (CPT) measurements and field manifestations to investigate the potential of multi-gene genetic programming (MGGP) based classification approach to evaluate liquefaction potential of soil in terms of liquefaction index (LI). CPT measurements, such as cone tip resistance, friction ratio, total vertical stress and effective vertical stress of soil, seismic parameters, such as peak horizontal ground surface acceleration and earthquake moment magnitude, and the depth under consideration have all been included in the database.

Gholampour *et al.* (2017) have observed that several runs have been carried out to develop the most accurate GP model. Different GP models have been created by varying the number of genes, chromosomes, head size, and linking function to find the model to best fit the experimental results. The optimal parameters of the selected GP model have been obtained using the trial and error method from 100 different runs. The number of chromosomes determines the running time; as the number of chromosomes increases, the running time increases. Using GP, Aval *et al.* (2017) have proposed a model for estimating the shear strength of a short rectangular reinforced concrete column. Lim *et al.* (2016) has proposed GP models for predicting the ultimate condition of FRP-confined concrete, and Mansouri *et al.* (2018) has proposed a GP model for predicting the ultimate axial strain of fiber-reinforced polymer-confined concrete.

Yadav *et al.* (2018) has predicted the model for estimating maximum moment capacity for beams using GP technique considering various parameters such as the diameter of the bar, percentage of corrosion, rotation of beam, area of steel, compressive strength of concrete, and yield strength of steel and it has been observed that the results obtained from GP are acceptable and best fit with the experimental results.

2.10 Closing Remarks

According to a literature review, extensive research has been carried out on the anchorage capacity of headed bars, but few have included the steel fibers in them. Additionally, the behavior of exterior beam-column joints has been extensively studied under monotonic and cyclic loading. Concrete compressive strength, anchorage detailing of longitudinal beam bars in

the joint region, axial load in the column, joint shear deformation have been identified as the main factors influencing joints. Some authors employ particular joint detail, which moves the plastic hinge away from the column face.

However, most of the authors gave special attention to the design parameters but did not consider the impact of all of the parameters mentioned above. The strength and deformation contributions from joint shear cracking and bond-slip behavior of beam and column reinforcement bars have been studied analytically.

CHAPTER 3

EXPERIMENTAL INVESTIGATION

3.1 Introduction

This chapter describes the experimental work that involved performing a pull-out test on headed bars to understand their behavior and anchorage capacity. The reasons for selecting specimen geometry, loading arrangement, and concrete mix design are explained in this chapter. The properties of concrete and reinforcement have been determined using appropriate material tests, as described in this chapter. The number of test specimens was chosen to allow the author to collect enough data to understand the behavior of the headed bar. The author systematically examined the impact of critical parameters on joint behavior, such as the diameter of the reinforcing bar and embedment depth and shape of the headed bar, compressive strength of concrete, and steel fiber percentage.

3.2 Methodology of Research work

The first phase of experimental work consists of manufacturing headed bars at different head shapes (square, rectangular and circular heads). In the second phase of casting the specimens (cylindrical specimens and beams-column joints), including steel fibers, and in the third phase, pull out testing on cylindrical specimens and testing of the beam-column joints has been performed to check for joint shear strength, ductility, stiffness, and energy dissipation. A total of 324 cylindrical specimens have been cast and tested for pull-out test. All the cylindrical specimens are of size (150 X 300 mm). After the pull-out test, the best shape of headed bars has been carried out based on the anchorage capacity of headed bars. The best shape of the headed bar has been used to cast eight beam-column joints with beam size (1000 X 200 X 150 mm) and column size (1260 X 150 X 200 mm). An analytical approach, i.e., non-linear regression analysis using dummy variables, and genetic programming (GP) using GP KERNEL software have been used to validate the experimental results, and then results are also compared to the

previous research findings. The flowchart for the methodology of the whole research work has been described in Figure 3.1.

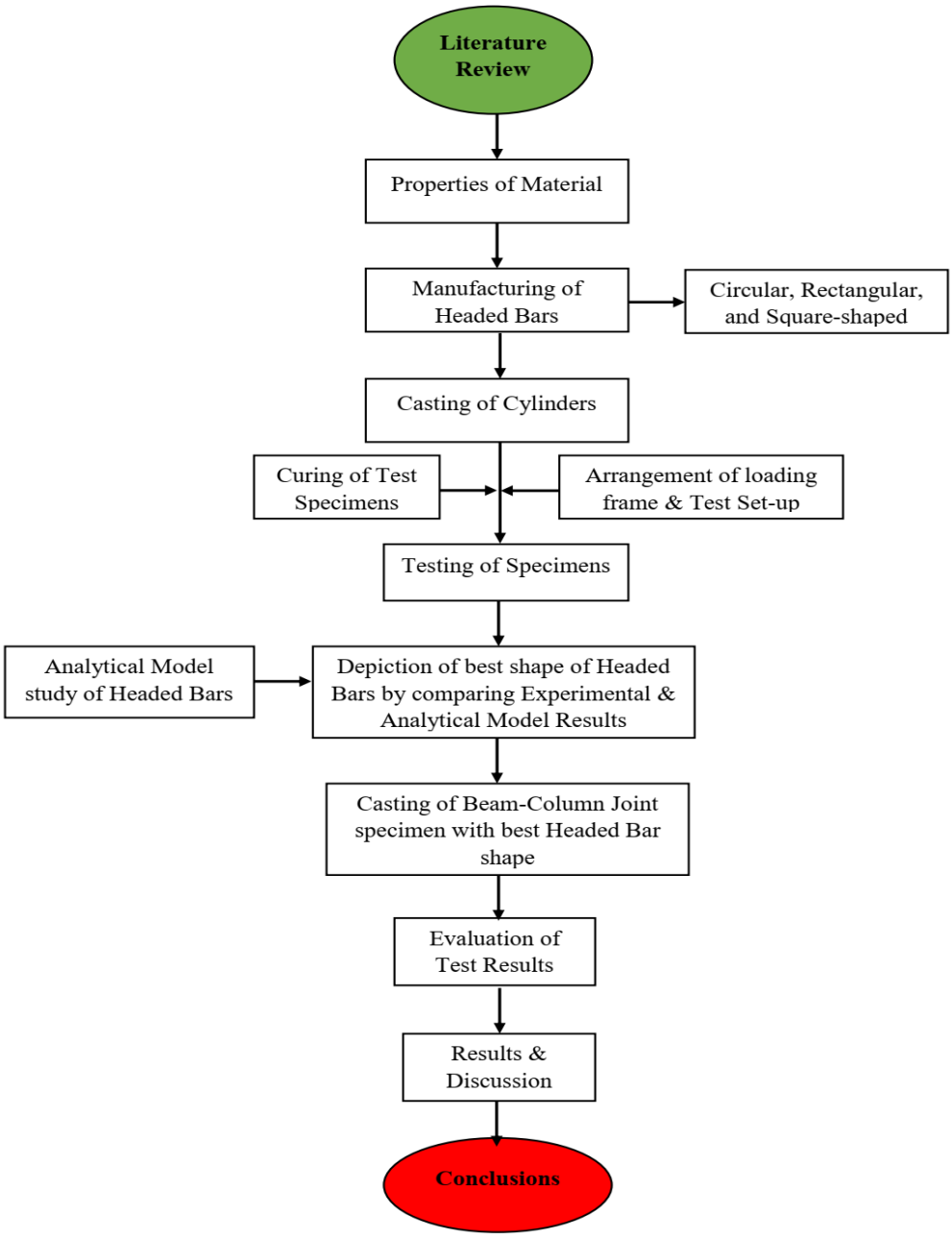

Figure 3. 1 Flow chart for research methodology

3.3 Experimental Program

The objective of this study is to evaluate the anchorage capacity of headed bars and also to analyze the behavior of headed bars in steel fibre reinforced concrete, and to evaluate the influence of diameter of bar, shape of headed bars and percentage of steel fibres on the bond behavior of concrete. A total of 324 cylindrical pull-out specimens of size 150 x 300 mm have been cast as per ASTM C900 guidelines and tested under monotonic tensile load. The embedment depth of the headed bar inside the cylinder has been kept $8d_b$ concentrically as per ACI 318-19 guidelines. The details of cylindrical specimens for the pull-out test are presented in Table 3.1. The first letter (S, R & C) in the abbreviation indicates square, rectangular and circular heads, the numerals (1,2 and 3) indicate the diameter of steel bars, i.e., 16, 20, and 25 mm, the letter SF for steel fiber, the numerals (0, 0.5, 1, and 1,5) indicate the percentage of steel fiber; M20, M40, and M60 indicate the concrete grades. These shapes of heads, diameter of bars and percentage of steel fibers have been selected based on previous literature and ACI 318-19 guidelines.

Table 3. 1 Specimen details for pull-out test

Specimen designation	**Diameter of bar (d_b) (mm)**	**Shape of head**	**Percentage of steel fibers (%)**
S_1S_F0M20	16	Square	0
R_1S_F0M20	16	Rectangular	0
C_1S_F0M20	16	Circular	0
$S_1S_F0.5M20$	16	Square	0.5
$R_1S_F0.5M20$	16	Rectangular	0.5
$C_1S_F0.5M20$	16	Circular	0.5
S_1S_F1M20	16	Square	1
R_1S_F1M20	16	Rectangular	1
C_1S_F1M20	16	Circular	1
$S_1S_F1.5M20$	16	Square	1.5

Specimen designation	Diameter of bar (d_b) (mm)	Shape of head	Percentage of steel fibers (%)
$R_1S_F1.5M20$	16	Rectangular	1.5
$C_1S_F1.5M20$	16	Circular	1.5
S_2S_F0M20	20	Square	0
R_2S_F0M20	20	Rectangular	0
C_2S_F0M20	20	Circular	0
$S_2S_F0.5M20$	20	Square	0.5
$R_2S_F0.5M20$	20	Rectangular	0.5
$C_2S_F0.5M20$	20	Circular	0.5
S_2S_F1M20	20	Square	1
R_2S_F1M20	20	Rectangular	1
C_2S_F1M20	20	Circular	1
$S_2S_F1.5M20$	20	Square	1.5
$R_2S_F1.5M20$	20	Rectangular	1.5
$C_2S_F1.5M20$	20	Circular	1.5
S_3S_F0M20	25	Square	0
R_3S_F0M20	25	Rectangular	0
C_3S_F0M20	25	Circular	0
$S_3S_F0.5M20$	25	Square	0.5
$R_3S_F0.5M20$	25	Rectangular	0.5
$C_3S_F0.5M20$	25	Circular	0.5
S_3S_F1M20	25	Square	1
R_3S_F1M20	25	Rectangular	1
C_3S_F1M20	25	Circular	1
$S_3S_F1.5M20$	25	Square	1.5
$R_3S_F1.5M20$	25	Rectangular	1.5
$C_3S_F1.5M20$	25	Circular	1.5
S_1S_F0M40	16	Square	0

Specimen designation	Diameter of bar (d_b) (mm)	Shape of head	Percentage of steel fibers (%)
R_1S_F0M40	16	Rectangular	0
C_1S_F0M40	16	Circular	0
$S_1S_F0.5M40$	16	Square	0.5
$R_1S_F0.5M40$	16	Rectangular	0.5
$C_1S_F0.5M40$	16	Circular	0.5
S_1S_F1M40	16	Square	1
R_1S_F1M40	16	Rectangular	1
C_1S_F1M40	16	Circular	1
$S_1S_F1.5M40$	16	Square	1.5
$R_1S_F1.5M40$	16	Rectangular	1.5
$C_1S_F1.5M40$	16	Circular	1.5
S_2S_F0M40	20	Square	0
R_2S_F0M40	20	Rectangular	0
C_2S_F0M40	20	Circular	0
$S_2S_F0.5M40$	20	Square	0.5
$R_2S_F0.5M40$	20	Rectangular	0.5
$C_2S_F0.5M40$	20	Circular	0.5
S_2S_F1M40	20	Square	1
R_2S_F1M40	20	Rectangular	1
C_2S_F1M40	20	Circular	1
$S_2S_F1.5M40$	20	Square	1.5
$R_2S_F1.5M40$	20	Rectangular	1.5
$C_2S_F1.5M40$	20	Circular	1.5
S_3S_F0M40	25	Square	0
R_3S_F0M40	25	Rectangular	0
C_3S_F0M40	25	Circular	0
$S_3S_F0.5M40$	25	Square	0.5

Specimen designation	Diameter of bar (d_b) (mm)	Shape of head	Percentage of steel fibers (%)
$R_3S_F0.5M40$	25	Rectangular	0.5
$C_3S_F0.5M40$	25	Circular	0.5
S_3S_F1M40	25	Square	1
R_3S_F1M40	25	Rectangular	1
C_3S_F1M40	25	Circular	1
$S_3S_F1.5M40$	25	Square	1.5
$R_3S_F1.5M40$	25	Rectangular	1.5
$C_3S_F1.5M40$	25	Circular	1.5
S_1S_F0M40	16	Square	0
R_1S_F0M40	16	Rectangular	0
C_1S_F0M40	16	Circular	0
$S_1S_F0.5M40$	16	Square	0.5
$R_1S_F0.5M40$	16	Rectangular	0.5
$C_1S_F0.5M40$	16	Circular	0.5
S_1S_F1M40	16	Square	1
R_1S_F1M40	16	Rectangular	1
C_1S_F1M40	16	Circular	1
$S_1S_F1.5M40$	16	Square	1.5
$R_1S_F1.5M40$	16	Rectangular	1.5
$C_1S_F1.5M40$	16	Circular	1.5
S_1S_F0M60	16	Square	0
R_1S_F0M60	16	Rectangular	0
C_1S_F0M60	16	Circular	0
$S_1S_F0.5M60$	16	Square	0.5
$R_1S_F0.5M60$	16	Rectangular	0.5
$C_1S_F0.5M60$	16	Circular	0.5
S_1S_F1M60	16	Square	1

Specimen designation	Diameter of bar (d_b) (mm)	Shape of head	Percentage of steel fibers (%)
R_1S_F1M60	16	Rectangular	1
C_1S_F1M60	16	Circular	1
$S_1S_F1.5M60$	16	Square	1.5
$R_1S_F1.5M60$	16	Rectangular	1.5
$C_1S_F1.5M60$	16	Circular	1.5
S_2S_F0M60	20	Square	0
R_2S_F0M60	20	Rectangular	0
C_2S_F0M60	20	Circular	0
$S_2S_F0.5M60$	20	Square	0.5
$R_2S_F0.5M60$	20	Rectangular	0.5
$C_2S_F0.5M60$	20	Circular	0.5
S_2S_F1M60	20	Square	1
R_2S_F1M60	20	Rectangular	1
C_2S_F1M60	20	Circular	1
$S_2S_F1.5M60$	20	Square	1.5
$R_2S_F1.5M60$	20	Rectangular	1.5
$C_2S_F1.5M60$	20	Circular	1.5
S_3S_F0M60	25	Square	0
R_3S_F0M60	25	Rectangular	0
C_3S_F0M60	25	Circular	0
$S_3S_F0.5M60$	25	Square	0.5
$R_3S_F0.5M60$	25	Rectangular	0.5
$C_3S_F0.5M60$	25	Circular	0.5
S_3S_F1M60	25	Square	1
R_3S_F1M60	25	Rectangular	1
C_3S_F1M60	25	Circular	1
$S_3S_F1.5M60$	25	Square	1.5
$R_3S_F1.5M60$	25	Rectangular	1.5
$C_3S_F1.5M60$	25	Circular	1.5

3.3.1 Material Properties

Ordinary Portland cement of 43-grade, fine aggregate, coarse aggregate, tap water, and steel reinforcing bars have been used to make the test specimens. The materials, in general, have been

confirmed to the requirements of the specifications laid down in the relevant Indian Standard Codes. The detailed characteristics of the materials are presented below.

3.3.1.1 Cement

OPC 43-grade cement conforming to IS 8112:1989 from a single batch has been used to prepare concrete mixes throughout this investigation. To prevent the cement degrading from the atmospheric effect, it was stored in an airtight silo in the laboratory as soon as it was received. The collected cement samples have been thoroughly tested to establish their compliance with the appropriate Indian standards (IS 4031:1988 and IS 4032:1985). The physical properties of the cement are presented and compared with the requirements of IS: 8112 (1989) in Table 3.2.

Table 3. 2 Physical properties of cement

Characteristics	**Result Obtained**	**Recommended values per IS 8112:1989 (BIS 1989)**
Cement grade	OPC 43	-
Specific gravity	3.13	-
Setting time (i) Initial setting time (minimum) (ii) Final setting time (maximum)	 64 201	 30(minimum) 600(maximum)
Standard consistency of cement (%)	25	30
Compressive strength (a) 3 days strength (N/mm^2) (b) 7 days strength (N/mm^2) (c) 28 days strength (N/mm^2)	 23.75 35.43 45.11	 23 33 43
Fineness (m^2/Kg)	312	225(minimum)
Soundness (mm)	1.3	10 (maximum)

3.3.1.2 Fine aggregates

Clean river sand complying with the specifications (Zone II) of IS 383 has been used as the fine aggregate. Table 3.3 shows the physical properties of the fine aggregate.

Table 3. 3 Physical properties of fine aggregates

Characteristics	Result Obtained	Requirements as per IS 383: 1970
Fineness modulus	2.65	2.0 to 3.5
Moisture content (%)	1.46	-
Grading	Conforming to grading Zone – II	-
Water absorption (%)	1.52	-
Specific gravity	2.68	2.6 to 2.7

3.3.1.3 Coarse aggregates

Crushed stone angular aggregates, having a maximum nominal size of 20 mm and conforming to (IS 383) grading requirements, have been used as coarse aggregates. Coarse aggregates have also been first sieved using a 150-micron sieve to remove dirt and other foreign material. The physical properties of coarse aggregates are given in Table 3.4.

Table 3. 4 Physical properties of coarse aggregates

Characteristics	Result Obtained	Requirements as per IS 383: 1970
Moisture content (%)	Nil	-
Fineness modulus	7.21	5.5 to 8
Water absorption (%)	0.95	-
Density (loose), kN/m^3	16.3	-
Specific gravity	2.69	2.6 to 2.7

3.3.1.4 Water

The water used in the mixing and curing of concrete should be free of harmful substances. As a result, potable water was used for this purpose throughout the casting and curing process.

3.3.1.5 Steel fibers

Hook end loose steel fibers with length 35 mm, diameter 0.55 mm, and aspect ratio 65 were added in the percentages of (0.5, 1, & 1.5%) to normal concrete to form SFRC, as shown in Figure 3.2. Carbon = 0.036%, Manganese = 0.411%, Silica = 0.38%, and Sulphur = 0.009% are the chemical compositions of the steel fibers provided by the manufacturer. The physical properties of steel fibers are summarized in Table 3.5.

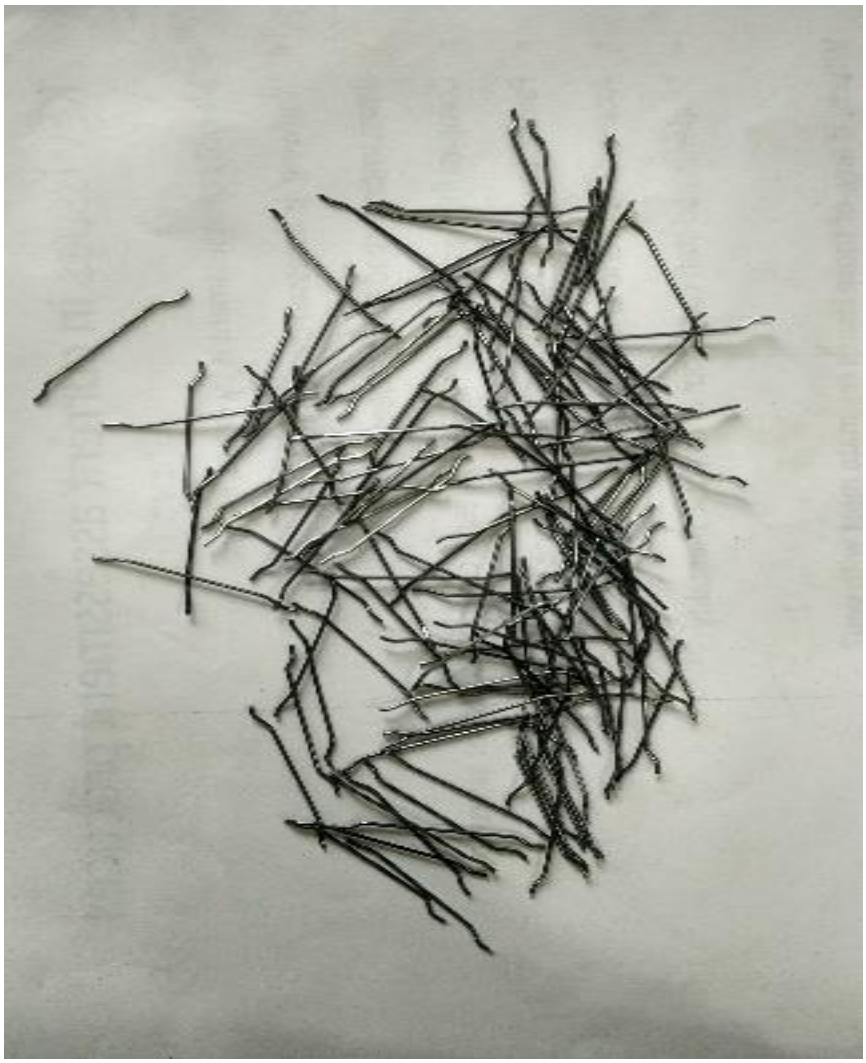

Figure 3. 2 Hooked steel fibers

Table 3. 5 Properties of steel fibers

Fiber Type	Dimension (mm)		Geometry	Young's Modulus (E) (GPa)	Tensile Strength (MPa)	Cross Section
	L	**D**				
Carbon Steel	35	0.55	Hooked-end	210	1200	Circular

3.3.1.6 Steel reinforcement

Steel reinforcing bars having nominal diameters of 16 mm, 20 mm, and 25 mm have yield strengths of 544 MPa, 496 MPa, and 460 MPa, respectively, as shown in Figure 3.3. Average test results of three samples were used as final test result. The properties of steel are given in Table 3.6. Whereas the headed reinforced bars of diameter 20 mm and 25 mm have yield strengths of 554 MPa and 571 MPa respectively, and ultimate strengths of 679 MPa and 709 MPa respectively as per the study of Devries (1999).

Figure 3. 3 Testing of steel reinforcement

Table 3. 6 Mechanical properties of steel

Diameter of bar, d_b (mm)	Young's Modulus (E) (GPa)	Yield strength for reinforcing steel in tension, f_y (MPa)	Ultimate strength (MPa)	Yield strain	Ultimate strain
16	231	544	680.9	0.002	0.003
20	240	490	612.2	0.002	0.003
25	237	460	506.2	0.002	0.003

3.3.2 Mixing, Casting and Curing of Specimens

A concrete mix of M20, M40, and M60, where M stands for mix and "20, 40, and 60" represents the compressive strengths of concrete in MPa, has been designed per the specification laid out in (IS 10262). The concrete mix proportion and measured compressive strength (f_{cm}) after 28 days of curing are shown in Tables 3.7 and 3.8, respectively. Due to the lower water-cement ratio in M60 concrete, superplasticizers were used to improve the workability of concrete.

The quantities of various concrete ingredients, such as cement, sand, coarse aggregate, and water, were kept on hand to meet the required proportions for each batch of casting. The fine aggregate and cement were thoroughly mixed in the dry state to achieve a uniform mix. The uniform color of the dry mix and the absence of any concentration of any one material indicated uniformity. The coarse aggregate was added to the dry mix and turned over many times in a tilting type rotary drum mixer for about one minute while still dry. After that, about half of the total water was slowly added to ensure a uniform mix. The remaining water was then added, and the mixing was continued for another minute. A rotary-drum type mixer was used for the mixing of various material ingredients. The reinforcement with different head shapes were fabricated in the laboratory. The fresh concrete was carefully placed in the moulds and vibrated for 15-20 seconds using a high-frequency vibrating table, thus ensuring removal of air voids and better concrete consolidation. After 24 hours, the specimens were de-molded, marked, and placed in a curing tank and then tested in a compression testing machine, as shown in Figure 3.4. Average test results of three samples were used as final test result whose detailed results with standard deviation are presented in Table A.2.

Figure 3. 4 Concrete cubes under compression testing machine

Table 3. 7 Concrete mix design

Mix Design (ACI code)	Material	W/C ratio	Mix Ratio	kg per cubic m
M20	Cement	0.52	1.00	355
	Water		0.52	185
	Fine Aggregate		2.25	799
	Coarse Aggregate		2.86	1016
M40	Cement	0.42	1.00	430
	Water		0.42	180.6
	Fine Aggregate		1.53	660
	Coarse Aggregate		2.71	1168
M60	Cement	0.3	1	504.21
	Water		0.28	151.2
	Fine Aggregate		1.35	683.24
	Coarse Aggregate		2.19	1108.13
	Superplasticizer		0.6% of cement	3.02

Table 3. 8 Compressive strength of steel fiber reinforced concrete (SFRC)

Grade of Concrete (MPa)	SF (%)	f_{cm} (MPa)
20	0	26.5
20	0.5	27.3
20	1	28.2
20	1.5	28.9
40	0	43.1
40	0.5	45.4
40	1	46.7
40	1.5	47.2
60	0	62.3
60	0.5	66.8
60	1	68.9
60	1.5	69.7

3.3.3 Test Variables, Head details, and Head geometry

ACI (ACI 318-19) and the American Society for Testing and Materials (ASTM) (ASTM A970) have given design guidelines for using the headed bars as reinforcement. The material used for the head (welded from both sides) is mild steel of Grade E410 (Fe 540) (Figure 3.5). Three heads are selected to check their effect on the behavior of the bond between steel and concrete and to find out the optimal shape of the head. The test variables are head shape (square, rectangular and circular), the diameter of bars (16, 20, and 25 mm), and the percentage of steel fibers (0, 0.5, 1, and 1.5%). The head geometry is outlined in Table 3.9. The embedment depth provided is $8d_b$, and the minimum thickness of the head is $0.8d_b$ according to the criteria of the ACI 318-19 code. The headed bars' embedment depth is selected so that the specimens do not fracture by failure of the headed bar, and anchorage failure is regulated by concrete failure. The net head area depends on the area of the reinforced bar, so it has been fixed as 10 times the area of the reinforced bar as recommended by ASTM A970.

Figure 3. 5 Double-sided weld joint

Table 3. 9 Head geometry used in the study

Diameter of bar, d_b (mm)	Area of bar (A_b) (mm^2)	Thickness of Head (mm) ($0.8d_b$)	Net head area (A_{nh}) (mm^2) ($10A_b$)	Square Head Size (mm)	Rectangular Head Size (mm)	Circular Head Size (mm)
16	201	12	2010	45x45	50x41	51
20	314	16	3141	56x56	62x52	63
25	490	20	4906	70x70	78x63	79

3.3.4 Selection of Weld and Welding Procedure

A pilot study has been conducted to check the efficiency of welds used for headed bars. Initially, the head and the bar joint were welded one-sided and tested (Figure 3.6). It was observed that the joint failed during the pull-out test. Subsequently, the bar was welded from both sides of the head. In the double-sided welding process, the steel bar is passed through the head by making a

hole. Then the bar on the other side of the head is welded with a weld thickness of 3mm (Figure 3.5), and out of the two welding processes, the latter performed better in the pull-out test by resisting higher load, and thus, the double-sided weld was adopted for the study.

Figure 3. 6 Single-sided weld joint

3.3.5 Test Procedure and Test Setup of Pull-out specimens

The pull-out test was performed using the universal testing machine (UTM) at the loading rate of 2.5 kN per minute according to ASTM C900-13 (Figure 3.7). The load was applied perpendicular to the cylinder (300 mm in height and having 150 mm diameter) placed in the vertical position as shown in Figure 3.7, after 28 days of curing (Figure 3.8). The cylinder was

placed between the two 40 mm thick plates, out of which the bottom plate has a 25 mm diameter bar attached to the metallic device. The linear variable differential transformer (LVDT) was attached to the headed bar, which is embedded at a depth of $8d_b$ (d_b: diameter of the bar) concentrically in the cylinder. The data acquisition system attached to the computer, was used to headed bars' initial positions.

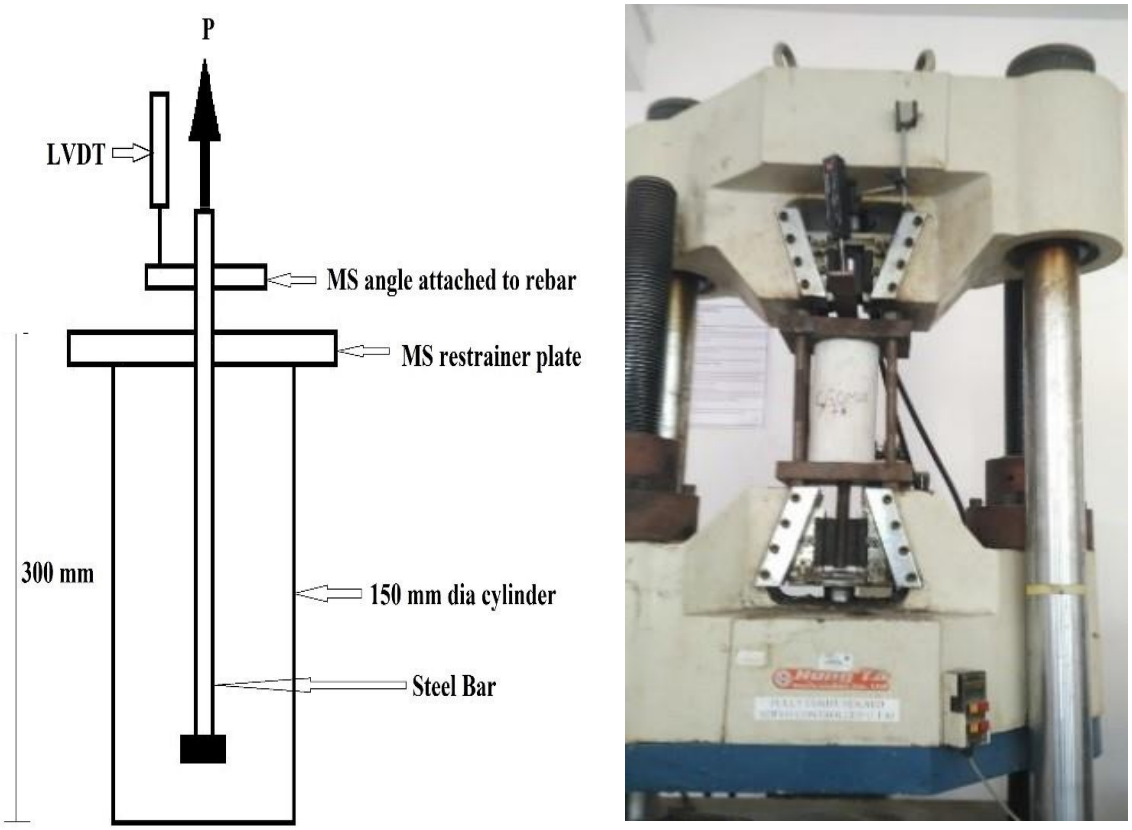

Figure 3. 7 Test Setup and Universal Testing Machine

Figure 3. 8 Curing of pull-out specimens

3.4 External beam-column joint specimens

The performance of headed bars in the exterior beam-column joint has been studied; a total of 8 beam-column joints were cast for M20 and M40 grades, where M represents the mix and 20 and 40 represents the compressive strength of concrete at 28 days in MPa having Young's modulus as 22360 and 31622 MPa. Table 3.7 provides the proportion of materials used for the concrete mix. The following percentage of steel fibers (i.e., 0, 1 and 1.5%), based on the study conducted by (Al-Shannag 2007; Sasmal *et al.* 2013), have been added to the concrete mix of the joint section of the specimens whose compressive strength is presented in Table 3.8.

The poison ratio of concrete which came out after the testing, was 0.2. The poison ratio of concrete is measured using the Poison ratio = Lateral strain/Longitudinal strain. Lateral strain is defined as a change in breadth dimensions compared to the original dimension. The longitudinal strain is the specimen's deformation per unit length in the direction of the applied load. The data of longitudinal and lateral strain was directly recorded on the computer during the experiment. From the data, the poison ratio of concrete and steel was calculated. The steel of grade Fe500 was used for the main bars and stirrups, whose tensile properties are presented

in Table 3.6. The poison ratio of steel was 0.3. Steel fibers of (0, 1 and 1.5%) were added in the BCJ only, whose tensile properties are mentioned in Table 3.5. Comparing compressive strength of M20 and M40 mix with and without steel fibers after 28 days of testing are indicated in Table 3.8.

Headed bars (welded from both sides of the head) of grade E410 (Fe 410) having circular shapes were selected based on the pull-out test results, in which the circular head performed better than the rectangular and square heads. The conclusion was reached in the study of Chourasia (2019). Based on a study conducted by Kang *et al.* (2009a) and Paknejadi and Behfarnia (2020), the head size was taken as $3A_b$ (Area of the bar); thus, the head diameter and thickness were kept as 20 and 10 mm, respectively. As per ACI 352R-02 and ACI 318-19, the development length of the longitudinal bars was provided, as shown in Table 3.10.

Table 3. 10 Development lengths of bars

Code details	Expressions	Type of bars	Development length provided (mm)	Specimen designation
ACI-318-19	$L_d = \frac{\alpha f_y \phi}{6.2\sqrt{f_c'}}$	Hooked bars	275.00	CS_1
			200.00	CS_2
ACI-352	$L_{dh} = \frac{3}{4} L_d$	Headed bars	130.00	HS_1-HS_3
			130.00	HS_4-HS_6

3.4.1 Specimen details and Test Setup of Beam column joint

Eight exterior BCJ specimens having beams of size 150 mm (width) x 200 mm (depth) with a length of 1000 mm and the columns of size 200 mm (width) x 150 mm (depth) with a length of 1260 mm were cast as shown in Figure 3.9(a-b) and Figure 3.10(a-b). To evaluate the specimens' hysteresis behavior, a quasi-static cyclic load was applied to the specimens. One control specimen (designated as CS) was cast for M20 and M40, each with conventional reinforcement. The other six specimens (designated as HS) consist of headed reinforcement and steel fibers in the joint area. The specimen details were described in Table 3.11. The detailing of the beam-

column joints was done according to ACI 318-19 and ACI-352 R (Table 3.12). A double-acting jack of capacity 300 kN was used to apply load on the specimens in the loading frame, which had displacement control (each step consisting of two cycles of the same displacement at intervals of 5mm) quasi-static cyclic loading setup. The load was applied to the specimens in a monotonous manner using hydraulic jacks at an increment of 5 mm, depending on the specimen's estimated failure load by ACI 374.1-05. The beam-column joint arrangements were made, so the column was laid on the loading frame's base, and the beam was aligned vertically at 90 degrees. To simulate gravity load, the column's 10% axial load carrying capacity was applied as the axial load (i.e., 40 kN) and maintained constant throughout the test. The same test setup was used in the study of Sharma and Bansal (2019). An axial load was applied through the hydraulic jack on one side of the column in this study, as shown in the test setup (Figure 3.11). The reaction was taken with the steel plate mounted to the reaction frame, as shown in Figure 3.11. The load-displacement plots were compiled using the data collected after testing the specimens to understand the behavior of headed bars in the exterior beam-column joints. During testing, the cracking in the concrete was observed and marked, and then the specimens were photographed. The test measurements were presented in hysteresis load-deformation curves, load-displacement envelope curves, energy dissipation curves, and stiffness curves.

Table 3. 11 Specimen details for beam-column joint test

Specimen Designation	Grade of concrete	Steel fibers ratio	With/without head
CS1	M20	0	Without head
CS2	M40	0	Without head
HS1	M20	0	Head
HS2	M20	1	Head
HS3	M20	1.5	Head
HS4	M40	0	Head
HS5	M40	1	Head
HS6	M40	1.5	Head

Note: CS: Control specimen; HS: Headed bar specimen

Table 3. 12 Detailing of the specimens

Specimen label	**Joint confinement**	**Longitudinal reinforcement in beam**	**Longitudinal reinforcement in column**	**Transverse reinforcement**
CS1	Without SF	2 nos. of conventional bars of 12mm ϕ at top and bottom each	2 nos. of conventional bars of 12mm ϕ at top and bottom each	10 nos. of 8mm ϕ@150mm c/c are provided in beams and columns.
CS2	Without SF			
HS1	Without SF	2 nos. of headed bars of 12mm ϕ at top and bottom each	2 nos. of conventional bars of 12mm ϕ at top and bottom each	10 nos. of 8mm ϕ@150mm c/c are provided in beams and columns.
HS2	With SF			
HS3	With SF			
HS4	Without SF			
HS5	With SF			
HS6	With SF			

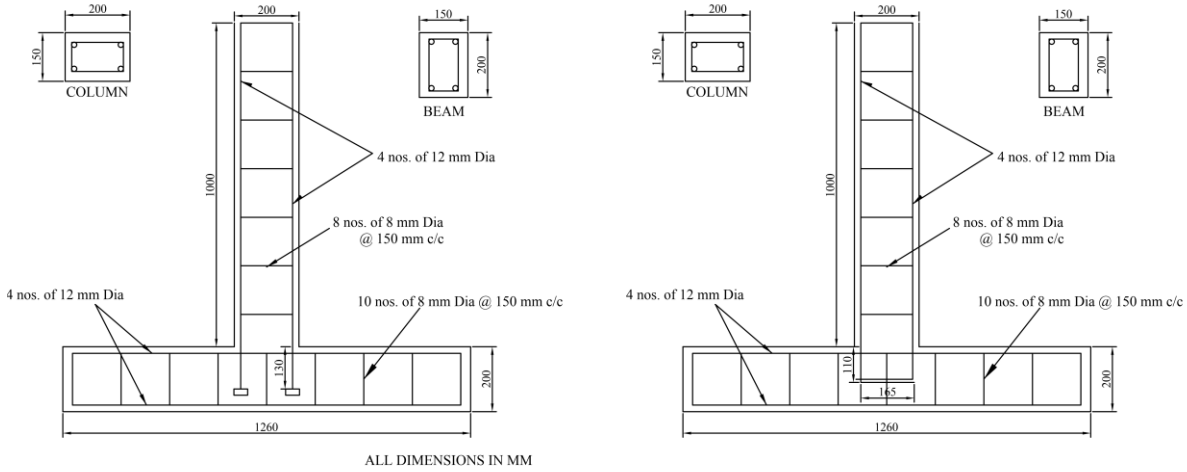

(a) BCJ with headed bar (b) BCJ with conventional (hooked) bar

Figure 3. 9 (a-b) Detailing of beam-column joint (BCJ): (a) with headed bar; (b) conventional bar

(a) BCJ with headed bar (b) BCJ with conventional bar

Figure 3. 10 (a-b) Casting of the beam-column joint (a) with headed bar; (b) conventional bar

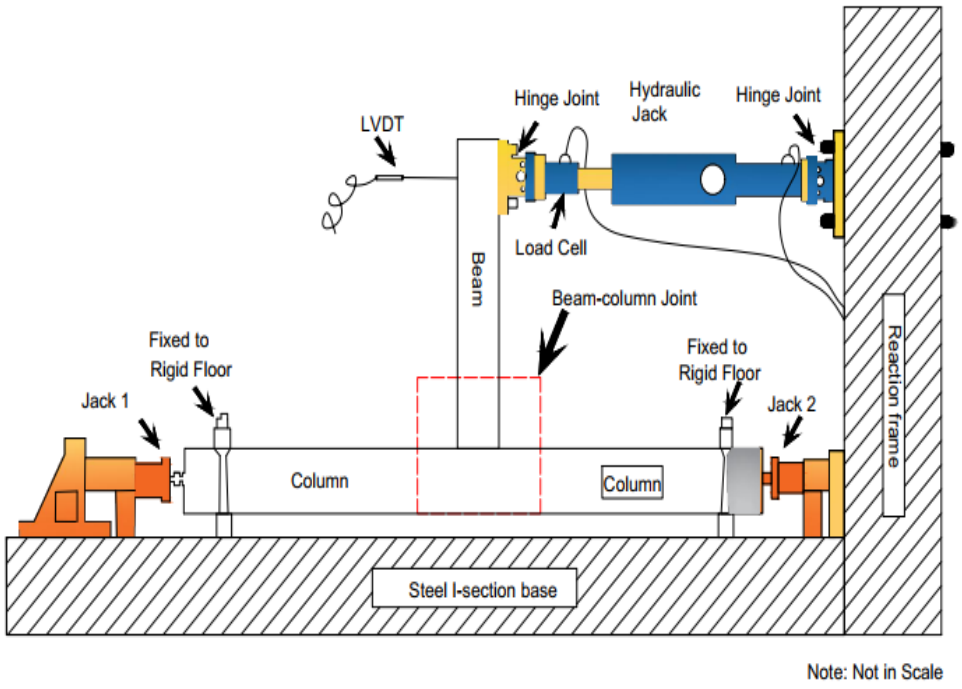

Figure 3.11 (a)

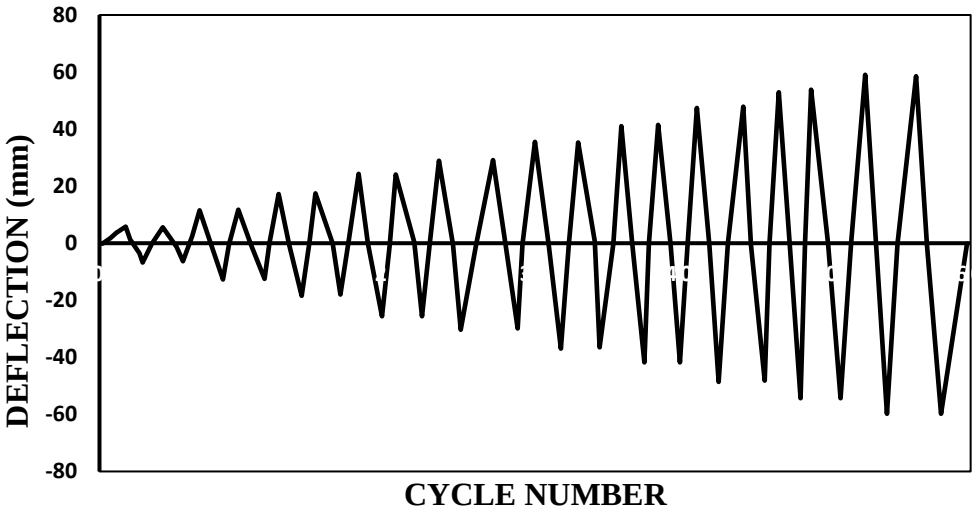

Figure 3. 11 (b)

Figure 3. 11 (a-b) (a) Beam-column joint test set-up **(b)** Load-history plot

3.5 Concluding remarks

The experimental methodology used in this study has been described. The testing program's goals are to provide additional, more in-depth data on the behavior of headed bars than had previously been available in the literature. The pull-out test on a total of 324 cylindrical specimens has been conducted, and 8 external beam-column joints have been investigated to evaluate the anchorage capacity of headed bars in SFRC.

The results of these tests, as well as comparisons, are presented in Chapters 4 and 5.

CHAPTER 4

PULL-OUT BEHAVIOR OF HEADED BARS EMBEDDED IN STEEL FIBER REINFORCED CONCRETE

4.1 General

In reinforced concrete (RC) constructions, mechanical anchorages/headed bars have been used in the design and construction of complicated details. Due to benefits such as reduced steel congestion, they are increasingly being used to replace conventional and hooked reinforcement bars in traditional concrete structures, particularly in exterior beam-column joints, lap joints, column footing connections, and other cutting-edge RC structures. (Choi *et al.* 2002; Ghali and Youakim 2005; Yang *et al.* 2012; Khederzadeh and Sennah 2014; Chiu *et al.* 2016). These heads confine the concrete beneath them and develop a bond in a comparatively short distance (Park *et al.* 2003; Delhomme *et al.* 2015; Delhomme *et al.* 2016; Shao 2016; Rabi 2020).

The anchorage capacity of headed bars in concrete is investigated using 324 pull-out tests in cylindrical specimens measuring 150 X 300 mm with an embedment depth of eight times the bar diameter. Headed bars have been manufactured using ASTM A970-16 and ACI 318-19 standards. The diameter of the steel bar, percentage of steel fibers, compressive strength of concrete, and head shapes are the primary parameters used in this study. The summary of peak load, bond strength, ultimate displacement, and failure modes for various specimens and the bar chart displaying the load-carrying capacity of the specimens are presented in this chapter. The values reported represent the average of three tests. The outcomes are presented as load-displacement responses. The failure mechanisms and crack patterns are also described. The average load-displacement curve for headed bars obtained from the pull-out test as described in Chapter 3 is included in the load-displacement plots. Also, the pull-out strengths of the specimens have been compared with codal provisions of (ACI 318-19, fib MC2010, and EN 1992-1-1 codes). A numerical and analytical model for improving the accuracy of anchorage capacity predictions of headed bars has also been

proposed. It has been analysed that the anchorage capacity of headed bars increases with the increase in concrete compressive strength, the diameter of the bar, and steel fibers, which is validating the model generated by non-linear regression analysis using dummy variables and a model generated by genetic programming. A model for bond strength of the headed bars has been developed using non-linear regression analysis and the model has been validated with the experimental results.

4.2 Pull-out behavior of headed bars

A pull-out test has been performed on the cylindrical specimens having headed bars embedded at a depth of $8d_b$ concentrically to check the bond behavior of headed bars with the surrounding concrete. The results from the pull-out test have been investigated through the load-displacement plot. It is clear that different head shapes, reinforcing bar diameters, steel fiber percentages, and concrete grades have behaved differently in the pull-out test. Load-displacement curves have been used to compare the bond behavior of headed bars in terms of steel fibers and reinforcing bar diameter. In Figures 4.1(a-i), 4.2 (a-i), and 4.3(a-i), the percentage of steel fibers is compared for each diameter of the bar, i.e., (16, 20, and 25 mm) of each shape of the head (S, R & C) for M20, M40, and M60, respectively. Whereas in Figures 4.4(a-c), 4.5(a-c), and 4.6(a-c), results of diameters of bars of each shape of the head are compared at 1.5 percentage of steel fibers only for M20, M40, and M60, respectively. In Figure 4.1(a), all the headed bars have an increasing elastic behavior until they reached the yielding point of 50 kN, then a peak with a slight increase in load until they reached a displacement of 1 mm. The load-displacement curve for all the four specimens has a similar pattern i.e. the curves are linear upto 50 kN load and 0.03 mm displacement. After the gradual increase in the applied load, the yielding of the specimens is observed at 69 kN load and 0.04 mm displacement which implies that there is no slippage at the bars' free ends. After that, the load-displacement curves for all the specimens of S1M20 are constantly increasing till failure. It is observed from Figure 4.1(a) that the specimen having 1.5SF has achieved maximum peak load out of all the specimens, i.e., 125 kN, and the ultimate displacement is 1 mm. It is also observed from Figure 4.1(a) that there has been no significant change, i.e., 5-10% in the peak load of the specimens due to the addition of steel fibers. In Figure 4.1(b), the load-displacement curve for all the four

specimens has an almost similar pattern, i.e., the curves are linear up to 100 kN load and 0.03 mm displacement. After the gradual increase in the applied load, early yielding in 0SF and 0.5SF specimens has been observed at 107.5 kN load and 0.04 mm displacement. At the same time, the specimens having 1SF and 1.5SF yield at 127.42 kN and 0.1 mm displacement. This implies that there is no slippage at the bars' free ends. After that, the load-displacement curves for all the specimens of S2M20 are constantly increasing till failure. It is observed from Figure 4.1(b) that the specimen having 1.5SF has achieved maximum peak load out of all the specimens, i.e., 189.6 kN and the ultimate displacement is 1.5 mm. It is also observed from Figure 4.1(b) that there has been only a 1-2% increase in the peak load of the specimens due to the addition of steel fibers. Whereas with an increase in the bar diameter, the peak load has increased from 125 to 189.1 kN, which is attributed to the larger area of the headed bar, which can carry more load and thus makes a better anchorage with the concrete.

The comparative analysis of load-displacement curves reveals some results validated by the study of Qian *et al.* (2018). It has been observed from Figures (4.1(a-i), 4.2(a-i), and 4.3(a-i)), that the general pattern of the load-displacement curves are similar overall, i.e., the curves are linear up to 50-100 kN and then yielding takes place after the gradual tensile load application on the specimens and increases above 100 kN. Consequently, the headed bars have been pulled out during loading. In general, increasing the bar diameter achieves a greater load-carrying capacity. The same behavior has been observed in the study of Nilforoush (2017). The linear ascending slope indicates that no slip occurred at the free end of the bar (which is exposed outside). From Figures (4.4(a-c), 4.5(a-c), and 4.6(a-c)), the difference between the three shapes of headed bars, i.e., square, rectangular, and circular, is graphically analyzed, leading to the conclusion that the circular head carries the maximum load with the highest steel fiber ratio of 1.5 %. The rectangular shape has the lowest load carrying capacity out of all the head shapes due to the non-uniform load distribution provided by its bearing area, which was observed through the crack pattern during the experiment. The peak load of the square head is 7.9 percent greater than that of the rectangular head. Figures 4.1 (a-i) show that at failure, the load drop and slip increase for circular-headed bars are slightly (10-15%) higher than for square and rectangular bars. At 50 kN applied load, the first displacement of the head is measured, which

is also the load at which the first diagonal crack has been observed. Beyond this point, the displacement increased almost linearly. The specimen failed at a load of 200 kN and a displacement of 1.25 mm. At failure, the applied load has dropped to 110 kN, and the displacement has increased to 1.8 mm. The load-displacement curves for all shapes of head and diameter of bars are nearly identical throughout the load history for all the specimens with M20 grade (Figures 4.1 (a-i)).

Similarly, the same load-deflection pattern has been observed in the case of M40 and M60 grades, but the ultimate load and ultimate displacement have been increased with an increase in compressive strength of concrete (Figures 4.2(a-i) and 4.3(a-i)). It can be observed from Figures 4.2(a-i) that the specimens have failed at a displacement of 2.5-3.5 mm compared to 1.5-2.5 mm in the case of Figures 4.1(a-i). It is due to the strong bond between the head and the surrounding concrete due to higher compressive strength.

The summary of peak load, bond strength, and failure modes for various specimens are presented in Table 4.1 and the value obtained represents the average of three tests. As per ACI 318-2019, the ultimate bond strength (τ_{max}**)** is calculated using equation 4.1. The bond stress of all the specimens has been compared using fib MC2010, ACI 318-19, and EN 1992-1-1 codes.

$$\tau_{max} = (P_{max}/3.14*d_b*l_{eh}) \quad (4.1)$$

where: P_{max} is the maximum peak load (kN), d_b is the diameter of the reinforced bar (mm), and l_{eh} is the embedment depth of the headed bar (mm).

As per Model code MC2010, the design bond strength (f_{bd}) is calculated using equation 4.2.

$$f_{bd} = ((\alpha_2+\alpha_3)f_{bd,0} - 2P_{tr}) < (2.0f_{bd,0}-0.4P_{tr}) < (1.5/\gamma_{cb})\times\sqrt{f_{ck}} \quad (4.2)$$

where: α_2 and α_3 represent the influence of passive confinement from cover (α_2) and from transverse reinforcement (α_3) and may conservatively be taken as 1.0. P_{tr} (P_{max}/area of the section) is the mean compression stress perpendicular to the potential splitting failure surface at the ultimate limit state. Due to the different failure modes during the pullout test, the area of the

section is varying i.e. during steel failure, the area of steel bar is taken and during concrete failure, the area of the cylinder is taken. Basic bond strength, ($f_{bd,0}$) is given by equation 4.3.

$$f_{bd,0} = (\eta_{1*}\ \eta_{2*}\ \eta_{3*}\ \eta_{4)*}(f_{ck} / 25)^{\ 0.5/\gamma_{cb}} \quad (4.3)$$

where: η_1 is a coefficient taken as 1.75 for ribbed bars (including galvanized and stainless reinforcement), η_2 represents the casting position of the bar during concreting and is taken as 0.7 for all the cases where ribbed bars are used, η_3 represents the bar diameter (ϕ) and is 1.0 for $\phi \leq 25$ mm, and η_4 represents the characteristic strength of steel reinforcement being anchored or lapped and is taken as 1.0 for yield strength for reinforcing steel in tension (f_{yk}) = 500 MPa, f_{ck} represents the compressive strength of concrete which is taken as 20, 40 and 60 MPa and γ_{cb} represents the partial safety coefficient for bond and is taken as 1.5.

As per EN 1992-1-1, the ultimate bond strength (f_{bd}) is calculated as per equation 4.4.

$$f_{bd} = 2.25\ (\eta_{1*}\eta_{2*}f_{ctd}) \quad (4.4)$$

where: η_1 is a coefficient related to the quality of the bond condition and the position of the bar during concreting and is taken as 1.0 for good condition. η_2 is related to bar diameter (d_b). It is taken as 1 (in the present study) when $d_b \leq 32$ mm. f_{ctd} is the design value of concrete tensile strength and is calculated using equation 4.5.

$$f_{ctd} = \alpha_{ct\ *}\ (F_{ctk,0.05} / \gamma_c) \quad (4.5)$$

where: α_{ct} is a coefficient taking account of long-term effects on the tensile strength and of unfavorable effects. The recommended value for use is 1. γ_c is the partial safety factor for concrete and is taken as 1.5 for 'persistent & transient' design situations. $F_{ctk,\ 0.05}$ is the characteristic tensile strength and is computed using equation 4.6.

$$F_{ctk,\ 0.05} = (0.7)*f_{ctm} \quad (4.6)$$

where: f_{ctm} is the mean value of axial tensile strength of concrete ($f_{ctm} = 0.3\ f_{ck}^{2/3}$) for concrete class $\leq$ C50/60. f_{ck} represents the compressive strength of concrete, which is taken as 20,40 and 60 MPa.

DeVries *et al.* (1999) proposed the equation for the bearing capacity of headed bars which is given by equation 4.7.

$$P_N = ((l_{eh}^{1.5} * \sqrt{f_c'})/112) * (\frac{A_N}{A_{No}}) \quad (4.7)$$

where: P_N is the bearing capacity of concrete in kN. l_{eh} is the embedment depth in mm, and f_c' is the compressive strength of concrete strength in MPa. A_N is the projected area of concrete breakout failure as defined in Figure A.1. A_{No} is the projected area of a single anchored bar, $9(l_{eh})^2$.

The bearing capacity of the specimens has been computed using equation 4.7. A_N is the function of embedment depth so the bearing capacity of the headed bars increases as the embedment depth increases, as it is directly proportional to embedment depth as A_{No} is equal to $9(l_{eh})^2$ which is used in equation 4.7. The headed bar's failure behavior is determined by the depth of embedment. A larger embedment depth causes the bar to yield, while a smaller embedment depth causes the concrete to split (DeVries *et al.* 1999). The circular head has the maximum bearing capacity (i.e., 35.1 percent larger than rectangular head and 56.9% larger than square head). Bearing stress of the specimens has been calculated by dividing the bearing capacity by net area of headed bars. From the results as per Table A.1 (given in annexure), It has been observed that the maximum load has been taken by the circular head bearing rather than the square and rectangular heads. One of the major reasons behind this is that corners are more responsible for the initiation and propagation of cracking rather than curves. The stress concentration is higher in case of the corners. This may cause the reinforcement to fail prematurely. To avoid this, circular headed bars are used to uniformly distribute the load. This is in agreement with the observation made by Park (2003). After following the guidelines of ACI 318-19, the head size was kept as per Table 3.9 and after conducting pull-out test on the headed bars, the heads did not fail before the concrete or the reinforced bars, therefore, it can be concluded that the head size chosen for the study is appropriate. The same has been observed in the study conducted by Park *et al*. (2003). The ultimate bond strength (τ_{max}) calculated using ACI 318-19 is higher than the design bond strength calculated using fib MC2010 and EN 1992-

1-1 because the ACI formula includes the embedment depth factor, which is not included in the bond strength formulas of fib MC2010 and EN 1992-1-1.

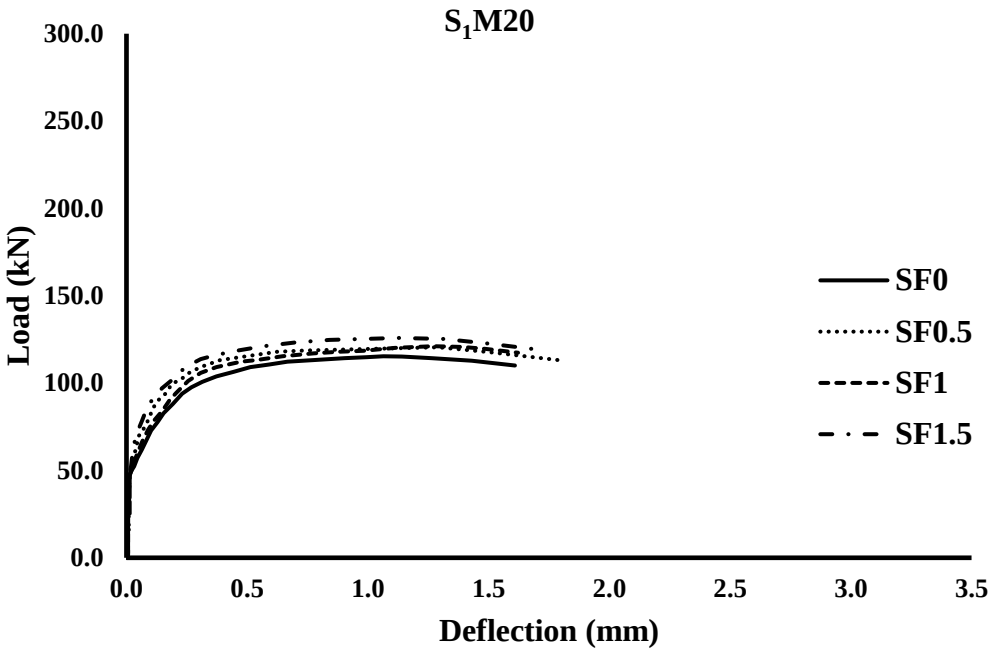

Figure 4.1 (a) 16mm diameter, square head

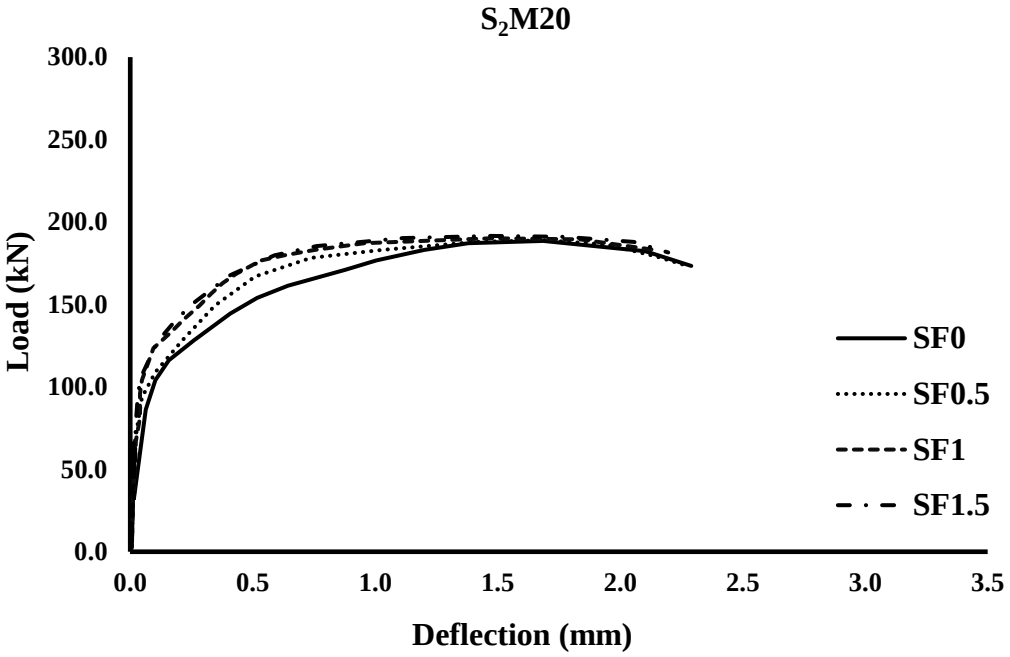

Figure 4.1 (b) 20mm diameter, square head

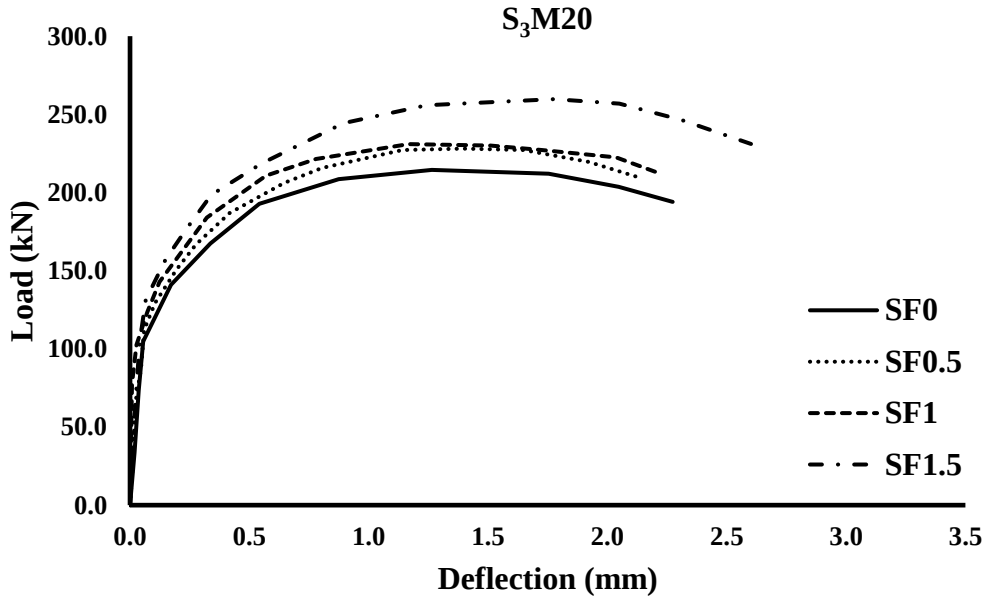

Figure 4.1 (c) 25mm diameter, square head

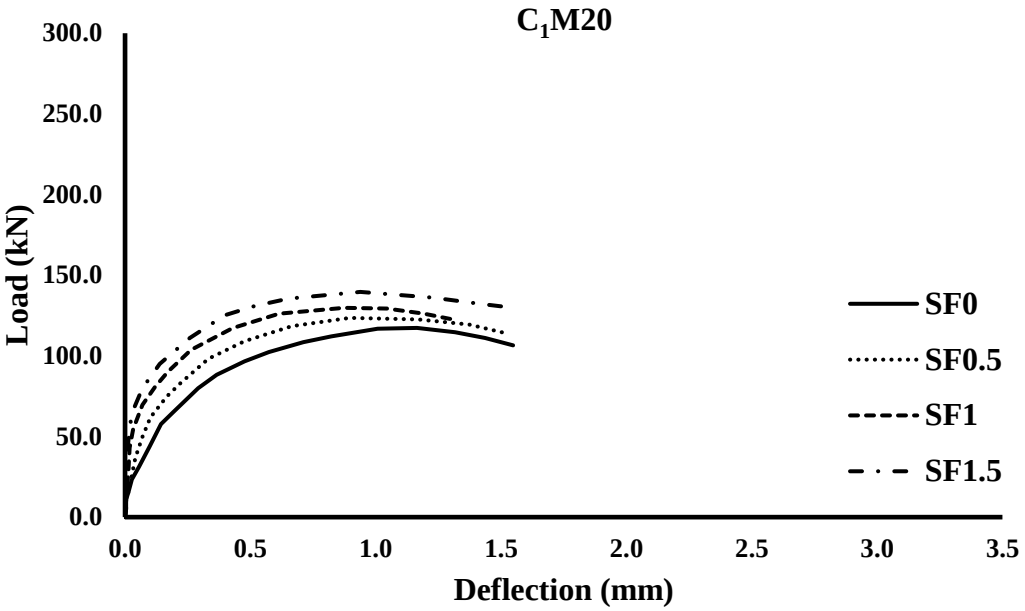

Figure 4.1 (d) 16mm diameter, circular head

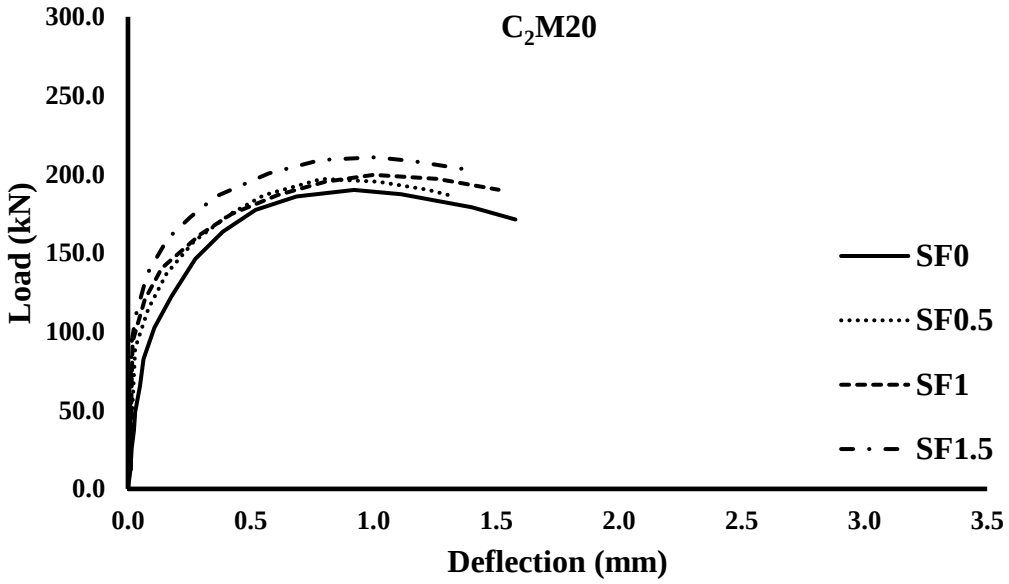

Figure 4.1 (e) 20mm diameter, circular head

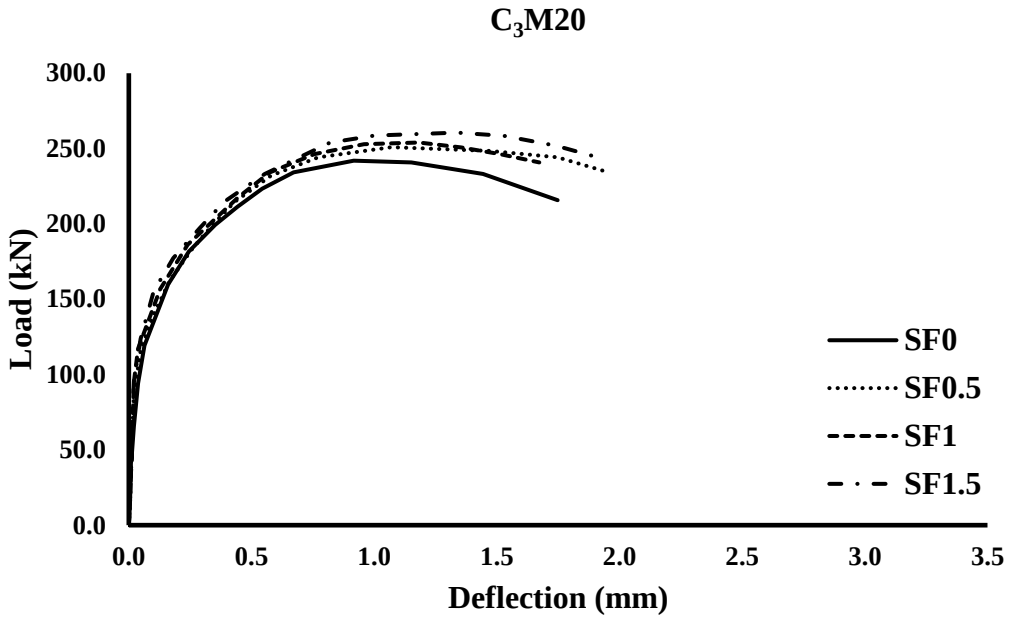

Figure 4.1 (f) 25mm diameter, circular head

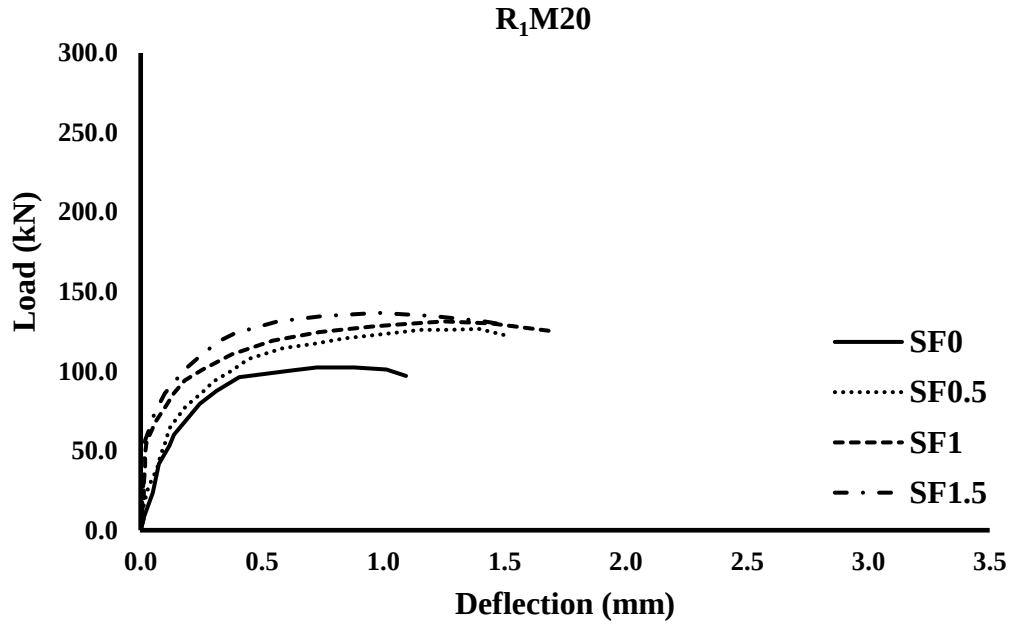

Figure 4.1 (g) 16mm diameter, rectangular head

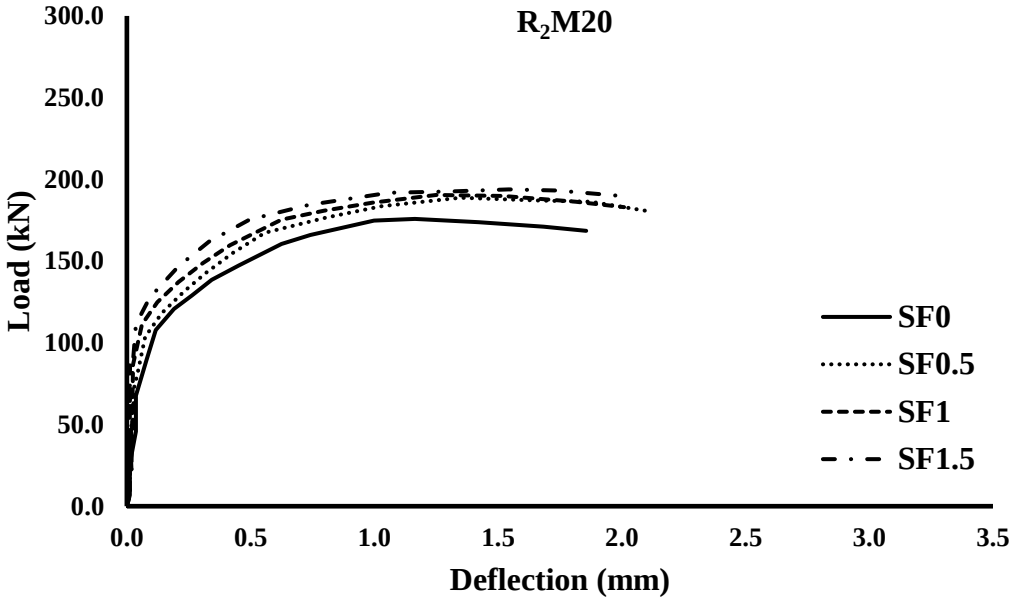

Figure 4.1 (h) 20mm diameter, rectangular head

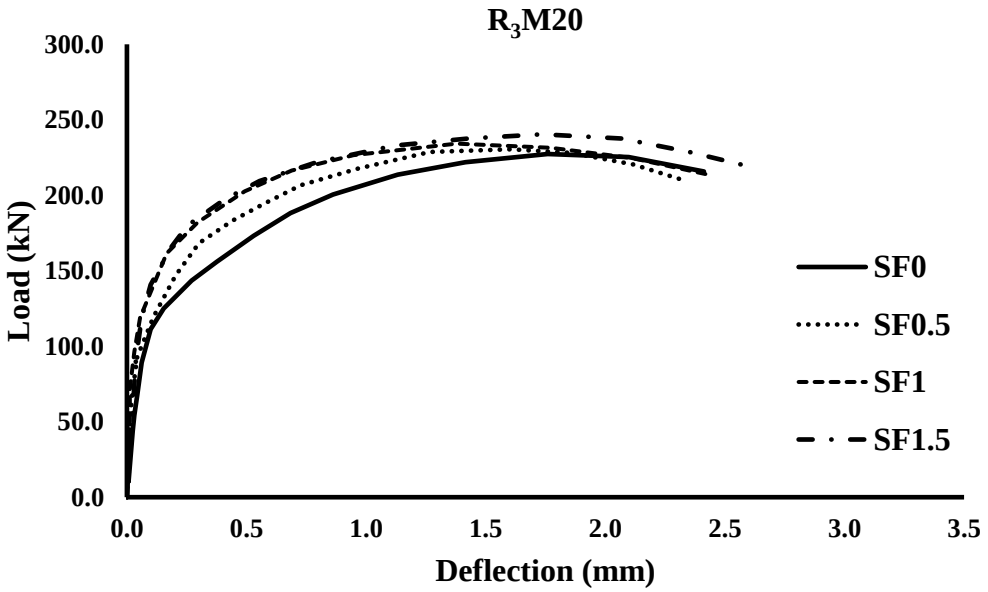

Figure 4.1 (i) 25mm diameter, rectangular head

Figure 4. 1 (a-i) Load-deflection curves for M20, comparing steel fibers

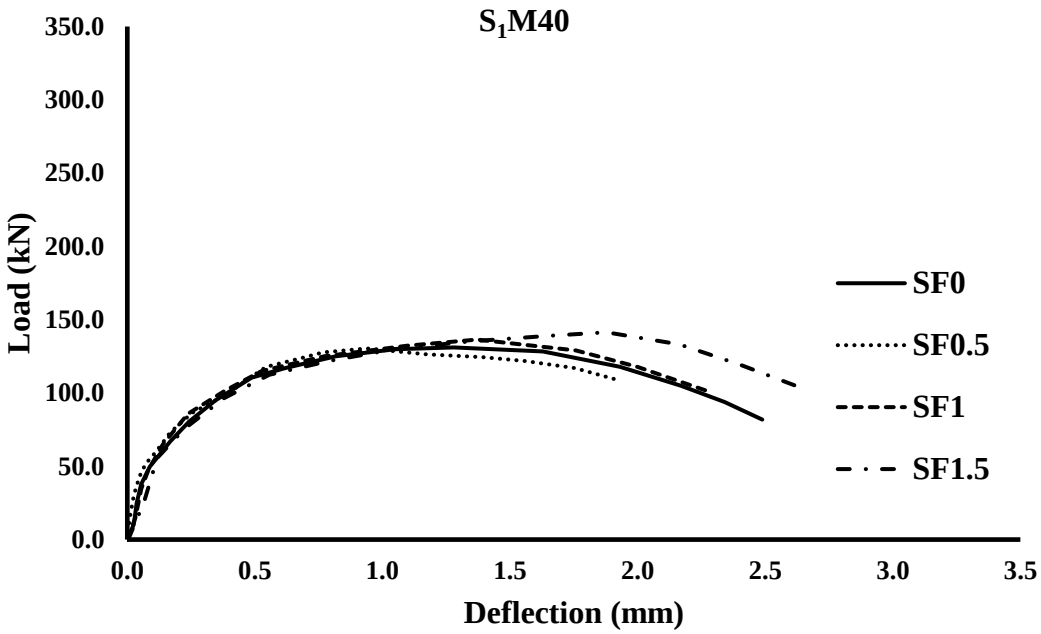

Figure 4.2 (a) 16mm diameter, square head

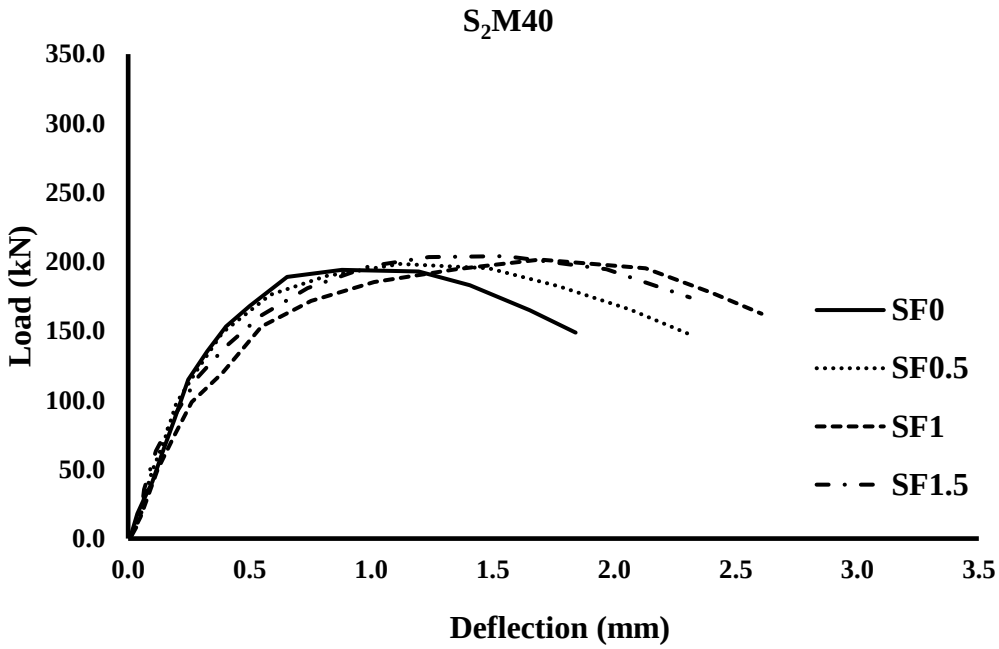

Figure 4.2 (b) 20mm diameter, square head

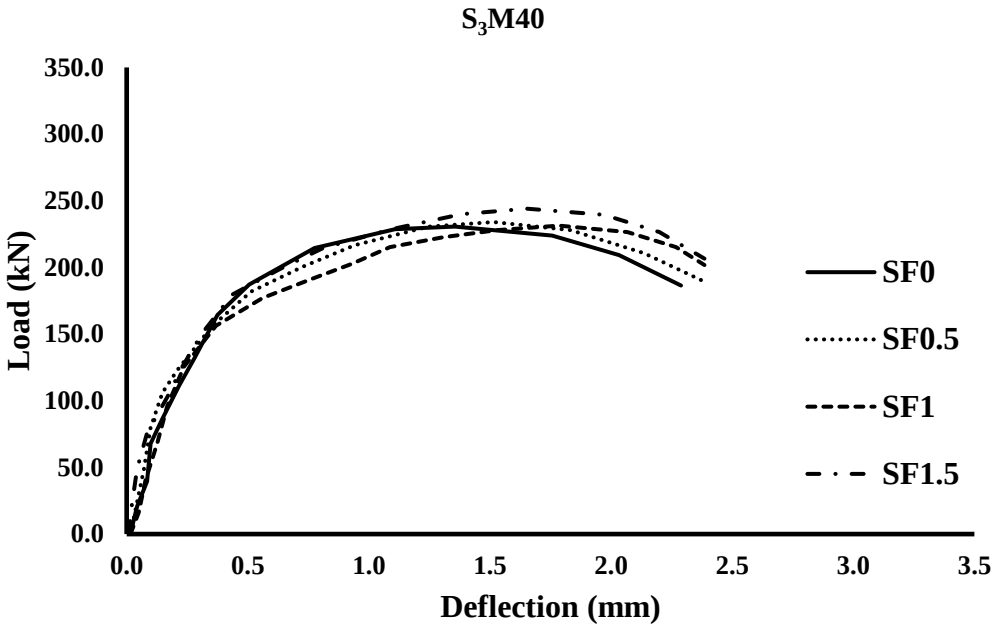

Figure 4.2 (c) 25mm diameter, square head

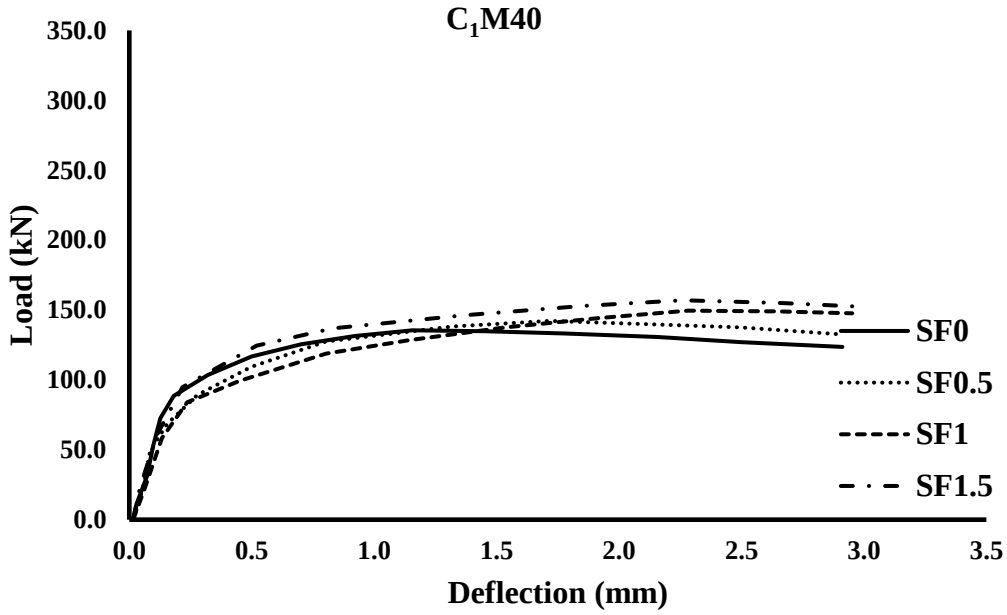

Figure 4.2 (d) 16mm diameter, circular head

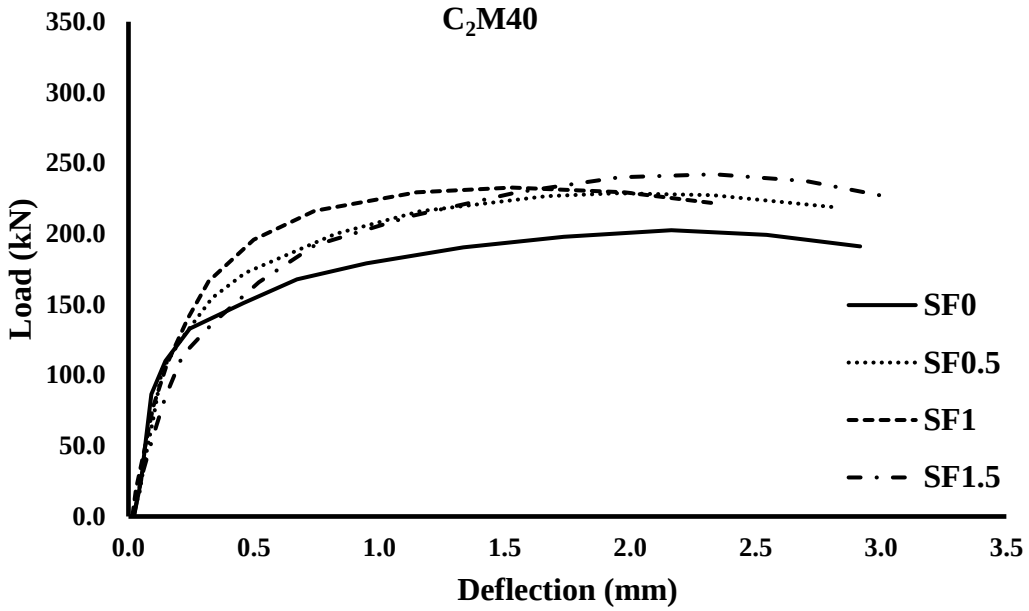

Figure 4.2 (e) 20mm diameter, circular head

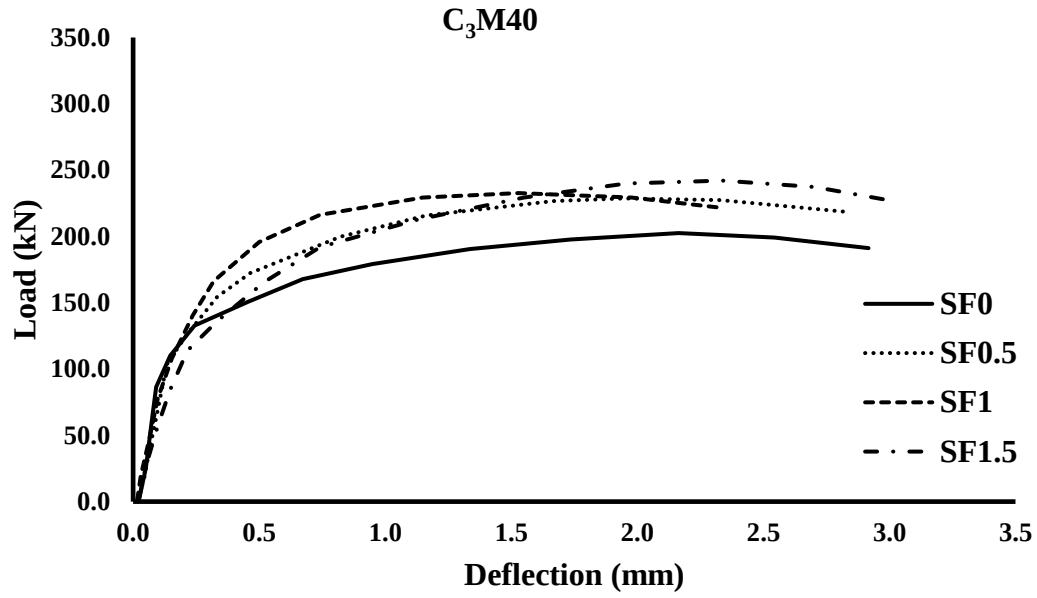

Figure 4.2 (f) 25mm diameter, circular head

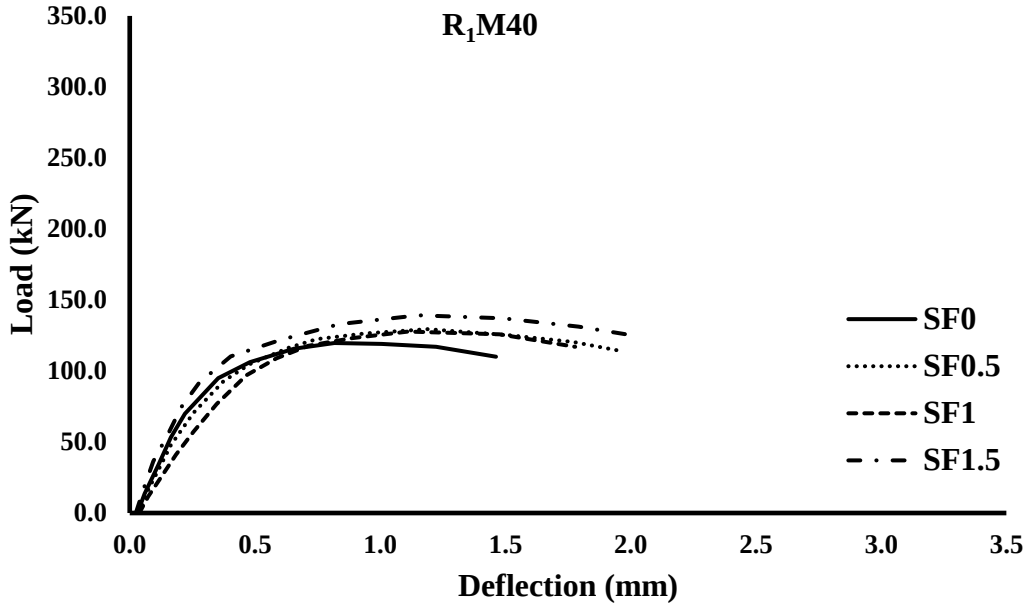

Figure 4.2 (g) 16mm diameter, rectangular head

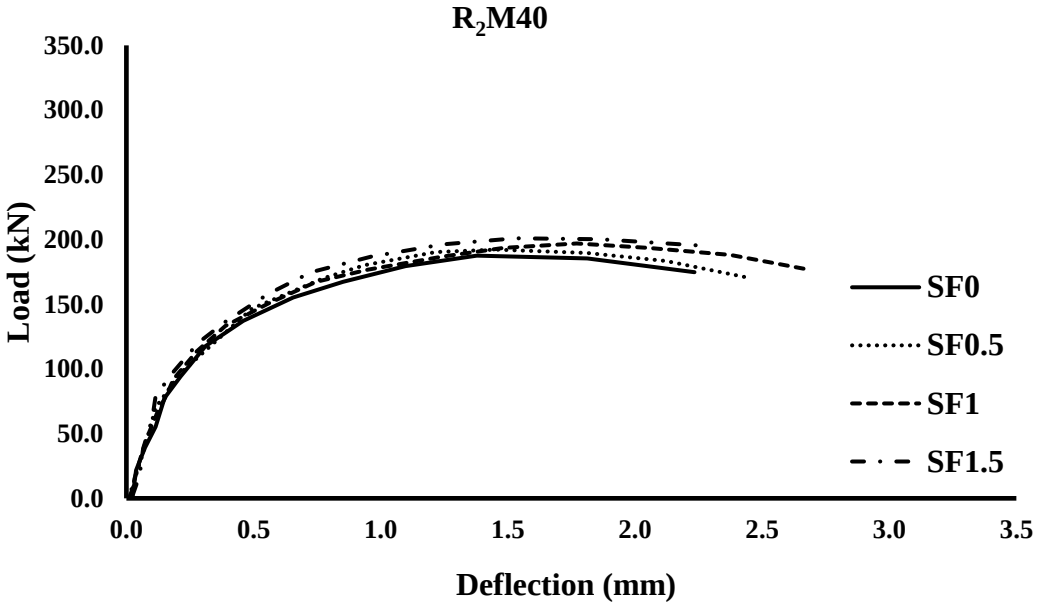

Figure 4.2 (h) 20mm diameter, rectangular head

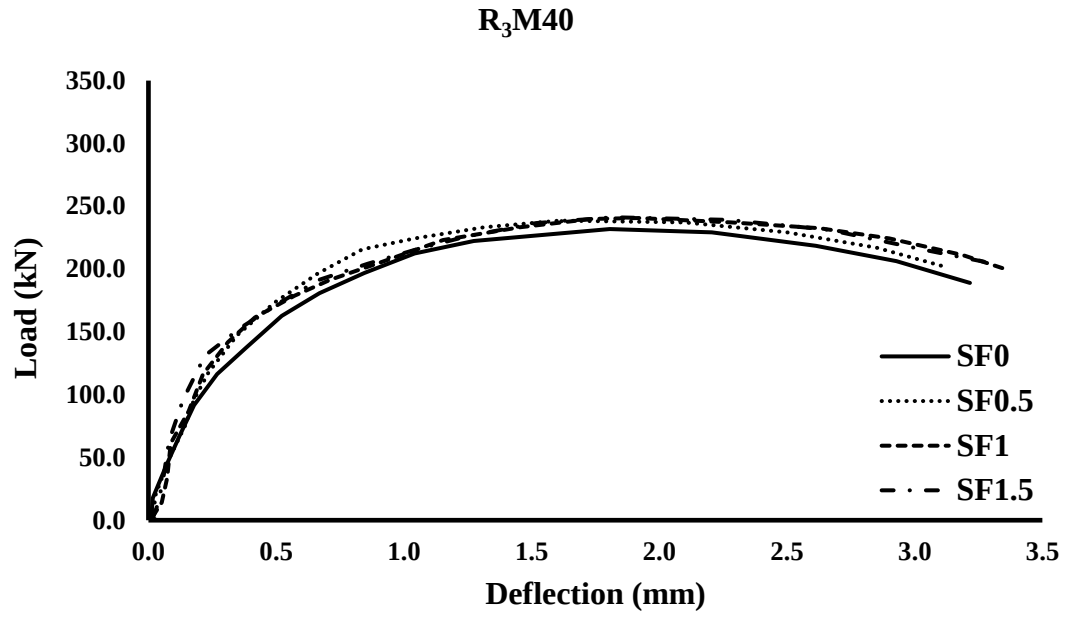

Figure 4.2 (i) 25mm diameter, rectangular head

Figure 4. 2 (a-i) Load-deflection curves for M40, comparing steel fibers

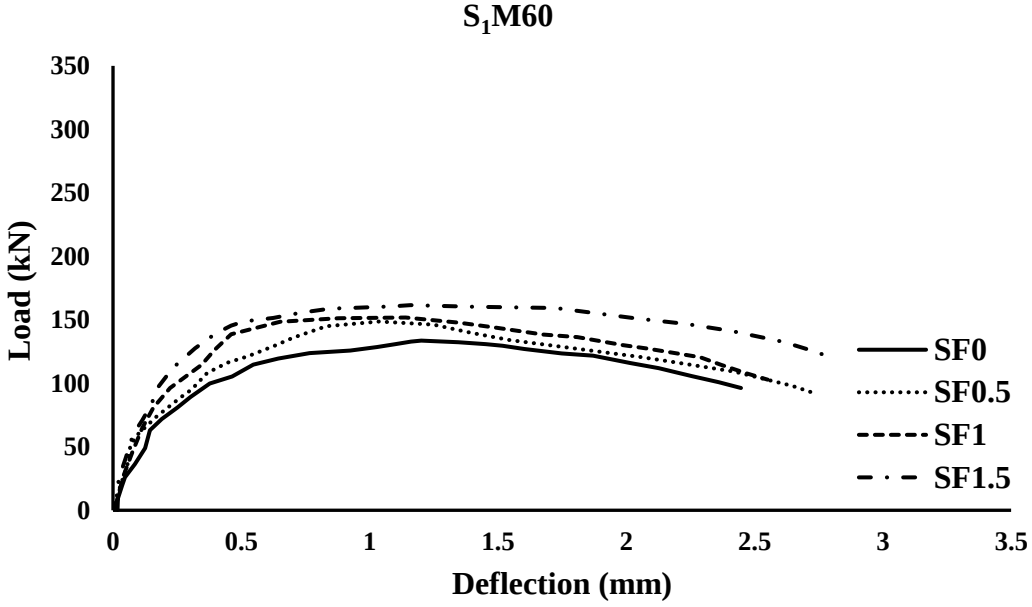

Figure 4.3 (a) 16mm diameter, square head

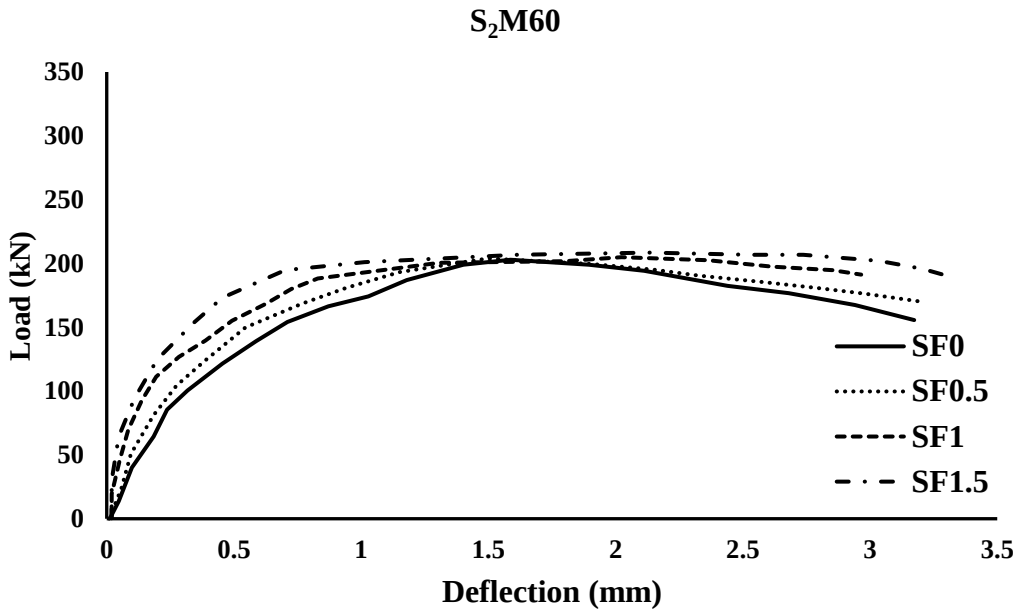

Figure 4.3 (b) 20mm diameter, square head

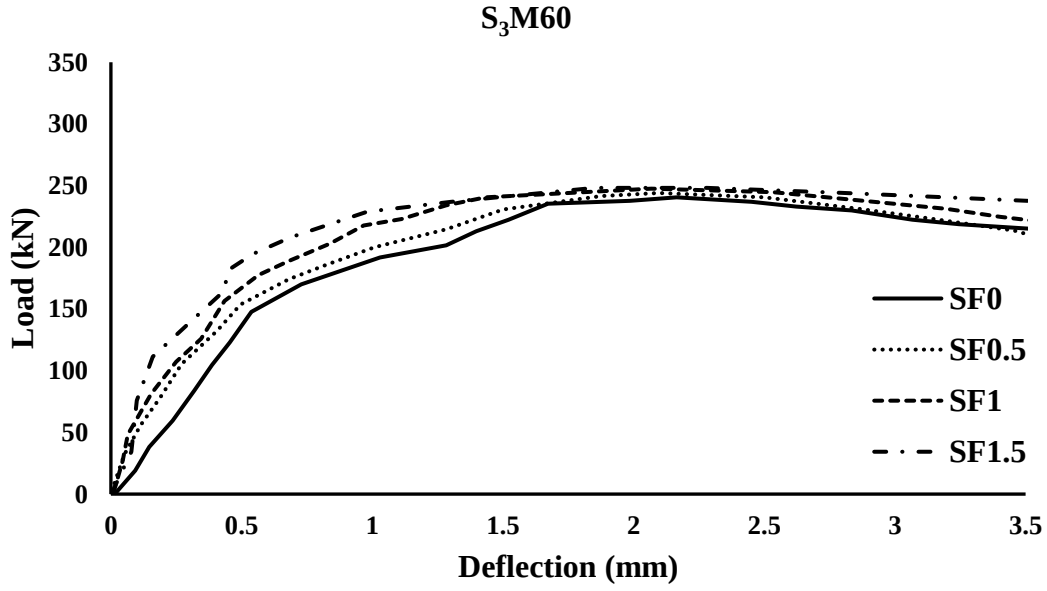

Figure 4.3 (c) 25mm diameter, square head

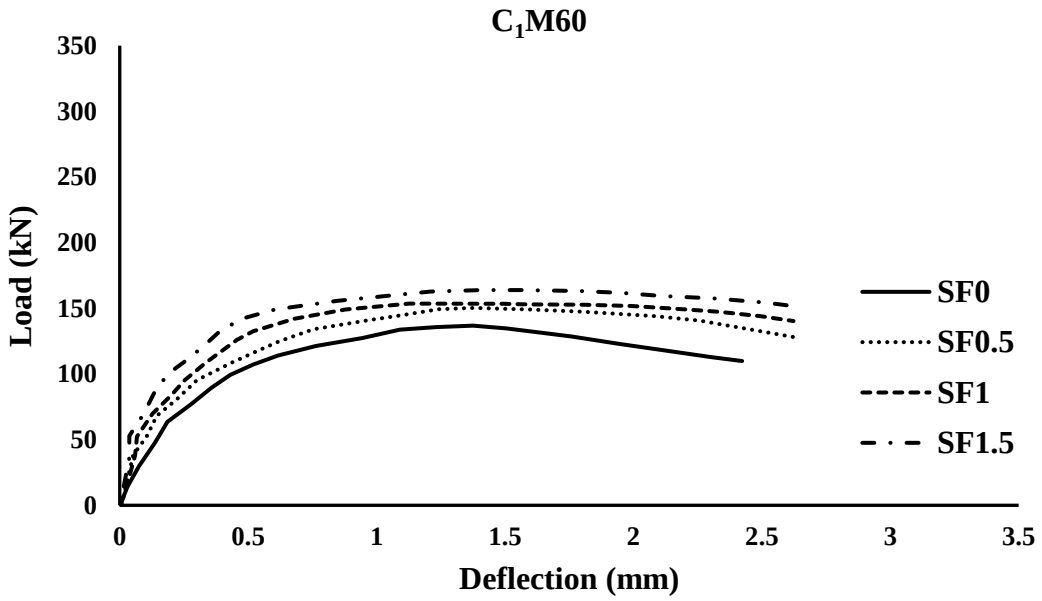

Figure 4.3 (d) 16mm diameter, circular head

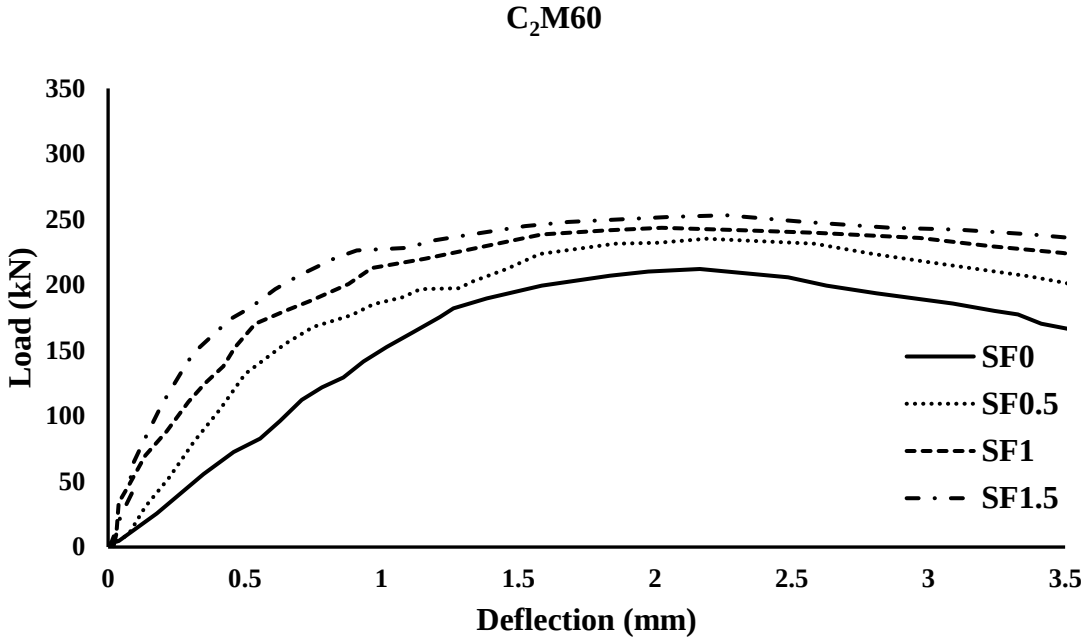

Figure 4.3 (e) 20mm diameter, circular head

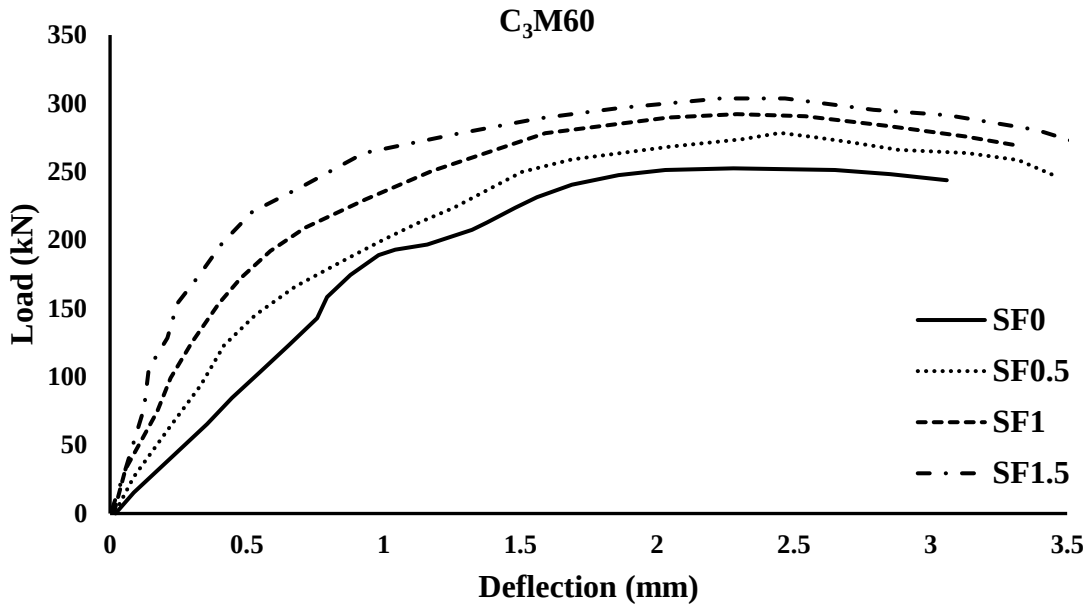

Figure 4.3 (f) 25mm diameter, circular head

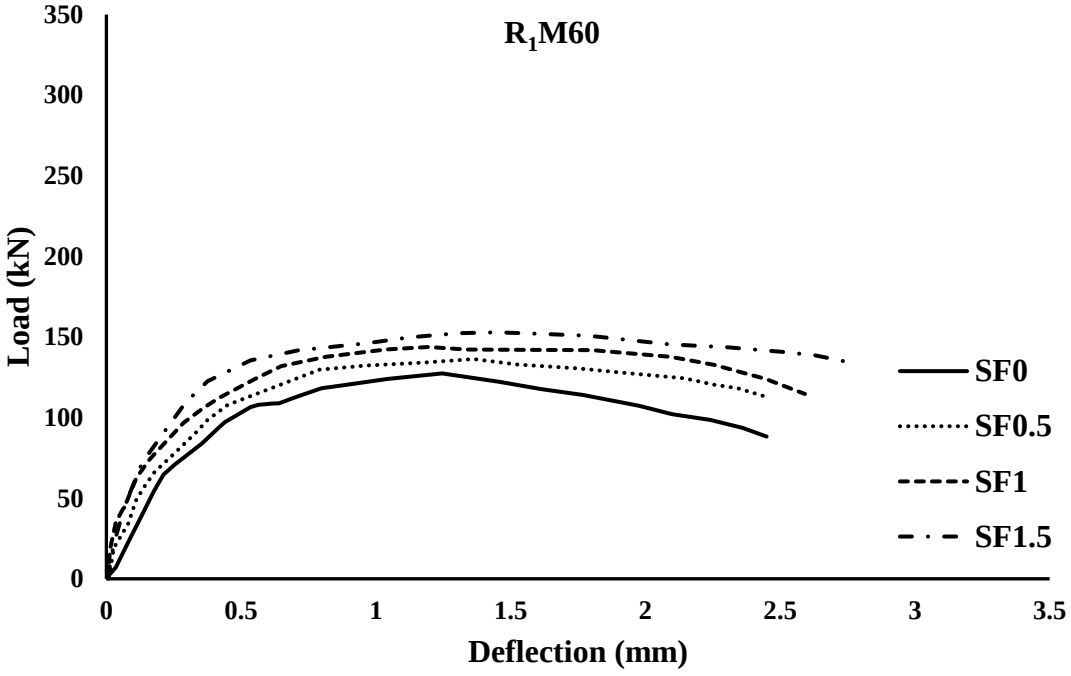

Figure 4.3 (g) 16mm diameter, rectangular head

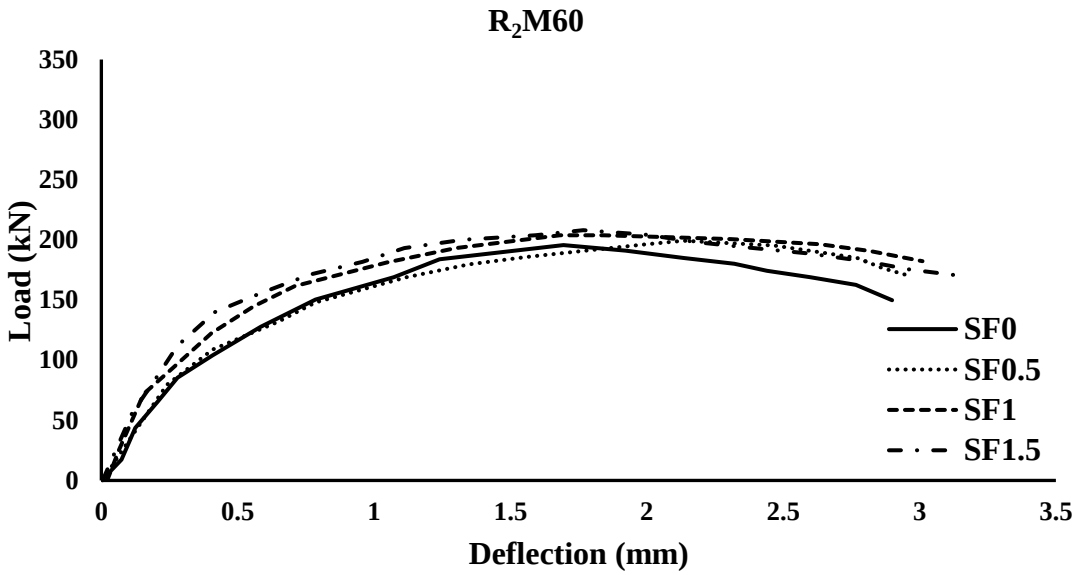

Figure 4.3 (h) 20mm diameter, rectangular head

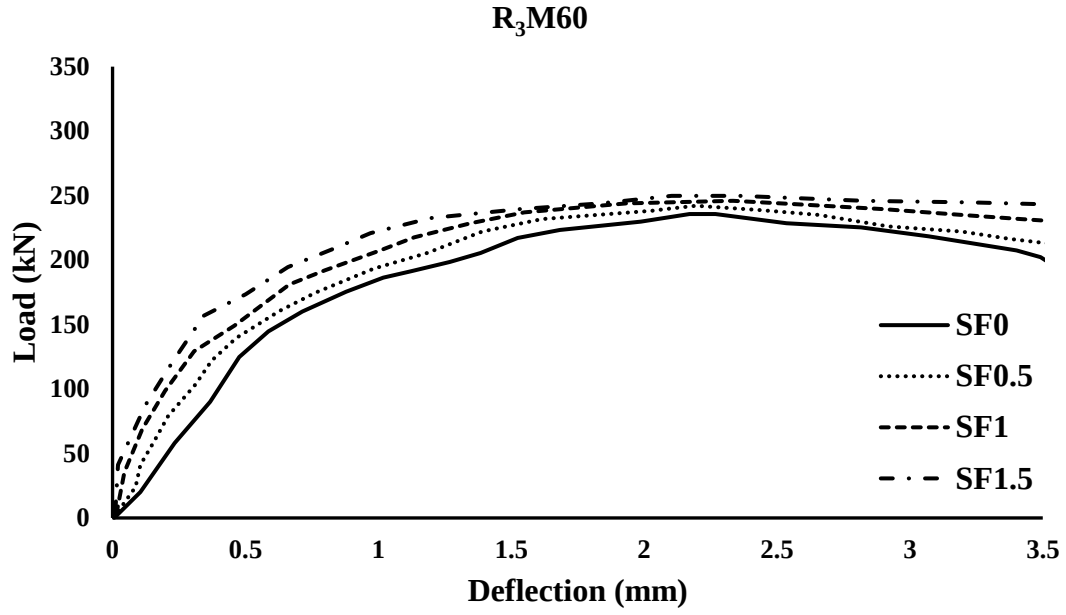

Figure 4.3 (i) 25mm diameter, rectangular head

Figure 4. 3 (a-i) Load-deflection curves for M60, comparing steel fibers

4.3 Influence of head shape

The variation between the three shapes of headed bars, i.e., square, rectangular & circular shapes, is evaluated graphically (Figures 4.4(a-c), 4.5(a-c), and 4.6(a-c)). For the same percentage of SF, i.e., at 1.5SF and for M20 grade, the peak load of S1, R1, and C1 are 125, 135, and 139 kN, respectively. Similarly, for the M40 grade, the peak load value for S1, R1, and C1 are 140.9 kN, 139.8 kN, and 156.3 kN, respectively. For M60 grade, S1, R1, and C1 have peak load values of 161.5 kN, 152.9 kN, and 164.9 kN, respectively. Therefore, out of all the three shapes of the head, the rectangular shape shows the minimum load carrying capacity because of the non-uniform load distribution provided by its bearing area. The peak load of the square head is 7.9% higher than the rectangular head. The peak load of the circular head is 15.7% and 16.2% higher than the square head and the rectangular head, respectively, due to the uniformity provided by its bearing, which is capable of taking the maximum load transferred through the steel bar. It concludes that the circular head takes the maximum load with the highest steel fiber ratio of 1.5%. However, overall, it can also be concluded that the head shape has no significant effect on the load-carrying capacity of headed bars.

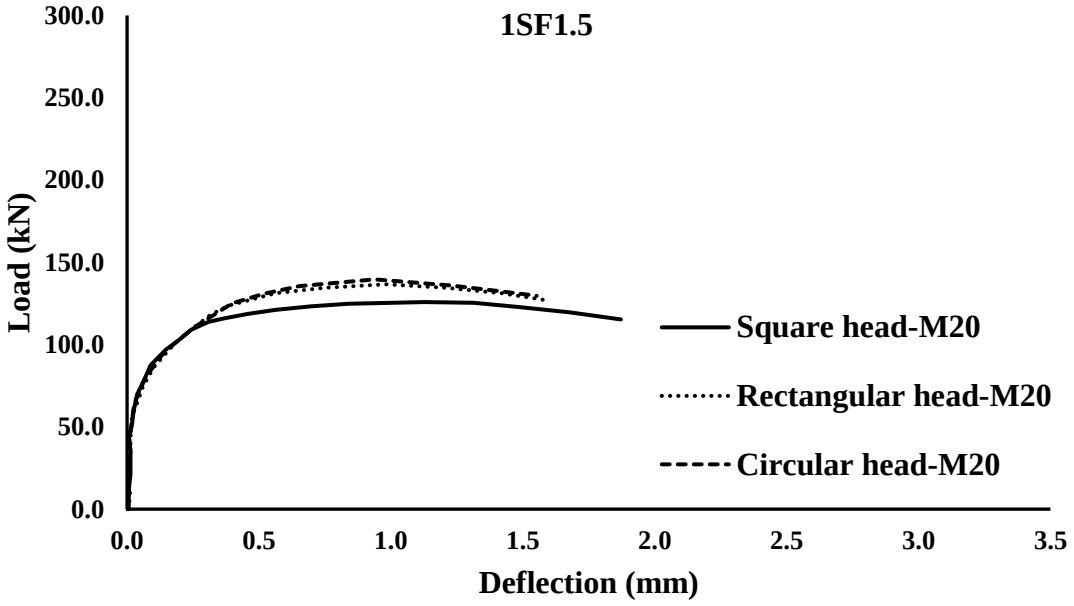

Figure 4.4 (a) 16mm diameter and 1.5% of steel fibers

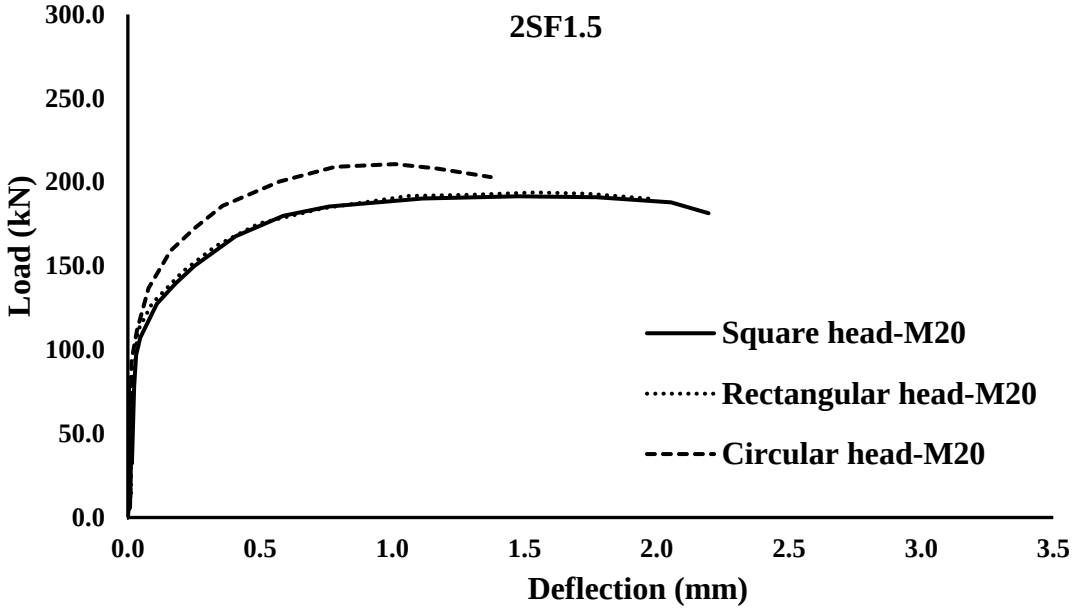

Figure 4.4 (b) 20mm diameter and 1.5% of steel fibers

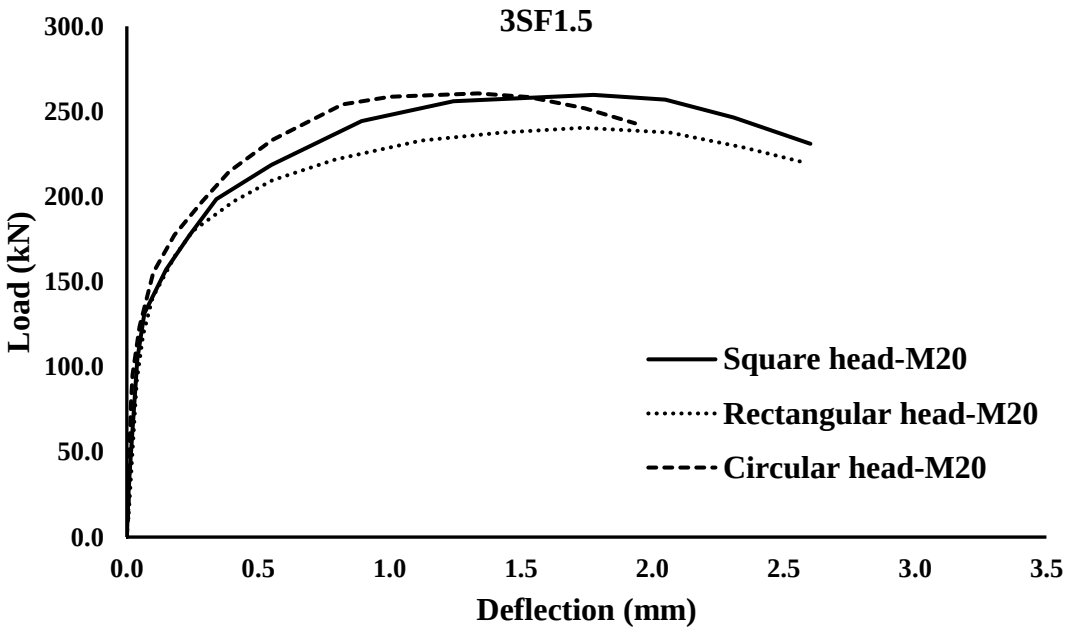

Figure 4.4 (c) 25mm diameter and 1.5% of steel fibers

Figure 4. 4 (a-c) Load-Deflection curves for M20, comparing shapes of head

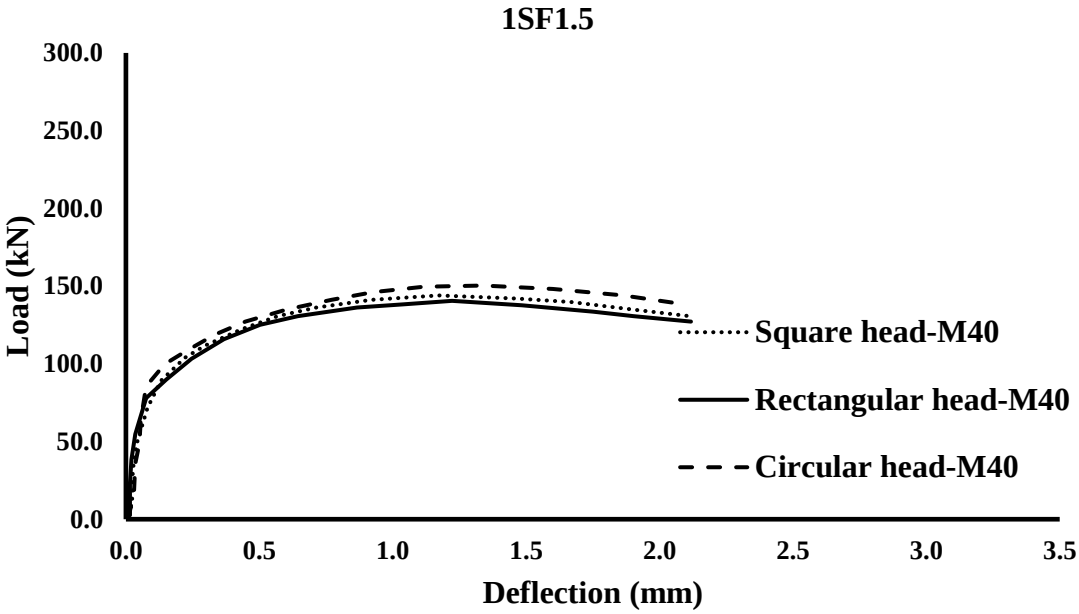

Figure 4.5 (a) 16mm diameter and 1.5% of steel fibers

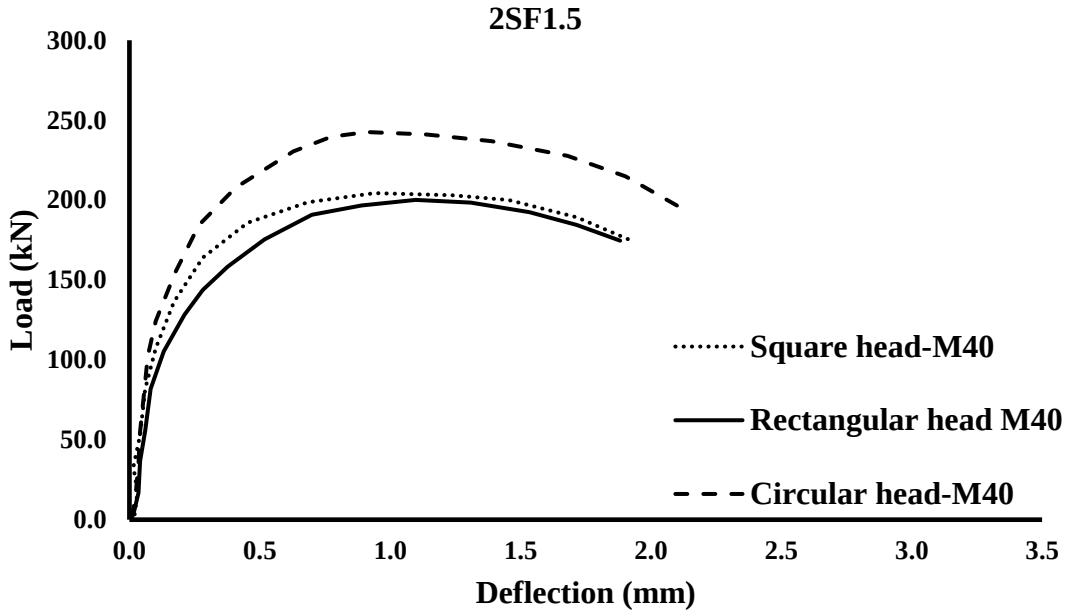

Figure 4.5 (b) 20mm diameter and 1.5% of steel fibers

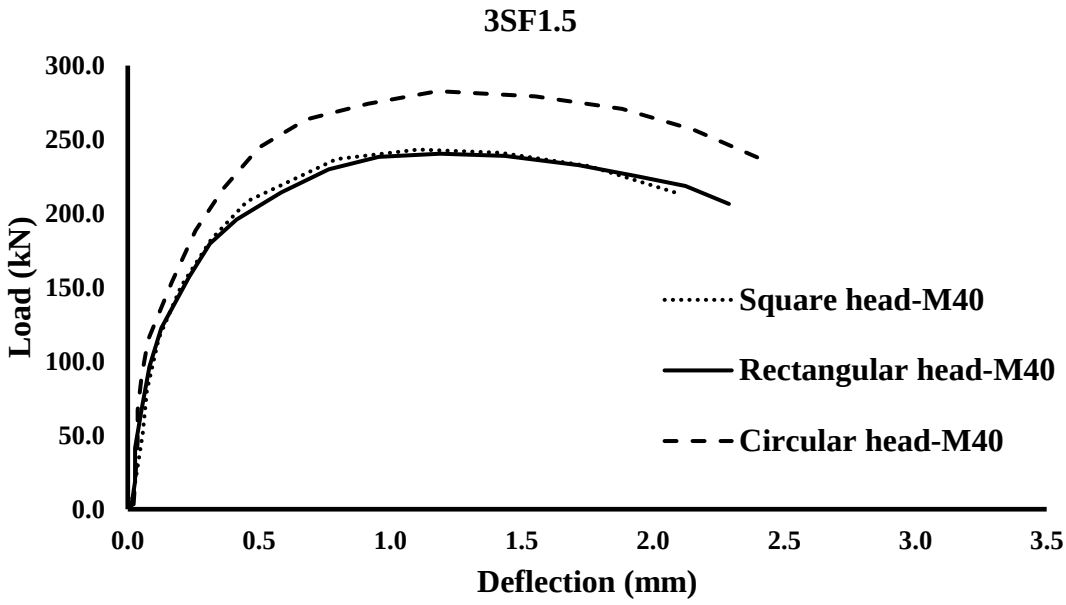

Figure 4.5 (c) 25mm diameter and 1.5% of steel fibers

Figure 4. 5 (a-c) Load-Deflection curves for M40, comparing shapes of head

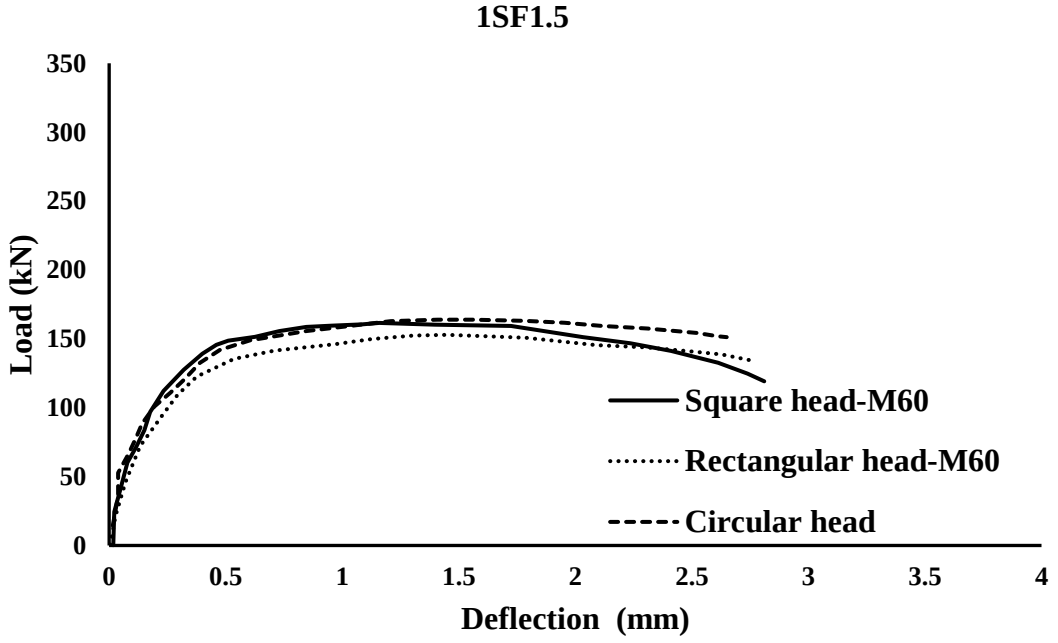

Figure 4.6 (a) 16mm diameter and 1.5% of steel fibers

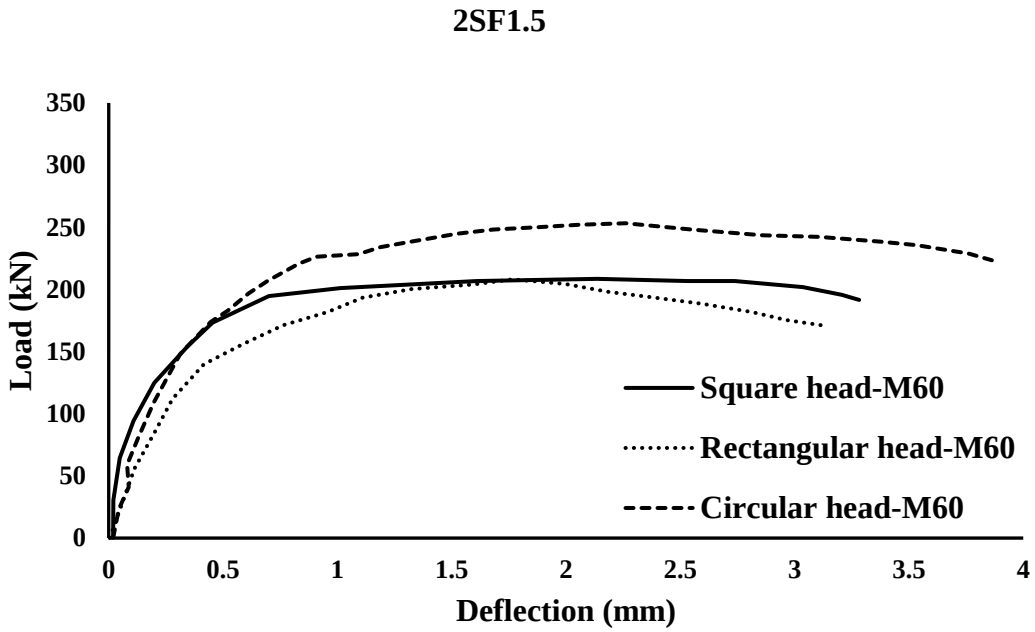

Figure 4.6 (b) 20mm diameter and 1.5% of steel fibers

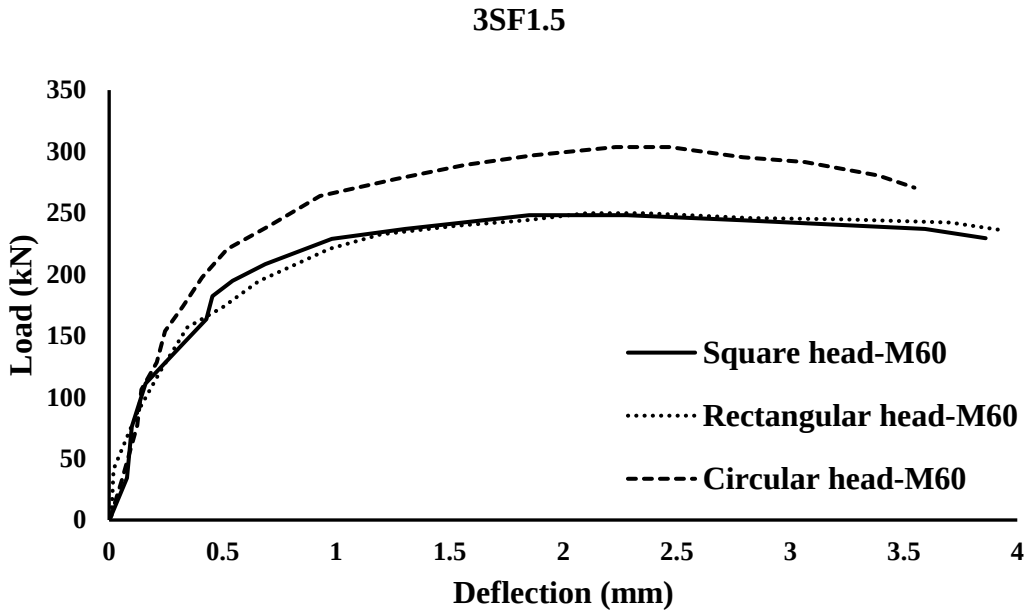

Figure 4.6 (c) 25mm diameter and 1.5% of steel fibers

Figure 4. 6 (a-c) Load-Deflection curves for M60, comparing shapes of head

Table 4. 1 Test results of Pull-out specimens

Specimen	Grade of concrete	d_b (mm)	l_{eh} (mm)	P_{max} (kN)	τ_{max} (MPa) (ACI 318-19)	Failure mode
S1SF0	M20	16	128	115	17.9	CBF
	M40	16	128	130.4	20.3	CBF
	M60	16	128	133.6	20.8	CBF
S1SF0.5	M20	16	128	120	18.7	CBF
	M40	16	128	127.8	19.9	SBF
	M60	16	128	148.6	23.1	CBF
S1SF1	M20	16	128	121	18.8	SBF
	M40	16	128	135.9	21.1	SBF
	M60	16	128	151.8	23.6	SBF
S1SF1.5	M20	16	128	125	19.4	SBF
	M40	16	128	140.9	21.9	SBF
	M60	16	128	161.5	25.1	SBF
S2SF0	M20	20	160	188.6	18.8	CBF
	M40	20	160	195.9	19.5	CBF
	M60	20	160	202.9	20.2	CBF
S2SF0.5	M20	20	160	188.7	18.8	CBF
	M40	20	160	198.2	19.7	SBF
	M60	20	160	203.9	20.3	SBF
S2SF1	M20	20	160	189.2	18.8	SBF
	M40	20	160	201.5	20.1	SBF
	M60	20	160	204.2	20.3	SBF
S2SF1.5	M20	20	160	189.6	18.9	SBF
	M40	20	160	204.6	20.4	SBF
	M60	20	160	208.5	20.8	SBF
S3SF0	M20	25	200	214.1	13.6	CBF
	M40	25	200	230	14.6	CBF
	M60	25	200	239.6	15.3	CBF

Specimen	Grade of concrete	d_b (mm)	l_{eh} (mm)	P_{max} (kN)	τ_{max} (MPa) (ACI 318-19)	Failure mode
S3SF0.5	M20	25	200	228.8	14.6	CBF
	M40	25	200	235.2	15	SBF
	M60	25	200	242.7	15.5	SBF
S3SF1	M20	25	200	230.5	14.7	SBF
	M40	25	200	231.4	14.7	SBF
	M60	25	200	246.2	15.7	SBF
S3SF1.5	M20	25	200	249.3	15.9	SBF
	M40	25	200	243.6	15.5	SBF
	M60	25	200	249.1	15.9	SBF
C1SF0	M20	16	128	117	18.2	CBF
	M40	16	128	135.2	21	CBF
	M60	16	128	136.8	21.3	SBF
C1SF0.5	M20	16	128	123.7	19.2	CBF
	M40	16	128	142.4	22.1	SBF
	M60	16	128	150.3	23.4	SBF
C1SF1	M20	16	128	129.2	20.1	SBF
	M40	16	128	149.7	23.3	SBF
	M60	16	128	153.6	23.9	SBF
C1SF1.5	M20	16	128	139	21.6	SBF
	M40	16	128	156.3	24.3	SBF
	M60	16	128	164.9	25.6	SBF
C2SF0	M20	20	160	189.7	18.9	CBF
	M40	20	160	202.4	20.1	CBF
	M60	20	160	208.5	20.8	SBF
C2SF0.5	M20	20	160	196.2	19.5	CBF
	M40	20	160	228.9	22.8	SBF
	M60	20	160	233.6	23.2	SBF
C2SF1	M20	20	160	199.8	19.9	SBF
	M40	20	160	232.5	23.1	SBF
	M60	20	160	240.9	24	SBF

Specimen	Grade of concrete	d_b (mm)	l_{eh} (mm)	P_{max} (kN)	τ_{max} (MPa) (ACI 318-19)	Failure mode
C2SF1.5	M20	20	160	210.4	20.9	SBF
	M40	20	160	242.8	24.2	SBF
	M60	20	160	250.2	24.9	SBF
C3SF0	M20	25	200	241.6	15.4	CBF
	M40	25	200	246	15.7	CBF
	M60	25	200	252.5	16.1	SBF
C3SF0.5	M20	25	200	250.1	15.9	CBF
	M40	25	200	260.3	16.6	SBF
	M60	25	200	278.4	17.7	SBF
C3SF1	M20	25	200	254	16.2	SBF
	M40	25	200	273.1	17.4	SBF
	M60	25	200	289.1	18.4	SBF
C3SF1.5	M20	25	200	260.2	16.6	SBF
	M40	25	200	281.9	18	SBF
	M60	25	200	300.7	19.2	SBF
R1SF0	M20	16	128	102	15.9	CBF
	M40	16	128	119.2	18.5	CBF
	M60	16	128	127.4	19.8	CBF
R1SF0.5	M20	16	128	126.6	19.7	CBF
	M40	16	128	130.8	20.3	SBF
	M60	16	128	136.3	21.2	SBF
R1SF1	M20	16	128	131.2	20.4	SBF
	M40	16	128	128.9	20	SBF
	M60	16	128	143.8	22.4	SBF
R1SF1.5	M20	16	128	135	21	CBF
	M40	16	128	139.8	21.7	SBF
	M60	16	128	152.9	23.8	SBF
R2SF0	M20	20	160	175.5	17.5	CBF
	M40	20	160	187.2	18.6	CBF
	M60	20	160	195.7	19.5	CBF
R2SF0.5	M20	20	160	188.9	18.8	CBF
	M40	20	160	192.3	19.1	SBF
	M60	20	160	199.3	19.8	SBF

Specimen	Grade of concrete	d_b (mm)	l_{eh} (mm)	P_{max} (kN)	τ_{max} (MPa) (ACI 318-19)	Failure mode
R2SF1	M20	20	160	190.9	19	SBF
	M40	20	160	196.9	19.6	SBF
	M60	20	160	201.5	20.1	SBF
R2SF1.5	M20	20	160	193.1	19.2	SBF
	M40	20	160	201.2	20	SBF
	M60	20	160	204.8	20.4	SBF
R3SF0	M20	25	200	226.6	14.4	CBF
	M40	25	200	231.3	14.7	CBF
	M60	25	200	237.6	15.1	CBF
R3SF0.5	M20	25	200	188	12	CBF
	M40	25	200	238.2	15.2	SBF
	M60	25	200	240.8	15.3	SBF
R3SF1	M20	25	200	234.2	14.9	SBF
	M40	25	200	240.6	15.3	SBF
	M60	25	200	243.5	15.5	SBF
R3SF1.5	M20	25	200	240.4	15.3	SBF
	M40	25	200	242.7	15.5	SBF
	M60	25	200	246.9	15.7	SBF

**where S, R, and C stands for square, rectangular and circular shapes. 1, 2, and 3 stand for diameters of bars, i.e., 16-, 20-, and 25-mm. SF stands for steel fibers having 0, 0.5, 1 and, 1.5% ratios in the concrete mix. CBF stands for concrete blowout failure, and SBF stands for steel bar failure.*

4.4 Influence of diameter of steel bar

The evaluation of the various diameters of the steel bar (16 mm, 20 mm & 25 mm) indicates that the ultimate load-carrying capacity is highly enhanced by increasing the diameter of reinforcing bars. So, the larger the bar area, the more it will be capable of carrying the load as the area of the headed bar is directly proportional to the diameter of the bar. It is depicted from Figure 4.7(a-c) when the diameter of the bar is increased from 16 mm to 25 mm, approximately (77% - 90%) increase in peak load of the specimens. Further, higher rebar diameters yielded higher bond strength values as larger bar diameters have more prominent ribs, increasing the

wedging action (Metwally 2014, Miao and Zheng 2019). Although, the peak load increased with increase in the diameter of bars, but failure modes of the specimens did not depend totally on the diameter of bar. The modes of failure have been further explained in section 4.8.

The influence of diameter of the headed bars on the anchorage capacity has been estimated by comparing the peak load developed by the headed bars. The peak load measured in the 16-, 20-, and 25-mm diameter of square-headed bars is 130.4 kN, 195.9 kN, and 230 kN in the case of square head having 0 % of SF, respectively. It signifies a 33 to 77% increase in the peak load of the headed bar as the bar diameter increases (Figures 4.1(a-i), 4.2(a-i), and 4.3(a-i)). Benmokrane *et al.* (1996) have also specified an increase in the peak load of headed bars with an increase in the diameter of the bar. The head bearing area of a larger bar is smaller than a smaller bar because the larger size is removed from the head's total projected area. This statement is valid only in the case of same head geometry. But in the present study, the head bearing area is also dependent on the area of the bar so the above said statement is invalid in the present study. The higher peak load of the 25 mm diameter headed bar compared to the 16 mm diameter is due to the larger diameter bars are having more prominent ribs and due to increase in the wedging action. The same behavior has been validated in the study of Islam *et al.* (2015).

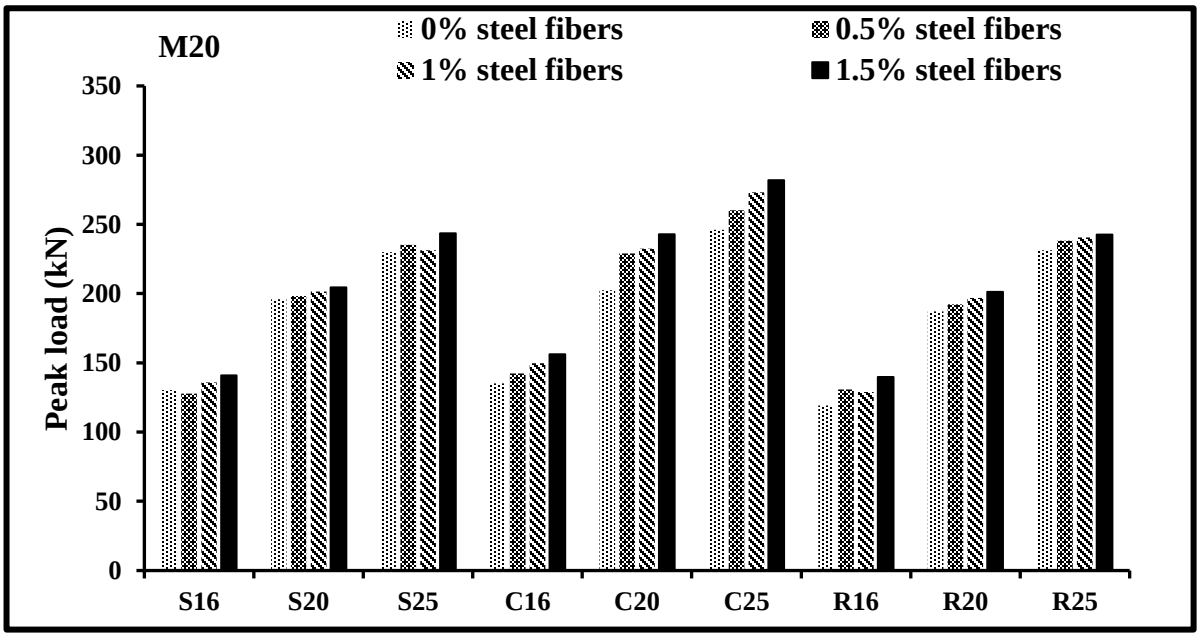

Figure 4.7 (a)

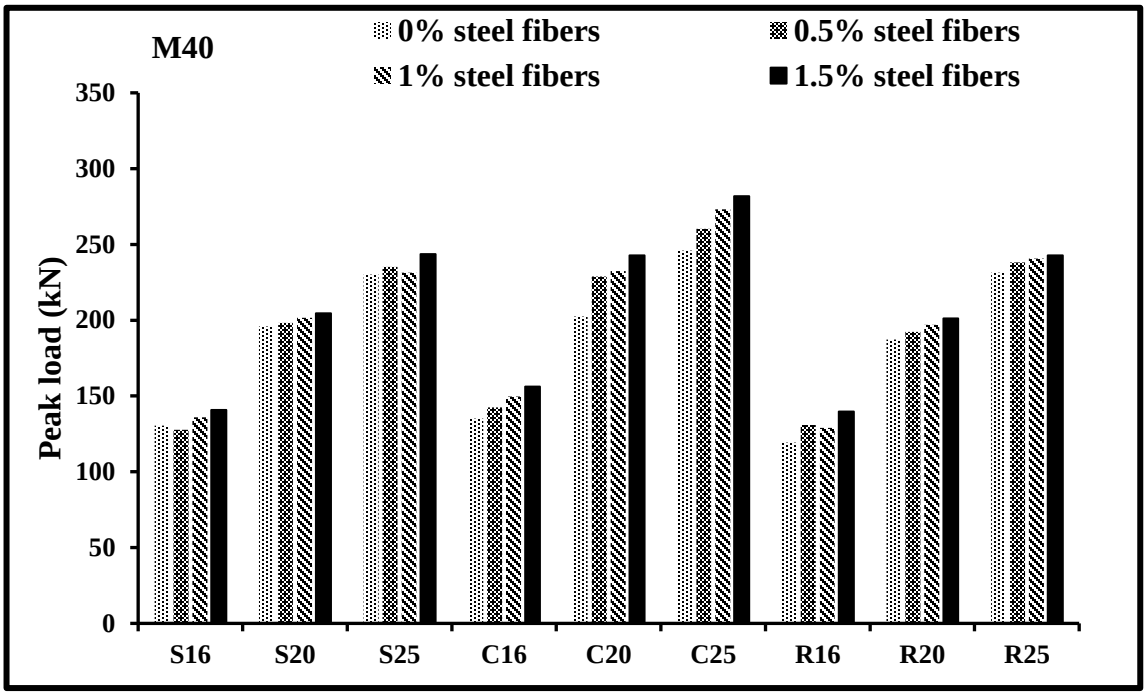

Figure 4.7 (b)

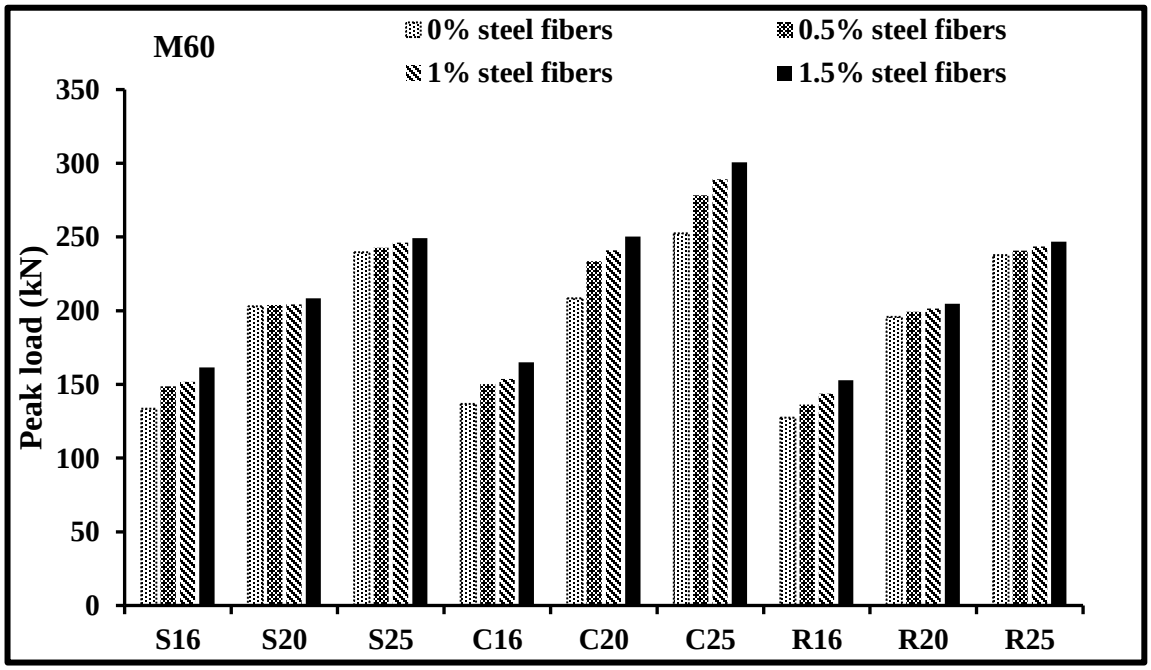

Figure 4.7 (c)

Figure 4. 7 (a-c) Bar-chart depicting the load-carrying capacity of headed bars

4.5 Effect of the percentage of steel fibers

As shown in Figures (4.1(a-i), 4.2(a-i), 4.3(a-i) and 4.7(a-c)), the peak load shows a slight variation with steel fibers at different percentages (0.5%, 1% & 1.5%) of the concrete mix. There is only a 5%-16% increase in the peak load as the steel fibers increased from 0 to 1.5%. Further, as the percentage of steel fibers increased, the bond strength also increases. It's because the presence of steel fibers bridges the propagation of cracks formed during the pull-out test. These steel fibers also improve the ductile behavior as they are distributed uniformly throughout the concrete. The same behavior has been investigated in the research of Holschemacher *et al.* (2010). The specimens with 1.5 percent of steel fibers exhibit the specimen's ductile nature in Figures (4.1(a-i), 4.2(a-i) and 4.3(a-i)) as the curve of SF1.5 extends until the maximum deflection, i.e., 2.5 to 3 mm, which shows that with the addition of steel fibers, the sudden failure of concrete is being avoided due to the setup constraint and the concrete is confined, and the deflection curve reaches its maximum limit. Due to the increase in peak load, the cracks tend to form, and the steel fibers are arresting them; consequently, the pull-out failure of the specimen occurs. The same behavior has been validated in the research of Hameed *et al.* (2013).

As shown in Figures (4.1(a-i), 4.2(a-i), 4.3(a-i) and 4.7(a-c)), the peak load shows a slight variation with steel fibers at different percentages (0.5%, 1% & 1.5%) of the concrete mix. The 5%-16% increase in the peak load because the steel fibers increased from 0 to 1.5%. Further, as the percentage of steel fibers increases, the bond strength also increases. It is because the presence of steel fibers bridges the propagation of cracks formed during the pull-out test. These steel fibers also improve the ductile behavior as they are distributed uniformly throughout the concrete. The specimens with 1.5 per cent of steel fibers exhibits ductile nature in Figures (4.1(a-i), 4.2(a-i) and 4.3(a-i)) as the curve of SF1.5 extends until the maximum deflection, i.e., 2.5 to 3 mm. The sudden failure of concrete is being avoided due to the setup constraint, and the concrete is confined. The deflection curve reaches its maximum limit. Due to the increase in peak load, the cracks tend to form, and the steel fibers arrest them; consequently, the pull-out failure of the specimen occurs. The same behavior has been observed in the research of Hameed *et al.* (2013). Having the same mix proportion, the specimens with 1.5% steel fibers show 13.6% higher compressive strength than the specimens without steel fibers in M40. In comparison,

specimens with 1.5% steel fibers show 8.3% higher compressive strength than specimens without steel fibers in the case of M20.

4.6 Influence of specimen size

The size of the specimen used in the present study, i.e., the cylindrical specimen having a diameter of 150 mm and height of 300 mm, has no influence as such on the anchorage capacity of headed bars during the pull-out test. Hawkins made the same observation in 1967. However, the placement of headed bars in the cylindrical specimen affects the anchorage capacity, overall bond strength, and failure modes of the headed bars. According to the research of Hawkins 1967, two loading criteria are eccentric and concentric loadings whose failure modes differ concerning the placement of headed bars in the specimen. As in the present study, the headed bars are placed concentrically in the cylinder; thus, the failure mode is conical, as shown in Figure 4.9(b). The purpose of including this section in the thesis was just to show that the present study is in the agreement of the observation made by Hawkins 1967.

4.7 Effect of compressive strength of concrete

The effect of compressive strength of concrete has been estimated by comparing the ultimate load developed by the headed bars. The Bar-chart presenting the load-carrying capacity of headed bars for all three grades of concrete (M20, M40, and M60) is shown in Figure 4.7(a-c). The peak load of square-headed bars with M20, M40, and M60 is 130.4 kN, 195.9 kN, and 230 kN, respectively. As the compressive strength increases, the peak load of the headed bar increases by 33 to 77 % (Figures 4.7(a-c) and Table 4.1). The impact of concrete compressive strength on the anchorage strength of headed bars is shown in Figure 4.10. Increasing the concrete compressive strength from 20 MPa to 60 MPa has resulted in a 30 to 40% increase in the measured bar force at failure. The fibers have improved the concrete's strength, which has strengthened the bond between the headed reinforced bar and the concrete as seen in the results presented in section 4.5. Thus, steel failure is occurring beyond its ultimate tensile capacity because the headed bars are embedded in high strength and fiber reinforced concrete. The specimens without head anchor leads to pull-out failure, also termed as bond failure due to

insufficient bonding between steel and concrete and found to have no beneficial effect of higher embedment depth. The heads on the bar can provide a means to develop bond strength through a separate load path. This path is provided in the headed bar by means of the bearing on the head itself. As bearing is a function of concrete so with increase in compressive strength of concrete and percentage of steel fibers, it leads to the more bearing capacity, subsequently. Approximately 75-85% of the yield load has been taken through bearing of the head and the remaining 15-25% through bond strength. The same has been observed in the study of Dahl (1995) and Thompson et al. (2003).

Additionally, the headed bars carried the applied load primarily through bearing rather than the steel-concrete bond. The same observation has been made in the study of Wright and McCabe (1997). Headed bars amplified the bearing capacity of the deformed bars, attributed to increase in bearing area of the bars due to presence of head anchors at their ends. The same has been observed by Shubham *et al.* (2020). Headed bars are anchored through a combination of bond and bearing at the head with tests showing that the full bar strength can be developed at the head when it has a net bearing area of ten times the bar area. Thus, the steel failure is occurring at higher loads in higher grade of concrete due to the strong bond made between the headed bars and SFRC with the help of higher percentage of steel fibers. Thus, the head transfers the bond stress through the bearing of the head to the length of the bar which is exposed outside of the concrete and thus necking occurred in the bar length after reaching the ultimate tensile capacity of the bars. The same observation has been made by (Vella *et al.* 2017).

4.8 Failure modes and Cracking Pattern of the specimens

All of the test specimens have been subjected to failure under tensile force. The load has been paused at various load stages so that the specimen could be examined by marking the crack propagation (Figure 4.8(a-c)). The various types of anchorage failure that have been observed, are discussed in this section. An anchorage failure occurs when the concrete around the head fails, causing the headed bar to slip and lose its capacity. The two failure modes which have occurred during the pull-out test are: (a) Steel Bar Failure (SBF) and (b) Concrete-Blowout Failure (CBF) (Figure 4.9 (a, b)). SBF has occurred mainly in higher steel fiber ratio, i.e. (1%

or 1.5%), as the compressive strength has increased in higher steel fibers usage because the bond between concrete and the reinforcing bar is strong enough to hold. CBF failure has occurred when the concrete reaches its tensile strength, which results in cracking and splitting of concretes with the propagation of a conical fracture surface from the bearing of the head as observed from the surface of the concrete. The same behavior has been observed by Park *et al.* (2003). CBF in heads occurs due to the lack of reinforcement to restore the stress flow to the concrete mass. The head transfers the bond stress along the bar which initiates from the bearing of the head. The bearing on the head is a function of concrete compressive strength, net bearing area of the head, and embedment length to column depth ratio, while the bond along the bar is a function of concrete compressive strength, embedment length, and bar diameter. The same observation is made by Chun *et al.* (2009). Also, it has been observed by DeVries (2015) that the portion of load carried by bearing for hooked bars is lower than for headed bars. The same was observed in the study conducted by DeVries (1997, 1999, 2015), Park *et al.* (2003), Thompson *et al.* (2005), Choi (2006), Lee and Yu (2009), Kang *et al.* (2010), Kang and Mitra (2012), Mitchell *et al.* (2014), Islam *et al.* (2015), Chun *et al.* (2017), Singhal *et al.* (2020), Abed *et al.* (2021).

The concrete cone-shaped failure occurs when this pressure exceeds the concrete load capacity. In this type of failure, initially, minor cracks have arisen on the specimen with the application of tensile load on the headed bar followed by splitting off some concrete. Suddenly, the bursting of concrete specimen occurred, resulting in the drop of pull-out peak load. Thus, there is minor damage near the head area and on the surface of the bar. CBF has occurred mainly in specimens without steel fibers (0% and 0.5%). With the increase in steel fibers percentage in the mix, the compressive strength of the concrete increases, thus resulting in a higher bond between the concrete and the headed bar, which is more difficult to break . Barros and Cruz (2001); Park *et al.* (2003); Chourasia and Gupta (2019) have observed the same behavior. Thus, CBF depends not on the specimen size but the embedment depth of the headed bar in the specimen, the percentage of steel fibers and compressive strength of concrete.

The cracking of concrete initiated internally from the level of headed bars (visually observed in Figure 4.9 (b)), which further propagated to the concrete surface as the load

increased. It was noticed due to the formation of a crushed concrete wedge pushed by the interior head. Consequently, the concrete splitting has caused the headed bars to fail when the peak load has been reached. The same failure has occurred in the study of Qian *et al.* (2018). Research carried out by DeVries (1996) and Papadopoulos *et al.* (2015) has shown that the bond failure of headed rebar can occur due to a blowout of the concrete close to the surface. The CBF occurs when the reinforcement is not sufficiently embedded (Qian *et al.* 2018). From Table 4.1, it is pretty clear that CBF changes to SBF with an increase in the percentage of steel fibers, which states the addition of steel fibers in the concrete mix imparts ductility in the specimen; thus, SBF occurs before CBF. At the same time, there is a minor influence of concrete strength on the failure modes of the specimen.

Although the cracking in different specimens differs in quantity and shape, the general pattern of cracks is similar in all the specimens. Firstly, there has been a horizontal crack on the front of the cylinder at the headed bar level, spreading slightly to either side of the cylinder. This cracking pattern can be related to (Figure A.1) given by (Park et al. 2003). With an increasing load, cracks from outside to the inside of the cylinder result in the specimen's expansion caused by the pressure from headed bars (Figure 4.8(a-c)). The number of cracks developing is directly linked to the steel fibers in the concrete mix; specimens with steel fibers generally have shown more number of cracks than without steel fibers before failure.

4.8.1 Failure of Steel Bar (SBF)

The ribs present in the headed bars provide a better bond between the bar and the surrounding concrete. The pull-out capacity of the headed bar remains unaffected from the concrete and head properties due to the proper bond between the concrete and the headed bar. This is true because of the strong bond made between the headed bars and concrete with the help of higher percentage of steel fibers. As only compressive strength of concrete is not important, but bond property is also important and pull-out capacity is a function of bond property. Further, bond property is getting more enhanced by addition of steel fibers in the concrete. Thus, pull-out capacity is increasing with increase in percentage of steel fibers in concrete. Thus, steel fibers play a significant role in enhancing the pull-out capacity of the headed bars. The same

observation has been made by Nilforoush (2019). Thus, the head transfers the bond stress through the bearing of the head to the length of the bar which is exposed outside of the concrete and thus necking occurred in the bar length after reaching the ultimate tensile capacity of the bars. Only the bar, which is exposed from the specimen, fails (Figure 4.9a). It is seen through the pull-out test results that SBF has occurred mainly in the case of a higher steel fiber ratio, i.e. (1% and 1.5%). The same was observed in the study conducted by Devries (1999).

4.8.2 Failure of Concrete-Blowout (CBF)

In this type of failure (Figure 4.9b), initially, minor cracks have arisen on the specimen with the application of tensile load on the headed bar followed by splitting off of some concrete and then suddenly bursting of concrete specimen occurred resulting in the drop of pull-out peak load. Thus, there is minor damage near the head area and on the surface of the bar. CBF has occurred mainly in specimens without steel fibers (0% and 0.5%). With the increase in steel fibers percentage in the mix, the compressive strength of the concrete increases, thus resulting in a higher bond between the concrete and the headed bar, which is more difficult to break.

Figure 4.8 (a) With 0% steel fibers

Figure 4.8 (b) With 0.5% steel fibers

Figure 4.8 (c) With 1.5% steel fibers

Figure 4. 8 (a-c) Cracking Pattern of the specimens

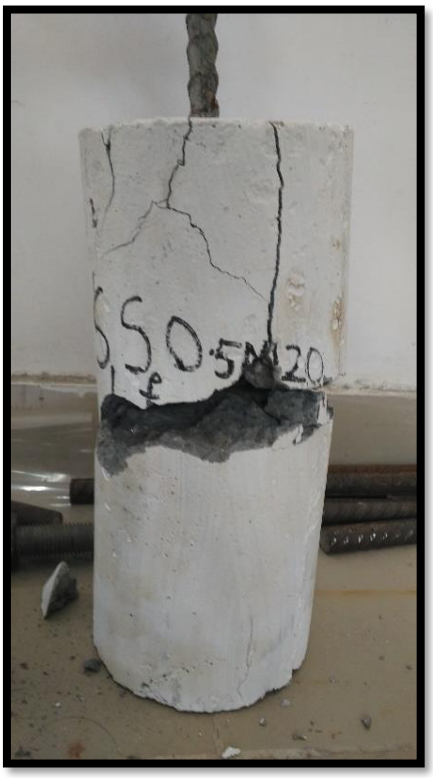

Figure 4.9 (a)

Figure 4.9 (b)

Figure 4. 9 (a-b) (a) Steel Bar Failure (SBF) and (b) Concrete-Blowout Failure (CBF)

4.9 Analysis based on anchorage provisions of ACI 318-19

The analysis of the pull-out test results of the specimens is focused on in this section. The test results are compared to the ACI 318-19 Building Code's development length equation for headed bars. The comparisons reveal the current code equation's limitations. Following the ACI 318-19 provisions, the development length of a headed bar ℓ_{eh} (mm) is given by equation (4.8).

$$l_{eh} = \left(\frac{0.19 f_y \Psi_e}{\sqrt{f_c'}} \right) d_b \tag{4.8}$$

Where f_c' is the concrete compressive strength (MPa), ψ_e is the modification factor taken as 1.0 for uncoated bars, f_y is the yield strength of steel (MPa), and d_b is the diameter of reinforced bars (mm). To determine the bond strength, the new equation (4.9) has been formed

using equation (4.8), in which $f_{s,\ ACI}$ has been substituted in place of f_y, and f_{cm} has been substituted in place of f_c'.

$$f_{s,\ ACI} = \frac{l_{eh}\sqrt{f_{cm}}}{0.19 d_b} \quad (4.9)$$

Where $f_{s,\ ACI}$ is the bar stress calculated using the formula given by ACI 318-19. The same formulas have been used in these studies (Shao 2016; Sperry *et al.* 2017; Ghimire *et al.* 2018; Ghimire *et al.* 2019a, b). The test results have been categorized based on the bar size and the percentage of steel fibers used for comparative analysis. The bar stress ratio (f_{su} /$f_{s,\ ACI}$), calculated using equation (4.9), is plotted against the measured compression strength of the concrete (Figures 4.10 and 4.11), where f_{su} is defined as the peak load applied on a specimen divided by the area of the headed bar. Each data point in the plot represents a single specimen. The details of measured values of bar stress ratio ($f_{su}/f_{s,\ ACI}$) for each shape of the head and steel fibers percentage have been provided in Table 4.2. In Figure 4.10, the head shapes and bar diameters have been compared for each SF. The trend lines in Figures 4.10 and 4.11 have been obtained by dummy analysis of variables. The order of lines has been shown in the legend from the highest to the lowest. In Figures 4.10 and 4.11, the trend line slope is negative, indicating that the ACI 318-19 equation overestimated the effect of concrete compression strength by a factor of 0.5, as validated by Ghimire *et al.* (2019a). In Figure 4.10, the ratio $f_{su}/f_{s,\ ACI}$ ranges from 0.16 to 0.28 for square-shaped headed bars, with a mean, standard deviation, and coefficient of variation of 0.23, 0.04, and -0.20, respectively; for circular-shaped headed bars, the ratio ranges from 0.18 to 0.31, with a mean, standard deviation, and coefficient of variation of 0.25, 0.03, and -0.15, respectively. The ratio for rectangular-shaped headed bars ranges from 0.17 to 0.30, with 0.23, 0.04, and -0.22 as the mean, standard deviation, and coefficient of variation. Furthermore, the R^2 values for square; circular; and rectangular headed bars having 16 mm, 20 mm and 25 mm diameter are 0.77, 0.85, and 0.87; 0.87, 0.88, and 0.98; and 0.69, 0.72, and 0.81, respectively. Similarly, in Figure 4.10, the coefficient of variation is 0.01 for both M20 and M40 and 0.04 for M60. Thus ACI 318-19 equation is over-conservative for all the specimens as the trend line decreases with an increase in bar diameter (Figure 4.10).

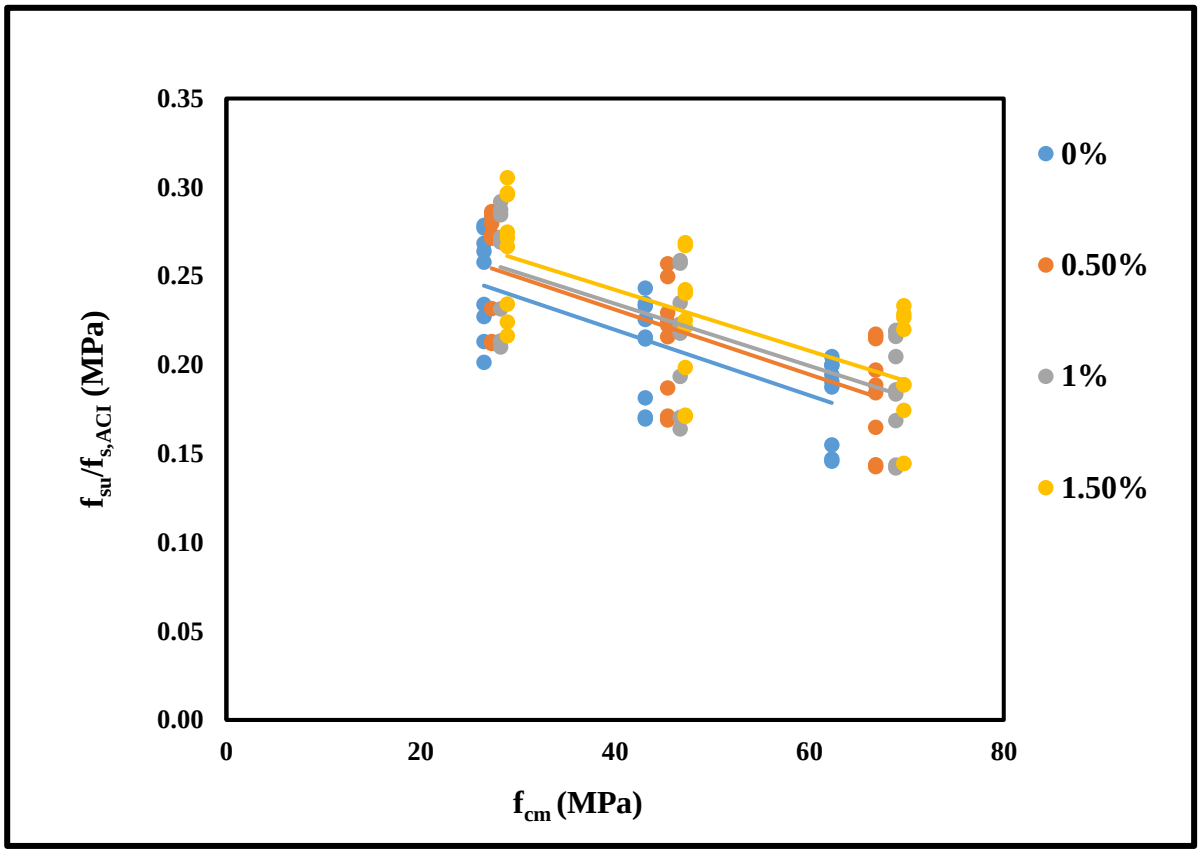

Figure 4. 10 Experimental/calculated bar stress $f_{su}/f_{s,\ ACI}$ versus measured compressive strength f_{cm} (MPa) comparing the steel fibers percentage.

Thus, based on the experimental and analytical results, it has been concluded that the circular shape of the head performs better than the square and rectangular shapes of the head. Besides the bar diameter and shape of the head, Figure 4.11 reveals that $f_{su}/f_{s,\ ACI}$ has increased because of the presence of SF within the specimen. Thus, the factor of SF should be considered in the ACI 318-19 requirements for the headed bars.

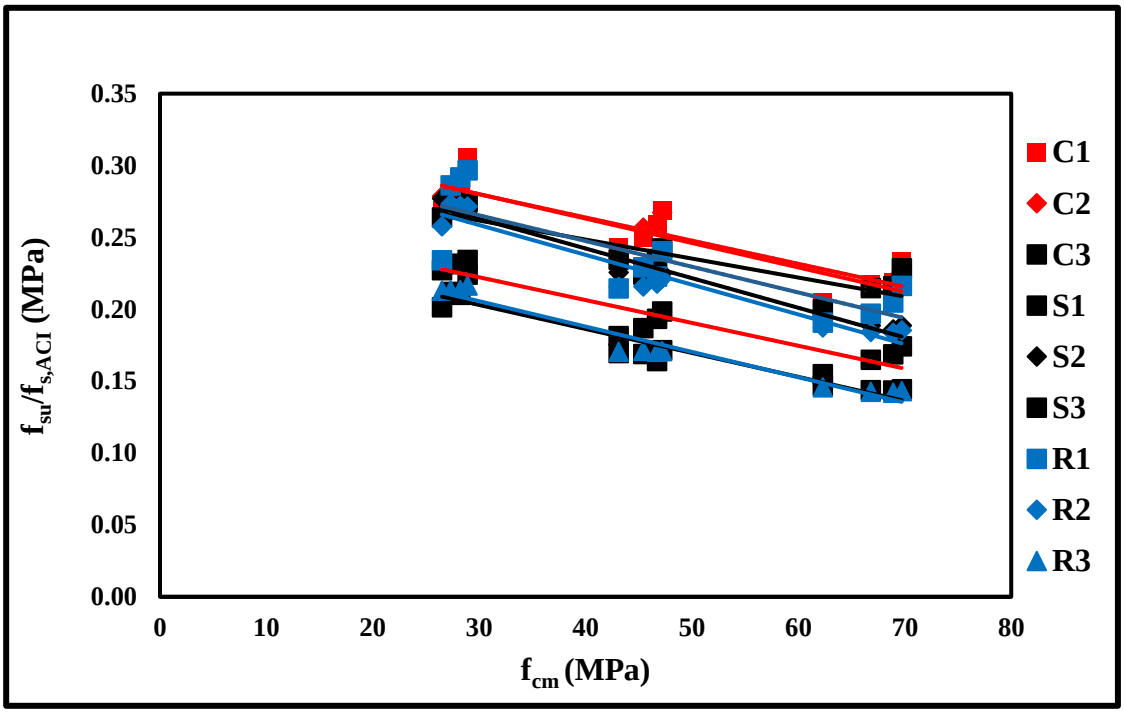

Figure 4. 11 (f_{su} /$f_{s,\ ACI}$) versus f_{cm} comparing the head shapes and bar diameters.

(Note: *S, R, and C refer to square, rectangular and circular heads, respectively. 1, 2, and 3 refer to 16 mm, 20 mm, and 25 mm diameter of bars, respectively*).

4.10 Non-linear regression analysis of headed bars with SFRC

The key factors influencing the anchorage strength of the headed bar are investigated, and descriptive equations are developed to capture the key factors influencing the anchorage strength. Dummy variables analysis with non-linear regression analysis is used to analyse the results. Dummy variables are variables used in regression analysis to distinguish multiple subgroups within a sample (Shao 2016). The anchorage strength with dummy variables representing bars of different sizes can be expressed as equation (4.10).

$$T' = \beta_0 Z_0 + \beta_1 Z_1 + \ldots + \beta_i Z_i \qquad (4.10)$$

Where β_0 denotes the slope of the regression line for all bar sizes, β_i denotes factors that represent changes in anchorage strength as a function of bar size, and Z_i denotes dummy variables with values of 0 or 1 that act as switches to turn off or on the effect of bar size. Dummy variable lines of T' have the same slope β_0 but different intercepts for bars of different sizes, allowing the common trend in l_{eh} to be observed while showing the difference in T' as a function of bar size.

Many researchers have proposed models or developed equations to forecast the anchorage capacity of headed bars (Draper and Smith 1981; Ghimire *et al.* 2019b). Most of the models have been proposed based on the regression analysis considering the parameters of the pull-out test. The effect of SF has not been considered in these models.

Ghimire *et al.* (2019b) have developed an equation given by (4.11) to predict the peak load of headed bars given by T_c.

$$T_c = 132 f_{cm}^{0.24} l_{eh}^{1.03} d_b^{0.35} \quad (4.11)$$

While fitting the parameters of the present study in the equation used in the study of Ghimire *et al.* (2019b) (given by equation (4.6)), the R^2 value of the trend lines is not showing satisfactory results, presenting a negative slope of the trend line (Figure 4.12). For the 324 specimens, Figure 4.12 compares the ratio T/Tc to the concrete compressive strength. The average peak load is denoted by the letter T. The dummy variable lines in Figure 4.12 are nearly horizontal, showing that the (0.07, 0.19, and 0.05) power for square, circular, and rectangular, respectively, accurately captures the influence of concrete compressive strength.

The experimental results of the present study revealed that there had been an enhancement of anchorage capacity of headed bars with an increase in the percentage of SF. Thus, considering SF as a parameter for the anchorage capacity of headed bars has been made. Thereby, equation (4.11) has been modified in the present study taking account of SF in the proposed equation given by (4.12), (4.13), and (4.14). With the help of iterative non-linear regression analysis, descriptive equations for anchorage capacity of headed bars for all three head shapes have been generated to ensure the test/calculated peak load ratio is equal to 1.0

while decreasing the sum of square (1-Test/Calculated)^2. Using iterative non-linear regression analysis as used in Ghimire *et al.* (2019a, 2019b), the equations (4.12), (4.13), and (4.14) have been formulated using the present data set of 324 pull-out tests. The same data is compared using the equation developed by Ghimire *et al.* (2019a, 2019b), as shown in Figure 4.12.

$$T_{c,\,square} = 255 f_{cm}^{0.07} l_{eh}^{1.21} d_b^{0.05} SF^{0.04} \quad (4.12)$$

$$T_{c,\,circular} = 157 f_{cm}^{0.19} l_{eh}^{1.27} d_b^{0.01} SF^{0.02} \quad (4.13)$$

$$T_{c,\,rectangular} = 288 f_{cm}^{0.05} l_{eh}^{1.23} d_b^{0.01} SF^{0.01} \quad (4.14)$$

The power of compressive strength (0.07, 0.19, and 0.05 for square, circular, and rectangular, respectively) has also been determined to produce the most excellent fit with experimental data. In combination, concrete tensile strength controls initial crack formation and increases with compressive strength to power between half and two-thirds, as well as fracture energy controls crack propagation and is independent of compressive strength, which justifies a lower compressive strength power (Darwin et al. 2001). A power between 0.5 and zero characterizes the entire effect.

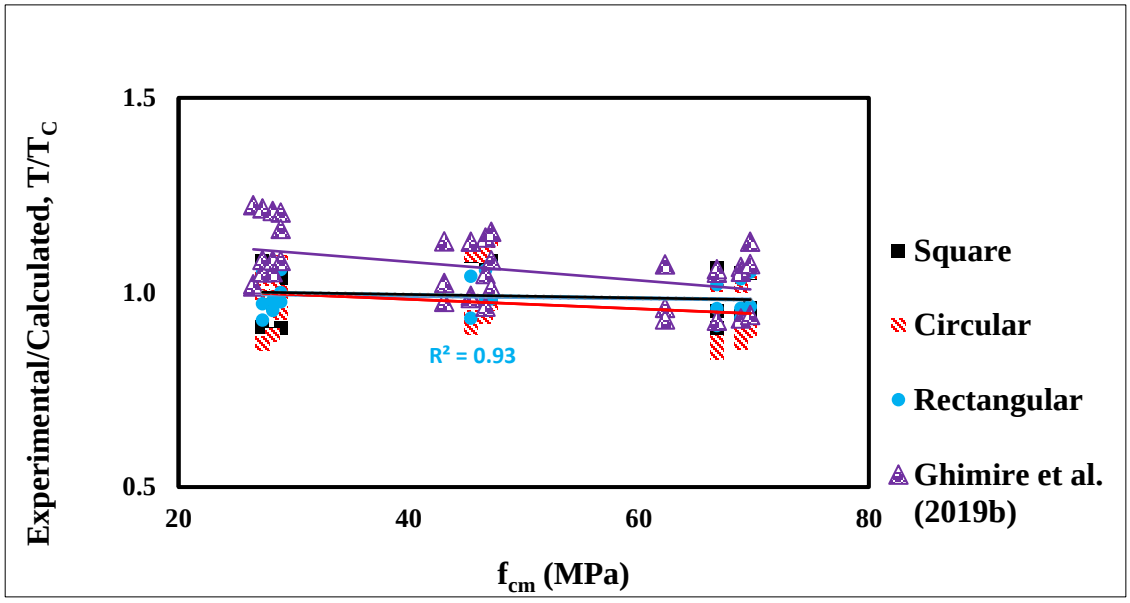

Figure 4. 12 Comparison of experimental/calculated bar stress (T/T_C) versus measured compressive strength f_{cm} (MPa)

In Figure 4.12, the trend lines are almost horizontal, which shows equations (4.12), (4.13), and (4.14) give a productive match with the experimental results for concrete strengths (20 to 60 MPa), thus validating the suggested improvements in the powers of f_{cm}, l_{eh}, d_b, and SF as per equations (4.12), (4.13), and (4.14). A value of R^2 =1.0 indicates a perfect fit and is thus a highly reliable model for future forecasts. In contrast, a value of 0.0 would indicate that the calculation fails to model the data accurately at all. Based on this analysis, we decided to take R^2 into account to assess the goodness-of-fit of the equations developed using non-linear regression. The higher the R^2 value, the better the model fits the data (Zhanping *et al.* 2012). Thus, the 0.97 R^2 value for circular heads indicates that the equations that predict the performance of circular shaped heads are good predictors of the actual performance of circular headed bars. The 0.94 R^2 value for square headed bars indicates that the equation that predicts the performance of square headed bars is slightly less reliable that that for circular headed bars. Also, the T/T_c ratios for circular, square, and rectangular range from 0.87-1.13, 0.89-1.09, and 0.93-1.07, with standard deviation and coefficient of variation of 0.06, and 0.04, respectively. The experimental results corresponded closely to the numerical results, both in terms of failure load and failure pattern, thereby confirming the validity of the proposed model, as shown in Figure 4.13.

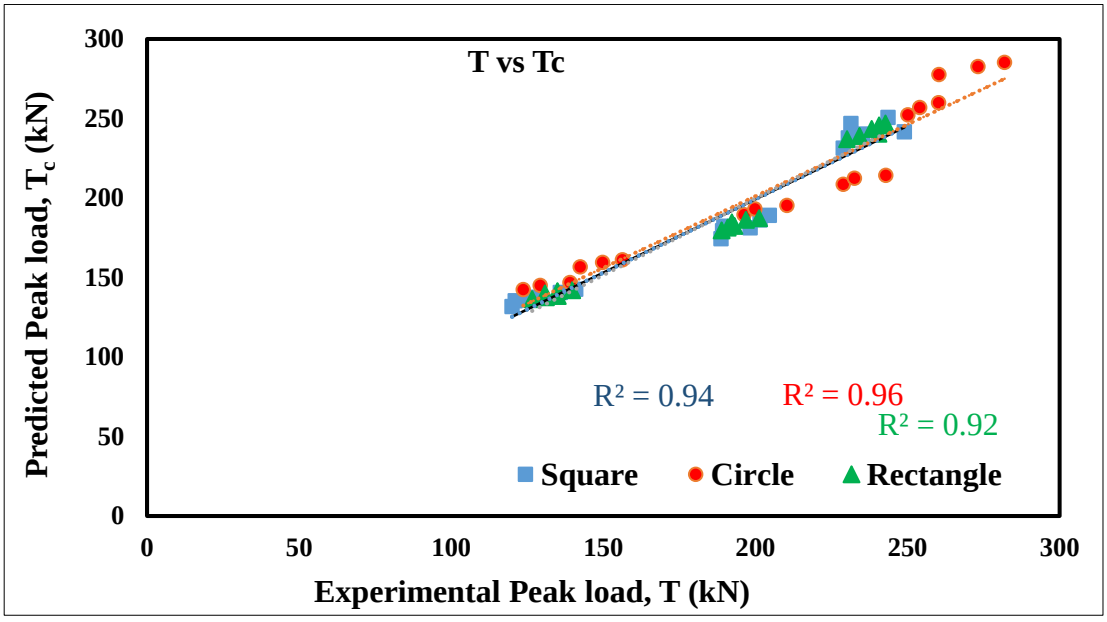

Figure 4. 13 Experimental peak load results versus predicted peak load

For the different diameters of bars (16, 20, and 25 mm), the results of peak load for all the shapes of heads calculated from equation (4.12), (4.13), and (4.14) have been compared to experimental peak load. The plot between the diameter of bars and peak load (calculated from REG and experimental peak load) has been compared for square, rectangular heads, and circular headed bars, respectively, as shown in Figures (4.14-4.16). It can be observed that peak load from experimental results provides the best fit with peak load from REG for circular heads rather than square or rectangular heads with an R^2 value of 0.91, 0.89, and 0.87, respectively.

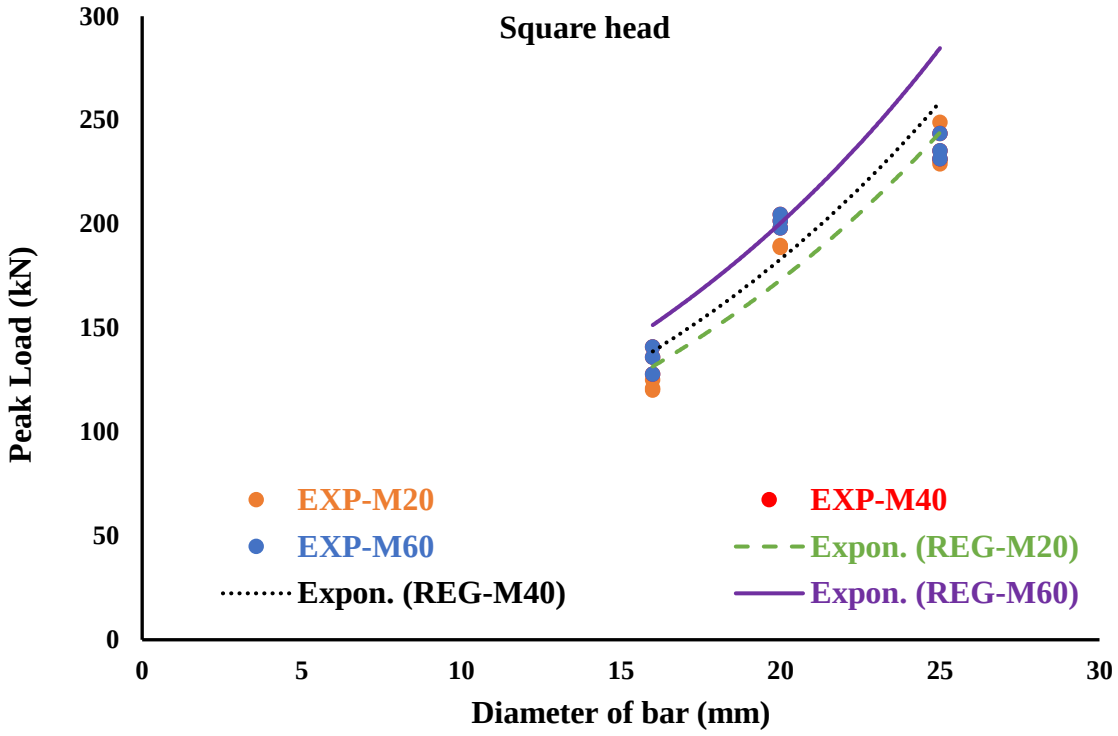

Figure 4. 14 Peak load vs diameter of bar for Square-headed bars

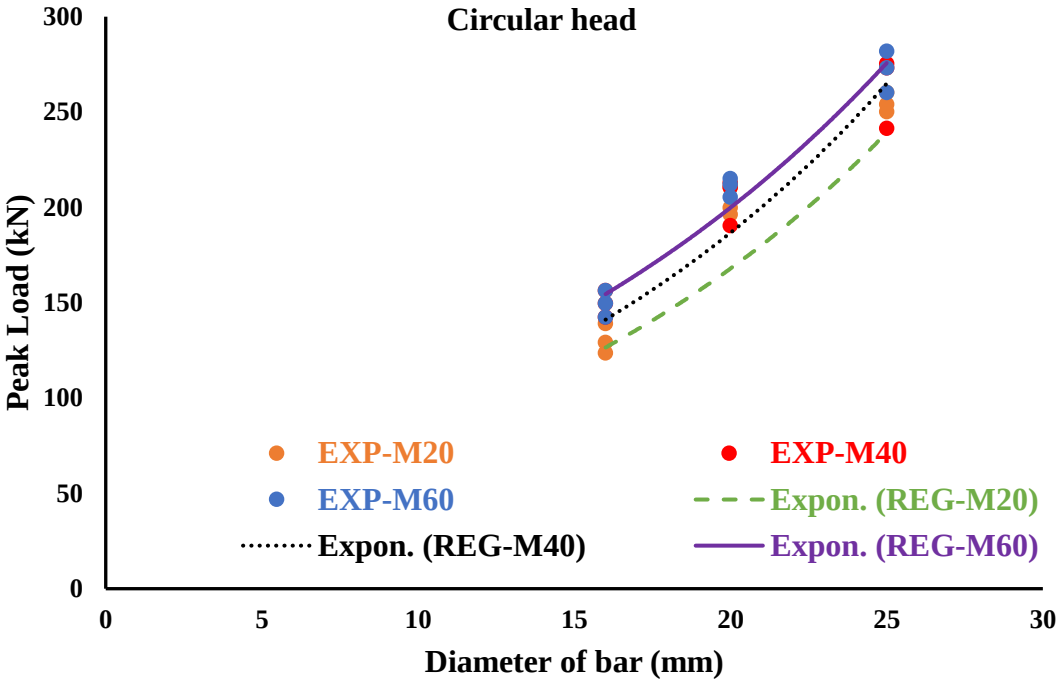

Figure 4. 15 Peak load vs diameter of bar for Circular headed bars

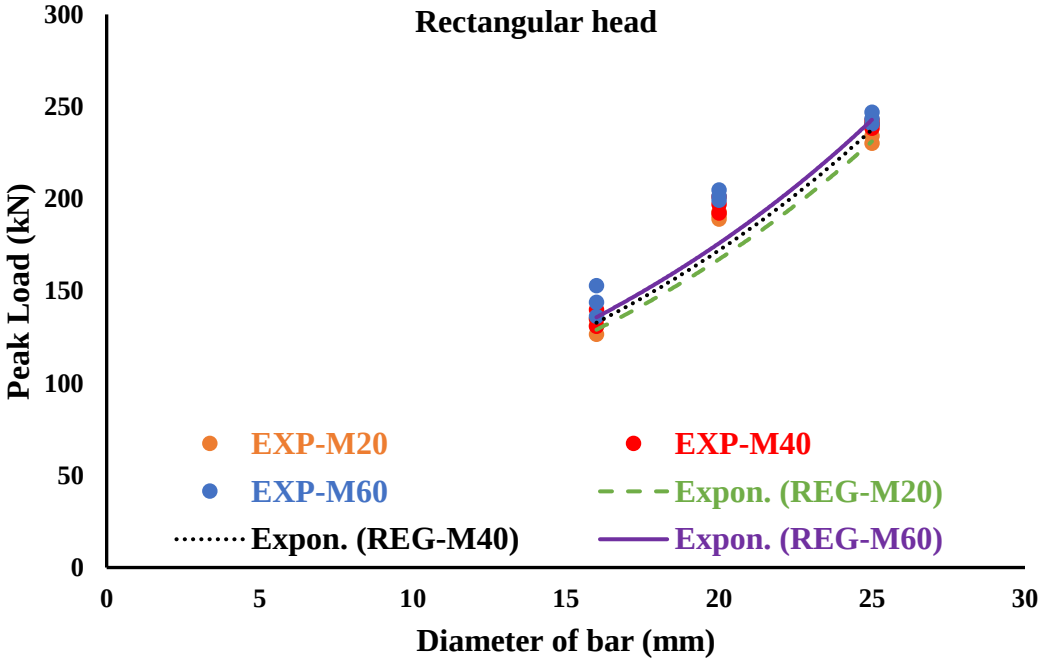

Figure 4. 16 Peak load vs diameter of bar for Rectangular headed bars

Table 4. 2 Experimental/calculated bar stress ($f_{su}/f_{s,\ ACI}$)

	d_b (mm)	l_{eh} (mm)	SF (%)	f_{cm} (MPa)	$f_{s,ACI}$ (MPa)	f_{su} (MPa)	$f_{su}/f_{s,\ ACI}$
M20 SQUARE	16	128	0.0	26.5	217	7.2	0.26
	20	160	0.0	26.5	217	60.1	0.28
	25	200	0.0	26.5	217	43.6	0.20
	16	128	0.5	27.3	220	9.7	0.27
	20	160	0.5	27.3	220	60.1	0.27
	25	200	0.5	27.3	220	46.7	0.21
	16	128	1.0	28.2	224	60.2	0.27
	20	160	1.0	28.2	224	60.2	0.27
	25	200	1.0	28.2	224	47.0	0.21
	16	128	1.5	28.9	226	62.2	0.27
	20	160	1.5	28.9	226	60.4	0.27
	25	200	1.5	28.9	226	50.8	0.22
	d_b (mm)	l_{eh} (mm)	SF (%)	f_{cm} (MPa)	$f_{s,ACI}$ (MPa)	f_{su} (MPa)	$f_{su}/f_{s,\ ACI}$
M20 CIRCULAR	16	128	0.0	26.5	217	58.2	0.27
	20	160	0.0	26.5	217	60.4	0.28
	25	200	0.0	26.5	217	49.2	0.23
	16	128	0.5	27.3	220	61.5	0.28
	20	160	0.5	27.3	220	62.5	0.28
	25	200	0.5	27.3	220	51.0	0.23
	16	128	1.0	28.2	224	64.3	0.29
	20	160	1.0	28.2	224	63.6	0.28
	25	200	1.0	28.2	224	51.8	0.23
	16	128	1.5	28.9	226	69.1	0.31
	20	160	1.5	28.9	226	67.0	0.30
	25	200	1.5	28.9	226	53.0	0.23
	d_b (mm)	l_{eh} (mm)	SF (%)	f_{cm} (MPa)	$f_{s,ACI}$ (MPa)	f_{su} (MPa)	$f_{su}/f_{s,\ ACI}$
M20 RECTANGULAR	16	128	0.0	26.5	217	50.7	0.23
	20	160	0.0	26.5	217	55.9	0.26
	25	200	0.0	26.5	217	46.2	0.21
	16	128	0.5	27.3	220	63.0	0.29
	20	160	0.5	27.3	220	60.1	0.27
	25	200	0.5	27.3	220	46.9	0.21

	16	128	1.0	28.2	224	65.3	0.29
	20	160	1.0	28.2	224	60.8	0.27
	25	200	1.0	28.2	224	47.7	0.21
	16	128	1.5	28.9	226	67.2	0.30
	20	160	1.5	28.9	226	61.5	0.27
	25	200	1.5	28.9	226	49.0	0.22
M40 SQUARE	**d_b (mm)**	**l_{eh} (mm)**	**SF (%)**	**f_{cm} (MPa)**	**$f_{s,ACI}$ (MPa)**	**f_{su} (MPa)**	**$f_{su}/f_{s,ACI}$**
	16	128	0.0	43.1	276	64.9	0.23
	20	160	0.0	43.1	276	62.4	0.23
	25	200	0.0	43.1	276	46.9	0.17
	16	128	0.5	45.4	284	63.6	0.22
	20	160	0.5	45.4	284	63.1	0.22
	25	200	0.5	45.4	284	47.9	0.17
M40 SQUARE	**d_b (mm)**	**l_{eh} (mm)**	**SF (%)**	**f_{cm} (MPa)**	**$f_{s,ACI}$ (MPa)**	**f_{su} (MPa)**	**$f_{su}/f_{s,ACI}$**
	16	128	1.0	46.7	288	67.6	0.23
	20	160	1.0	46.7	288	64.2	0.22
	25	200	1.0	46.7	288	47.2	0.16
	16	128	1.5	47.2	289	70.1	0.24
	20	160	1.5	47.2	289	65.1	0.23
	25	200	1.5	47.2	289	49.7	0.17
M40 CIRCULAR	**d_b (mm)**	**l_{eh} (mm)**	**SF (%)**	**f_{cm} (MPa)**	**$f_{s,ACI}$ (MPa)**	**f_{su} (MPa)**	**$f_{su}/f_{s,ACI}$**
	16	128	0.0	43.1	276	67.3	0.24
	20	160	0.0	43.1	276	64.4	0.23
	25	200	0.0	43.1	276	50.1	0.18
	16	128	0.5	45.4	284	70.8	0.25
	20	160	0.5	45.4	284	72.9	0.26
	25	200	0.5	45.4	284	53.1	0.19
	16	128	1.0	46.7	288	74.5	0.26
	20	160	1.0	46.7	288	74.0	0.26
	25	200	1.0	46.7	288	55.7	0.19
	16	128	1.5	47.2	289	77.8	0.27
	20	160	1.5	47.2	289	77.3	0.27
	25	200	1.5	47.2	289	57.5	0.20

	d_b (mm)	l_{eh} (mm)	SF (%)	f_{cm} (MPa)	$f_{s,ACI}$ (MPa)	f_{su} (MPa)	$f_{su}/f_{s,ACI}$
M40 RECTANGULAR	16	128	0.0	43.1	276	59.3	0.21
	20	160	0.0	43.1	276	59.6	0.22
	25	200	0.0	43.1	276	47.1	0.17
	16	128	0.5	45.4	284	65.1	0.23
	20	160	0.5	45.4	284	61.2	0.22
	25	200	0.5	45.4	284	48.6	0.17
	16	128	1.0	46.7	288	64.1	0.22
	20	160	1.0	46.7	288	62.7	0.22
	25	200	1.0	46.7	288	49.0	0.17
	16	128	1.5	47.2	289	69.5	0.24
	20	160	1.5	47.2	289	64.1	0.22
	25	200	1.5	47.2	289	49.5	0.17
M60 SQUARE	d_b (mm)	l_{eh} (mm)	SF (%)	f_{cm} (MPa)	$f_{s,ACI}$ (MPa)	f_{su} (MPa)	$f_{su}/f_{s,ACI}$
	16	128	0.0	62.3	332.34	66.46	0.20
	20	160	0.0	62.3	332.34	64.60	0.19
	25	200	0.0	62.3	332.34	48.84	0.15
	16	128	0.5	66.8	344.13	73.92	0.21
	20	160	0.5	66.8	344.13	64.92	0.19
	25	200	0.5	66.8	344.13	49.47	0.14
	16	128	1.0	68.9	349.50	75.51	0.22
	20	160	1.0	68.9	349.50	65.01	0.19
	25	200	1.0	68.9	349.50	50.18	0.14
	16	128	1.5	69.7	351.52	80.35	0.23
	20	160	1.5	69.7	351.52	66.38	0.19
	25	200	1.5	69.7	351.52	50.77	0.14
M60 CIRCULAR	d_b (mm)	l_{eh} (mm)	SF (%)	f_{cm} (MPa)	$f_{s,ACI}$ (MPa)	f_{su} (MPa)	$f_{su}/f_{s,ACI}$
	16	128	0.0	62.3	332.34	66.46	0.20
	20	160	0.0	62.3	332.34	64.60	0.19
	25	200	0.0	62.3	332.34	48.84	0.15
	16	128	0.5	66.8	344.13	73.92	0.21
	20	160	0.5	66.8	344.13	64.92	0.19
	25	200	0.5	66.8	344.13	49.47	0.14
	16	128	1.0	68.9	349.50	75.51	0.22

	20	160	1.0	68.9	349.50	65.01	0.19
	25	200	1.0	68.9	349.50	50.18	0.14
	16	128	1.5	69.7	351.52	80.35	0.23
	20	160	1.5	69.7	351.52	66.38	0.19
	25	200	1.5	69.7	351.52	50.77	0.14
M60 RECTANGULAR	**d_b (mm)**	**l_{eh} (mm)**	**SF (%)**	**f_{cm} (MPa)**	**$f_{s,ACI}$ (MPa)**	**f_{su} (MPa)**	**$f_{su}/f_{s,ACI}$**
	16	128	0.0	62.3	332.34	66.46	0.20
	20	160	0.0	62.3	332.34	64.60	0.19
	25	200	0.0	62.3	332.34	48.84	0.15
	16	128	0.5	66.8	344.13	73.92	0.21
	20	160	0.5	66.8	344.13	64.92	0.19
	25	200	0.5	66.8	344.13	49.47	0.14
	16	128	1.0	68.9	349.50	75.51	0.22
M60 RECTANGULAR	**d_b (mm)**	**l_{eh} (mm)**	**SF (%)**	**f_{cm} (MPa)**	**$f_{s,ACI}$ (MPa)**	**f_{su} (MPa)**	**$f_{su}/f_{s,ACI}$**
	20	160	1.0	68.9	349.50	65.01	0.19
	25	200	1.0	68.9	349.50	50.18	0.14
	16	128	1.5	69.7	351.52	80.35	0.23
	20	160	1.5	69.7	351.52	66.38	0.19
	25	200	1.5	69.7	351.52	50.77	0.14

4.11 Development of analytical model using Genetic Programming

Genetic programming (GP) is a concept derived from the natural evolutionary process. The principle of "survival of the fittest" governs how species survive (Joshi *et al.* 2014). Genetic algorithms (GA) are comparable to GP. GP's solution, unlike the GA, is a computer program or equation for a collection of numbers in GA (Gaur and Deo. 2008). An unknown mathematical function (for example, x +-* operator) is transformed multiple times in the search phase of the genetic programming algorithm to approximate the input to the desired output as much as possible. Only the x + - * operators are used to producing the GP equation. GP has to be applied because GP has the capacity to dynamically generate very complex algorithms (functions) to optimize specific utility functions (i.e., minimum fitting error). Pandey *et al.* devised a generalized scour depth equation based on multi-linear regression (MLR) and the Genetic algorithm (GA), with GA predicting scour depth more accurately than MLR. GP is a novel

concept introduced by Koza, although research on GP technology can go back to the 1960s and 1970s (Johari, Habibagahi & Ghahramani, 2006).

4.11.1 Advantages of genetic Programming

The fundamental advantage of GP over traditional modeling methods is that it does not presume any preexisting functional form of the solution. The building blocks (input variables, target variables, and function sets) are defined first in GP. Then the learning approach is used to determine the best model structure and coefficients (Joshi *et al.* 2014). Although some applications of Genetic Programming for plastic hinge models of RC beams can be found in geotechnical engineering, the use of GP in civil engineering is a relatively new development. The author found no references in the field of application of GP for headed bars. Using Genetic An attempt has been made using GP KERNEL PROGRAMMING, to develop a model for anchorage capacity that includes the compressive strength of concrete (f_{cm}), embedment length of headed bars (l_{eh}), the diameter of steel bar (d_b), and percentage of steel fibers (SF).

4.11.2 Procedure

Genetic programming model has been are constructed under three different grades of concrete (M20, M40, and M60) to estimate the response of the pull-out test in terms of peak load. After multiple simulations, the data division was determined i.e., 70% of the data was used for training, and the remaining 30% was used to test the model. The GP model is created to obtain the fewest possible input parameters. Root Mean Square Error (RMSE) and Coefficient of Efficiency (CE) are two statistical measures used to assess the accuracy of the produced model. The root mean square error (RMSE) is the residuals' standard deviation (prediction errors). The lower value of RMSE means that the model is the best fit. If the RMSE value is “0”, it means the model is perfectly fit. The efficiency coefficient, CE, is a measure that evaluates the differences between observations and forecasts about the variability in the measured data (Guven and Aytek, 2010). The higher the value of CE, the better will be the results. These models have been created using GP Kernel software developed by Babovic and Keijzer (2000), based on tree-based GP.

4.11.3 Development of model and Results

The peak load (T_{GP}) of the specimen is the output model of GP program.

Equation (4.15) shows the model for peak load developed after running the GP program:

$$T_{GP} = 0.01\left(\frac{{l_{eh}}^{1.22}{f_{cm}}^{0.07}{d_b}^{0.01}SF^{0.04}}{20}\right) - 5 \quad (4.15)$$

The findings of the GP model are shown in Table 4.3.

Table 4. 3 Results of GP model

Performance parameters		**T_{GP}**
Root Mean Square Error (RMSE)	Square head	0.082
	Rectangular head	0.091
	Circular head	0.074
Coefficient of Efficiency (CE)	Square head	0.930
	Rectangular head	0.920
	Circular head	0.960
Standard Deviation (SD)		0.050
Coefficient of Variance (COV)		0.030

The GP equation given by equation (4.15) for peak load of the specimens is straightforward, concise, and meaningful since the equation (4.15) shows that the peak load of the specimen increases with the increase in diameter of the bar. Using Experimental and GP-based models, Figures (4.17-4.19) depict the link between peak load and diameter of the bar. For maximum load-carrying capacity, the performance parameters (for GP), RMSE for square, rectangular and circular heads is 0.082, 0.091, and 0.074, respectively, and CE for square, rectangular and circular heads is 0.93, 0.92, and 0.96, respectively. The accuracy of the results is reasonable and acceptable. For the different diameters of bars (16, 20, and 25 mm), the results calculated from equation (4.15) have been compared to experimental results. The plot between

the diameter of bars and peak load (calculated from GP and experimental peak load) has been compared for square, rectangular heads, and circular headed bars, respectively, as shown in Figure (4.17-4.19). The comparison of peak load by GP and peak load by experimental results has been plotted in Figure 4.20. It can be observed from Figure (4.17-4.19) that the values obtained from GP are more or less matching the experimental values. The maximum error that could be seen in the comparison has been ±5%. The plot of peak load (Experimental vs. GP) shows that some values from GP are more or less equal to experimental values, and only a few match experimental values exactly, which shows that peak load increases as the diameter of the bar increases. It can be observed from Figures (4.17-4.19) that the average error is found to be maximum, i.e., ±5% in case of 20 mm diameter of bar due to the variation in peak load for the experimental and proposed model from GP. This shows that the GP model is sensitive to input parameters, and the results confirm the model's accuracy. Thus, the proposed model has been validated with research test results, concluding that the proposed model is compatible with the research findings.

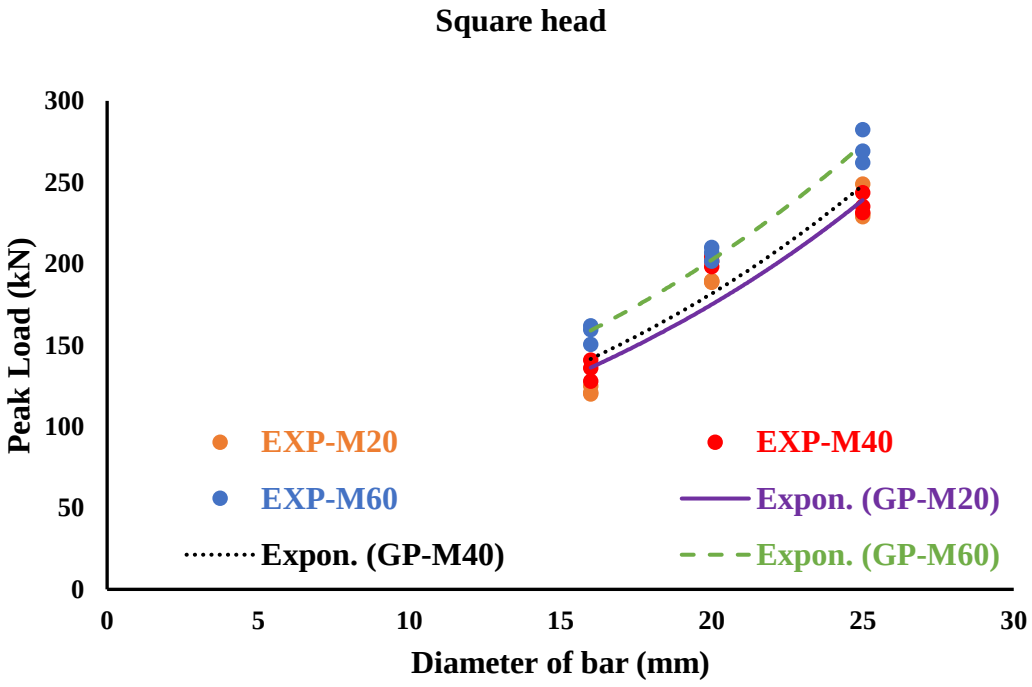

Figure 4. 17 Peak load vs diameter of the bar for Square-headed bars

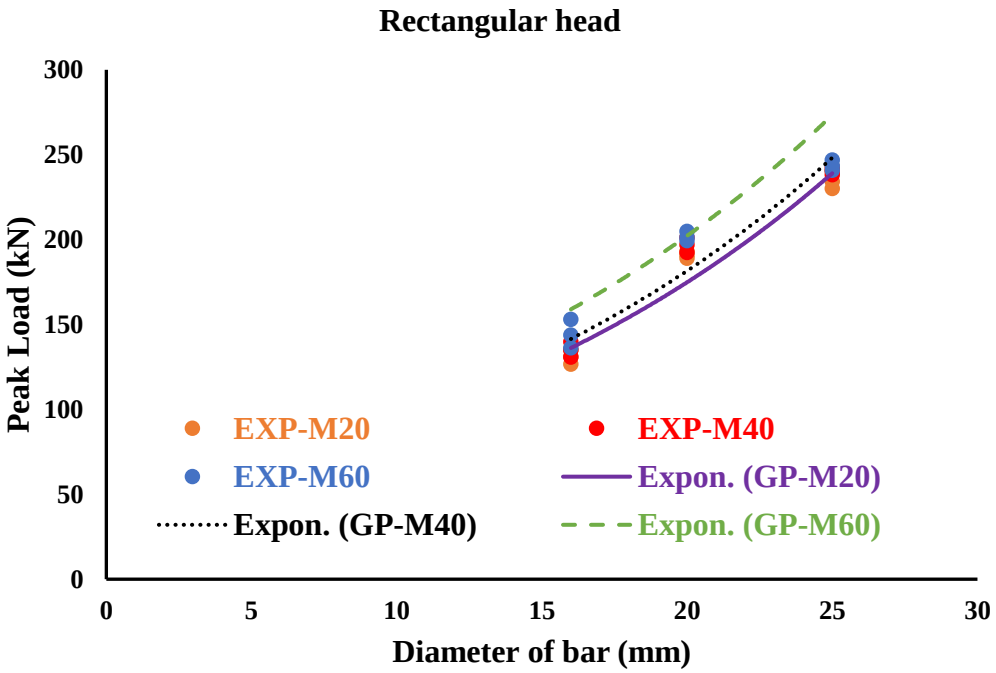

Figure 4. 18 Peak load vs diameter of the bar for Rectangular headed bars

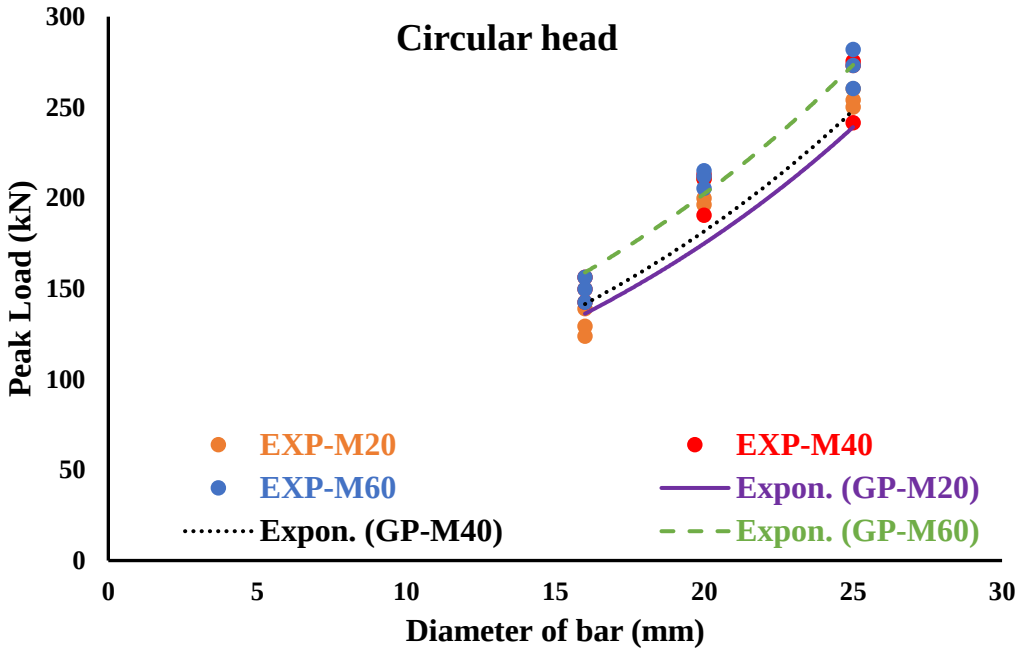

Figure 4. 19 Peak load vs diameter of the bar for Circular headed bars

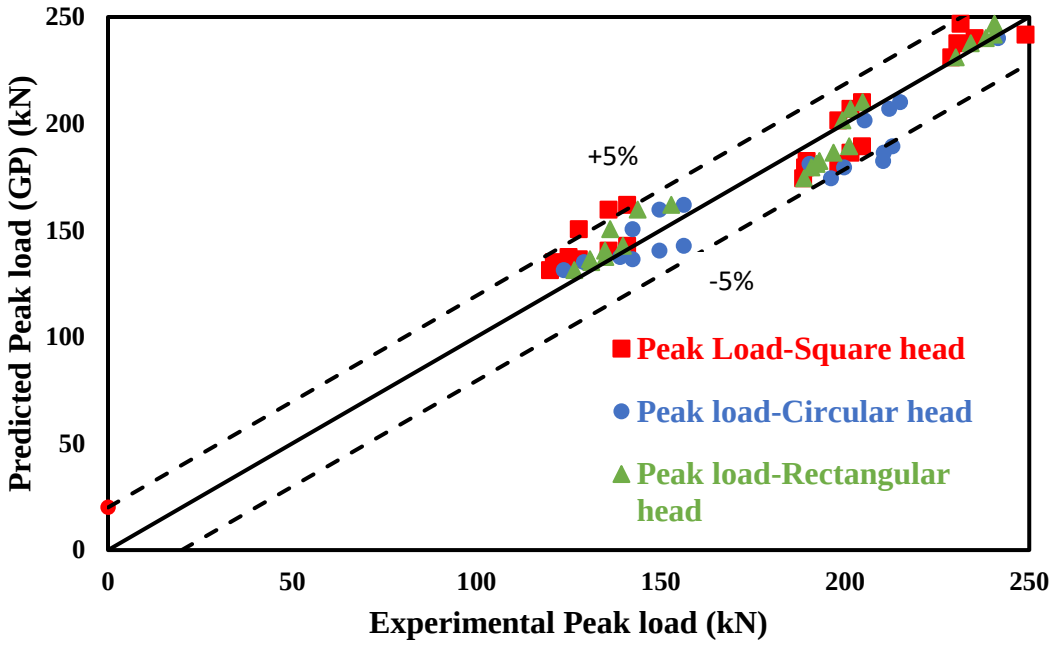

Figure 4. 20 Experimental Peak load vs Predicted peak load depicted from GP model for all the shapes of headed bars

4.12 Comparison of the analytical model developed from GP and regression analysis

The predicted peak load from both the methods, i.e., analytical model (GP) and regression analysis (REG), has been compared with the experimental load as shown in Figure 4.21. It can be observed that the values of peak load predicted from regression analysis are 5% higher than peak load predicted from GP in the case of square-headed bars. Whereas in the case of circular and rectangular heads, the GP model has provided better results than the equation developed by regression analysis. The R^2 value for a peak load of circular-headed bars predicted by GP and REG is 0.96 and 0.95, respectively. Also, the error line of peak load predicted from regression analysis is ±10% than the experimental peak load, whereas the error line in GP is ±5%. Thus, when the GP-based model has been compared to equations obtained from regression analysis, the obtained values show considerably better results. The peak load predicted from GP provides a better match with experimental results as compared to regression analysis.

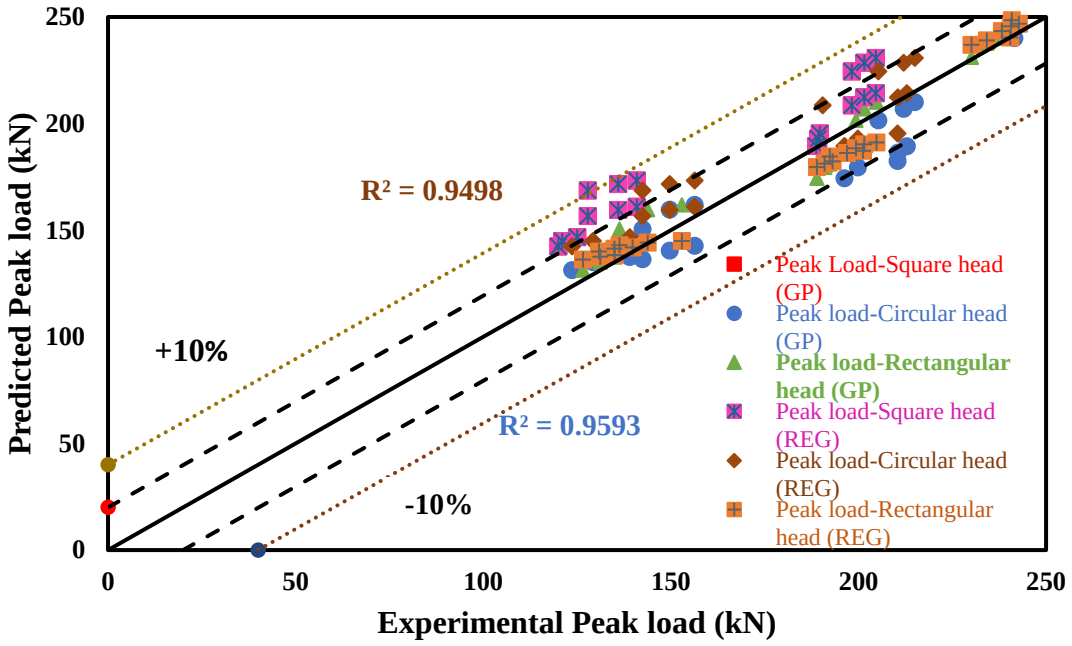

Figure 4. 21 Experimental peak load versus predicted peak load depicted from both Regression analysis (REG) and GP

4.13 Development of Bond strength model

The bond strength between concrete and headed bars has been calculated after the pull-out test using experimental peak load values. The formula for ultimate bond strength (τ_{max}**)** as per ACI 318-2019, is given by equation (4.16).

$$\tau_{max} = (P_{max}/3.14*d_b*l_{eh}) \quad (4.16)$$

where, P_{max} is the maximum experimental peak load (kN), d_b is the diameter of the reinforced bar (mm), and l_{eh} is the embedment depth (mm). This formula has been extensively used by various researchers for calculating the bond strength of headed bars (Park *et al.* 2003; Delhomme *et al.* 2015; Rabi *et al.* 2020). It can be observed from equation (4.12) that bond strength depends on the peak load, diameter of the bar and embedment depth of the bar. The effect of steel fibers and compressive strength has not been considered in the ACI formula of

bond strength. Thus, a reference model for bond strength has been taken from the research of Nilforoush (2019) and a new modified model has been developed using regression analysis considering the percentage of steel fibers (SF), compressive strength of concrete measured after 28 days of testing (f_c'), the diameter of steel bar (d_b) and embedment depth of bar (l_{eh}), which is given by equation (4.17).

$$\text{Bond Strength (B.S)} = \frac{\left[a_1\sqrt{f_c'}+(a_3 f_c'-a_2)0.66SF\right]l^{0.5}{}_{eh}}{3.14*d_b} \quad (4.17)$$

The constants a_1 and a_2 have been found from the regression analysis, the constant a_3 has been calculated by trial and error, and 0.66 is the constant calculated with the help of aspect ratio of steel fibers (i.e. 65 in the present study). Thus, the final equation after applying regression analysis is given by equation (4.18).

$$\text{Bond Strength (B.S)} = \frac{\left[17.9\sqrt{f_c'}+(0.33 f_c'-0.4)0.66SF\right]l^{0.5}{}_{eh}}{3.14*d_b} \quad (4.18)$$

The plot between bond strength and measured compressive strength of concrete has been shown in Figure 4.22. The ultimate bond strength has been calculated for all the three shapes of heads using experimental peak load values through ACI formula. It can be clearly seen in Figure 4.22 that after considering the SF and f_{cm} factors, the predicted bond strength increases as compared to the bond strength (ACI) having R^2 value of 0.96 and predicted bond strength lies within ±5% of the error line with the bond strength (ACI). As the compressive strength increases from 20 MPa to 60 MPa, there has been 98.7% increase in the bond strength. Higher concrete strength has resulted in the higher interfacial bond strength of steel fibers, which increases the post-cracking strength of concrete having steel fibers. Thus, the predicted model of bond strength shows the importance of compressive strength and steel fibers which is absent in the formula given by ACI 318-19. From the plot between experimental and predicted bond strength (Figure 4.23), it can be observed that the average absolute variation and integral absolute error value obtained are 10.12% and 10.29%, respectively. It has been found that the proposed model performs well with the experimental values obtained in this study and accurately predicts

engineering properties. The coefficient of variance between predicted bond strength and experimental bond strength for circular, square, and rectangular head is 6.06, 7.08, and 10.02, respectively. Thus, it can be concluded that the circular head performs the best out of all the shapes.

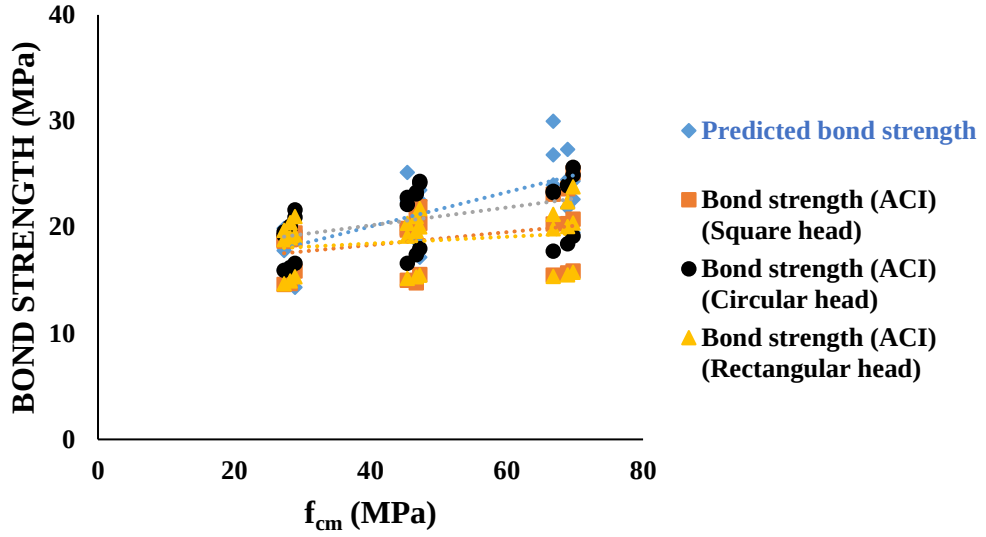

Figure 4. 22 Experimental and predicted bond strength vs measured compressive strength

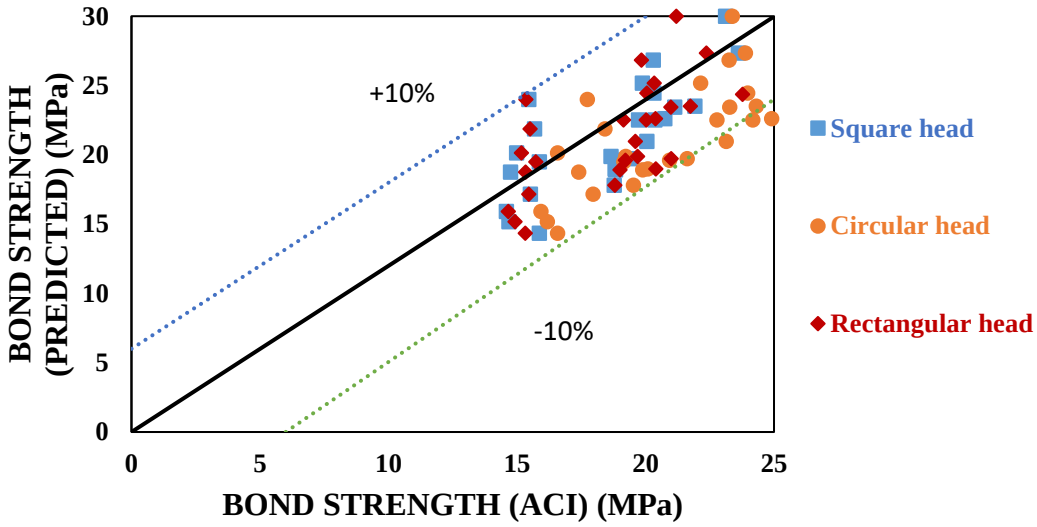

Figure 4. 23 Comparison of experimental and predicted bond strength of headed bars for all the shapes of heads

4.14 Concluding Remarks

The test results of the pull-out of cylindrical specimens are presented in this study. Under this program, a total of 324 specimens have been tested. A parametric study incorporates experimental results to investigate the effect of various parameters, like the diameter of bars, the shape of heads, percentage of steel fibers, and compressive strength of concrete on the anchorage capacity of headed bars non-linear regression model using dummy variables. This chapter includes a summary of peak load, bond strength, ultimate displacement, and failure modes for various specimens, as well as a bar chart displaying the specimens' load-carrying capacity. Additionally, the specimens' pull-out strength has been compared using codal provisions (fib MC2010, ACI 318-19, and EN 1992-1-1). According to the findings, the anchorage capacity of headed bars increases as concrete compressive strength, the diameter of bars, and steel fibers increase, according to the findings, which have been confirmed using non-linear regression analysis with dummy variables. Steel and concrete-blowout failure modes have both been observed, with steel failure being the most common. This study uses genetic programming to develop a model that predicts headed bars' maximum load-carrying capacity when subjected to direct pull-out tension. The GP model has been developed based on an extensive database containing 324 test specimens with four variables. The concrete compressive strength, bar diameter, bar embedment depth, and percentage of steel fibers control the load-carrying capacity of headed bars. Compared to the equation developed using regression analysis for peak load, the proposed GP model provides an accurate prediction of peak load that most fits the experimental database. In comparison to the regression equation, the GP model has the highest R^2 values. According to load-deflection curves, GP model, and derived descriptive equations, the circular headed bar has shown the highest peak load and is chosen as the best shape of head out of all the shapes and has further been opted for a beam-column joint test whose results have been discussed in Chapter 5.

CHAPTER 5

CYCLIC BEHAVIOR OF EXTERIOR BEAM-COLUMN JOINT WITH HEADED BARS EMBEDDED IN STEEL FIBER REINFORCED CONCRETE

5.1 Introduction

Reinforced cementitious composites have been increasingly used during recent years in beam-column joints. The introduction of headed bars is a practical solution to eliminate the congestion problem caused by hooked bars in beam-column joints. This chapter emphasizes evaluating the performance of steel fiber reinforced concrete (SFRC) in external beam-column joints (BCJ) using headed bars as an anchorage mechanism. The comparison has been made with the conventional bars detailed by ACI 318-19 and ACI 352R-02. The repository of previous BCJ work has been further expanded by investigating the effect of structural parameters, i.e., compressive strength (M20 and M40), headed bars and steel fibers (1 and 1.5%) on the hysteresis curve, ductility, stiffness, energy dissipation, and cracking on all specimens. Circular-shaped headed bars have been used in the BCJ as they have performed the best out of the three shapes, i.e. (Square, rectangular and circular) as discussed in Chapter 4. The percentage of steel fibers (1 and 1.5%) has also been selected based on the outcome of the pull-out test, as discussed in Chapter 4. The experimental results have revealed that the conventional bars can significantly be replaced by the headed bars in areas vulnerable to earthquakes due to their higher load carrying capacity with better ductility and stiffness response and reducing congestion in BCJ. Also, a descriptive equation for anchorage capacity of headed bars has been generated using iterative non-linear regression analysis, including a steel fiber parameter, which is missing in the earlier models developed by previous researchers (Zuo and Darwin (1998); Shao 2016; Sperry *et al.* (2017); Ghimire *et al.* (2019b)).

5.2 Loading Sequence

The lateral reversal load applied at the top of the beam, and the load history for the beam-column joint assemblage has been plotted as shown in Figure 5.1. A 300 kN double-acting jack has been used to apply load to the specimens in the loading frame, which has a quasi-static cyclic loading setup with displacement control (each step consists of two cycles of the same displacement at intervals of 5mm). The load has been applied to the specimens in a monotonous manner using hydraulic jacks at 5 mm intervals of increments, based on the ACI 374.1-05 estimated failure load. The column's 10% axial load carrying capacity is applied as the axial load (i.e., 40 kN) and kept constant during the test to simulate gravity load. In this work, an axial force on one side of the column has been applied using a hydraulic jack. With the steel plate affixed to the reaction frame, the reaction has been taken.

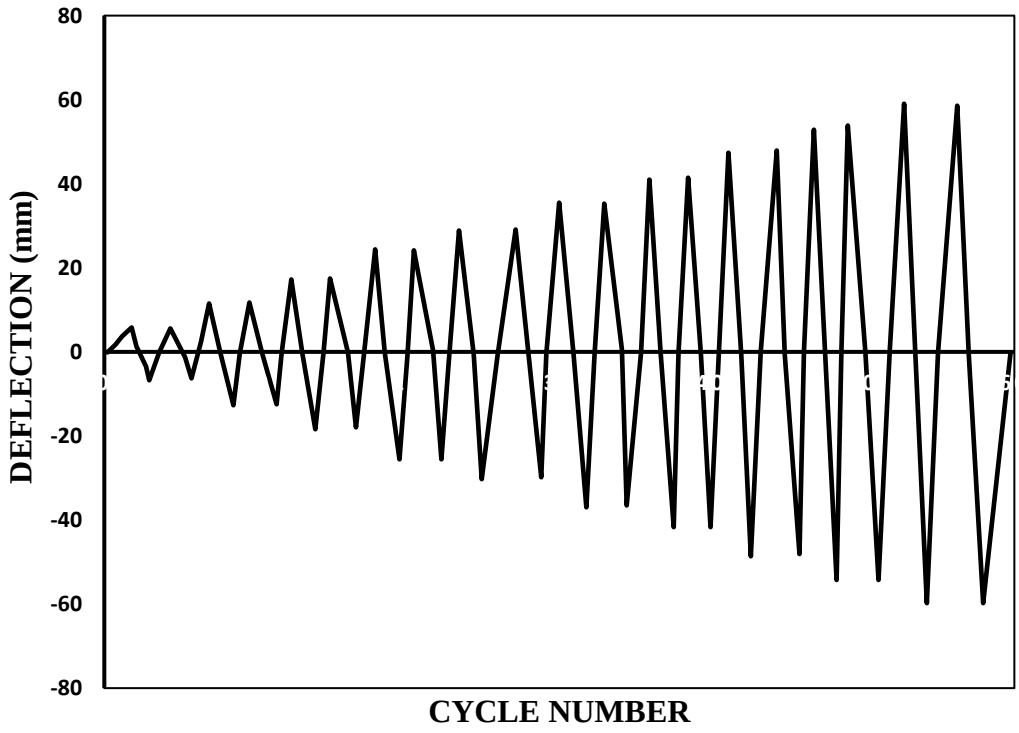

Figure 5. 1 Load-history plot

5.3 Analysis of Hysteresis Plot and load-deflection envelope

The plot between lateral load versus displacement of any specimen after the experimental testing results can be defined as a hysteresis plot. From Figures 5.2(a-h), it is evident that the overall load carrying capacity of HS (Headed bar Specimen) is more than the CS (Control Specimen). The specimens' load-displacement curve similarity can be observed as the specimens are tested under quasi-static reversed cyclic loading. For the CS1 specimen, the load-displacement hysteresis curve is plotted as shown in Figure 5.2(a). Initial flexural cracks were discovered in the beam-column assemblage in the joint where the beam is connected to the column junction with a displacement of 5 mm during the second cycle. The specimen was loaded, unloaded, and reloaded until it reached the ultimate load on the eighth cycle, with an average ultimate load of 45.72 kN and displacement of 9.6 mm, as shown in Table 5.1. For the low seismic prone area, the CS1 specimen has been designed having 90^{o} bent hook anchorages, according to ACI 318-19 with no steel fibers and having M20 grade of concrete. After attaining the ultimate load, the shear panel area of the joint core has multiple diagonal cracks, and concrete has been crushed and spalled out due to compression failure. Figure 5.2(b) shows the load-displacement hysteresis curve for the CS2 specimen. During the second cycle, initial flexural cracks were discovered in the beam-column assemblage at the joint where the beam is connected to the column junction with a displacement of 5 mm. As shown in Table 5.1, the specimen was loaded, unloaded, and reloaded until reaching the ultimate load on the ninth cycle, with an average ultimate load of 50.30 kN and displacement of 16.3 mm. There are many diagonal cracks on the shear panel area of the joint core after reaching the ultimate load, and concrete has also been crushed and spalled out due to compression failure. For the low seismic prone area, these specimens with conventional 90° hook bent anchorages without confinement reinforcement or steel fibers, and M40 grade of concrete is detailed according to ACI-318-19. Figure 5.2(c) shows the load-displacement hysteresis curve for the HS1 specimen. HS1 specimen has been detailed according to ACI 352, having headed bars in the joint without steel fibers and having M20 grade of concrete. During the fourth cycle, initial flexural cracks were discovered in the beam-column assemblage at the joint where the beam was connected to the column junction with a displacement of 10 mm. As shown in Table 5.1,

the specimen was loaded, unloaded, and reloaded until reaching the ultimate load on the thirteenth cycle, with an average ultimate load of 102.1 kN and displacement of 30.1 mm. There were no diagonal cracks on the shear panel area of the joint core after it has reached the ultimate load. Figure 5.2(d) shows the load-displacement hysteresis curve for the HS2 specimen. HS2 specimen was detailed according to ACI 352, having headed bars in the joint with 1% of steel fibers and having M20 grade of concrete for the low seismic prone area. During the fifth cycle, initial flexural cracks were discovered in the beam-column assemblage at the joint where the beam is connected to the column junction with a displacement of 12 mm. As shown in Table 5.1, the specimen was loaded, unloaded, and reloaded until reaching the ultimate load on the tenth cycle, with an average ultimate load of 148.65 kN and displacement of 18.3 mm. There were no symptoms of diagonal cracks on the shear panel region of the joint core after attaining the ultimate load; however, broad open cracks were appeared on the column face. Figure 5.2(e) shows the load-displacement hysteresis curve for the HS3 specimen. HS3 specimen has been detailed according to ACI 352, having headed bars in the joint with 1.5% of steel fibers and having M20 grade of concrete for low to the moderate seismic prone area. During the ninth cycle, initial flexural cracks were discovered in the beam-column assemblage at the joint where the beam was connected to the column junction with a displacement of 15 mm. As shown in Table 5.1, the specimen was loaded, unloaded, and reloaded until reaching the ultimate load on the thirteenth cycle, with an average ultimate load of 173.1 kN and displacement of 23.7 mm. There were no symptoms of diagonal cracks on the shear panel region of the joint core after attaining the ultimate load; however, broad open cracks have appeared on the column face. Figure 5.2(f) shows the load-displacement hysteresis curve for the HS4 specimen. HS4 specimen was detailed according to ACI 352, having headed bars in the joint with no steel fibers and having M40 grade of concrete for the low seismic prone area. During the ninth cycle, initial flexural cracks were discovered in the beam-column assemblage at the joint where the beam is connected to the column junction with a displacement of 20 mm. As shown in Table 5.1, the specimen was loaded, unloaded, and reloaded until reaching the ultimate load on the sixteenth cycle, with an average ultimate load of 142.4 kN and displacement of 36.9 mm. As a result of the lack of confinement offered by the steel fibers, cracks appeared at the anchorage portion of headed bars, propagating towards

the joint face and eventually rupturing concrete at the joint face. Figure 5.2(g) shows the load-displacement hysteresis curve for the HS5 specimen. The HS5 specimen was detailed according to ACI 352, having headed bars in the joint with 1% of steel fibers and having M40 grade of concrete for the low seismic prone area. During the thirteenth cycle, initial flexural cracks were discovered in the beam-column assemblage at the joint where the beam was connected to the column junction when the displacement of 20 mm was reached. As shown in Table 5.1, the specimen was loaded, unloaded, and reloaded until reaching the ultimate load on the thirteenth cycle, with an average ultimate load of 186.50 kN and a displacement of 36.2 mm. The wider cracks were observed on the face of BCJ at 45.0 mm displacement, followed by flexural cracks in the beam and minor diagonal cracks in the column, indicating the strong column-weak beam design. Figure 5.2(h) shows the load-displacement hysteresis curve for the HS6 specimen. HS6 specimen was detailed according to ACI 352, having headed bars in the joint with 1.5% steel fibers and having M40 grade of concrete for the low seismic prone area. During the fourteenth cycle, initial flexural cracks were discovered in the beam-column assemblage at the joint where the beam was connected to the column junction when the displacement of 25 mm was reached. As shown in Table 5.1, the specimen was loaded, unloaded, and reloaded until reaching the ultimate load on the sixteenth cycle, with an average ultimate load of 193.30 kN and displacement of 27.3 mm. Wider cracks were observed on the face of BCJ at a displacement of 50.50 mm, followed by flexural cracks in the beam and minor diagonal cracks in the column, indicating the strong column-weak beam design.

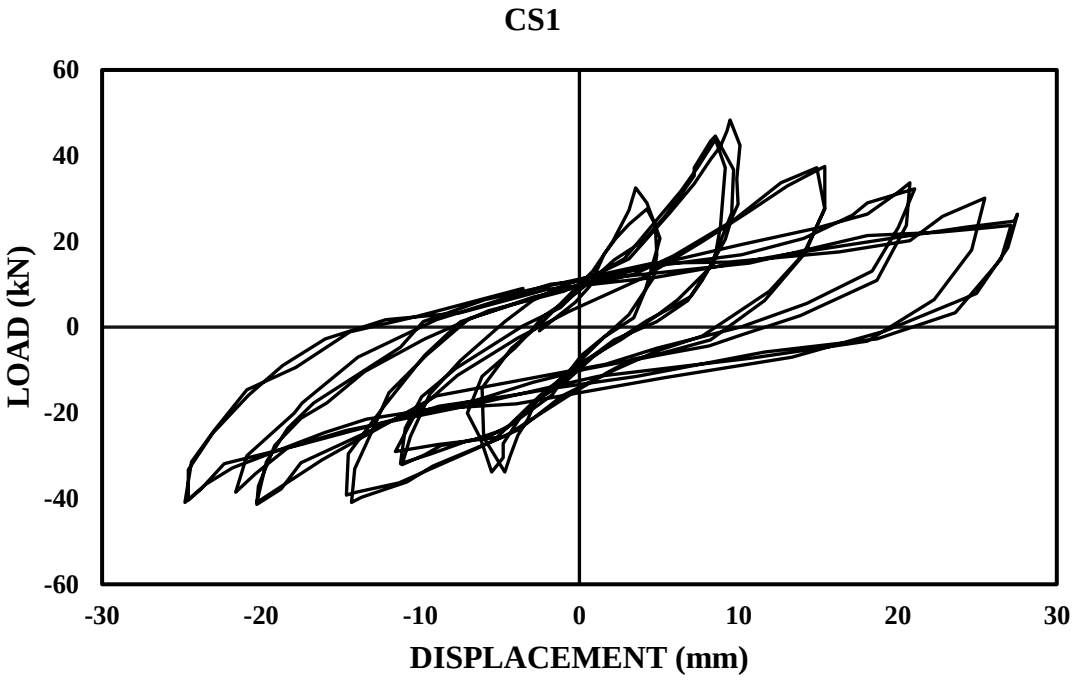

Figure 5.2 (a)

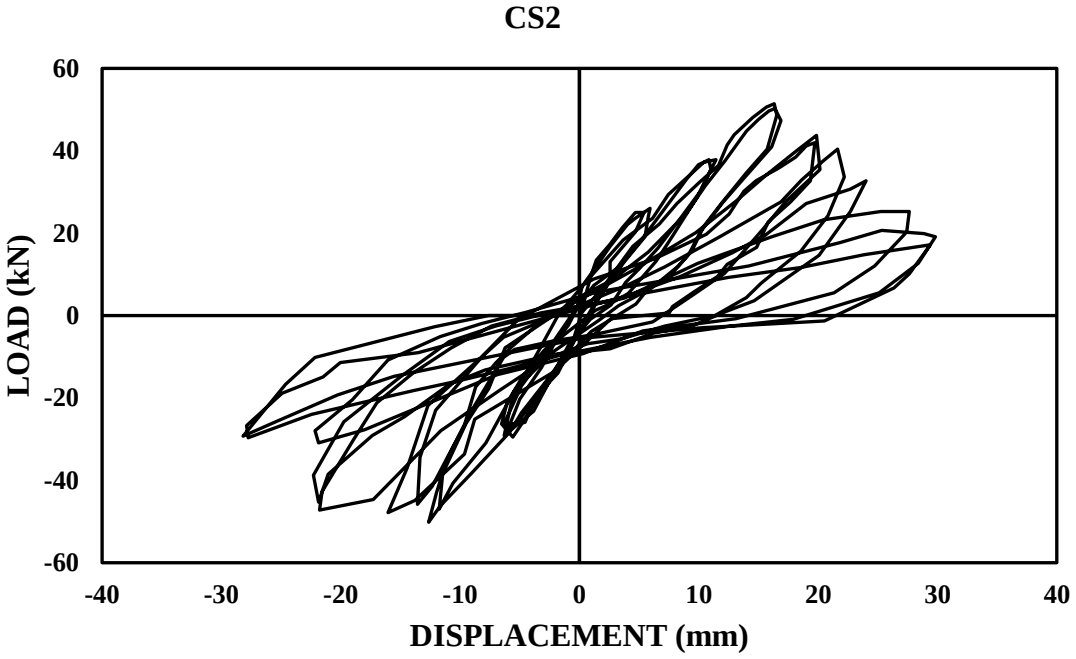

Figure 5.2 (b)

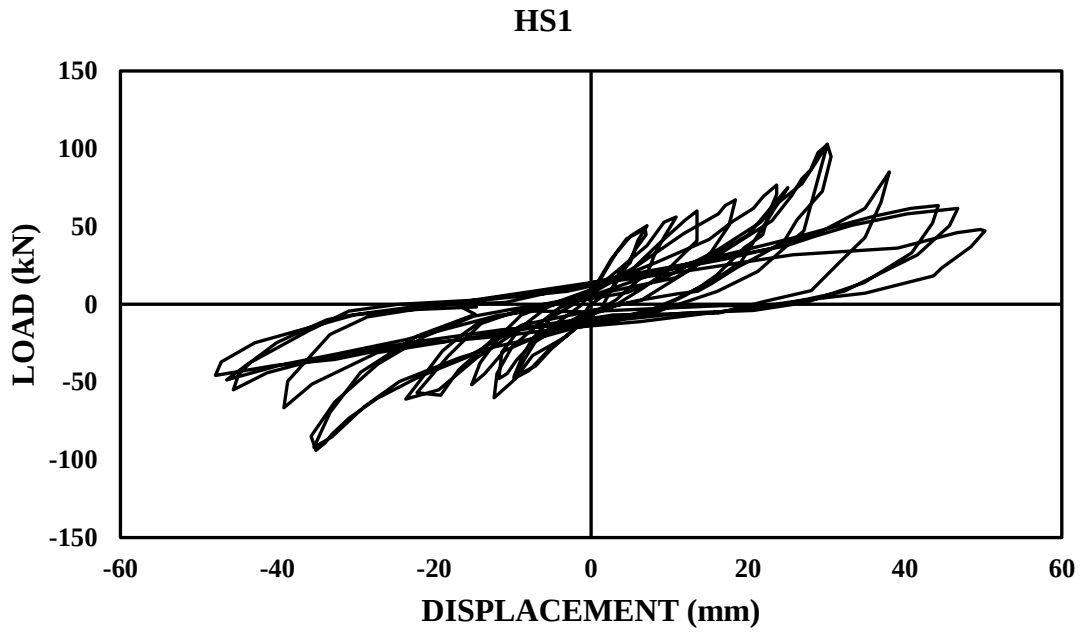

Figure 5.2 (c)

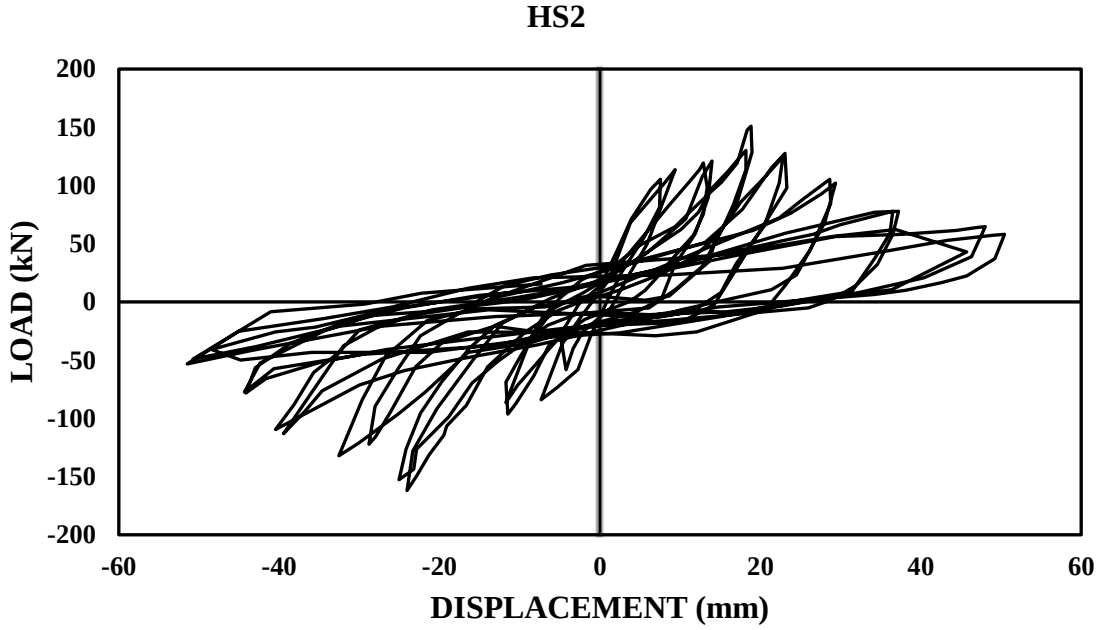

Figure 5.2 (d)

HS3

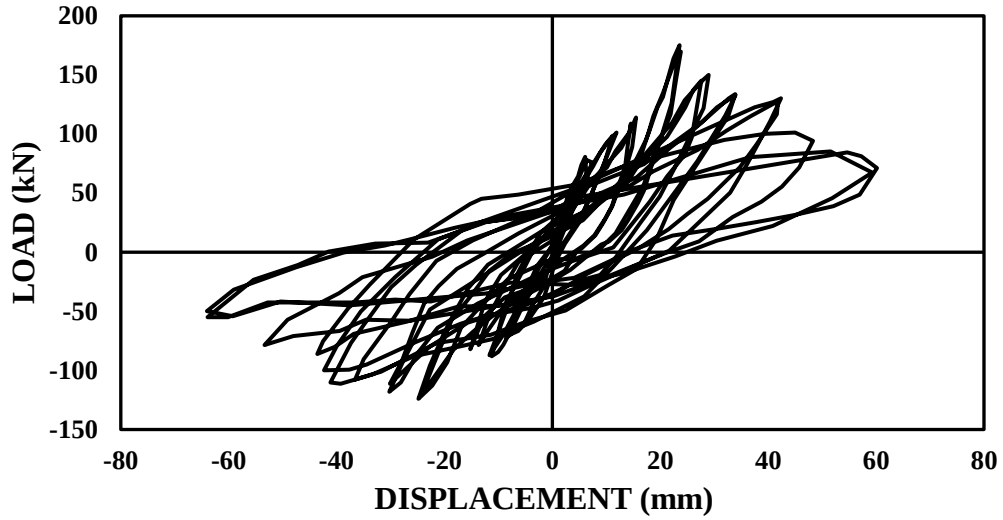

Figure 5.2 (e)

HS4

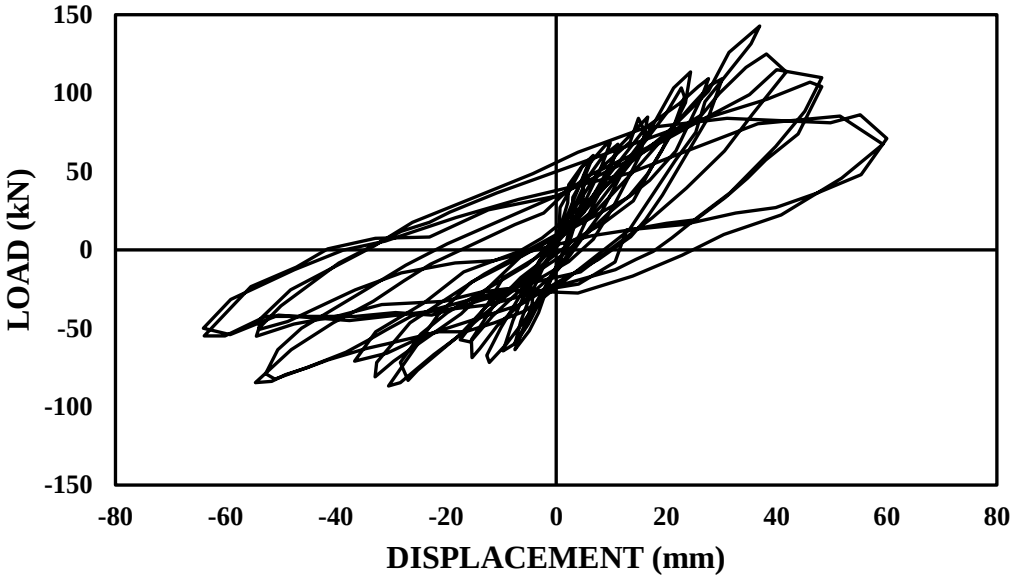

Figure 5.2 (f)

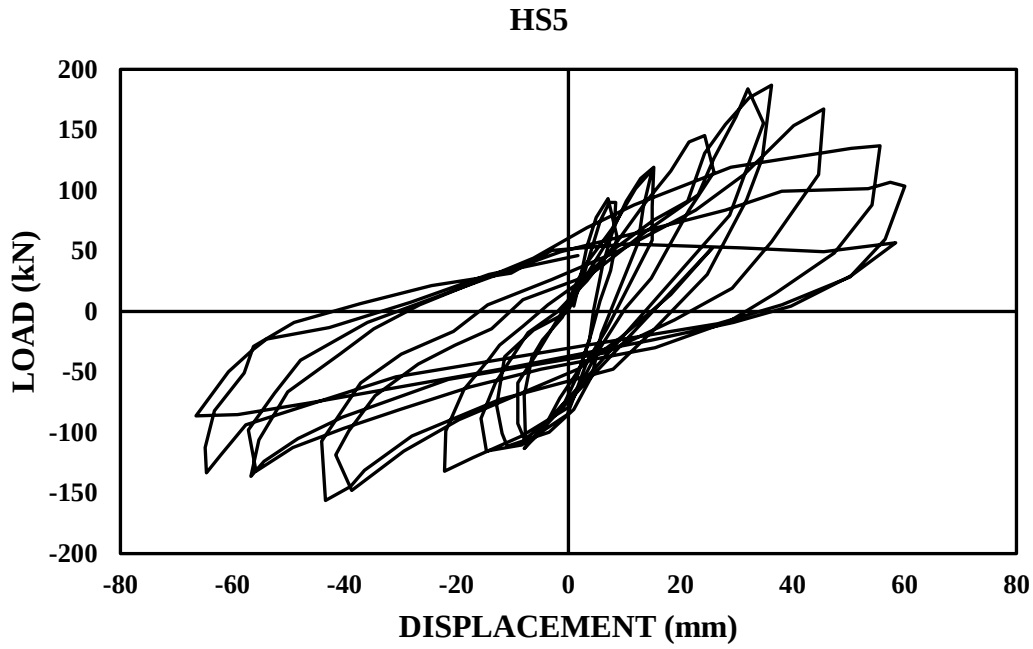

Figure 5.2 (g)

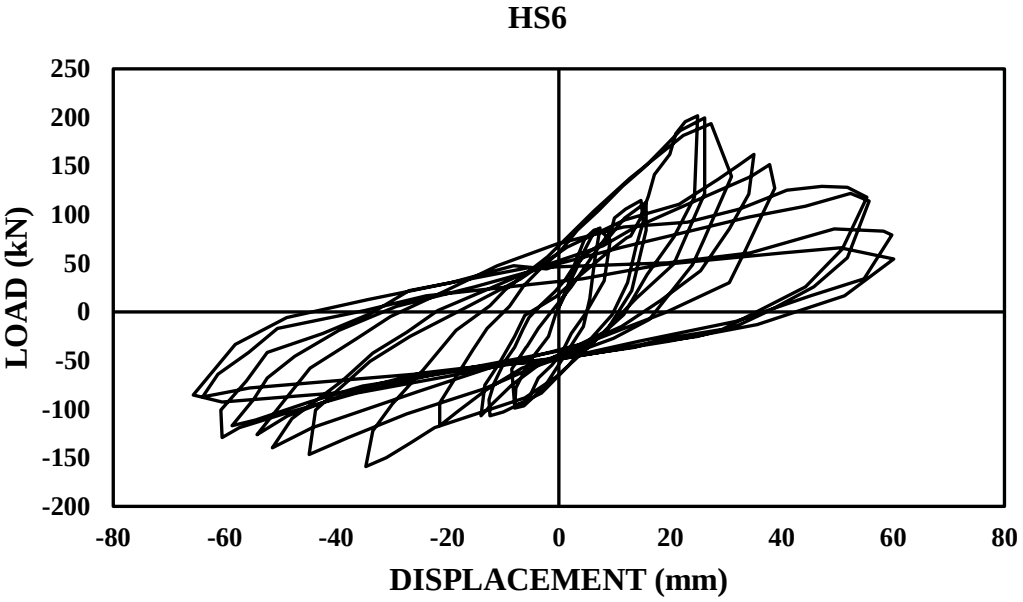

Figure 5.2 (h)

Figure 5. 2 (a-h) Load-displacement hysteresis plot

5.4 Effect of headed bars and steel fibers on ductility

Ductility (μ) is defined as a structure's ability to withstand large deformations beyond the point of yield displacement under sustained loading. It is the ratio of the specimen's ultimate displacement (δ_u) to its yield displacement (δ_y) (Chidambaram and Agarwal 2015). All the headed-bar specimens (HS) have performed well in a ductile mode with the objective of seismic design. The failure of CS1 is comparatively less ductile than CS2, which is observed from the hysteresis plot since the load carrying capacity dropped suddenly after achieving the peak load with a higher degree of degradation relative to CS2. The yielding of the beam leading to flexural cracks, cracking at the joint face, spalling of concrete in BCJ, and finally distorting the BCJ in CS1 and CS2, as observed by Lee and Ko (2007). HS shows more ductility and minor pinching than the CS because the mode of anchorage in the joints is headed bars compared to the conventional bars, and the joints have steel fibers in the concrete mix (Lee and Yu 2009a). A substantial decline has been observed in the peak load of HS1, which is recorded at 102.1 kN load and 30.1 mm displacement (Figure 5.3). This decline is attributed to the loss of anchorage bond provided by the headed bar at the joint region and due to the lack of steel fibers' confinement in the joint and subsequently failure of the specimen. A similar hysteresis plot can be observed in HS2, and HS3 as the only percentage of steel fibers distinguishes the specimens. The smaller strength degradation can be observed in both the cases after post-peak behavior as the initial slippage of the longitudinal reinforcement is prevented by the confinement provided by the steel fibers and the anchorage capacity of headed bars. It is observed from Figure 5.3 and Table 5.1 that the load-carrying capacity of HS4, HS5, and HS6 is 28.17%, 20.2%, and 10.42% higher than HS1, HS2, and HS3 specimens having the same percentage of steel fibers, respectively. This increase in the load-carrying capacity is attributed to the higher compressive strength of the HS4, HS5, and HS6 specimens, which provide a better bond with the headed bars and delays the slippage of the bars. It can be observed from Figure 5.3 that the peak load of HS4 at 50 mm displacement is 15.7% and 9% less than that of HS5 and HS6, respectively, due to the lack of bridging effect provided by the steel fibers in HS4.

It can be observed clearly from Figure 5.3 that the pre-peak curve is similar for almost all the specimens, i.e., yielding of all the specimens occurs in the range of 3.75 to 6.10 mm displacement. A critical contrast has been seen in the post-peak curve, which is elongated more after the ultimate load, with the failure displacement going till 60 mm. The same has been observed in the study conducted by Sharma (2019). The addition of steel fibers in the joints having headed bars improves the specimens' ductility and strain hardening properties. Lee and Yu (2009) have observed the same behavior. It has been observed from Table 5.1 that the ductility factor of headed bar specimens (HS1-HS6) is comparatively 21.6 to 52.8% more than control specimens (CS1 and CS2). Among the six specimens of headed bars, i.e. (HS1-HS6), the ductility imparted by HS6 was the maximum because of the high volume of steel fibers in the M40 grade of the concrete joint having headed bars. The same combination of anchorage and steel fibers in the BCJ can be imparted in challenging high ductility circumstances, which was been observed in the study of Rajagopal and Prabavathy (2015). Ultimately, the HS specimens can recover the specimens' post-peak activities, but no substantial enhancement in the elastic range was observed.

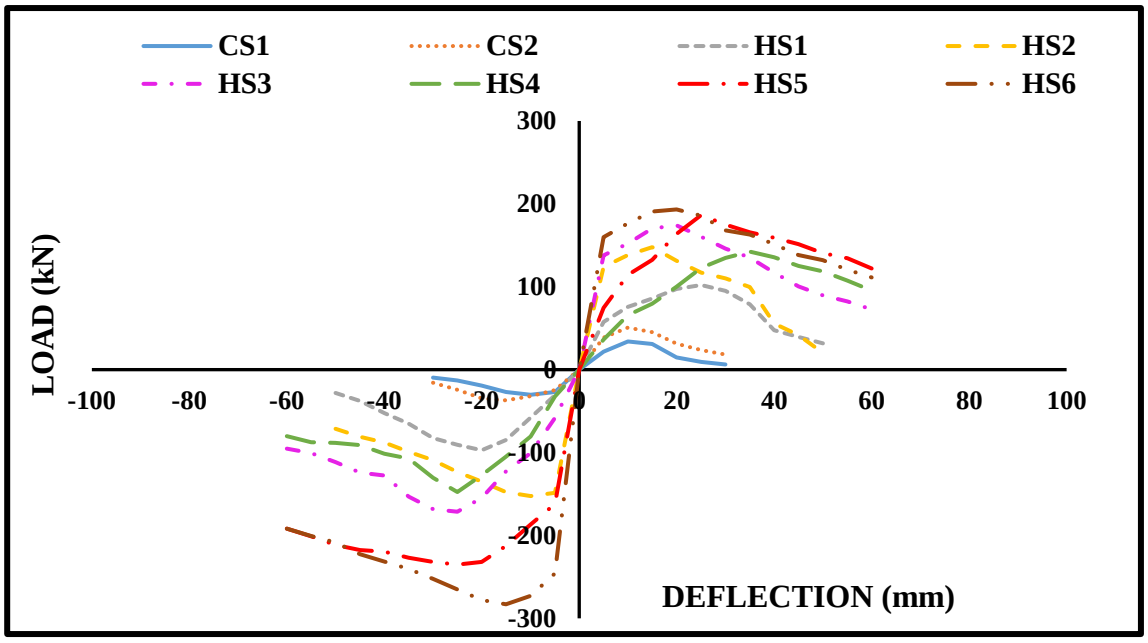

Figure 5. 3 Load-deflection envelope depicting ductility of specimens

Table 5. 1 Ductility Factor

Specimen designation	Ultimate load (P_u) (kN)		Average ultimate load (kN)	Ultimate displacement (δ_u) (mm)		Average ultimate displacement (δ_u) (mm)	Average yield displacement (δ_y) (mm)	Ductility Factor ($\mu = \delta_u/\delta_y$)
	Forward Cycle	Reverse cycle		Forward Cycle	Reverse cycle			
CS1	27.20	24.24	25.72	16.20	14.00	15.10	3.75	4.02
CS2	40.24	29.60	34.92	15.80	22.30	19.05	4.00	4.76
HS1	81.60	77.76	79.68	21.20	25.00	23.10	4.50	5.13
HS2	118.92	121.99	120.45	17.10	28.20	22.65	4.25	5.32
HS3	138.53	137.10	137.81	33.00	39.00	36.00	5.00	7.20
HS4	113.92	118.10	116.01	52.00	35.00	43.50	6.10	7.13
HS5	149.21	188.13	168.67	45.00	45.00	45.00	5.00	9.00
HS6	154.64	226.42	190.53	40.00	61.00	50.50	5.00	10.10

5.5 Effect of different variables on behavior of external BCJ

The effects of each variable on the ultimate anchorage capacity throughout the load history in terms of control and headed bar specimens have been discussed in this section. The different specimens have been compared using the hysteresis plot as shown in Figure 5.2(a-h) and Table 5.1.

5.5.1 Effect of compressive strength of concrete

The behavior of external BCJ has been investigated for two different grades of concrete, i.e., M20 (Low compressive strength) and M40 (Medium compressive strength). One control specimen (CS1) and three specimens with headed bars (HS1, HS2, and HS3) have been cast with M20 grade of concrete, and the other four specimens, i.e., CS2, HS4, HS5, and HS6, were cast with M40 grade. It is observed from Table 5.1 that the peak load increases with an increase in the compressive strength of concrete. There has been a 26.34% increase in the average peak load of CS2 compared to CS1 with an increase in the compressive strength of concrete, and the average peak load of HS6 has been increased 38.4% as compared with HS3 with an increase in

the compressive strength of concrete (Table 5.1). Due to the higher compressive strength of CS2, the cracks initiated later, increasing the length of the plastic hinge formed in the beam and more extreme deterioration at the face of the joint region than CS1. From Figure 5.3 and Table 5.1, it can be observed that the load-carrying capacity of HS4, HS5, and HS6 specimens with the same percentage of steel fibers is 28.17%, 20.2 %, and 10.42% higher than HS1, HS2, and HS3 specimens with the same percentage of steel fibers, respectively. The higher compressive strength of HS4, HS5, and HS6 specimens, which provides a better bond with the headed bars and delays bar slippage, is responsible for the increase in load-carrying capacity. The yielding of HS1, HS2, and HS3 specimens occurs earlier because they dissipate less energy than HS4, HS5, and HS6 specimens due to their lower compressive strength, as shown in 5.2(a-h).

5.5.2 Effect of steel fibers

The specimens with headed bars have more ductility and minor pinching effects than the control specimens due to the addition of steel fibers in the concrete mix. The peak load of HS1 has decreased significantly from 102.1 kN to 49 kN at 30.1 mm and 50 mm, respectively (Figure 5.3). This decrease is due to the loss of the headed bar's anchorage bond at the joint region and a lack of steel fiber confinement in the joint, causing the specimen to fail. In the case of HS2 and HS3, both the specimens are having similar hysteresis plot but the only difference between the specimens is the percentage of steel fibers. According to Table 5.1, the ductility factor of headed bar specimens (HS1-HS6) is 21.6 to 52.8% higher than that of control specimens (CS1 and CS2). Because of the high volume of steel fiber in the BCJ with headed bars, the ductility imparted by HS6 has been the highest of the six specimens of headed bars (HS1-HS6). Due to identical reinforcement detailing, the cracking and failure patterns of HS2 and HS3 have been observed to be similar, except for the percentage of steel fibers ratio (Figure 5.6(d-e)). The toughness of SFRC limits the development of crack width at the joint, which explains why cracks appear later in HS3 than in HS2. The lack of steel fibers in HS4 causes cracks to form early, at a drift ratio of 1.5%, and then propagate faster as the beam continues to yield (till 4%); where drift ratio is the ratio of the specimen’s maximum lateral drift (displacement) to its total height.

5.6 Evaluation of Stiffness

Stiffness is the property of a material defined by the ability to resist deflection. It is calculated by the ratio of peak load to ultimate displacement corresponding to the peak load when the specimen is tested under reversed cyclic loading. The line joining the peak-to-peak load in the forward and reverse cycle throughout the first repetition of every cyclic loading is known as peak stiffness. Figure 5.3 shows the plot between the stiffness and drift ratio. The stiffness is measured using a load-deflection plot but represented using the drift ratio in the graph. In this study, the lateral load has been applied on the beam, so the total height of the beam for calculating the drift ratio has been calculated from the column's face to the point of loading. It has been observed from the curve that the HS6 specimen exhibits the highest stiffness out of all the specimens. HS5 and HS6 specimens containing headed reinforced bars experienced degradation tendencies in stiffness analogous to their counterpart specimens HS2 and HS3, respectively. Overall, the peak-peak stiffness of headed bar specimens (HS) is 2.63 to 4.12 times higher than the control specimens (CS). The significant effect of adding steel fibers on the stiffness has been observed during the first cycle from Figure 5.4. This behavior is attributed to the fact that the micro-cracks begin early during the first cycle in the BCJ. According to the provisions of ACI 374.1-05, the range of the drift ratio should lie between 1.25 and 1.50 times the preceding drift ratio, and the testing should carry on until the drift ratio of 3.5%. Furthermore, after increasing the number of cycles and the drift ratio, the cracks have been controlled by the arbitrarily disseminated fibers placed in the purlieu of joints, which controls the further propagation of cracks. Thus, the rate of stiffness degradation decreases with an increase in the steel fiber ratio in the BCJ (Ganesan *et al.* 2007). HS6 specimen drops its 94.2% of stiffness at a 6% drift ratio, and it is two times greater than the drift ratio of control specimen CS1, which drops the same percentage of stiffness at a 3% drift ratio (Table 5.2). This is due to the bond provided by the headed bars and the steel fibers to the BCJ (Kang *et al.* 2009b). The degradation of stiffness is due to the deterioration of the bond provided by the longitudinal-headed bars or conventional bars in the BCJ (Alavi-Dehkordi *et al.* 2019).

Table 5. 2 Depiction of Stiffness and Relative Energy Dissipation (RED)

Connections with designations ➡	**Control specimen**		**Headed bars**					
Parameters ⬇	**CS1**	**CS2**	**HS1**	**HS2**	**HS3**	**HS4**	**HS5**	**HS6**
I. Initial Stiffness at 5mm displacement for 0.5% drift ratio (kN/mm)	4.38	7.76	11.55	24.84	27.56	7.29	14.90	31.97
II. 0.05 times initial stiffness (kN/mm)	0.22	0.38	0.57	1.24	1.37	0.36	0.74	1.59
III. Stiffness at 3.5% drift ratio (kN/mm)	-	-	2.25	2.85	3.85	4.06	4.73	4.65
Ratio of III/II	-	-	3.94	2.29	2.81	11.27	6.39	2.92
Percentage of stiffness degraded from first to sixth cycle for 3% drift ratio	95.20	92.10	72.50	85.20	82.30	38.40	60.80	82.40
Relative Energy Dissipation (RED) at 0.5% drift ratio (kN-mm)	109.40	194.10	288.85	620.89	689.11	182.36	372.74	799.48

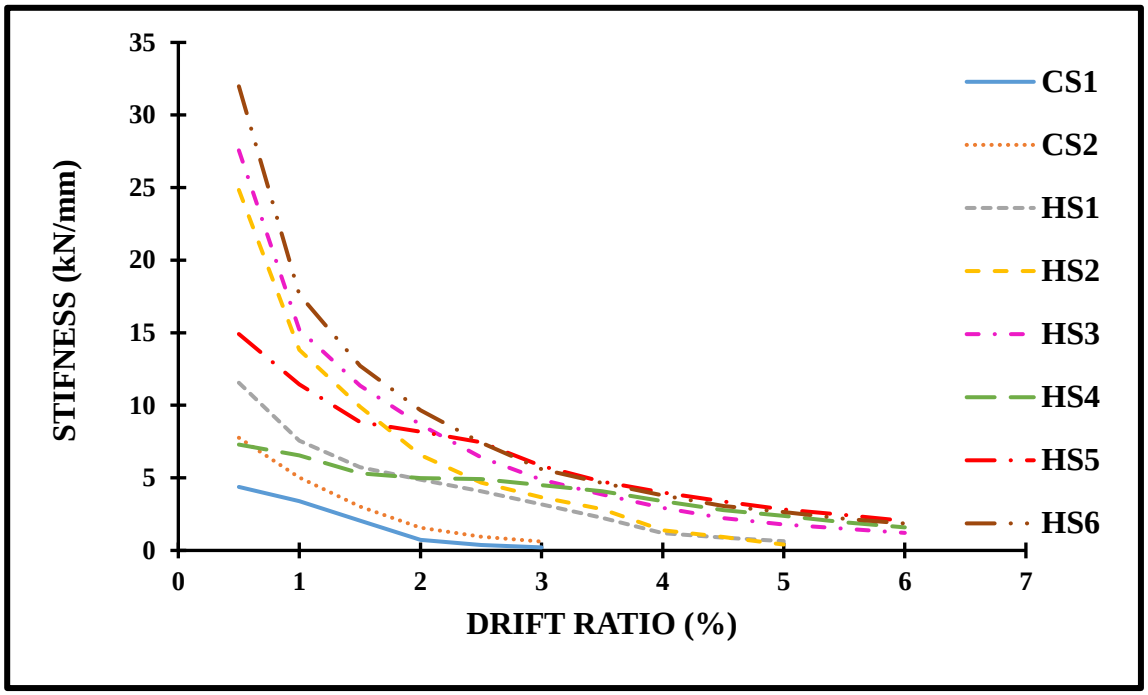

Figure 5. 4 Stiffness of all the specimens

5.7 Evaluation of Energy Dissipation

To evaluate post-peak behavior, Relative Energy Dissipation (RED) is a significant parameter, which is associated with the energy dissipated by the specimen after every consequent cycle. The higher energy dissipation in subsequent cycles controls the ductile response when the deformation increases after output and vice versa, the fragile behavior of the material manifests. Two types of energy dissipation parameters are examined in this study: the first is RED, which involves energy dissipation in each subsequent cycle, and the second is Cumulative Energy Dissipation (CED), which involves energy dissipation after each subsequent cycle. It has been observed from the RED versus drift ratio plot (Figure 5.5a) and (Table 5.3) that all the headed bar specimens (HS) are dissipating higher energy than the control specimens (CS). This indicated clearly that the HS could resist the growth of cracks by dissipating higher energy than the CS. The same behavior has been observed in the study of Lee and Yu (2009). At a 4% drift ratio, the yielding of HS1, HS2, and HS3 specimens has occurred because these specimens are

dissipating lesser energy than HS4, HS5, and HS6 specimens due to the lower compressive strength. The energy dissipation in HS specimens (HS3 to HS6) is sustainable and stable without any abrupt shift or decline (Figure 5.5b), with which HS's superiority over CS is demonstrated. As failure approaches, the slope of the CED-drift ratio for each specimen increases, suggesting a higher risk of substantial damage leading to the development of plastic hinges and diagonal shear damage to the joint. The curve HS1 and HS2 declined after a 3.5% drift ratio due to the absence of steel fibers and lower compressive strength used than the HS4, HS5, and HS6 specimens. It is apparent from Figure 5.5b that HS have 18-27 times higher CED capacity than CS.

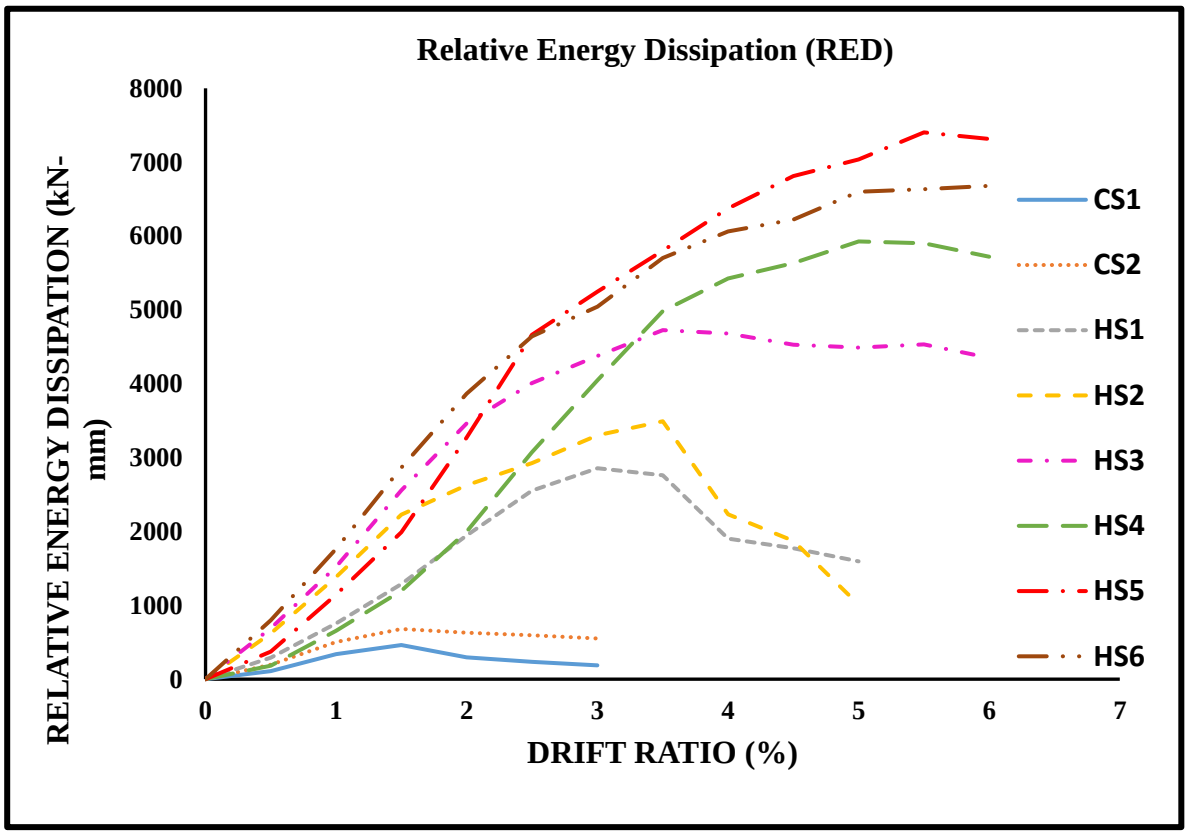

Figure 5. 5(a) Relative Energy dissipation (RED) curve of all the specimens

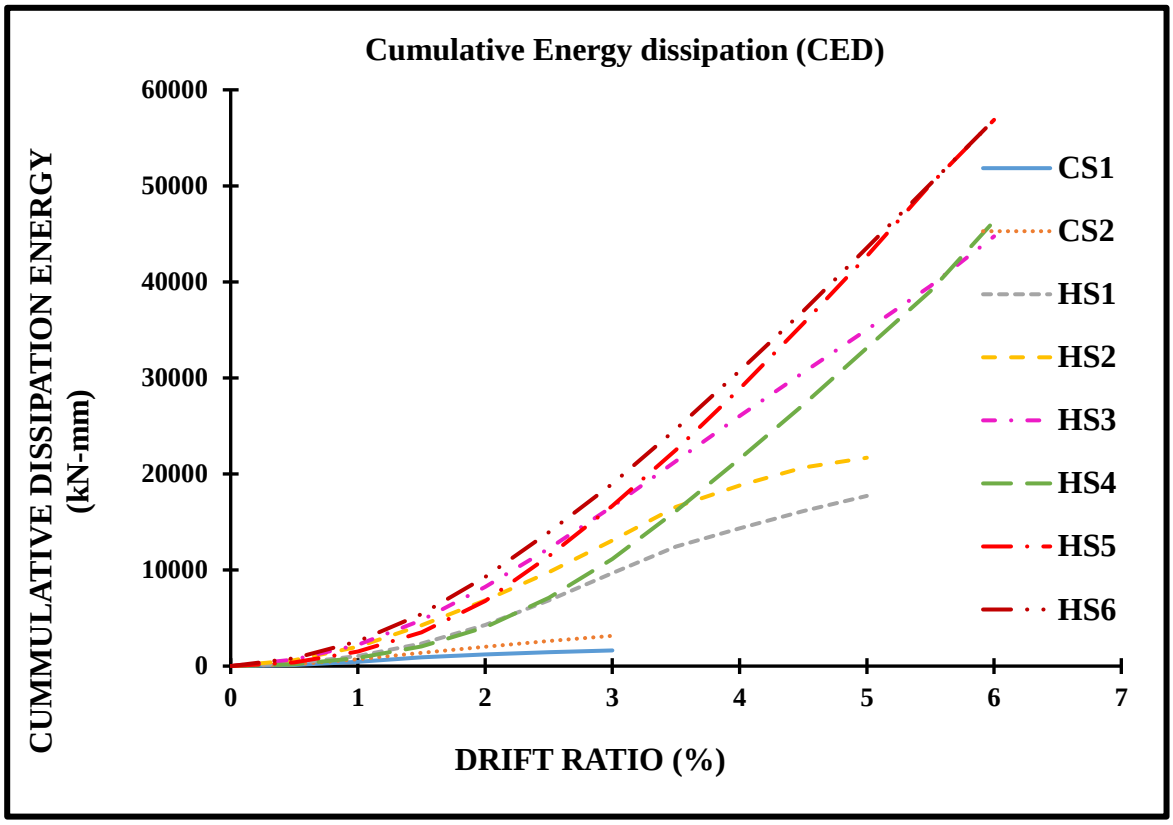

Figure 5. 6(b) Cumulative Energy dissipation (CED) curve of all the specimens

5.8 Analysis of cracks and failure pattern

The crack pattern of all the specimens has been represented in Figure 5.6(a-h); it can be observed that the minor spalling and cracks are common in the BCJ portion since the flexural plastic hinge has been developed at the end of the beam, which is adjoining with the column. Due to increased shear stress, cracks in concrete beams form near the support, such as a wall or column, which are known as shear cracks. Shear cracks are inclined at 45 degrees to the horizontal (Dehkordi *et al.* 2019). Initially, the minor cracks have appeared on the beams and columns at a 0.5% drift ratio trailed by the diagonal cracks in the BCJ area at 1 and 1.5% drift ratio because of the tension developed by the shear stress occurring in the core of the joint due to the applied loading in all the specimens. The same behavior has been observed in the study of Dehkordi *et al.* (2019). The pattern of cracks and failure modes of CS are different from HS. Shear cracks were observed in the case of CS1 specimen during the yielding of the beam followed by the complete failure

of the compression face of the beam after the ultimate loading, which was not seen in the case of CS2 (Figure 5.6(a-b)). Flexural cracks are those which are caused by direct and bending stresses caused by an external load. Initial flexural cracks were observed in the column joint where the beam is attached to the column junction at the second cycle, generating a displacement of 5.0 mm, and the average ultimate failure load was 46.5 kN with a displacement of 9.6 mm in the CS1 specimen. Since CS1 has 90^0 bent anchorage bars to develop the compression strut and tension tie action, there were diagonal cracks on the beam-column joint, shear cracks on the column, very wide-open flexural cracks on the face of the column, and concrete had also spalled out from the assemblage due to reversal loading. It was observed that in the case of CS2, the cracks initiated later due to the higher compressive strength, which led to the increase in the length of plastic hinge formed in the beam, and more extreme deterioration at the face of the joint region was observed in plastic hinge zone than CS1. After the gradual increase in the applied load, the diagonal shear cracks were observed at the joint region of CS2. Thus, it can be concluded that the governing mode of failure in CS1 was the compression face of the beam, which was absent in the case of CS2. Whereas in CS2, the governing mode of failure is the diagonal shear cracks at the face of BCJ. The exact mode of failure was observed in the study of Chidambaram and Aggarwal (2015) and Sharma (2019). In the case of headed bar specimen HS1 with a 0% steel fiber ratio, the cracks were initiated after a 3% drift ratio. The delay is attributed to the bond between the concrete and the headed bars that anchor the joint sturdily. At a 3.5% drift ratio, the cracks were observed at the anchorage portion of headed bars due to loss in the bond, which further propagates towards the face of the joint, which ultimately failed in the joint face at a 6% drift ratio (Figure 5.6c).

On the contrary, HS2 having a 1% steel fiber ratio, resisted the cracks better than HS1 due to the bridging effect of steel fibers, which further controlled the spalling of the concrete (Figure 5.6d). Additionally, it was observed that the propagation of cracks speeds up after a 4% drift ratio in the case of HS2. The cracking and failure pattern of HS2 and HS3 [Figure 5.6(d-e)] were observed to be similar due to the identical reinforcement detailing, except for the percentage of steel fibers ratio. The toughness of SFRC constrained the development of crack width at the joint, which attributed to the delay of cracks in HS3 compared to HS2. Due to the

lack of steel fibers in HS4, the cracks initiated at an early stage, i.e., at a drift ratio of 1.5%, and then propagated faster as the yielding of the beam continued up to the higher drift ratio (till 4%). Afterward, the rupture of concrete was observed, which initiated from the anchorage of the headed bar and grew to the face of the joint. Thus, the primary failure in HS4 was the rupture of concrete due to the absence of confinement provided by the steel fibers. A similar failure and crack pattern was observed in HS5 and HS6 (Figure 5.6(g-h)). The wider cracks initiated at a 4.5% drift ratio at the face of BCJ, followed by the flexural cracks in the beam and minor diagonal cracks in the column, which signified the strong column-weak beam mechanism.

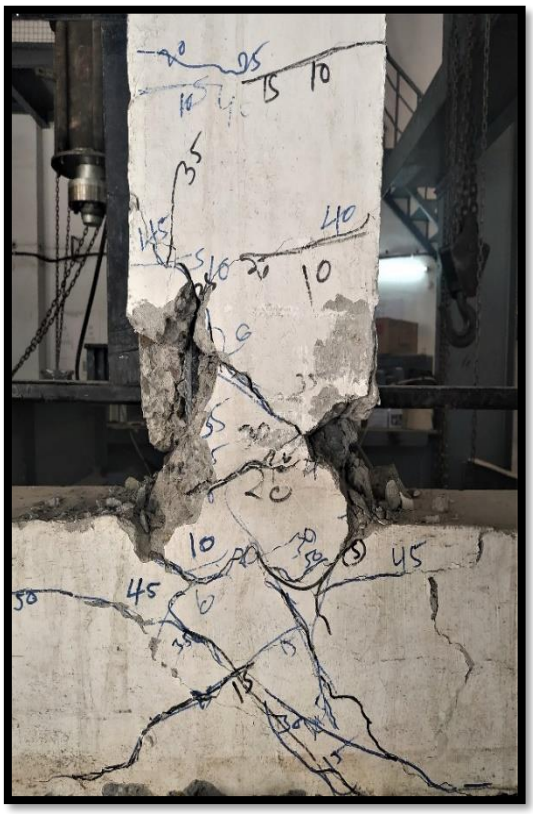

Figure 5.7 (a) CS1

Figure 5.7 (b) CS2

Figure 5.7 (c) HS1

Figure 5.7 (d) HS2

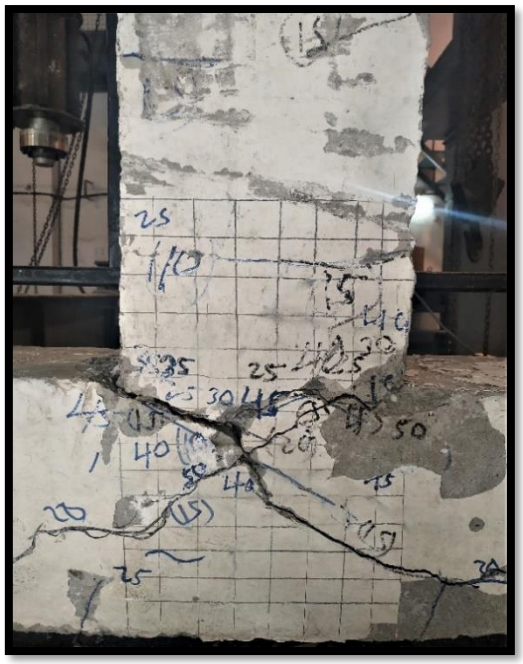

Figure 5.7 (e) HS3

Figure 5.7 (f) HS4

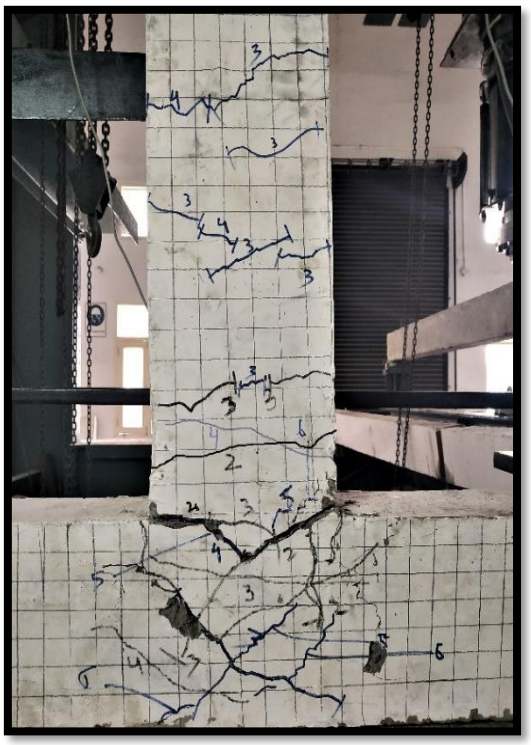

Figure 5.7 (g) HS5

Figure 5.7 (h) HS6

Figure 5. 7 (a-h) Crack pattern and failure modes of all the specimens

5.9 Joint shear strength

Columns are subjected to the opposite and approximately equal horizontal forces and moments at both columns' ends at each floor in frames subjected to seismic forces. The contra-flexure points are located near the columns' mid height and the beams' mid span. Thus, to avoid shear failure, the joint shear force (V_u) on a horizontal plane at the mid-high joint should be ≤ 0.85 of the nominal shear force (V_n) (ACI 352R-02). Under the following equations, the ACI 352R-02 specifications for the shear strength of the joint should be fulfilled.

$$\phi V_n = \phi 0.083 \gamma \sqrt{f_c'} b_{js} d_c \geq V_u \qquad (5.1)$$

Where ϕ is the strength reduction factor, γ is the shear strength factor reflecting joint confinement by lateral members, f_c' is the specified compressive strength of concrete, b_{js} is the effective width of joint transverse to the direction of shear, d_c is the depth of the column.

The demand for horizontal joint shear force (V_u) is determined based on the amount of beam, slab, and other reinforcements within the beam area as

$$V_u = T_f - V_c = \alpha f_y A_{ts} - V_c \quad (5.2)$$

Where, T_f is tension force in the reinforcement, V_c is shear in the column calculated based on M_{pr} for beam, α is stress multiplier for longitudinal reinforcement at the joint-member interface (≥ 1.25), A_{ts} is the area of tension reinforcement.

Shear in column (V_c) has been determined based on M_{pr} for beams

$$V_c = \frac{M_{pr}}{h_{st}} \quad (5.3)$$

All the specimens satisfy the criteria mentioned above, as indicated in Table 5.3. To sum up, the capacity of joint shear (V_u) calculated for specimens CS1, HS1, HS2, and HS3 (M20) have been compared to its counterparts CS2, HS4, HS5, and HS6 (M40), and it has been concluded that the grade of concrete has no significant influence on the joint shear force.

Table 5. 3 Joint shear strength calculations

Specimen	**Grade of concrete**	**Shear force in the column, V_c (kN)**	**Joint shear force, V_u (kN) (Experimental)**	**Ultimate shear strength of the joint, V_j (kN) (Predicted) (Jiuru *et al.* 1992)**	**Nominal joint shear force, V_n (kN) (ACI 318-19)**	**Nominal shear force, φV_n (kN) (ACI 352R)**	**$\varphi V_n \geq V_u$ (ACI 352R)**	**V_u/V_j Joint shear strength ratio (Experimental/Predicted)**
CS1	C20	11.69	129.66	101.2	154.4	178.16	Acceptable	1.28
CS2	C40	12.85	128.51	103.4	156.7	251.97	Acceptable	1.24
HS1	C20	11.69	129.66	103.9	159.3	178.16	Acceptable	1.24
HS2	C20	11.69	129.66	109.5	161.3	178.16	Acceptable	1.18
HS3	C20	11.69	129.66	110.7	197.1	178.16	Acceptable	1.17
HS4	C40	12.85	128.51	113.9	202.1	251.97	Acceptable	1.12
HS5	C40	12.85	128.51	116.2	205.0	251.97	Acceptable	1.10
HS6	C40	12.85	128.51	120.8	206.1	251.97	Acceptable	1.06

5.9.1 Comparison of experimental and predicted joint shear strength

The nominal joint shear strength, V_n has been calculated as $\sqrt{f_c'}A_j$ by ACI 318-19, where A_j is an effective cross-sectional area within the beam-column joint in a plane parallel to the headed bars. The values of V_n calculated using both the ACI 318-19 and ACI 352R-02 codes have been compared in Table 5.3.

To determine the ultimate shear strength of an SFRC joint, Jiuru *et al.* (1992) proposed the following equation:

$$V_j = V_{ct} + V_f + V_s \tag{5.4}$$

Where,

V_j = Ultimate shear strength of the joint

V_{ct} = Shear carried by concrete

$$V_{ct} = 0.1\left(1 + \frac{N}{b_c h_c f_c}\right) b_j h_j f_c' \tag{5.5}$$

V_f = Shear carried by steel fibers

$$V_f = 2\frac{l_f}{d_f} v_f b_j h_j \tag{5.6}$$

V_s = Shear carried by stirrups at joint

$$V_s = f_y \frac{A_{sh}}{S}(h_0 - a_s') \tag{5.7}$$

Where, h_c: depth of column, b_c: width of a column, f_c: concrete compressive strength, b_j: effective joint width perpendicular to shear direction, h_j: effective joint depth perpendicular to shear direction, d_f: fiber diameter, l_f: fiber length, f_y: yield strength, v_f: steel fiber ratio, A_{sh}: area of shear reinforcement, h_o: the beam's effective depth, S: stirrup spacing; a_s': distance between extreme compressive fiber and compressive reinforcement's centroid.

The predicted joint shear strength, V_j (kN), has been calculated using equation (5.4) and the values presented in Table 5.3. As ($V_u/V_j > 1.0$) is ranging from 1.06 to 1.28, hence it can be concluded that the specimens have high joint shear strength and have a specific impact on the overall strength of the anchorage capacity of headed bars as the specimens experience joint deterioration before the complete failure of joint. The contribution of concrete, stirrups, and fiber has been included in the equation Jiuru *et al.* (1992) proposed. The physical meaning of fiber contribution is incorrect as its presenting result is in mm^2 rather than kN.

5.10 Comparison of anchorage capacity of headed bars using non-linear regression analysis

To predict the anchorage capacity of headed bars in exterior BCJ, many researchers have proposed models or developed equations (Zuo and Darwin (1998); Shao, 2016; Sperry *et al.* (2017); Ghimire *et al.* (2019b)). The majority of the models have been developed using regression analysis, but the impact of steel fibers has not been considered in these models. Shao (2016) has developed an equation given by (5.8) to predict the peak load of closely spaced headed bars given by T_s.

$$T_s = (781 f_{cm}^{0.24} l_{eh}^{1.03} d_b^{0.35})\left(0.0836\frac{s}{d_b} + 0.3444\right) \quad (5.8)$$

Where, f_{cm} = concrete compressive strength (MPa), l_{eh} = development length of headed bars (mm), d_b = diameter of headed bars (mm), and s = center-to-center spacing between the bars (mm).

It can be clearly stated from Figure 5.7 that the predicted capacity of headed bars is less in the case of Shao (2016) than in the present study due to the absence of steel fibers in equation (5.8). The R^2 value (0.35) of the trend line (Figure 5.7) does not show satisfactory results when fitting the parameters of the current study into the equation used in Shao (2016) given by equation (5.8).

The current study's experimental results show that an increase in the percentage of steel fibers leads to an increase in the peak load of headed bars in BCJ. As a result, an attempt has

been made to use steel fibers as a parameter for the anchorage capacity of headed bars. As a result, in the current study, equation (5.8) has been modified to include steel fibers in the proposed equation given by (5.9). With the help of iterative non-linear regression analysis, a descriptive equation for anchorage capacity of headed bars (T_h) has been generated to ensure the test/calculated peak load ratio is equal to 1.0 while decreasing the sum of square (1-Test/Calculated)^2.

$$T_h = (842 f_{cm}^{0.30} l_{eh}^{0.83} d_b^{0.32}\ SF^{0.71})\left(0.0836\frac{s}{d_b} + 0.3444\right) \quad (5.9)$$

In Figure 5.7, the comparison of experimental peak load values and predicted peak load values (using equation 5.9) had been shown. The trend line in Figure 5.7 is nearly horizontal, having (R^2 =0.8), indicating that equation (5.9) effectively matches experimental results for concrete strengths (20 and 40 MPa), validating the suggested improvements in the f_{cm}, l_{eh}, d_b, and SF i.e. the power of compressive strength, embedment depth and diameter of bar has been modified to (0.30, 0.83 and 0.32), respectively given by equation (5.9), as compared to equation (5.8). Also, an additional parameter of steel fibers has been added in the equation whose power is 0.71.

In addition, the T_c/T_h ratio ranges from 0.77-1.28, with standard deviation and coefficient of variation of 0.07 and 0.06, respectively. The proposed model has been validated with research test results, concluding that the proposed model is very compatible with the research findings.

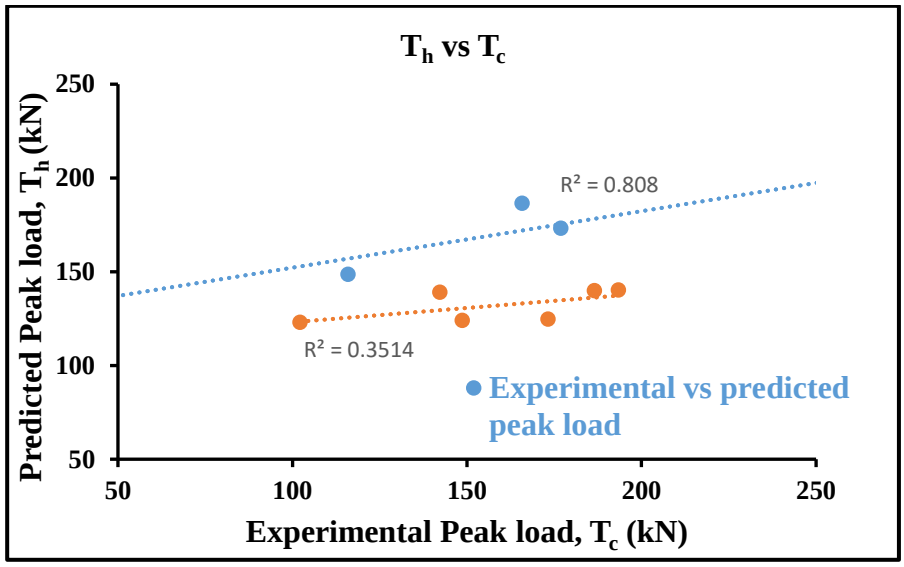

Figure 5. 8 Experimental peak load versus predicted peak load

5.11 Concluding Remarks

The purpose of this study is to compare the performance of steel fiber reinforced concrete (SFRC) external beam-column joints (BCJ) with headed bars as an anchorage mechanism to that of conventional bars under reversed cyclic loading detailed by ACI 318-19 and ACI 352R-02. The hysteresis curve, ductility, stiffness, energy dissipation, and cracking on all specimens have been investigated using structural parameters such as compressive strength (M20 and M40) and steel fibers (1 and 1.5 %). Due to their higher load carrying capacity, better ductility and stiffness response, and reduced congestion in BCJ, the experimental results revealed that headed bars in earthquake-prone areas should significantly replace conventional bars to some extent as they performed better than the conventional bars.

CHAPTER 6

CONCLUSIONS

6.1 General

This experimental research aims to investigate the influence of headed bars subjected to pull-out loads in cylindrical specimens and reversed cyclic loading in beam-column joints. The prime aim of this work is to examine the performance of the headed bars with different grades of concrete, percentage of steel fiber, bar diameter, and head shapes. For members subjected to pull-out load and reversed cyclic loading, the proposed code provisions for headed bar development length and steel fiber inclusion are presented as design provisions that accommodate the application of headed bars. Three hundred and twenty-four cylindrical specimens and eight exterior beam-column joints have been tested as part of the investigation to draw valuable conclusions from the findings. The research program has expanded our knowledge of headed bars for reinforced concrete structures.

6.2 Conclusions on Behavior of Pull-out specimens

On the basis of the experimental investigations, the following conclusions may be drawn:

1. In this study, two types of failure modes investigated through the pull-out test are (a) steel bar failure, (b) concrete blowout failure. Out of these two failures, it is observed that CBF has occurred in the specimens with a lesser steel fiber ratio (in most of the cases). At the same time, the specimens with more steel fiber ratio have SBF because of the bridging effect of steel fibers that improve the compressive and the tensile strength of the concrete.
2. The addition of steel fibers in the concrete mix has minimal effect in square heads having 20 mm diameter (S2) and significantly affects circular and rectangular heads having 16 mm diameter (C1 and R1, respectively).
3. The addition of steel fibers in the concrete mix has increased the capacity of the S2 specimens from 188.62 kN to 189.63 kN. But in the case of C1, the capacity is increased from 117 kN to 139 kN, i.e., 18.8 %. In the case of R1, the capacity is increased from 102

kN to 135 kN, i.e., 32.3%, as they improve the ductility and durability of concrete by controlling cracks.

4. The influence of bar diameter has a substantial effect on the load-carrying capacity of headed bars. When the diameter of the bar is increased from 16 mm to 25 mm, the peak load of the specimens increases by approximately (77 % to 90%). Therefore, increasing the bar diameter achieves a greater load-carrying capacity which dictates the head size and embedment depth of the headed bars too.
5. Based on the pull-out results, it is concluded that the circular-shaped-headed bars show the maximum load-carrying capacity. The peak load of the circular head is 4.4% higher than the square head and 8.3% higher than the rectangular head. The peak load has increased significantly in circular-headed specimens because of the uniform stress transfer through the circular head to the steel bar. Square & rectangular-headed bars are found to be relatively less effective in increasing the pull-out load. As the headed bars with circular heads are have a larger angle of anchor inclination near the surface of the concrete along with a large area of surface failure as compared to square and rectangular heads, thus the rectangular-shaped heads showed minimum load carrying capacity.
6. The effects of concrete compressive strength on the anchorage capacity of headed bars can be seen as the results of exponentiation with compressive strength as the base and 0.07, 0.19, and 0.05 as exponent for square, circular, and rectangular heads, respectively through the descriptive equation modelled using dummy variables, resulting in a less conservative prediction of headed bar anchorage capacity than in the ACI 318-19 equation.
7. The inclusion of SFRC, which is not included in the current design requirements of ACI 318-19, has increased the anchorage capacity of the headed bars.
8. Based on the pull-out results, it is concluded that the circular-shaped-headed bars show the maximum load-carrying capacity, which is also validated by the regression analysis using dummy variables. The peak load of the circular head is 4.4% higher than the square head and 8.3% higher than the rectangular head.
9. The bearing capacity of the headed bars decreases with increase in an embedment depth of the headed bars as it is inversely proportional to embedment depth and the circular head is having the maximum bearing capacity (i.e. 35.1% larger than rectangular head and 56.9%

larger than square head) due to the larger head area. Additionally, square & rectangular headed bars are found to be relatively less effective in increasing the pullout load because of the lesser head area as compared to the circular head.

10. The ultimate bond strength (τ_{max}) calculated using ACI 318-19 is higher than the design bond strength calculated using fib MC2010 and EN 1992-1-1 because of the inclusion of embedment depth factor in ACI formula which is excluded in the bond strength formula of fib MC2010 and EN 1992-1-1. Thus, fib MC2010 and EN 1992-1-1 should take into account the embedment depth factor that affects the strength of the concrete structure. Thus, it has been concluded that ACI 318-19 provides the best results as compared to the other two codes used in the study.
11. The results of the tests have been compared to the ACI Building Code's development length provisions (ACI 318-19). The anchorage strength of headed bars has been calculated as embedment length, concrete compressive strength, bar diameter, and percentage of steel fibers. These expressions have been compared to previous studies' test results and used to create design provisions for the development length of the headed bar.
12. The compressive strength of concrete determines the maximum load-carrying capacity of headed bar, diameter, embedment depth of bar and percentage of steel fibers, according to an analytical model developed using Genetic Programming. GP provides better results as compared to the regression equation. The R^2 value for a peak load of circular-headed bars predicted by GP and REG is 0.96 and 0.95, respectively. Also, the error line of peak load predicted from regression analysis is ±10% than the experimental peak load, whereas the error line in GP is ±5%.

6.3 Conclusions on behavior of Beam-Column Joint

1. Headed bars have performed better than the conventional bars as an anchorage mechanism for BCJ, when tested under quasi-static reverse loading with a considerable reduction in cracking. Additionally, the detailing of exterior BCJ with headed bars (HS) has resulted in less congestion and quicker assembly of reinforcement in the joint region. HS has been placed more easily in the concrete than the conventional bars (CS). Consequently, it can be concluded that the headed bars in the BCJ with steel fibers in the concrete mix perform better

than the conventional bars due to the bond provided by the headed bars aided with the bridging effect of steel fibers.

2. The combination of headed bars with steel fibers has shown a moderate increase in the compressive strength of the specimens. Having the same mix proportion, the specimens with 1.5% steel fibers show 13.6% higher compressive strength than the specimens without steel fibers in M40. In comparison, specimens with 1.5% steel fibers show 8.3% higher compressive strength than specimens without steel fibers in the case of M20.
3. Analysis of the hysteresis plot concludes that there has been a substantial enhancement in the pre and post-yield performance of all the HS under reversed cyclic loading. Different grades of concrete and steel fibers ratios have been used to compare the load-carrying capacity of headed bar specimens. It is justified that difference in concrete grade results in the peak load of HS4, HS5, and HS6 having 28.17%, 20.2%, and 10.42% higher than HS1, HS2, and HS3 at the same percentage of steel fibers. HS1 and HS4 increase peak load by 66.6% and 64.6%, respectively, over CS1 and CS2, which have no steel fibers in the joint. As a result, it can be concluded that the overall performance of headed bars in seismic response is far superior to that of conventional bars.
4. The improvement in the ductility factor exhibited by HS is 1.12-2.12 times CS, specifically in the post-peak yielding. There has been a 29.40% increase in the ductility of HS6 (1.5% SF) for HS4 (0% SF) in the case of M40 grade and a 28.75% increase in the ductility of HS3 (1.5% SF) for HS1 (0% SF). This leads to the conclusion that the rise in the ductility factor is due to an increase in the amount of steel fibers in the concrete mix, which restricts the joint and aids in crack control, hence enhancing the ductility of the joint.
5. The stiffness degradation of specimens HS4, HS5, and HS6 has been 18-40% lower at a 3.5% drift ratio than HS1, HS2, and HS3, respectively, indicating the efficiency of M40 grade of concrete over M20 grade of concrete, according to the stiffness curve. All of the HS have fulfilled the ACI 374.1-05 stiffness standards.
6. The percentage increase of steel fibers and the presence of headed bars have substantially delayed the initiation of cracks and overall controlled cracks in the specimens. In comparison to CS, where cracks appear at a 0.5 percent drift ratio, HS1, (HS2 and HS3), and (HS5 and HS6), respectively, have 3 percent, (3.5%), and (4%) drift ratios. Additionally, the bond

provided by the headed bars has been ascertained to be effective in case of failure of the specimens. Failure at the joint face is more common in all HS, but failure at the compression face of the beam is more common in CS. This is attributed to the headed bars' more persistent anchorage bond when compared to ordinary bars.

7. The anchorage strength of headed bars in beam-column joints subjected to reversed cyclic loading has been modified by adding additional parameters, i.e., percentage of steel fibers, to develop a descriptive equation using non-linear regression analysis, in which the anchorage strength of the headed bar is a function of embedment length, concrete compressive strength, bar spacing, and bar diameter within the joint region.

6.4 Future Scope

Headed bars cannot be used in lightweight concrete under the current design provisions or in ACI 318-19 due to a lack of data. As a result, research into the anchorage behavior of headed bars in light concrete is highly recommended. The largest headed bars examined in this study have a diameter of 25 mm. Only a few tests have been done on larger-headed bars. According to some theories, the low strength has been caused by a lack of bearing surface area and a clear cover (Kang and Mitra 2007; Chun *et al.* 2009; Nilforoush *et al.* 2017). It is therefore recommended that more research should be done on the anchorage strength of larger-headed bars.

List of Publications

1. Sachdeva, P., Roy, A.B.D., & Kwatra, N. (2021). Anchorage Capacity of Headed Bars in Steel Fiber Reinforced Concrete. *Canadian Journal of Civil Engineering*, 49(1), 134-137. https://doi.org/10.1139/cjce-2020-0608
2. Sachdeva, P., Roy, A.B.D., & Kwatra, N. (2021). Performance evaluation of different shapes of headed bars in steel fiber reinforced concrete. *Advances in Concrete Construction: An International Journal (Techno Press)*, 11(5), 387-396. https://doi.org/10.12989/acc.2021.11.5.387
3. Sachdeva, P., Roy, A.B.D., & Kwatra, N. (2021). Behaviour of steel fibers reinforced exterior beam column joint using headed bars under reverse cyclic loading. *Structures (Elsevier)*, 33, 3929-3943. https://doi.org/10.1016/j.istruc.2021.06.074

References

Abbas, Y.M., & Iqbal Khan, M. (2016). Fiber–Matrix Interactions in Fiber-Reinforced Concrete: A Review. *Arabian Journal for Science and Engineering*, 41(4), 1183–1198. doi: 10.1007/s13369-016-2099-1

ACI 318. (2011). *Building Code Requirements for Structural Concrete*. Farmington Hills, MI: American Concrete Institute.

ACI 374.1. (2005). *Acceptance Criteria for Moment Frames Based on Structural Testing and Commentary: an ACI Standard*. Farmington Hills, MI: American Concrete Institute.

ACI 352R-02. (2002). *Recommendations for design of beam-column connections in monolithic reinforced concrete structures*. Farmington Hills, MI: American Concrete Institute.

Al-Shannag, M.J. (2007). *Durability of steel fiber reinforced concrete in sulfate environment*. Final Research Report No. 38/426, King Saud University, Saudi Arabia.

Al-Ta'An, S. A., & Rahomy, S. S. M. (2013). Effect of steel fibres on the developed stresses in deformed headed bars. *Fibre Concrete 2013*, 1–10.

Alavi-Dehkordi, S., Mostofinejad, D., & Alaee, P. (2019). Effects of high-strength reinforcing bars and concrete on seismic behavior of RC beam-column joints. *Engineering Structures*, 183, 702–719. https://doi.org/10.1016/j.engstruct.2019.01.019

Alrasyid, H., Yoganata, Y. S., Suluch, M., & Iranata, D. (2017). Headed reinforcement in concrete structure: State of the art. *AIP Conference Proceedings*, 1903. https://doi.org/10.1063/1.5011495

ASTM (American Society for Testing and Materials) A970/A970M. (2016). *Standard Specification for Headed Steel Bars for Concrete Reinforcement*. ASTM International, West Conshohocken, PA, USA.

ASTM (American Society for Testing and Materials) C900. (2013). *Standard test method for pullout strength of hardened concrete*. ASTM International, West Conshohocken, PA, USA.

Aval, S. B. B., Ketabdari, H., & Gharebaghi, A. S. (2017). Estimating shear strength of short rectangular reinforced concrete columns using nonlinear regression and Gene Expression Programming. *Structures*, 12, 13-23. https://doi.org/10.1016/j.istruc.2017.07.002

Banthia, N. (1990). A study of some factors affecting the fiber-matrix bond in steel fiber reinforced concrete. *Canadian Journal of Civil Engineering*, 17(4), 610-620.

Barros, J. A. O., & Cruz, J. S. (2001). Fracture Energy of Steel Fiber-Reinforced Concrete. *Mechanics of Advanced Materials and Structures*, 8(1), 29–45. doi:10.1080/10759410119428

Bashandy, T. R. (1996). *Application of Headed Bars in Concrete Members*. Ph.D Thesis.

Benmokrane, B., Mohamed, H. M., Manalo, A., & Cousin, P. (2017). Evaluation of Physical and Durability Characteristics of New Headed Glass Fiber–Reinforced Polymer Bars for Concrete Structures. *Journal of Composites for Construction*, 21(2), 04016081. https://doi.org/10.1061/(ASCE)CC.1943-5614.0000738

Bentur, A., & Mindess, S. (1990). *Fibre reinforced cementitious composites*. Elsevier Applied Science, London.

Bindhu, K.R., Jeya, K.P., Manickaselvam, V.K. (2008). Seismic resistance of exterior beam column joints non-conventional reinforcement detailing. *Structural Engineering and Mechanics an International Journal*, 30(6), 733–761.

Bjorhovde, R. (1983). Discussion: Headed shear stud connectors in a stub-girder floor system: a preliminary study. *Canadian Journal of Civil Engineering*, 10, 165-167.

Brantschen, F., Faria, D. M. V., Fernández Ruiz, M., & Muttoni, A. (2016). Bond behaviour of

straight, hooked, U-shaped and headed bars in cracked concrete. *Structural Concrete*, 17(5), 799–810. https://doi.org/10.1002/suco.201500199

Cairns, J. (2015). Bond and anchorage of embedded steel reinforcement in fib Model Code 2010. *Structural Concrete*, 16(1), 45–55. https://doi.org/10.1002/suco.201400043

Canadian Standards Association (CSA) A23.3-04. (2004). Design of Concrete Structures. CSA, Ontario, Canada.

Chiu, C. K., Chi, K. N., & Lin, K. C. (2016). Experimental investigation on the seismic Anchorage behavior of headed bars based on full-size specimens of exterior and interior beam-column joints. *Advances in Structural Engineering*, 19(5), 777–794. https://doi.org/10.1177/1369433216630346

Choi, D.-U. (2006a). Test of headed reinforcement in pullout II: Deep Embedment. *International Journal of Concrete Structures and Materials*, 18(3E), 151–159.

Choi, D.-U. (2006b). Test of Headed Reinforcement in Pullout II: Deep Embedment. *International Journal of Concrete Structures and Materials*, 18, 151–159. https://doi.org/10.4334/ijcsm.2006.18.3e.151

Choi, D.-U.K., Hong, S.-G.U.I., & Lee, C.Y. (2002). Test of Headed Reinforcement in Pullout. KCI Concrete Journal, 14, 102-110.

Chourasia, A., & Gupta, S. (2019). Influential Parameters for Headed Bars in RC Beam-Column Joint. *Current Science*, 116(10), 1666. https://doi.org/10.18520/cs/v116/i10/1666-1673

Chun, S. C., Lee, S. H., Kang, T. H. K., Oh, B., & Wallace, J. W. (2007). Mechanical Anchorage in Exterior Beam-Column Joints Subjected to Cyclic Loading. *ACI Structural Journal*, 104(1). https://doi.org/10.14359/18438

Chun, S. C., Oh, B., Lee, S. H., & Naito, C. J. (2009). Anchorage Strength and Behavior of Headed Bars in Exterior Beam-Column Joints. *ACI Structural Journal*, 106(5). https://doi.org/10.14359/51663098

Chun, S. C., & Shin, Y. S. (2014). Cyclic testing of exterior beam-column joints with varying joint aspect ratio. *ACI Structural Journal*, 111(3), 693–704. https://doi.org/10.14359/51686730

Chutarat, N., & Aboutaha, R. S. (2003). Cyclic Response of Exterior Reinforced Concrete Beam-Column Joints Reinforced with Headed Bars—Experimental Investigation. *ACI Structural Journal*, 100(2). https://doi.org/10.14359/12490

Dancygier, A.N., Katz, A., & Wexler, U. (2010). Bond between deformed reinforcement and normal and high-strength concrete with and without fibers. *Materials and Structures*, 43, 839-856.

Dancygier, A.N., & Katz, A. (2012). Bond over direct support of deformed rebars in normal and high strength concrete with and without fibers. *Materials and Structures*, 45, 265-275.

Danie Roy, A. B., Sharma, U. K., & Bhargava, P. (2016). Bond Properties of GFRP Laminate with Heat-Damaged Concrete. *Journal of Composites for Construction*, 20(2), 04015053. https://doi.org/10.1061/(ASCE)CC.1943-5614.0000620

Daniel, A., Joshua, & Dubey, R.N. (2015). Finite element simulation of traditional and earthquake resistant brick masonry building under shock loading. *Coupled Systems Mechanics*, 4, 19–36. https://doi.org/10.12989/CSM.2015.4.1.019

Delhomme, F., Roure, T., Arrieta, B., & Limam, A. (2015). Static and cyclic pullout behavior of cast-in-place headed and bonded anchors with large embedment depths in cracked concrete. *Nuclear Engineering and Design*, 287, 139–150. https://doi.org/10.1016/j.nucengdes.2015.03.012

Delhomme, F., Roure, T., Arrieta, B., & Limam, A. (2016). Pullout behavior of cast-in-place headed and bonded anchors with different embedment depths. *Materials and Structures*, 49(5), 1843–1859. https://doi.org/10.1617/s11527-015-0616-4

DeVries, R.A. (1996). *Anchorage of Headed Reinforcement in Concrete*. Ph.D. Dissertation, pp. 1-314.

Dong-Uk, Choi., Sung-GUI, Hong., & C.-Y. L. (2002). Test of Headed Reinforcement in Pullout. *KCI Concrete Journal*, Vol. 14, pp. 102–110.

Draper, N.R., & Smith, H. (1981). *Applied Regression Analysis*. New York, John Wiley and Sons, pp. 241-249.

EN 1992-1-1. (2004). *Eurocode 2: Design of concrete structures- Part 1.1: General rules and rules for buildings*. Brussels, Belgium.

Farhan, N.A., Sheikh, M.N., & Hadi, M. (2020) Effect of Steel Fiber on Engineering Properties of Geopolymer Concrete. *Materials Journal*, 117, 29-40.

Fib MC2010. (2012). *Model Code for Concrete Structures*. International Federation for Structural Concrete, Berlin, Ernest & John.

Gandomi, A. H., Alavi, A. H., Ting, T. O., & Yang, X.-S. (2013). Intelligent Modeling and Prediction of Elastic Modulus of Concrete Strength via Gene Expression Programming. *Advances in Swarm Intelligence*, 564–571. doi:10.1007/978-3-642-38703-6_66

Ganesan, N., Indira, P. V., & Abraham, R. (2007). Steel fibre reinforced high performance concrete beam-column joints subjected to cyclic loading. *ISET Journal of Earthquake Technology*, 44(3–4), 445–456.

Ghali, A., & Youakim, S. A. (2005b). Headed Studs in Concrete: State of the Art. *ACI Structural Journal*, 102(5), 657-667. https://doi.org/10.14359/14661

Ghimire, K. P., Darwin, D., & O'Reilly, M. (2018). *Anchorage of Headed Reinforcing Bars in Concrete*. University of Kansas Center for Research, Lawrence, Report No. 127, p. 278.

Ghimire, K. P., Shao, Y., Darwin, D., & O'Reilly, M. (2019a). Conventional and high-strength headed bars-Part 1: Anchorage tests. *ACI Structural Journal*, 116(3), 255–264.

https://doi.org/10.14359/51714479

Ghimire, K. P., Shao, Y., Darwin, D., & O'Reilly, M. (2019b). Conventional and high-strength headed bars—Part 2: Data analysis. *ACI Structural Journal*, 116(3), 265–272. https://doi.org/10.14359/51714480

Gholampour, A., Gandomi, A. H., & Ozbakkaloglu, T. (2017). New formulations for mechanical properties of recycled aggregate concrete using gene expression programming. *Construction and Building Materials*, 130, 122-145. https://doi.org/10.1016/j.conbuildmat.2016.10.114

Gupta, A. (2017). *Development of an Efficient Anchorage Mechanism for RC Beam-Column Joints*. CSIR-Central Building Research Institute.

Hameed, R., Turatsinze, A., Duprat, F., & Sellier, A. (2013). Bond stress-slip Behaviour of Steel Reinforcing Bar Embedded in Hybrid Fiber-reinforced Concrete. *KSCE Journal of Civil Engineering*, 17, 1700-1707.

Harajli, M. H., & Gharzeddine, O. (2007). Effect of steel fibers on bond performance of steel bars in NSC and HSC under load reversals. *Journal of Materials in Civil Engineering*, 19, 864-873.

Harajli, M. H., Hamad, B., & Karam, K. (2002). Bond-slip response of reinforcing bars embedded in plain and fiber concrete. *Journal of Materials in Civil Engineering*, 14, 503-511.

Harajli, M. H., & Shalloukh, K. A. (1997). Effects of fibers on developments/splice strength of reinforcing bars in tension. *ACI Materials Journal*, 94, 317-324.

Hasaballa, M., & El-Salakawy, E. (2018). Anchorage Performance of GFRP Headed and Bent Bars in Beam-Column Joints Subjected to Seismic Loading. *Journal of Composites for Construction*, 22(6), 04018060. https://doi.org/10.1061/(ASCE)CC.1943-5614.0000888

Hawkins, N. M. (1967). *The bearing strength of concrete-I. Loading through rigid plates covering part of the full supporting area*. Ph.D Thesis, School of Civil Engineering, University of Sydney.

Henriques, J., Raposo, J.M., da Silva, L.S., & Neves, L.C., (2013). Tensile resistance of steel-reinforced anchorages: experimental evaluation. ACI Structural Journal, 110:239–50.

Hiremath, P. N., & Yaragal, S. C. (2018). Performance evaluation of reactive powder concrete with polypropylene fibers at elevated temperatures. *Construction and Building Materials*, 169, 499–512. https://doi.org/10.1016/j.conbuildmat.2018.03.020

Holschemacher, K., Mueller, A. T., & Ribakov, Y. (2010). Effect of steel fibers on mechanical properties of high-strength concrete. *Materials and Design*, 31, 2604-2615.

Hong, S. G., Chun, S. C., Lee, S. H., & Oh, B. (2007a). Strut-and-Tie model for development of headed bars in exterior beam-column joint. *ACI Structural Journal*, 104(5), 590–600. https://doi.org/10.14359/18861

Hong, S. G., Chun, S. C., Lee, S. H., & Oh, B. (2007b). Strut-and-Tie Model for Development of Headed Bars in Exterior Beam-Column Joint. *ACI Structural Journal*, 104(5). https://doi.org/10.14359/18861

Hwang, H. J., Park, H. G., Choi, W. S., Chung, L., & Kim, J. K. (2014). Cyclic loading test for beam column connections with 600 MPa (87 ksi) beam flexural reinforcing bars. *ACI Structural Journal*, 111, 913.

Islam, S., Afefy, H. M., Sennah, K., & Azimi, H. (2015). Bond characteristics of straight- and headed-end, ribbed-surface, GFRP bars embedded in high-strength concrete. *Construction and Building Materials*, 83, 283–298.

Janssens, V., O'Dwyer, D.W., & Chryssanthopoulos, M.K. (2012). Assessing the Consequences of Building Failures. *Structural Engineering International*, 22, 99-104.

Jeffrey, L., & Wright, S. L. M. (1997). *The Develpment Length and Anchorage Behavior of*

Headed Reinforcing Bars. Report, pp. 1–153.

Jiuru, T., Chaobin, H., Kaijian, Y., & Yongcheng, Y. (1992). Seismic behavior and shear strength of framed joint using steel-fiber reinforced concrete. *Journal of Structural Engineering*, 118(2), 341-358.

John, R. P. M., & Singh, B. (2013). Bond behaviour of deformed steel bars embedded in recycled aggregate concrete. *Construction and Building Materials*, 49, 852–862. https://doi.org/10.1016/j.conbuildmat.2013.08.031

Joshi, S. G., Londhe, S. N., & Kwatra, N. (2014). Determination of natural periods of vibration using genetic programming. *Earthquakes and structures,* 6, No.2. doi: http://dx.doi.org/10.12989/eas.2014.6.2.000

Kaikea, A., Achoura, D., Duplan, F., & Rizzutic, L. (2014). Effect of mineral admixtures and steel fiber volume contents on the behavior of high-performance fiber reinforced concrete. *Materials and Design*, 63, 493-499.

Kaliluthin, A. K., & Kothandaraman, S. (2017). Performance Evaluation of Exterior Beam–Column Joint with Core Reinforcement Technique Subjected to Reverse Cyclic Loading. *Arabian Journal for Science and Engineering*, 42(9), 3673–3687. https://doi.org/10.1007/s13369-017-2440-3

Kamel, A., Elwi, A., & Cheng, R. (2006). Experimental study on the behavior of carbon fiber reinforced polymer sheets bonded to concrete. *Canadian Journal of Civil Engineering*, 33, 1438-1449.

Kanchanadevi, A., & Ramanjaneyulu, K. (2019). Investigations on the behaviour of corrosion damaged gravity load designed beam-column sub-assemblages under reverse cyclic loading. *Earthquake and Structures*, 16(2), 235–251. https://doi.org/http://dx.doi.org/10.12989/eas.2019.16.2.235

Kang, T. H.-K., Shin, M., & Mitra, N. (2009). Headed Reinforcement Applications for

Reinforced Concrete Beam-Column Connections. *Structures Congress 2009*, 1–10. https://doi.org/10.1061/41031(341)164

Kang, T. H. K., Shin, M., Mitra, N., & Bonacci, J. F. (2009a). Seismic design of reinforced concrete beam-column joints with headed bars. *ACI Structural Journal*, 106(6), 868–877. https://doi.org/10.14359/51663188

Kang, T. H. K., Shin, M., Mitra, N., & Bonacci, J. F. (2009b). Seismic Design of Reinforced Concrete Beam-Column Joints with Headed Bars. *ACI Structural Journal*, 106(06). https://doi.org/10.14359/51663188

Kang, T. H. K., Ha, S. S., & Choi, D. U. (2010a). Bar pullout tests and seismic tests of small-headed bars in beam-column joints. *ACI Structural Journal*, 107(1), 32–42.

Kang, T. H. K., Ha, S. S., & Choi, D. U. (2010b). Bar Pullout Tests and Seismic Tests of Small-Headed Bars in Beam-Column Joints. *ACI Structural Journal*, 107(01). https://doi.org/10.14359/51663386

Kang, T. H. K., Kim, W., & Shin, M. (2012). Cyclic Testing for Seismic Design Guide of Beam-Column Joints with Closely Spaced Headed Bars. *Journal of Earthquake Engineering*, 16(2), 211–230. https://doi.org/10.1080/13632469.2011.610497

Kang, T. H. K., & Mitra, N. (2012). Prediction of performance of exterior beam-column connections with headed bars subject to load reversal. *Engineering Structures*, 41, 209–217. https://doi.org/10.1016/j.engstruct.2012.03.036

Kawale, A., & Patil, Y. D. (2016). Pullout Capacity and Bond Behaviour of Headed Reinforcement in concrete. *International Journal of Innovative Research in Science, Engineering and Technology*, 5(7), 12114–12119. https://doi.org/10.15680/IJIRSET.2016.0507014

Kermani, E., Jafarian, Y. & Baziar, M.H. (2009). New predictive models for the vmax/amax ratio of strong ground motions using Genetic Programming. *International Journal of Civil*

Engineering, 7(4), 236-247.

Khederzadeh, H., & Sennah, K. (2014). Development of Cost-Effective PL-3 Concrete Bridge Barrier Reinforced with Sand-Coated GFRP Bars: Static Load Tests. *Canadian Journal of Civil Engineering*, 41, 368-379.

Kheyroddin, A., & Dabiri, H. (2020). Cyclic performance of RC beam-column joints with mechanical or forging (GPW) splices; an experimental study. *Structures*, 28, 2562–2571. https://doi.org/10.1016/j.istruc.2020.10.071

Kim, S. (2016). Pullout strength of high strength headed reinforcement vertically jointed to RC member. *International Journal of Latest Research in Engineering and Technology*, 2(5), 57–62.

Kim, W., & Laman, J. A. (2010). Integral abutment bridge response under thermal loading. *Engineering Structures*, 32(6), 1495–1508. https://doi.org/10.1016/j.engstruct.2010.01.004

Kotynia, R., Szczech, D., & Kaszubska, M. (2017). Bond Behavior of GRFP Bars to Concrete in Beam Test. *Procedia Engineering*, 193, 401–408. https://doi.org/10.1016/j.proeng.2017.06.230

Kumar, P., & Chaudhary, S. (2019). Effect of reinforcement detailing on performance of composite connections with headed studs. *Engineering Structures*, 179, 476–492. doi:10.1016/j.engstruct.2018.05.069

Lee, H. J., & Yu, S. Y. (2009a). Cyclic response of exterior beam-column joints with different anchorage methods. *ACI Structural Journal*, 106(3), 329–339. https://doi.org/10.14359/56497

Lee, H. J., & Yu, S. Y. (2009b). Cyclic Response of Exterior Beam-Column Joints with Different Anchorage Methods. *ACI Structural Journal*, 106(3). https://doi.org/10.14359/56497

Lim, J. C., Karakus, M., & Ozbakkaloglu, T. (2016). Evaluation of ultimate conditions of FRP-confined concrete columns using genetic programming. *Computers & Structures*, 162, 28-37. https://doi.org/10.1016/j.compstruc.2015.09.005

Looney, T. J., Arezoumandi, M., Volz, J. S., & Myers, J. J. (2012). An Experimental Study on Bond Strength of Reinforcing Steel in Self-Consolidating Concrete. *International Journal of Concrete Structures and Materials*, 6(3), 187–197. https://doi.org/10.1007/s40069-012-0017-9

Lu, J., Park, B. J., Kumar, B., Castro, M., Choi, H. J., & Feller, J.-F. (2010). Polyaniline nanoparticle–carbon nanotube hybrid network vapour sensors with switchable chemo-electrical polarity. *Nanotechnology*, 21(25), 255501. https://doi.org/10.1088/0957-4484/21/25/255501

Kalaivani, M., & Karthik, S. (2016). Steel Fibre Reinforced Concrete Beam-Column Joint – A Review. *International Journal of Engineering Research And*, 5(05), 166–173. https://doi.org/10.17577/ijertv5is050067

Oinam, R. (2013). Experimental Study on Beam- Column Joint with Fibres under Cyclic Loading. *IOSR Journal of Engineering*, 3(7), 13–23. https://doi.org/10.9790/3021-03721323

Mahan, M. (2016). *Seismic Requirements for Headed Bar Reinforcement*. Retrieved from http://www.dot.ca.gov/des/techpubs/mtd.html

Mansouri, I., Azmathulla, H. M., & Hu, W. J. (2018). Gene expression programming application for prediction of ultimate axial strain of FRP-confined concrete. *Elektronički Časopis Građevinskog Fakulteta Osijek*, *9*(16), 64-76. https://doi.org/10.13167/2018.16.6

Marchetto, F. (2015). *Use of Headed Reinforcement Bars in Construction*. Ph.D. Dissertation.

Marchetto, F., Caldentey, A. P., & Peiretti, H. C. (2016). Structural performance of corner joints subjected to a closing moment using mechanical anchorages: an experimental study. *Structural Concrete*, 17, 987-1002.

Marques, J. L. G., & Jirsa, J. O. (1975). A study of hooked bar anchorages in beam-column joints. *ACI Structural Journal*, 72, 198–209.

McMackin, P. J., Slutter, R. G., & Fisher, J. W. (1973). Headed Steel Anchor under Combined Loading. *AISC Engineering Journal*, 10, 43-52.

Megget, L. M. (2003). The Seismic Design and Performance of Reinforced Concrete Beam-Column Knee Joints in Buildings. *Earthquake Spectra*, 19(4), 863–895. https://doi.org/10.1193/1.1623782

Metwally, I. M. (2014). Three-dimensional finite element analysis of reinforced concrete slabs strengthened with epoxy-bonded steel plates. *Advances in Concrete Construction*, 2(2), 91-108.

Miao, T., & Zheng, W. (2019). Local bearing capacity of concrete under the combined action of pressure force and bond stress. *Construction and Building Materials*, 226, 152–161. https://doi.org/10.1016/j.conbuildmat.2019.07.288

Moreno, D. M., Trono, W., Jen, G., Ostertag, C.P., & Billington, S. L. (2014). Tension stiffening in reinforced high performance fiber reinforced cement-based composites. *Cement and Concrete Composites*, 50, 36–46. doi:10.1016/j.cemconcomp.2014.03

Muduli, P.K., Das, S.K. (2013). CPT-Based Seismic Liquefaction Potential Evaluation using Multi-gene Genetic Programming Approach. *Indian Geotechnical Journal*, 44, 86–93. https://doi.org/10.1007/s40098-013-0048-4

Murty, C. V. R., Raj, D. C., Bajpai, K. K., & Jain, S. K. (2003). Effectiveness of reinforcement details in exterior reinforcement concrete beam–column joints for earthquake resistance. *ACI Structural Journal*, 100(2), 149-156.

Naito, J. N., Moehle, J. P., & Mosalam, K. M. (2001). *Experimental and Computational Evaluation of Reinforced Concrete Bridge Beam-Column Connections for Seismic Performance*. University of California, Berkeley, Caltrans Contract No. 59A131.

Nilforoush, R. (2019). A Refined Model for Predicting Concrete-Related Failure Load of Tension Loaded Cast-in-Place Headed Anchors in Uncracked Concrete. *Nordic Concrete Research*, 60(1), 105–129. https://doi.org/10.2478/ncr-2019-0091

Nilforoush, R., Nilsson, M., & Elfgren, L. (2017). Experimental evaluation of tensile behaviour of single cast-in-place anchor bolts in plain and steel fibre-reinforced normal- and high-strength concrete. *Engineering Structures*, 147, 195–206. https://doi.org/10.1016/j.engstruct.2017.05.062

Nilforoush, R., Nilsson, M., & Elfgren, L. (2018). Experimental Evaluation of Influence of Member Thickness, Anchor-Head Size, and Orthogonal Surface Reinforcement on the Tensile Capacity of Headed Anchors in Uncracked Concrete. *Journal of Structural Engineering*, 144(4), 04018012. https://doi.org/10.1061/(asce)st.1943-541x.0001976

Nitsure, S.P., Londhe, S.N. and Khare, K.C. (2009). Application of Genetic Programming for estimation of ocean wave heights. *Nature and Biologically Inspired Computing*, 1520-1523. https://doi.org/10.1109/NABIC.2009.5393666

Ou, Y. C., Canseco, H. A., & Kurniawan, D. P. (2017). Anchorage performance of headed deformed bars in exterior beam-column joints under cyclic loading. *KSCE Journal of Civil Engineering*, 21(7), 2837–2849. https://doi.org/10.1007/s12205-017-1868-z

Paknejadi, A. H., & Behfarnia, K. (2020). Performance of reinforced self-consolidating concrete beam-column joints with headed bars subjected to pseudo-static cyclic loading. *Ain Shams Engineering Journal*. https://doi.org/10.1016/j.asej.2019.12.008

Papadopoulos, V., Murcia-Delso, J., & Shing, P. B. (2015). *Development Length for Headed Bars in Slab-Column Joints of RC Slab Bridges*. Department of Civil Engineering, University of California, San Diego, Report No. SSRP-15/10.

Parate, K., & Kumar, R. (2019). Shear strength criteria for design of RC beam–column joints in building codes. In *Bulletin of Earthquake Engineering* (Vol. 17). https://doi.org/10.1007/s10518-018-0492-8

Park, H.-K., Yoon, Y.-S., & Kim, Y.-H. (2004). The effect of head plate details on the pull-out behaviour of headed bars. *Magazine of Concrete Research*, 55(6), 485–496. https://doi.org/10.1680/macr.55.6.485.37602

Parmar, M., & Jamnu, M. A. (2014). Experimental study on direct pull out test : straight bar , bent-up and headed bar. *International Journal of Innovative Research & Development*, 3(6), 513–518.

Paulay, T. (1989). Equilibrium criteria for reinforcement concrete beam–column joints. *ACI Structural Journal*, 86(6), 635–643.

Prasanna, K., Ramasubramani, R., Anandh, K. S., Saisabarish, S., & Maddu, V. K. (2017). Strengthening of beam - Column joint with steel fibre reinforced concrete under seismic loading. *IOP Conference Series: Earth and Environmental Science*, 80(1). https://doi.org/10.1088/1755-1315/80/1/012040

Prince, M. J. R., & Singh, B. (2014). Investigation of bond behaviour between recycled aggregate concrete and deformed steel bars. *Structural Concrete*, 15(2), 154–168. https://doi.org/10.1002/suco.201300042

Prince, M. J. R., & Singh, B. (2015a). Bond behaviour of normal- and high-strength recycled aggregate concrete. *Structural Concrete*, 16(1), 56–70. https://doi.org/10.1002/suco.201300101

Prince, M. J. R., & Singh, B. (2015b). Bond strength of deformed steel bars in high-strength recycled aggregate concrete. *Materials and Structures/Materiaux et Constructions*, 48(12), 3913–3928. https://doi.org/10.1617/s11527-014-0452-y

Qian, Zz., Lu, Xl. & Sheng, Mq. (2019). Experimental Investigation of the Tensile Capacity for

Anchor Groups with Different Spacing Between Cast-in-Place Headed Anchors of High Strength and Deep Embedment. *Arabian Journal for Science and Engineering*, 44(5), 4745–4755. https://doi.org/10.1007/s13369-018-3548-9

Rabi, M., Cashell, K. A., Shamass, R., & Desnerck, P. (2020). Bond behaviour of austenitic stainless steel reinforced concrete. *Engineering Structures*, 221, 111027. https://doi.org/10.1016/j.engstruct.2020.111027

Rajagopal, S., & Prabavathy, S. (2015). Investigation on the seismic behavior of exterior beam–column joint using T-type mechanical anchorage with hair-clip bar. *Journal of King Saud University - Engineering Sciences*, 27(2), 142–152. https://doi.org/10.1016/j.jksues.2013.09.002

Ramanjaneyulu, K., Novák, B., Sasmal, S., Roehm, C., Lakshmanan, N., & Iyer, N. R. (2013a). Seismic performance evaluation of exterior beam-column sub-assemblages designed according to different codal recommendations. *Structure and Infrastructure Engineering*, 9(8), 817–833. https://doi.org/10.1080/15732479.2011.625954

Rautenberg, J.M. (2011). *Drift capacity of concrete columns reinforced with high-strength steel.* Ph.D Thesis, Purdue University, USA.

Robins, P., Austin, S., & Jones, P. (2002). Pull-out behavior of hooked steel fibers. *Materials and Structures*, 35, 434–442.

Sachdeva, P., Roy, A.B.D., & Kwatra, N. (2021). Anchorage Capacity of Headed Bars in Steel Fiber Reinforced Concrete. *Canadian Journal of Civil Engineering*. https://doi.org/10.1139/cjce-2020-0608

Sachdeva, P., Roy, A.B.D., Kwatra, N. (2021a). Performance evaluation of different shapes of headed bars in steel fiber reinforced concrete. *Advances in Concrete Construction: An International Journal*, 11(5), 387-396.

Sallal, R.A, Munther, L.A-H., Nadheer, S.A., Sajjad H.A., & Ahmed L.K. (2020). Repeated drop-weight impact tests on self-compacting concrete reinforced with micro-steel fiber. *Heliyon*, 6(1), e03198. doi: 10.1016/j.heliyon.2020.e03198

Sarıdemir, M. (2010). Genetic programming approach for prediction of compressive strength of concretes containing rice husk ash. *Construction and Building Materials*, 24(10), 1911-1919. https://doi.org/10.1016/j.conbuildmat.2010.04.011

Sasmal, S., Novák, B., Ramanjaneyulu, K., Srinivas, V., Roehm, C., Lakshmanan, N., & Iyer, N. R. (2010). Seismic retrofitting of damaged exterior beam–column joints using fibre reinforced plastic composite–steel plate combined technique. *Structure and Infrastructure Engineering*, 1–14. https://doi.org/10.1080/15732479.2010.529918

Sasmal, S., & Voggu, S. (2019). Nonseismic and seismic designed beam-column joints with rebar end anchors–Behaviour under reverse cyclic loading. *Journal of Earthquake Engineering*, 1–23. https://doi.org/10.1080/13632469.2019.1657990

Setia, S., Murty, C.V.R., & Sehgal, V.K. (2009). Seismic behavior of weak-axis beam-column connections. In F. Mazzolani, J. M. Ricles, R. Sause (Eds.). *Behaviour of Steel Structures in Seismic Areas*. CRC Press, Italy.

Shao, Y. (2016). *Anchorage of Headed Reinforcing Bars in Exterior Beam-Column Joints*. Ph.D Thesis.

Sharma, R., & Bansal, P. P. (2019). Behavior of RC exterior beam column joint retrofitted using UHP-HFRC. *Construction and Building Materials*, 195, 376–389. https://doi.org/10.1016/j.conbuildmat.2018.11.052

Sim, H.-J., & Chun, S.-C. (2018). A Reevaluation of Anchorage Strength of Headed Bars in Exterior Beam-Column Joints. *Journal of the Korea Concrete Institute*, 30(2), 207–216. https://doi.org/10.4334/JKCI.2018.30.2.207

Siva Chidambaram, R., & Agarwal, P. (2015). Seismic behavior of hybrid fiber reinforced

cementitious composite beam-column joints. *Materials and Design*, 86, 771–781. https://doi.org/10.1016/j.matdes.2015.07.164

Sperry, J., Yasso, S., Searle, N., DeRubeis, M., Darwin, D., O'Reilly, M., Matamoros, A., Feldman, L., Lepage, A., & Lequesne, R. (2017). Conventional and High-Strength Hooked Bars-Part 1: Anchorage Tests. *ACI Structural Journal*, 114, 255-266.

Stoker, J.R., Boulware, R.L., Crozier, W.F., & Swirsky, R.A. (1974). *Anchorage Devices for Large Diameter Reinforcing Bars*. Caltrans, Report No. CA-DOT-TL-6626-1-73-30, USA.

Sulaiman, M. F., Ma, C.-K., Apandi, N. M., Chin, S., Awang, A. Z., Mansur, S. A., & Omar, W. (2017). A Review on Bond and Anchorage of Confined High-strength Concrete. *Structures*, 11, 97–109. https://doi.org/10.1016/j.istruc.2017.04.004

Thompson, M. K., Jirsa, J. O., Breen, J. E., & Klingner, R. E. (2002). *Anchorage behavior of headed reinforcement : literature review*. Research Report 1855-1.

Tran, M.-T., Bui, Q.-B., Sentosa, B., Nguyen, N.-T., Duong, T.-H., & Plé, O. (2018). Sustainable RC Beam-Column Connections with Headed Bars: A Formula for Shear Strength Evaluation. *Sustainability*, 10(2), 401. https://doi.org/10.3390/su10020401

Tsonos, A.G., Tegos, I.A., & Penelis, G.Gr. (1993). Seismic resistance of Type 2 exterior beam–column joints reinforcement with inclined bars. *ACI Structural Journal*, 89(1), 3–12.

Uma, S. R., & Jain, S. K. (2006). Seismic design of beam-column joints in RC moment resisting frames - Review of codes. *Structural Engineering and Mechanics*, 23(5), 579–597. https://doi.org/10.12989/sem.2006.23.5.579

Wallace, J. W., McConnell, S. W., Gupta, P., & Cote, P. A. (1998). Use of headed reinforcement in beam-column joints subjected to earthquake loads. *ACI Structural Journal*, 95(5), 590–606. https://doi.org/10.14359/574

Wright, J. L., & McCabe, S. L. (1997). *The Develpment Length and Anchorage Behavior of*

Headed Reinforcing Bars. Ph.D Thesis.

Yadav, D., Kwatra, N., and Agarwal P. (2018). Post Yield deformation parameters of reinforced concrete beam with corroded reinforcement. *Structural Concrete, 20*, 318-329. https://doi.org/10.1002/suco.201800037.

Yang, J.-M., Lee, J.-H., Yoon, Y.-S., Cook, W. D., & Mitchell, D. (2012). Influence of Steel Fibers and Headed Bars on the Serviceability of High-Strength Concrete Corbels. *Journal of Structural Engineering*, 138(1), 123–129. https://doi.org/10.1061/(asce)st.1943-541x.0000427

Yang, J. M., Min, K. H., Shin, H. O., & Yoon, Y. S. (2010). The use of T-headed bars in high-strength concrete members. *Proceedings of FraMCoS-7*, 1328–1334.

Yuji, I., Nishinosono, K., Iida, M., & Hirabayashi, M. (2016). Steel Fiber Reinforced Interior Beam-column Joints without Shear Reinforcement and Beam Bars Passing through Joint. *Concrete Journal*, 54, 694-701.

Zhanping, Y., ShuWei, G., & Jianping, D. (2012). Predictive models for dynamic modulus using weighted least square nonlinear multiple regression model. *Canadian Journal of Civil Engineering*, 39, 589-597.

Zuo, J., & Darwin, D. (1998). *Bond Strength of High Relative Rib Area Reinforcing Bars*. SM Report No. 46, University of Kansas Center for Research, Inc., Lawrence, Kansas.

Annexure

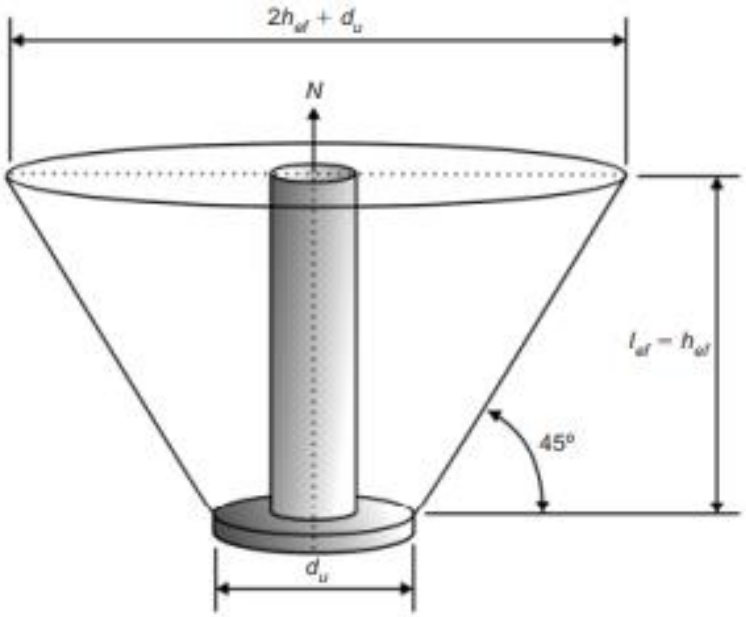

Figure A. 1 Projected concrete breakout area (A_N) when the headed bar is placed at the center of the specimen (Park *et al.* 2003)

Table A. 1 Bond strength and failure modes of the specimens

Specimen	Grade of concrete	d_b (mm)	l_{eh} (mm)	P_{max} (kN)	P_n (kN)	Area of Section (mm^2)	P_{tr}	τ_{max} (MPa) (ACI 318-19)	f_{bd} (MPa) (MC2010)	f_{bd} (EN 1992-1-1)	Bearing Stress (MPa)	Failure mode
S1SF0	M20	150	128	115.0	72.17	17662.5	0.007	17.90	1.973	2.290	0.39	CBF
	M40	150	128	130.4	102.07	17662.5	0.007	20.30	2.487	3.643	0.56	CBF
	M60	150	128	133.6	125.00	17662.5	0.008	20.80	2.850	4.774	0.68	CBF
S1SF0.5	M20	150	128	120.0	72.17	17662.5	0.007	18.70	1.972	2.290	0.39	CBF
	M40	16	128	127.8	102.07	201.0	0.636	19.90	1.230	3.643	0.56	SBF
	M60	150	128	148.6	125.00	17662.5	0.008	23.10	2.848	4.774	0.68	CBF

Specimen	Grade of concrete	d_b (mm)	l_{eh} (mm)	P_{max} (kN)	P_n (kN)	Area of Section (mm^2)	P_{tr}	τ_{max} (MPa) (ACI 318-19)	f_{bd} (MPa) (MC2010)	f_{bd} (EN 1992-1-1)	Bearing Stress (MPa)	Failure mode
S2SF0	M20	150	160	188.6	64.55	17662.5	0.011	18.80	1.965	2.290	0.35	CBF
	M40	150	160	195.9	91.29	17662.5	0.011	19.50	2.480	3.643	0.50	CBF
	M60	150	160	202.9	111.81	17662.5	0.011	20.20	2.842	4.774	0.61	CBF
S2SF0.5	M20	150	160	188.7	64.55	17662.5	0.011	18.80	1.965	2.290	0.35	CBF
	M40	20	160	198.2	91.29	314.0	0.631	19.70	1.240	3.643	0.50	SBF
	M60	20	160	203.9	111.81	314.0	0.649	20.30	1.566	4.774	0.61	SBF
S3SF0	M20	150	200	214.1	57.74	17662.5	0.012	13.60	1.962	2.290	0.31	CBF
	M40	150	200	230.0	81.65	17662.5	0.013	14.60	2.476	3.643	0.44	CBF
	M60	150	200	239.6	100.00	17662.5	0.014	15.30	2.838	4.774	0.54	CBF

Specimen	Grade of concrete	d_b (mm)	l_{eh} (mm)	P_{max} (kN)	P_n (kN)	Area of Section (mm^2)	P_{tr}	τ_{max} (MPa) (ACI 318-19)	f_{bd} (MPa) (MC2010)	f_{bd} (EN 1992-1-1)	Bearing Stress (MPa)	Failure mode
S3SF0.5	M20	150	200	228.8	57.74	17662.5	0.013	14.60	1.960	2.290	0.31	CBF
	M40	25	200	235.2	81.65	490.6	0.479	15.00	1.543	3.643	0.44	SBF
	M60	25	200	242.7	100.00	490.6	0.495	15.50	1.876	4.774	0.54	SBF
R1SF0	M20	150	128	102.0	108.28	17662.5	0.006	15.90	1.974	2.290	0.39	CBF
	M40	150	128	119.2	153.14	17662.5	0.007	18.50	2.489	3.643	0.55	CBF
	M60	150	128	127.4	187.55	17662.5	0.007	19.80	2.851	4.774	0.68	CBF
R1SF0.5	M20	150	128	126.6	108.28	17662.5	0.007	19.70	1.972	2.290	0.39	CBF
	M40	16	128	130.8	153.14	201.0	0.651	20.30	1.200	3.643	0.55	SBF
	M60	16	128	136.3	187.55	201.0	0.678	21.20	1.509	4.774	0.68	SBF

Specimen	Grade of concrete	d_b (mm)	l_{eh} (mm)	P_{max} (kN)	P_n (kN)	Area of Section (mm^2)	P_{tr}	τ_{max} (MPa) (ACI 318-19)	f_{bd} (MPa) (MC2010)	f_{bd} (EN 1992-1-1)	Bearing Stress (MPa)	Failure mode
R1SF1.5	M20	150	128	135.0	108.28	17662.5	0.008	21.00	1.971	2.290	0.39	CBF
	M40	16	128	139.8	153.14	201.0	0.696	21.70	1.111	3.643	0.55	SBF
	M60	16	128	152.9	187.55	201.0	0.761	23.80	1.343	4.774	0.68	SBF
R2SF0	M20	150	160	175.5	96.85	17662.5	0.010	17.50	1.966	2.290	0.35	CBF
	M40	150	160	187.2	136.97	17662.5	0.011	18.60	2.481	3.643	0.50	CBF
	M60	150	160	195.7	167.75	17662.5	0.011	19.50	2.843	4.774	0.61	CBF
R2SF0.5	M20	150	160	188.9	96.85	17662.5	0.011	18.80	1.965	2.290	0.35	CBF
	M40	20	160	192.3	136.97	314.0	0.612	19.10	1.277	3.643	0.50	SBF
	M60	20	160	199.3	167.75	314.0	0.635	19.80	1.596	4.774	0.61	SBF

Specimen	Grade of concrete	d_b (mm)	l_{eh} (mm)	P_{max} (kN)	P_n (kN)	Area of Section (mm^2)	P_{tr}	τ_{max} (MPa) (ACI 318-19)	f_{bd} (MPa) (MC2010)	f_{bd} (EN 1992-1-1)	Bearing Stress (MPa)	Failure mode
R3SF0	M20	150	200	226.6	86.63	17662.5	0.013	14.40	1.960	2.290	0.31	CBF
	M40	150	200	231.3	122.51	17662.5	0.013	14.70	2.476	3.643	0.44	CBF
	M60	150	200	237.6	150.04	17662.5	0.013	15.10	2.838	4.774	0.54	CBF
R3SF0.5	M20	150	200	188.0	86.63	17662.5	0.011	12.00	1.965	2.290	0.31	CBF
	M40	25	200	238.2	122.51	490.6	0.486	15.20	1.531	3.643	0.44	SBF
	M60	25	200	240.8	150.04	490.6	0.491	15.30	1.883	4.774	0.54	SBF
C1SF0	M20	150	128	117.0	166.19	17662.5	0.007	18.20	1.973	2.290	0.39	CBF
	M40	150	128	135.2	235.03	17662.5	0.008	21.00	2.487	3.643	0.55	CBF
	M60	16	128	136.8	287.85	201.0	0.681	21.30	1.504	4.774	0.68	SBF

Specimen	Grade of concrete	d_b (mm)	l_{eh} (mm)	P_{max} (kN)	P_n (kN)	Area of Section (mm^2)	P_{tr}	τ_{max} (MPa) (ACI 318-19)	f_{bd} (MPa) (MC2010)	f_{bd} (EN 1992-1-1)	Bearing Stress (MPa)	Failure mode
C1SF0.5	M20	150	128	123.7	166.19	17662.5	0.007	19.20	1.972	2.290	0.39	CBF
	M40	16	128	142.4	235.03	201.0	0.709	22.10	1.085	3.643	0.55	SBF
	M60	16	128	150.3	287.85	201.0	0.748	23.40	1.369	4.774	0.68	SBF
C2SF0	M20	150	160	189.7	148.65	17662.5	0.011	18.90	1.965	2.290	0.35	CBF
	M40	150	160	202.4	210.22	17662.5	0.011	20.10	2.479	3.643	0.50	CBF
	M60	20	160	208.5	257.46	314.0	0.664	20.80	1.537	4.774	0.61	SBF
C2SF0.5	M20	150	160	196.2	148.65	17662.5	0.011	19.50	1.964	2.290	0.35	CBF
	M40	20	160	228.9	210.22	314.0	0.729	22.80	1.044	3.643	0.50	SBF
	M60	20	160	233.6	257.46	314.0	0.744	23.20	1.377	4.774	0.61	SBF

Specimen	Grade of concrete	d_b (mm)	l_{eh} (mm)	P_{max} (kN)	P_n (kN)	Area of Section (mm^2)	P_{tr}	τ_{max} (MPa) (ACI 318-19)	f_{bd} (MPa) (MC2010)	f_{bd} (EN 1992-1-1)	Bearing Stress (MPa)	Failure mode
C3SF0	M20	150	200	241.6	132.95	17662.5	0.014	15.40	1.959	2.290	0.31	CBF
	M40	150	200	246.0	188.03	17662.5	0.014	15.70	2.474	3.643	0.44	CBF
	M60	25	200	252.5	230.28	490.6	0.515	16.10	1.836	4.774	0.54	SBF
C3SF0.5	M20	150	200	250.1	132.95	17662.5	0.014	15.90	1.958	2.290	0.31	CBF
	M40	25	200	260.3	188.03	490.6	0.531	16.60	1.441	3.643	0.44	SBF
	M60	25	200	278.4	230.28	490.6	0.567	17.70	1.730	4.774	0.54	SBF
S1SF1	M20	16	128	121.0	72.17	201.0	0.602	18.80	0.782	2.290	0.39	SBF
	M40	16	128	135.9	102.07	201.0	0.676	21.10	1.149	3.643	0.56	SBF
	M60	16	128	151.8	125.00	201.0	0.755	23.60	1.354	4.774	0.68	SBF

Specimen	Grade of concrete	d_b (mm)	l_{eh} (mm)	P_{max} (kN)	P_n (kN)	Area of Section (mm^2)	P_{tr}	τ_{max} (MPa) (ACI 318-19)	f_{bd} (MPa) (MC2010)	f_{bd} (EN 1992-1-1)	Bearing Stress (MPa)	Failure mode
S1SF1.5	M20	16	128	125.0	72.17	201.0	0.622	19.40	0.742	2.290	0.39	SBF
	M40	16	128	140.9	102.07	201.0	0.701	21.90	1.100	3.643	0.56	SBF
	M60	16	128	161.5	125.00	201.0	0.804	25.10	1.258	4.774	0.68	SBF
S2SF1	M20	20	160	189.2	64.55	314.0	0.603	18.80	0.781	2.290	0.35	SBF
	M40	20	160	201.5	91.29	314.0	0.642	20.10	1.219	3.643	0.50	SBF
	M60	20	160	204.2	111.81	314.0	0.650	20.30	1.564	4.774	0.61	SBF
S2SF1.5	M20	20	160	189.6	64.55	314.0	0.604	18.90	0.778	2.290	0.35	SBF
	M40	20	160	204.6	91.29	314.0	0.652	20.40	1.199	3.643	0.50	SBF
	M60	20	160	208.5	111.81	314.0	0.664	20.80	1.537	4.774	0.61	SBF

Specimen	Grade of concrete	d_b (mm)	l_{eh} (mm)	P_{max} (kN)	P_n (kN)	Area of Section (mm^2)	P_{tr}	τ_{max} (MPa) (ACI 318-19)	f_{bd} (MPa) (MC2010)	f_{bd} (EN 1992-1-1)	Bearing Stress (MPa)	Failure mode
S3SF1	M20	25	200	230.5	57.74	490.6	0.470	14.70	1.046	2.290	0.31	SBF
	M40	25	200	231.4	81.65	490.6	0.472	14.70	1.559	3.643	0.44	SBF
	M60	25	200	246.2	100.00	490.6	0.502	15.70	1.861	4.774	0.54	SBF
S3SF1.5	M20	25	200	249.3	57.74	490.6	0.508	15.90	0.970	2.290	0.31	SBF
	M40	25	200	243.6	81.65	490.6	0.497	15.50	1.509	3.643	0.44	SBF
	M60	25	200	249.1	100.00	490.6	0.508	15.90	1.850	4.774	0.54	SBF
R1SF1	M20	16	128	131.2	108.28	201.0	0.653	20.40	0.680	2.290	0.39	SBF
	M40	16	128	128.9	153.14	201.0	0.641	20.00	1.219	3.643	0.55	SBF
	M60	16	128	143.8	187.55	201.0	0.716	22.40	1.434	4.774	0.68	SBF

Specimen	Grade of concrete	d_b (mm)	l_{eh} (mm)	P_{max} (kN)	P_n (kN)	Area of Section (mm^2)	P_{tr}	τ_{max} (MPa) (ACI 318-19)	f_{bd} (MPa) (MC2010)	f_{bd} (EN 1992-1-1)	Bearing Stress (MPa)	Failure mode
R2SF1	M20	20	160	190.9	96.85	314.0	0.608	19.00	0.770	2.290	0.35	SBF
	M40	20	160	196.9	136.97	314.0	0.627	19.60	1.248	3.643	0.50	SBF
	M60	20	160	201.5	167.75	314.0	0.642	20.10	1.582	4.774	0.61	SBF
R2SF1.5	M20	20	160	193.1	96.85	314.0	0.615	19.20	0.756	2.290	0.35	SBF
	M40	20	160	201.2	136.97	314.0	0.641	20.00	1.220	3.643	0.50	SBF
	M60	20	160	204.8	167.75	314.0	0.652	20.40	1.561	4.774	0.61	SBF
R3SF1	M20	25	200	234.2	86.63	490.6	0.477	14.90	1.031	2.290	0.31	SBF
	M40	25	200	240.6	122.51	490.6	0.490	15.30	1.521	3.643	0.44	SBF
	M60	25	200	243.5	150.04	490.6	0.496	15.50	1.872	4.774	0.54	SBF

Specimen	Grade of concrete	d_b (mm)	l_{eh} (mm)	P_{max} (kN)	P_n (kN)	Area of Section (mm^2)	P_{tr}	τ_{max} (MPa) (ACI 318-19)	f_{bd} (MPa) (MC2010)	f_{bd} (EN 1992-1-1)	Bearing Stress (MPa)	Failure mode
R3SF1.5	M20	25	200	240.4	86.63	490.6	0.490	15.30	1.006	2.290	0.31	SBF
	M40	25	200	242.7	122.51	490.6	0.495	15.50	1.513	3.643	0.44	SBF
	M60	25	200	246.9	150.04	490.6	0.503	15.70	1.859	4.774	0.54	SBF
C1SF1	M20	16	128	129.2	166.19	201.0	0.643	20.10	0.700	2.290	0.39	SBF
	M40	16	128	149.7	235.03	201.0	0.745	23.30	1.012	3.643	0.55	SBF
	M60	16	128	153.6	287.85	201.0	0.764	23.90	1.336	4.774	0.68	SBF
C1SF1.5	M20	16	128	139.0	166.19	201.0	0.692	21.60	0.603	2.290	0.39	SBF
	M40	16	128	156.3	235.03	201.0	0.778	24.30	0.946	3.643	0.55	SBF
	M60	16	128	164.9	287.85	201.0	0.821	25.60	1.224	4.774	0.68	SBF

Specimen	Grade of concrete	d_b (mm)	l_{eh} (mm)	P_{max} (kN)	P_n (kN)	Area of Section (mm^2)	P_{tr}	τ_{max} (MPa) (ACI 318-19)	f_{bd} (MPa) (MC2010)	f_{bd} (EN 1992-1-1)	Bearing Stress (MPa)	Failure mode
C2SF1	M20	20	160	199.8	148.65	314.0	0.636	19.90	0.713	2.290	0.35	SBF
	M40	20	160	232.5	210.22	314.0	0.740	23.10	1.021	3.643	0.50	SBF
	M60	20	160	240.9	257.46	314.0	0.767	24.00	1.331	4.774	0.61	SBF
C2SF1.5	M20	20	160	210.4	148.65	314.0	0.670	20.90	0.646	2.290	0.35	SBF
	M40	20	160	242.8	210.22	314.0	0.773	24.20	0.956	3.643	0.50	SBF
	M60	20	160	250.2	257.46	314.0	0.797	24.90	1.271	4.774	0.61	SBF
C3SF1	M20	25	200	254.0	132.95	490.6	0.518	16.20	0.951	2.290	0.31	SBF
	M40	25	200	273.1	188.03	490.6	0.557	17.40	1.389	3.643	0.44	SBF
	M60	25	200	289.1	230.28	490.6	0.589	18.40	1.687	4.774	0.54	SBF

Specimen	Grade of concrete	d_b (mm)	l_{eh} (mm)	P_{max} (kN)	P_n (kN)	Area of Section (mm^2)	P_{tr}	τ_{max} (MPa) (ACI 318-19)	f_{bd} (MPa) (MC2010)	f_{bd} (EN 1992-1-1)	Bearing Stress (MPa)	Failure mode
C3SF1.5	M20	25	200	260.2	132.95	490.6	0.530	16.60	0.925	2.290	0.31	SBF
	M40	25	200	281.9	188.03	490.6	0.575	18.00	1.353	3.643	0.44	SBF
	M60	25	200	300.7	230.28	490.625	0.613	19.20	1.639	4.774	0.54	SBF

**where S, R, and C stands for square, rectangular and circular shapes. 1, 2, and 3 stand for diameters of bars, i.e., 16-, 20-, and 25-mm. SF stands for steel fibers having 0, 0.5, 1 and, 1.5% ratios in the concrete mix. CBF stands for concrete blowout failure, and SBF stands for steel bar failure.*

Table A. 2 Descriptive statistics of compressive strength of steel fiber reinforced concrete

Grade of Concrete (MPa)	**SF (%)**	**Number of Specimens**	**f_{cm} (MPa)**	**Average f_{cm} (MPa)**	**Standard deviation (MPa)**
20	0	Specimen 1	26	26.5	0.50
		Specimen 2	26.5		
		Specimen 3	27		
20	0.5	Specimen 1	26.84	27.3	0.46
		Specimen 2	27.76		
		Specimen 3	27.3		
20	1	Specimen 1	28.2	28.2	0.71
		Specimen 2	28.91		
		Specimen 3	27.49		
20	1.5	Specimen 1	29.05	28.9	0.15
		Specimen 2	28.75		
		Specimen 3	28.9		
40	0	Specimen 1	43.1	43.1	0.93
		Specimen 2	44.03		
		Specimen 3	42.17		

Grade of Concrete (MPa)	SF (%)	Number of Specimens	f_{cm} (MPa)	Average f_{cm} (MPa)	Standard deviation (MPa)
40	0.5	Specimen 1	45.4	45.4	1.40
		Specimen 2	44.0		
		Specimen 3	46.8		
40	1	Specimen 1	46.8	46.7	0.58
		Specimen 2	46.12		
		Specimen 3	47.28		
40	1.5	Specimen 1	47.84	47.2	0.64
		Specimen 2	47.2		
		Specimen 3	46.56		
60	0	Specimen 1	61.85	62.3	0.45
		Specimen 2	62.75		
		Specimen 3	62.3		
60	0.5	Specimen 1	66.8	66.8	0.74
		Specimen 2	67.54		
		Specimen 3	66.06		
60	1	Specimen 1	68.39	68.9	0.51
		Specimen 2	68.8		
		Specimen 3	69.41		

Grade of Concrete (MPa)	**SF (%)**	**Number of Specimens**	**f_{cm} (MPa)**	**Average f_{cm} (MPa)**	**Standard deviation (MPa)**
60	1.5	Specimen 1	70.09	69.7	0.39
		Specimen 2	69.68		
		Specimen 3	69.31		